Frank Lindseth

Ultrasound Guided Surgery:
Multimodal Visualization and Navigation Accuracy

NTNU Trondheim
Norges teknisk-naturvitenskapelige universitet

Doktor ingeniør avhandling 2002:143
Fakultet for informasjonsteknologi, matematikk og elektronikk
Institutt for datateknikk og informasjonsvitenskap
IDI-rapport: 2002:13

Ultrasound Guided Surgery: Multimodal Visualization and Navigation Accuracy

Frank Lindseth

Norwegian University of Science and Technology
December 2002

Ultrasound Guided Surgery: Multimodal Visualization and Navigation Accuracy
Frank Lindseth

Norges teknisk-naturvitensapelige universitet
Fakultet for informasjonsteknologi, matematikk og elektroteknikk
Institutt for datateknikk og informasjonsvitenskap

ISBN: 82-471-5538-9
ISSN (NTNU): 0809-103X
Doktor ingeniør avhandling: 2002-143

ISSN (IDI): 0802-6394
IDI-rapport: 2002-13

Preface

This thesis is submitted to the Norwegian University of Science and Technology (NTNU) in partial fulfillment of the requirements for the degree "Doktor Ingeniør".

The research work has been carried out at the Department of Ultrasound, SINTEF Unimed, in the period 1999-2002, in collaboration with the Department of Computer and Information Science (IDI) at the Faculty of Information Technology, Mathematics and Electrical Engineering, NTNU and the University Hospital in Trondheim, particularly the Departments of Neurosurgery, Vascular Surgery, and Laparoscopic Surgery.

My supervisors have been Jørn Hokland, IDI, NTNU and Åge Grønningsæter, MISON AS while Toril A. Nagelhus Hernes, SINTEF Unimed have provided me with daily guidance.

During the period from 1999 to 2001 the work was supported by the Norwegian Research Council through the strategic University program for Medical Technology at NTNU; the remainder of the work was supported by SINTEF Unimed, where I am currently employed.

Acknowledgements

First of all, I would like to thank Jørn Hokland for accepting the formal responsibilities as my supervisor and Åge Grønningsæter for introducing me to the field of ultrasound-based neuronavigation.

A special thank to everybody at the department of ultrasound, SINTEF Unimed:
Toril A. Nagelhus Hernes, Jon Harald Kaspersen, Thomas Langø, Jon Bang, Steiner Ommedal, Geir Arne Tangen, Tormod Selbekk, Ela Sjølie, Hege A. Brekken, Erlend Salberg, Stig Tore Svee, Jahn Otto N. Andersen and Mona K. Eidem. They have all contributed in creating an inspiring and joyful work environment. Furthermore, I would like to thank my co-authors, especially Toril, Jon Harald, Thomas and Jon, for interesting discussions and invaluable scientific contributions. Also thanks to my former co-workers now at MISON: Åge Grønningsæter, Torgrim Lie, Atle Kleven and Tore E. Årseth.

I wish to thank our collaborating doctors at the University Hospital in Trondheim:
Geirmund Unsgård, Neurosurgery, Hans Olav Myhre, Vascular Surgery and Ronald Mårvik, Laparoscopic Surgery for an unique collaboration between surgeons and engineers. Without the close teamwork our joint achievements would not be possible.

The financial support from the Norwegian Research Council and SINTEF Unimed is greatly appreciated.

Finally, I would like to thank friends and family, especially my parents, Mariann and my incredible daughter Katrine, for their love, understanding, encouragement and belief in me during my work with this thesis.

Table of contents

List of papers

Paper I
F. Lindseth, J. H. Kaspersen, S. Ommedal, T. Langø, G. Unsgaard and T. A. N. Hernes, ***Multimodal image fusion in ultrasound-based neuronavigation: improving overview and interpretation by integrating preoperative MRI with intraoperative 3D ultrasound***, Submitted to Comp Aided Surg, 2002.

Paper II
T. Langø, **F. Lindseth**, G. A. Tangen, J. H. Kaspersen, S. Ommedal and T. A. N. Hernes, ***Tool navigation in ultrasound-guided interventions***, Submitted to J Ultrasound Med Biol, 2002.

Paper III
F. Lindseth, T. Langø, J. Bang and T. A. N. Hernes, ***Accuracy evaluation of a 3D ultrasound-based neuronavigation system***, Comp Aided Surg, vol. 7, pp. 197-222, 2002.

Paper IV
F. Lindseth, G. A. Tangen, T. Langø and J. Bang, ***Probe Calibration for freehand 3D ultrasound reconstruction and surgical navigation***, Submitted to J Ultrasound Med Biol, 2002.

Paper V
F. Lindseth, J. Bang and T. Langø, ***A robust and automatic method for evaluating the accuracy in 3D ultrasound-based navigation***, Submitted to J Ultrasound Med Biol, 2002.

Paper VI
T. A. N. Hernes, S. Ommedal, T. Lie, **F. Lindseth**, T. Langø and G. Unsgaard, ***Stereoscopic navigation-controlled display of preoperative MRI and intraoperative 3D ultrasound in planning and guidance of neurosurgery - New technology for minimally invasive image guided surgery approaches***, Minim Invasive Neurosurg, In Press, 2002.

Paper VII
J. H. Kaspersen, E. Sjølie, J. Wesche, J. Åsland, J. Lundbom, A. Ødegård, **F. Lindseth** and T. A. N. Hernes, ***3D Ultrasound Based Navigation Combined with Preoperative CT During Abdominal Interventions, A Feasibility Study***, Submitted to Cardiovascular and Interventional Radiology, 2002.

Paper VIII
J. H. Kaspersen, T. Langø and **F. Lindseth**, ***Wavelet-based edge detection in ultrasound images***, J Ultrasound Med Biol, vol. 27, pp. 89-99, 2001.

Paper IX
A. Gronningsaeter, A. Kleven, S. Ommedal, T. E. Aarseth, T. Lie, **F. Lindseth**, T. Langø and G. Unsgård, ***SonoWand, An ultrasound-based neuronavigation system***, Neurosurgery, vol. 47, pp. 1373-1380, 2000.

Overview of work

This thesis is divided in two: A short introduction followed by the papers specified in the "List of papers" section. The section "Image Guided Surgery", together with paper I and IX, give an introduction to the field in which this work has been carried out. The aims that have guided the work are then listed and a summery of each paper is given. This is followed by a section of concluding remarks and possible future directions.

The journal articles [1-9], conference proceedings [10-13] and abstracts/oral presentations [14-27] submitted and published during the work with this thesis are listed in the reference section. The nine separate papers [1-9] have all been submitted for publication in scientific journals and are complete with abstracts and references. The articles are focused on two main topic areas: Visualization [1, 2, 6-9] and Accuracy [1, 3-5, 7]. Papers I and II [1, 2] focus on navigation, visualization, segmentation and registration, while paper III-V [3-5] deals with measuring the overall navigation accuracy, identifying the main error sources and reducing the inaccuracy associated with these.

The thesis is part of the ongoing research activity in ultrasound-guided surgery at the department of ultrasound, SINTEF Unimed, Trondheim, Norway. The research activity is concentrated on ultrasound-guided neurosurgery, vascular surgery and laparoscopic surgery.

Image Guided Surgery

In the field of minimal invasive image guided surgery images from modalities like CT, MRI and ultrasound are used to plan a surgical procedure, to guide surgical instruments down to lesions (e.g. brain tumors) in a safe manner through a narrow channel, to monitor the surgical resection and to control and evaluate the result.

The first computer-assisted systems that tried to bridge the gap between preoperative diagnostic image data (CT, MRI) and the patient in the operating room were termed *frame-based stereotactic systems* [28-30]. These systems used specially designed frames, attached to the patient's head during preoperative image acquisition and surgery, in order to *register* the images to the patient. Though highly accurate these systems had several disadvantages (invasive, cumbersome and time-consuming) and were gradually replaced by *frame-less* stereotactic systems [31-38] as the sensing and computer technology matured. Frame-less *neuronavigation systems* have proven to be very useful over the last decade, especially in the preoperative planning phase, and are among the most common systems in use today. The systems differ in the way they integrate preoperative image data with physical space (i.e. *patient registration*), the kind of tracking technology they use to follow the surgical tools that are used (e.g. optical, magnetic, ultrasonic or mechanical) and in the way the image information is presented to the surgeon. However, stereotactic systems based on preoperative images have a serious disadvantage. As surgery proceeds, the anatomy move and deform so that images acquired before surgery (i.e. the map) will not correspond to the patient (i.e. the terrain) any more.

The brain shift problem [39-41] can only be solved adequately by integrating *intraoperative imaging* with navigation technology. A common way of doing this is to transport the patient in and out of an *intraoperative CT* [42, 43] *or MRI* [44-50] scanner in order to update the images (i.e. the map) during surgery (the scanners can also be moved over the patient). This has obvious logistic drawbacks that limit the practical number of 3D scans acquired during surgery. *Interventional MRI* systems [51-55] solve these problems by allowing the surgeon to operate inside the magnet. And by choosing speed over quality it is possible to obtain close to real time 2D images defined by the location of the surgical tool used, in addition to update the 3D map in minutes without moving the patient. However, these systems require high investments, high running costs, and a special operating room as well as surgical equipment. *Intraoperative ultrasound* [9, 56-59] is a flexible, relatively low costs alternative that recently has gained a broader acceptance as a result of improved image quality and integration with navigation technology. This allows for real-time 2D ultrasound, repetitive 3D ultrasound and future real time 3D possibilities. However, a 3D ultrasound acquisition covers only a limited part of the surgical field making it hard to get an overview of surrounding anatomy, which frequently is needed. In addition, high quality preoperative CT and MRI data are often generated anyway for diagnostic and planning purposes and additional functional MRI will often be beneficial, both for preoperative planning and guidance. Furthermore, ultrasound and MRI / CT might image the same object differently and both pre- and intraoperative data are needed to easily assess the degree of brain shift. Hence in order to perform safe and accurate surgery it will be beneficial to use intraoperative ultrasound in combination with preoperative MRI / CT.

There exist different strategies for the combined use of both pre- and intraoperative data. *Indirect* use of ultrasound to track the anatomical changes that occur, apply these changes to elastically modify preoperative data and navigate according to manipulated MRI/CT volumes have been suggested [58, 60]. The present work is based on a more *direct* approach [9, 56, 57, 59, 61, 62] where ultrasound data are used as maps for intraoperative navigation and preoperative data are used for surgical planning, brain shift assessment and to provide an overview of the anatomy during minimally invasive image guided surgery. At the same time it will be possible to deform MRI / CT data acquired before surgery to match the intraoperative anatomy detected by ultrasound when an automatic, robust and accurate method (rigid and non-rigid multimodal *image registration* [63-65]) for doing this exists in order to enhance the intraoperative value of preoperative data.

The vast amount of multimodal image information available for any given patient raises the following question; what is the optimal way to present all this information to the surgeon? The most common way of doing this today is to let the surgical instruments extract corresponding 2D slices from pre- and intraoperative image volumes that are displayed in separate windows. This often leads to many windows that must be mentally merged in order to compare the content in each. An integrated multimodal 3D navigation scene showing only the relevant objects at any given time might be beneficial (e.g. to explore complex 3D structures and relationships). It should be possible to render both *geometric* [66] and *volumetric* objects [67-71] simultaneously in the same scene. And in most cases the important anatomical / pathological structures must be *extracted / segmented* [72-79] from the volume data before geometric models can be generated. [66]

In minimal invasive procedures where the surgeon is operating through a small incision with limited free sight, it is of outmost importance that the information presented to him on the computer screen corresponds to what is actually happening inside the patient. It is crucial to know the exact locations of the surgical tools used in relation to important anatomical and pathological structures at all time. When real-time imaging of the instrument with surrounding tissue is performed, the location of the tool will be directly available as an "artifact" in the image. However, for real-time 2D ultrasound it is difficult to align the instrument with the invisible ultrasound plane and to be certain that the tool really is in the plane. A virtual 3D navigation scene that can be viewed from any location and may consist of virtual representations of the tracked surgical tool, the tracked ultrasound probe with real-time 2D ultrasound data attached and segmented 3D models of important structures, might make the navigation easer. For real-time 3D guidance, direct visual feedback of tool location in relation to current anatomy will require real-time 3D acquisition, reconstruction as well as visualization. Using the instrument "artifacts" in a reconstructed ultrasound volume to visualize the tool in addition to surrounding structures using 3D rendering techniques might not be sufficient. A virtual representation of the tool might also be needed. And in order to let the surgical tool extract arbitrary real-time slices from the volume, the tool must be tracked in real time and the volume must be positioned correctly in surgical space. Thus, navigation technology will be required for practical use of both real-time 2D and real-time 3D ultrasound, as well as for repetitive freehand or motorized 3D ultrasound. In addition, all multimodal integration in a common 3D scene requires tracking systems. And when navigating technology is required, the overall clinical navigation accuracy tells the surgeon what kind of procedures that can be performed based on the image information presented. The overall accuracy of a navigation system is a result of a whole chain of error sources working together in a random fashion. In order to improve the accuracy of a system it is important to know the magnitude of these error sources.

Aims of study

The overall goal of this study was to develop new and improved techniques in the field of ultrasound-guided minimal invasive surgery that could be implemented in future navigation systems based on ultrasound. The focus has been on development of technology for:

- Improved patient outcome and reduced hospital stay and patient trauma.
- Improved safety and quality.
- Improved efficiency and resource utilization.

This was accomplished through concentrating on the following main topics:

- *Visualization*, with special focus on multimodal image-fusion between preoperative MRI / CT and intraoperative 3D ultrasound in order to fully take advantage of the best features of each modality, registration to bring the different volumes into a common coordinate system and segmentation to extract relevant information used to generate models that can be included in the 3D navigation scene.
- *Accuracy in ultrasound-based surgical navigation*, with special focus on identifying the different error sources that contribute to the overall clinical accuracy, investigating ways to measure this accuracy, identifying the main error contributors and finding ways to reduce the errors associated with these sources.

It is believed that advanced multimodal visualization of complex 3D structures and relationships will improve a number of processes in future health services: *Education and training* of both clinical and technical personnel (e.g. using simulator technology). *Communication* between medical, as well as technical personnel working in increasingly integrated multi-disciplinary teams. And as a communication tool between health care personnel and patients. *Diagnostic decision* and choice of therapy, *planning* of therapy, *guidance* of therapy and *evaluation* of therapy. *Telemedicine / teleradiology / telesurgery* for second or specialist opinion, immediate help and future robotic assisted image guided surgical procedures over safe broadband networks.

Accuracy is crucial for computer assisted minimally invasive image guided procedures. The surgeon must be confident that a navigation system operates within a specified accuracy range in a clinical setting in order to perform a safe operation. Improving the accuracy means that procedures that previously was impossible now can be performed through small incisions.

Summary of papers

This section contains a brief outline of how the different papers in the "List of papers" section are interconnected, followed by a more detailed summery of each paper.

Paper I is about multimodal visualization of preoperative MRI in combination with intraoperative 3D freehand ultrasound. The paper presents new ways to extract and fuse the best properties of both modalities in an integrated 3D scene. However, tracking technology is not integrated, so the scene cannot be populated with intraoperative features like virtual representations of the tracked surgical instruments and real-time 2D ultrasound. These features are presented in paper II, and the two papers should be looked on as the basis of a future ultrasound-based navigation system. Also, the visualization module in paper I can be used to reconstruct and experiment with the data acquired with a prototype of the SonoWand ® system during a neurosurgical operation. SonoWand ®, the single-rack navigation system with integrated 3D ultrasound is presented in paper IX. The most common display technique used for surgical navigation is to present 2D slices from a 3D volume, paper VI shows how stereoscopic visualization can be integrated with navigation technology in the operating room. Paper VII investigates whether preoperative data could be used together with ultrasound data in minimal invasive abdominal surgery and deals with both visualization and accuracy. The image fusion module in paper I was used to quantify as well as visualize the mismatch between preoperative CT and intraoperative ultrasound. Paper VIII presents a novel method for edge-detection in ultrasound images. This method was used for initialization in an active contour framework developed for the automatic segmentation of ultrasound volumes of AAA (Abdominal Aortic Aneurism) patients. The algorithm was used to generate the geometric surface models presented in paper I and VII (i.e. tumor and AAA models extracted from MRI and CT respectively).

Accuracy in image guided surgery is becoming increasingly important as more procedures are done minimal invasive. In order to quantify the overall navigation accuracy for ultrasound-based navigation systems the robust and automatic method presented in paper V was developed. As can be seen in paper III, this method was then used to evaluate the navigation accuracy of the SonoWand ® system. The fact that the evaluation method was automatic, allowed us to investigate an extensive dataset. And by analyzing a subset of the whole dataset, we were able to identify ultrasound probe calibration as the main error source. Probe calibration is a requirement for all navigation based on ultrasound data and in paper IV we present a new and automatic probe calibration method that significantly reduces the errors associated with this process. The automatic evaluation method presented in paper V was used extensively to measure the performance of one probe calibration method relative to another. Also, the edge-detection algorithm described in paper VIII was primarily developed for a membrane-based probe calibration method.

Paper I

F. Lindseth, J. H. Kaspersen, S. Ommedal, T. Langø, G. Unsgaard and T. A. N. Hernes, ***Multimodal image fusion in ultrasound-based neuronavigation: improving overview and interpretation by integrating preoperative MRI with intraoperative 3D ultrasound***, Submitted to Comp Aided Surg, 2002.

Objective: We have investigated alternative ways to integrate intraoperative 3D ultrasound images and preoperative MR images in the same 3D scene for visualizing brain shift and improving overview and interpretation in ultrasound-based neuronavigation.
Materials and Methods: A Multi-Modal Volume Visualizer (MMVV) was developed that can read data exported from the SonoWand® neuronavigation system and reconstruct the spatial relationship between the volumes available at any given time during an operation, thus enabling us to explore new ways to

fuse pre- and intraoperative data for planning, guidance and therapy control. In addition, we qualified the mismatch between MRI volumes registered to the patient and intraoperative ultrasound acquired from the dura.
Results: The results show that image fusion of intraoperative ultrasound images in combination with preoperative MRI will make perception of available information easier both by providing updated (real time) image information and an extended overview of the operational field during surgery. This will assess the degree of anatomical changes during surgery and give the surgeon an understanding of how identical structures are imaged using the different imaging modalities. The present study showed that in 50% of the cases there were indications of brain shift even before the surgical procedure had started.
Conclusions: We believe that image fusion between intraoperative 3D ultrasound and preoperative MRI might improve the quality of the surgical procedure and hence also the patient outcome.

Paper II

T. Langø, **F. Lindseth**, G. A. Tangen, J. H. Kaspersen, S. Ommedal and T. A. N. Hernes, ***Tool navigation in ultrasound-guided interventions***, Submitted to J Ultrasound Med Biol, 2002.

We describe novel methods for navigating surgical instruments during real time 2-D ultrasound-guided surgery. The methods provide the surgeon with complete and direct visual information about the position and orientation of the ultrasound image relative to the surgical tool. This means that the surgeon easily can adjust either the orientation of the ultrasound probe or the surgical tool in order to obtain an optimal view of the tool at all times in the real time 2-D image. This is important for safe and accurate patient treatment. The method requires a tracking device on both the tool and the probe; it also requires that both the probe and tool have been calibrated. The probe calibration procedure establishes the position and orientation of the ultrasound image relative to the tracking device attached to the probe. Similarly, the tool calibration calculates the tip location and orientation relative to the origin of the tracking device attached to the tool. It is a prerequisite that the tool has a straight and rigid tip portion. The method can easily be expanded to include preoperative image data and segmented or modeled objects.

Paper III

F. Lindseth, T. Langø, J. Bang and T. A. N. Hernes, ***Accuracy evaluation of a 3D ultrasound-based neuronavigation system***, Comp Aided Surg, vol. 7, pp. 197-222, 2002.

Objective: We have investigated the 3D navigation accuracy of a frameless ultrasound-based neuronavigation system (SonoWand®) for surgical planning and intraoperative image guidance. In addition, we present a detailed description and review of the error sources associated with surgical neuronavigation based on preoperative MRI data, and based on intraoperative ultrasound.
Materials and Methods: A phantom with 27 precisely defined points was scanned with ultrasound by various translation and tilt movements of the ultrasound probe (180 3D scans in total), and the 27 image points in each volume were located using an automatic detection algorithm. These locations were compared to the physically measured locations of the same 27 points. The accuracy of the neuronavigation system and the effect of varying acquisition conditions, were found through a thorough statistical analysis of the differences between the two point sets.
Results: The accuracy was found to be 1.40 ± 0.45 mm (arithmetic mean) for the ultrasound-based neuronavigation system in our laboratory setting. Improper probe calibration was the major contribution to this number.
Conclusions: Based on our extensive data set and thorough evaluation, we expect the accuracy found in the laboratory setting to be close to the overall clinical setting in ultrasound-based neuronavigation. Our analysis indicate that the overall clinical accuracy may be as low as 2 mm when using intraoperative imaging to eliminate the brain shift.

Paper IV

F. Lindseth, G. A. Tangen, T. Langø and J. Bang, ***Probe Calibration for freehand 3D ultrasound reconstruction and surgical navigation***, Submitted to J Ultrasound Med Biol, 2002.

Ultrasound probe calibration is an important requirement for correct freehand 3D ultrasound reconstruction and accurate surgical navigation based on ultrasound. The probe calibration procedure establishes the rigid body transformation between the ultrasound scan plane (image) and an attached tracking device. A regular volume can then be reconstructed from the tracked images. Real-time 2D, as well as motorized and 2D-array based 3D ultrasound will also require probe calibration when used in an integrated navigation scene. We propose two new methods for probe calibration, one alignment-based, and one based on freehand scanning. In addition, we use an established method for comparison. For all three methods we have developed novel algorithms for robust and automatic identification of image points. Three different ultrasound probes are used for assessment and a new evaluation method based on automatically extracted features in reconstructed volumes is used as our main quality measure. The freehand method performed best with a navigation accuracy of 0.62 mm for one of the probes. This indicates that sub-millimeter accuracy can be achieved in ultrasound-based surgical navigation when a precise probe calibration is performed.

Paper V

F. Lindseth, J. Bang and T. Langø, ***A robust and automatic method for evaluating the accuracy in 3D ultrasound-based navigation***, Submitted to J Ultrasound Med Biol, 2002.

We present a robust and automatic method for evaluating the 3D navigation accuracy in ultrasound-based image-guided systems. The method is based on a precisely built and accurately measured wire phantom and an automatic 3D template matching by correlation algorithm. We investigate the accuracy and robustness of the algorithm and also address optimization of algorithm parameters. Finally, we apply the method to an extensive data set from an in-house ultrasound-based navigation system. To evaluate the method, eight skilled observers identified the same crosses manually, and the average over all observers constitute our reference data set. We found no significant differences between the automatic and the manual method, and the average distance between the point sets for one particular volume (27 point pairs) was 0.27±0.17 mm. Furthermore, the spread of the automatically determined points compared to the reference set was lower than the spread for any individual operator. This indicates that the automatic algorithm is more accurate than manual determination of the wire-cross locations, in addition to being faster and non-subjective. In the application example we used a set of 35 3D ultrasound scans of the phantom under various acquisition configurations. The accuracy, represented by the mean distance between automatically determined wire-cross locations and physically measured locations, was found to be 1.34±0.62 mm.

Paper VI

T. A. N. Hernes, S. Ommedal, T. Lie, **F. Lindseth**, T. Langø and G. Unsgaard, ***Stereoscopic navigation-controlled display of preoperative MRI and intraoperative 3D ultrasound in planning and guidance of neurosurgery - New technology for minimally invasive image guided surgery approaches***, Minim Invasive Neurosurg, In Press, 2002.

Objective: This paper demonstrates a method that brings together three essential technologies for surgery planning and guidance: *Neuronavigation systems, 3D visualization techniques* and *intraoperative 3D imaging technologies.* We demonstrate the practical use of an in-house interactive stereoscopic visualization module that is integrated with a 3D ultrasound based neuronavigation system.
Materials and methods: A stereoscopy volume visualization module has been integrated with a 3D ultrasound based neuronavigation system, which also can read preoperative MR and CT data. The various stereoscopic display modalities, such as "cut plane visualization" and "interactive stereoscopic tool guidance" are controlled by a pointer, a surgical tool or an ultrasound probe. Interactive stereoscopy was tested in clinical feasibility case studies for planning and guidance of surgery procedures.

Results: By orientating the stereoscopic projections in accordance to the position of the patient on the operating table, it is easier to interpret complex 3D anatomy and to directly take advantage of this 3D information for planning and surgical guidance. In the clinical case studies, we experienced that the probe controlled cut plane visualization was promising during tumor resection. By combining 2D and 3D display, interpretation of both detailed and geometric information may be achieved simultaneously. The possibilities of interactively guiding tools in a stereoscopic scene seemed to be a promising functionality for use during vascular surgery, due to specific location of certain vessels.
Conclusion: Interactive stereoscopic visualization improves perception and enhances the ability to understand complex 3D anatomy. The practical benefit of 3D display is increased considerably when integrated with surgical navigation systems, since the orientation of the stereoscopic projection corresponds to the orientation of the patient on the operating table. Stereoscopic visualizations work well on MR and CT images, although volume rendering techniques are especially suitable for intraoperative 3D ultrasound image data.

Paper VII

J. H. Kaspersen, E. Sjølie, J. Wesche, J. Åsland, J. Lundbom, A. Ødegård, **F. Lindseth** and T. A. N. Hernes, ***3D Ultrasound Based Navigation Combined with Preoperative CT During Abdominal Interventions, A Feasibility Study***, Submitted to Cardiovascular and Interventional Radiology, 2002.

3D intraoperative ultrasound may be easier to interpret while used in combination with less noisier preoperative image data such as CT. The purpose of this study was to evaluate the use of preoperative image data in a 3D ultrasound based navigation system especially designed for minimally invasive abdominal surgery. A prototype system has been tested in patients with aortic aneurysms undergoing clinical assessment before and after abdominal aortic stent-graft implantation. All patients included were first imaged by spiral CT followed by 3D ultrasound scanning. The CT volume was registered to the patient using fiducial markers. This enabled us to compare corresponding slices from 3D ultrasound and CT volumes. The accuracy of the patient registration was evaluated both using the external fiducial markers (artificial landmarks which is glued on the patients skin) and using intraoperative 3D ultrasound as a measure of the true positioning of anatomical landmarks inside the body. The mean registration accuracy on the surface was found to be 7.1mm, but increased to 13.0 mm for specific landmarks inside the body. CT and ultrasound gave supplementary information of surrounding structures and position of the patients anatomy. Fine-tuning the initial patient registration of the CT data with a multimodal CT to intraoperative 3D ultrasound registration (e.g mutual information), as well as ensuring no movements between this registration and image guidance may improve the registration accuracy. In conclusion preoperative CT in combination with 3D ultrasound might be helpful for guiding minimal invasive abdominal interventions.

Paper VIII

J. H. Kaspersen, T. Langø and **F. Lindseth**, ***Wavelet-based edge detection in ultrasound images***, J Ultrasound Med Biol, vol. 27, pp. 89-99, 2001.

We introduce a new wavelet-based method for edge detection in ultrasound images. Each beam that is analyzed is first transformed into the wavelet domain using the continuous wavelet transform (CWT). As the CWT preserves both scale and time information, it is possible to separate the signal into a number of scales. The edge is localized by first determining the scale at which the power spectrum, based on the wavelet transform, has its maximum value. Next, at this scale we find the position of the peak for the squared CWT. This method does not depend on any threshold, once the range of scales have been determined. We suggest a range of scales for ultrasound images in general. Sample edge detections are demonstrated in ultrasound images of straight and jagged edges of simple structures submerged in water bath, and of an abdominal aorta aneurysm phantom.

Paper IX

A. Gronningsaeter, A. Kleven, S. Ommedal, T. E. Aarseth, T. Lie, **F. Lindseth**, T. Langø and G. Unsgård, ***SonoWand, An ultrasound-based neuronavigation system***, Neurosurgery, vol. 47, pp. 1373-1380, 2000.

Objectives: We have integrated a neuronavigation system into an ultrasound scanner and developed a single-rack system that enables the surgeon to perform frameless and armless stereotactic neuronavigation by means of intraoperative 3D ultrasound data as well as preoperative MRI- or CT images.
Technical developments: The system consists of a high-end ultrasound scanner, a modest cost computer and an optical positioning/digitizer system. Special technical and clinical efforts have been made in order to achieve high image quality. A special interface between the ultrasound instrument and the navigation computer ensures that there is a rapid transfer of digital 3D data with no loss of image quality. The positioning system tracks the position and orientation of the patient, ultrasound probe, pointer and various surgical instruments.
Results: The image quality improvements have enabled us, in most cases, to extract information from ultrasound that has a similar clinical value as preoperative MRI. The overall clinical accuracy of the ultrasound-based navigation system is expected to be comparable to, or better than that of an MRI-based system.
Conclusions: SonoWand enables neuronavigation by the direct use of intraoperative 3D ultrasound. However, further research will be necessary to explore the potential clinical value and the limitations of this technology.

Future prospects

From open surgery to minimally invasive therapy
Minimal invasive therapy is one of the most important trends in modern medicine. Such therapy is believed to improve patient outcome and reduce hospital stay by allowing faster recovery (i.e. it benefits the patient at the same time as it is cost-effective). In minimally invasive surgery, the manipulation of the surgical field through small incisions frequently reduces free sight, dexterity and tactile feedback. In order to compensate for this, image data showing both the surface of the organs as well as beyond must be used. In addition, haptic devices will further compensate for the loss of free sight and palpation possibilities. The ultimate aim must be to provide the surgeon with a real-time stereoscopic x-ray vision in a user-friendly environment with a natural human-computer interface. Additionally, micro-positioning systems will make it easier to navigate inside the body and for example enable the placement of stents using ultrasound-based navigation technology. Furthermore, navigation technology in combination with various local treatment methods such as radiation and radiofrequency will probably improve the target definition and hence the outcome.

From image guidance to multimodal information guidance
Vast amount of information (1D patient-monitoring data, 2D image and video data, 3D / real-time 3D volume data, 3D surface data and tracking and sensor data) can be generated during diagnostics, preoperative planning, therapy and treatment evaluation. And from the raw-data additional meta-information can be extracted using advanced processing techniques. Some types of data are most effectively acquired preoperatively, for example functional MRI. Different modalities might reveal different information and this may be important for example when determining tumor border. Also, intraoperative data allows us to track the anatomical changes that occur during surgery. For these reasons, pre- and intraoperative data should be integrated in an optimal way. However, from the huge information pool available for a given patient only the most important and relevant information should be extracted to enhance the value in every step of the patient treatment process. This could be obtained by displaying the information in an integrated 3D scene, were each object in the scene should be visualized in an optimal way, not only individually, but also in relation to the other objects and instruments in the scene. The interaction should be directly with the objects in the 3D scene (e.g. using special haptic feedback devices) or by voice recognition and control.

From preoperative diagnostic imaging to intraoperative real-time 3D imaging
For surgical navigation of minimal invasive procedures intraoperative imaging presented in an accurate way is of outmost importance. Ideally, the surgical field should be monitored by real-time 3D imaging throughout the procedure in order to make sure that the images always reflect the true patient anatomy, that the surgical instruments avoid crucial structures and that all tumor tissue is removed. MRI and ultrasound are the most promising intraoperative imaging modalities that can see beyond the organ surface in the foreseeable future. There exists high-end ultrasound scanners today that are capable of both acquiring and visualizing volume data in near real-time. We will see an increasing number of ultrasound scanners with real-time volumetric capabilities in the future, especially as the 2D transducer array technology

matures. This will make it possible to perform real time image guided minimally invasive surgery with an increased precision in the very near future.

From single user displays to distributed collaborative augmented reality displays
The computer monitor is the most common display device today, in the future we will see that large walls and rooms as well as small head mounted displays will emerge for special applications. Presenting the 3D scene on a large wall is mainly done for collaboration purposes among a broader audience, e.g. when key health care personnel are gathered to discuss the patient at hand in a given step of the treatment process. This is particularly useful in the surgical planning phase (for discussions between the radiologist and surgeon for example), in the evaluation phase as well as for broadcasting a surgical procedure for educational purposes. The audience can be in the same physical room, or distributed on several locations. Distributed collaboration can be used when a non-specialist gets a second opinion from a specialist at a major hospital and will be the next-generation of telemedicine where all the relevant information is presented in an integrated scene that is easy to interact with. This will also make it easier and safer to perform tele-surgery based on robot technology in the future. Also, the same 3D scene can be distributed to many different displays simultaneously, e.g. into the microscope of the surgeon and onto the wall in the room next to the operating theater where a class of students or a visiting group is located. The opportunity of feeling immersed in a given patient's data will continue to increase as new visualization rooms and haptic devices become available.

From textbooks and surgical hands to simulators and robots
Simulators and robots are increasingly introduced in the field of image-guided surgery. Simulators are frequently used to train surgeons to use new technology and a robot scales and performs the movements of the surgeon. However, it is not impossible to imagine that based on patient specific image data the optimal surgical procedure could be planned and simulated. This operational plan is then transferred to a robot that executes the plan on a patient. The surgeon that sent the robot its instructions or directly steers the robot (e.g. by joystick and voice control) can be at a completely different spatial location than the patient.

Minimal invasive image guided surgery is by far one of the most interesting research fields to be working in. Although alternative therapeutic methods (e.g. gene- and nano technology) are believed to emerge, there will still be a strong need for new and more precise surgery techniques in the future. The present thesis has hopefully made some important contributions in order to improve multimodal visualization and accuracy in ultrasound-based navigation. This might improve the quality of the surgical procedure and hence also the patient outcome.

References

[1] F. Lindseth, J. H. Kaspersen, S. Ommedal, T. Langø, G. Unsgaard and T. A. N. Hernes, "Multimodal image fusion in ultrasound-based neuronavigation: improving overview and interpretation by integrating preoperative MRI with intraoperative 3D ultrasound," *Submitted to Comp Aided Surg*, 2002.

[2] T. Langø, F. Lindseth, G. A. Tangen, J. H. Kaspersen, S. Ommedal and T. A. N. Hernes, "Tool navigation in ultrasound-guided interventions," *Submitted to J Ultrasound Med Biol*, 2002.

[3] F. Lindseth, T. Langø, J. Bang and T. A. N. Hernes, "Accuracy evaluation of a 3D ultrasound-based neuronavigation system," *Comp Aided Surg*, vol. 7, pp. 197-222, 2002.

[4] F. Lindseth, G. A. Tangen, T. Langø and J. Bang, "Probe calibration for freehand 3D ultrasound reconstruction and surgical navigation," *Submitted to J Ultrasound Med Biol*, 2002.

[5] F. Lindseth, J. Bang and T. Langø, "A robust and automatic method for evaluating the accuracy in 3D ultrasound-based navigation," *Submitted to J Ultrasound Med Biol*, 2002.

[6] T. A. N. Hernes, S. Ommedal, T. Lie, F. Lindseth, T. Langø and G. Unsgaard, "Stereoscopic navigation-controlled display of preoperative MRI and intraoperative 3D ultrasound in planning and guidance of neurosurgery - New technology for minimally invasive image guided surgery approaches," *Minim Invasive Neurosurg, In Press*, 2002.

[7] J. H. Kaspersen, E. Sjølie, J. Wesche, J. Åsland, J. Lundbom, A. Ødegård, F. Lindseth and T. A. N. Hernes, "3D Ultrasound Based Navigation Combined with Preoperative CT During Abdominal Interventions, A Feasibility Study," *Submitted to Cardiovascular and Interventional Radiology*, 2002.

[8] J. H. Kaspersen, T. Langø and F. Lindseth, "Wavelet-based edge detection in ultrasound images," *J Ultrasound Med Biol*, vol. 27, pp. 89-99, 2001.

[9] A. Gronningsaeter, A. Kleven, S. Ommedal, T. E. Aarseth, T. Lie, F. Lindseth, T. Langø and G. Unsgård, "SonoWand, An ultrasound-based neuronavigation system," *Neurosurgery*, vol. 47, pp. 1373-1380, 2000.

[10] T. A. N. Hernes, F. Lindseth, T. Langø, S. Ommedal and G. Unsgård, "Neuronavigation with intraoperative 3D ultrasound; Multimodal 2D and 3D display techniques and interactive stereoscopic visualization for guiding surgical procedures," in Proceedings of Computer Assisted Radiology and Surgery (CARS), Paris, France, pp. 127-132, 2002.

[11] T. Langø, J. Bang, F. Lindseth and T. A. N. Hernes, "Accuracy evaluation of a 3D ultrasound-based neuronavigation system," in Proceedings of Computer Assisted Radiology and Surgery (CARS), Paris, France, pp. 63-68, 2002.

[12] F. Lindseth, S. Ommedal, J. Bang, U. G. and T. A. N. Hernes, "Image fusion of ultrasound and MRI as an aid for assessing anatomical shifts and improving overview and interpretation in ultrasound guided neurosurgery," in Proceedings of Computer Assisted Radiology and Surgery (CARS), Berlin, Germany, pp. 247-252, 2001.

[13] E. Sjølie, J. H. Kaspersen, J. Wesche, F. Lindseth and T. A. N. Hernes, "Minimal invasive abdominal surgery based on ultrasound vision, possible?," in Proceedings of Computer Assisted Radiology and Surgery (CARS), Berlin, Germany, pp. 39-44, 2001.

[14] G. A. Tangen, F. Lindseth, T. Langø and T. A. N. Hernes, "Virtual 3D navigation scene with real time ultrasound," presented at Society for Medical Innovation and Technology (SMIT), Oslo, Norway, 2002.

[15] S. Ommedal, T. Langø, F. Lindseth, J. Bang, G. Unsgård and T. A. N. Hernes, "Multimodal display of intraoperative 3d ultrasound for updating 3d maps in neuronavigation," presented at Euroson, 14th Congress of EFSUMB (European Federation of Societies for Ultrasound in Medicine and Biology), Warsaw, Poland, 2002.

[16] J. H. Kaspersen, G. A. Tangen, T. Langø, E. Sjølie, F. Lindseth, T. A. N. Hernes, J. Weshe and J. Lundbom, "Real-time ultrasound integrated in a 3D segmented representation of the lesion," presented at Medicine Meets Virtual Reality (MMVR), Newport Beach, CA, USA, 2002.

[17] J. Bang, F. Lindseth and T. Langø, "Experience with 2d and 3d correlation in processing of ultrasound images," presented at Euroson, 14th Congress of EFSUMB (European Federation of Societies for Ultrasound in Medicine and Biology), Warsaw, Poland, 2002.

[18] F. Lindseth, G. Unsgård and T. A. N. Hernes, "3D Ultrasound and MRI Image Fusion for Assessing Anatomical Shifts and Improving Overview and Interpretation in Ultrasound Guided Neurosurgery," presented at Seminar in Medical Technology, Trondheim, Norway, 2001.

[19] T. A. N. Hernes, T. Langø, F. Lindseth, J. Bang, A. Gronningsaeter and G. Unsgård, "Intraoperative 3D ultrasound in neuronavigation; Accuracy analysis and clinical considerations," presented at 12th World Congress of Neurosurgery, Sydney, Australia, 2001.

[20] T. A. N. Hernes, F. Lindseth, T. Langø, S. Ommedal, J. Bang and G. Unsgård, "High quality intraoperative 3D ultrasound for updating 3D maps in neuronavigatio; Display techniques for planning and surgery guidance," presented at 12th World Congress of Neurosurgery, Sydney, Australia, 2001.

[21] T. A. N. Hernes, F. Lindseth, T. Langø, S. Ommedal, J. Bang and G. Unsgård, "Intraoperative 3D ultrasound in neuronavigation; Multimodal imaging and interactive stereoscopic visualization for guiding surgical procedures," presented at 4th Congress for Neurosurgical Instrument Inventions, Cairns, Australia, 2001.

[22] T. A. N. Hernes, T. Langø, F. Lindseth, J. Bang, A. Gronningsaeter and G. Unsgård, "Accuracy of ultrasound based neuronavigation systems; error sources and clinical considerations," presented at 4th Congress for Neurosurgical Instrument Inventions, Cairns, Australia, 2001.

[23] O. Haraldseth, G. Torheim, A. W. Bidar, R. Jones, F. Lindseth, G. Myhr, G. Unsgård and K. A. Kvistad, "Functional MRI for presurgical mapping of eloquent brain of brain tumor patients and combined with minimal invasive brain surgery," presented at International Society for Magnetic Resonance in Medicine (ISMRM), Glasgow, Scotland, 2001.

[24] F. Lindseth, "Integrating pre (MR)- and intra (Ultrasound)-operative data for better surgical planning and navigation, and the importance of accuracy in minimal invasive image guided surgery," presented at Seminar in Medical Technology, Trondheim, Norway, 2000.

[25] T. Langø, F. Lindseth, S. Ommedal, A. Kleven, G. Unsgard, T. A. N. Hernes and A. Gronningsater, "Instrument navigation in ultrasound guided surgery," presented at CARS 2000, San Francisco, USA, 2000.

[26] T. A. N. Hernes, F. Lindseth, S. Ommedal, A. Gronningsaeter, T. Lie, T. Langø, A. Kleven and R. Maarvik, "3D visualization techniques in minimally invasive ultrasound guided surgery," presented at 7th Interantinal Congress of the European Association for Endoscopic Surgery (E.A.E.S.), Linz, Austria, 1999.

[27] A. Gronningsaeter, G. Unsgaard, S. Ommedal, A. Kleven, T. Lie, F. Lindseth and T. Lango, "State of the art and future perspectives in intra-operative ultrasound in neurosurgery," presented at 4th International Congress on Minimally Invasive Neurosurgery, Barcelona, Spain, 1999.

[28] P. J. Kelly, G. J. Alker and S. Goerss, "Computer-assisted stereotactic microsurgery for the treatment of intracranial neoplasms," *Neurosurgery*, vol. 10, pp. 324-331, 1982.

[29] N. D. Kitchen, L. Lemieux and D. G. T. Thomas, "Accuracy in frame-based and frameless stereotaxy," *Stereotactic Functional Neurosurgery*, vol. 61, pp. 195-206, 1993.

[30] K. R. Smith, K. J. Frank and R. D. Bucholz, "The neurostation - A highly accurate, minimal invasive solution to frameless stereotactic neurosurgery," *Computerized Medical Imaging and Graphics*, vol. 18, pp. 247-256, 1994.

[31] E. Watanabe, T. Watanabe, S. Manaka, Y. Mayanagi and K. Takakura, "Three-dimensional digitizer (neuro-navigator)," *Surg Neurol*, vol. 27, pp. 543-547, 1987.

[32] G. H. Barnett, D. W. Kormos, C. P. Steiner and J. Weisenberber, "Use of a Frameless, Armless Stereotactic Wand for Brain Tumor Localization with Two-Dimensional and Three-Dimensional Neuroimaging," *Neurosurgery*, vol. 33, pp. 674-678, 1993.

[33] N. L. Dorward, O. Alberti, J. D. Palmer, N. D. Kitchen and D. G. T. Thomas, "Accuracy of true frameless stereotaxy: in vivo measurement and laboratory phantom studies," *J Neurosurg*, vol. 90, pp. 160-168, 1999.

[34] H. K. Gumprecht, D. C. Widenka and C. B. Lumenta, "BrainLab VectorVision Neuronavigation System: Technology and Clinical Experiences in 131 Cases," *Neurosurgery*, vol. 44, pp. 97-105, 1999.

[35] A. Kato, T. Yoshimine, T. Hayakawa, Y. Tomita, T. Ikeda, M. Mitomo, K. Harada and H. Mogami, "A frameless, armless navigational system for computer-assisted neurosurgery," *J Neurosurg*, vol. 74, pp. 845-849, 1991.

[36] H. F. Reinhardt, G. A. Horstmann and O. Gratzl, "Sonic Stereometry in Microsurgical Procedures for Deep-Seated Brain Tumors and Vascular Malformations," *Neurosurgery*, vol. 32, pp. 51-57, 1993.

[37] H. Reinhardt, M. Trippel, B. Westermann and O. Gratzl, "Computer aided surgery with special focus on neuronavigation," *Comput Med Imaging Graph*, vol. 23, pp. 237-244, 1999.

[38] D. W. Roberts, J. W. Strohbehn, J. F. Hatch, W. Murrray and H. Kettenberger, "A frameless stereotactic integration of computerized tomographic imaging and the operating microscope," *J Neurosurg*, vol. 65, pp. 545-549, 1986.

[39] C. Nimsky, O. Ganslandt, P. Hastreiter and R. Fahlbusch, "Intraoperative compensation for brain shift," *Surg Neurol*, vol. 56, pp. 357-364, 2001.

[40] C. Nimsky, O. Ganslandt, P. Cerny, P. Hastreiter, G. Greiner and R. Fahlbush, "Quantification of, Visulaization of, and Compnsating for Brain Shift Using Intraoperative Magnetic Resonance Imaging," *Neurosurgery*, vol. 47, pp. 1070-1080, 2000.

[41] D. W. Roberts, A. Hartov, F. E. Kennedy, M. I. Miga and K. D. Paulsen, "Intraoperative brain shift and deformation: A quantitative analysis of cortical displacement in 28 cases," *Neurosurgery*, vol. 43, pp. 749-760, 1998.

[42] C. Matula, K. Rössler, M. Reddy, E. Schindler and W. T. Koos, "Intraoperative computed tomography guided neuronavigation: Concepts, efficiency, and work flow," *Comp Aid Surg*, vol. 3, pp. 174-182, 1998.

[43] P. Grunert, W. Müller-Forell, K. Darabi, R. Reisch, C. Busert, N. Hopf and A. Perneczky, "Basic principles and clinical applications of neuronavigation and intraoperative computed tomography," *Comp Aid Surg*, vol. 3, pp. 166-173, 1998.

[44] S. K. Yrjänä, J. P. Katisko, R. O. Ojala, O. Tervonen, H. Schiffbauer and J. Koivukangas, "Versatile Intraoperative MRI in Neurosurgery and Radiology," *Acta Neurochir (Wien)*, vol. 144, pp. 271-278, 2002.

[45] G. J. Rubino, K. Farahani, D. McGill, B. Wiele, J. P. Villablanca and A. Wang-Mathieson, "Magnetic Resonance Imaging-guided Neurosurgery in the Magnetic Fringe Fields: The Next Step in Neuronavigation," *Neurosurgery*, vol. 46, pp. 643-654, 2000.

[46] A. J. Martin, W. A. Hall, H. Liu, C. H. Pozza, E. Michel, S. O. Casey, R. E. Maxwell and C. L. Truwit, "Brain Tumor Resection: Intraoperative Monitoring with High-Field-Strength MR Imaging-Initial Results," *Radiology*, vol. 215, pp. 221-228, 2000.

[47] T. Kaibara, J. K. Saunders and G. R. Sutherland, "Advances in Mobile Intraoperative Magnetic Resonance Imaging," *Neurosurgery*, vol. 47, pp. 131-138, 2000.

[48] W. A. Hall, A. J. Martin, H. Liu, E. S. Nussbaum, R. E. Maxwell and C. L. Truwit, "Brain Biopsy Using High-Field Strength Interventional Magnetic Resonance Imaging," *Neurosurgery*, vol. 44, pp. 807-814, 1999.

[49] R. Steinmeier, R. Fahlbusch, O. Ganslandt, C. Nimsky, M. Buchfelder, M. Kaus, T. Heigl, L. Gerald, R. Kuth and W. Huk, "Intraoperative Magnetic Resonance Imaging with the Magnetom Open Scanner: Concepts, Neurosurgical Indications, and Procedures: A Preliminary Report," *Neurosurgery*, vol. 43, pp. 739-748, 1998.

[50] V. Tronnier, C. R. Wirtz, M. Knauth, G. Lenz, O. Pastyr, M. M. Bonsanto, F. K. Albert, R. Kuth, A. Staubert, W. Schlegel, K. Sartor and S. Kunze, "Intraoperative Diagnostic and Interventional Magnetic Resonance Imaging in Neurosurgery," *Neurosurgery*, vol. 40, pp. 891-902, 1997.

[51] T. M. Moriarty, A. Quinones-Hinojosa, P. S. Larson, E. Alexander, P. L. Gleason, R. B. Schwartz, F. A. Jolesz and P. M. Black, "Frameless Stereotactic Neurosurgery Using Intraoperative Magnetic Resonance Imaging: Stereotactic Brain Biopsy," *Neurosurgery*, vol. 47, pp. 1138-1146, 2000.

[52] V. Seifert, M. Zimmermann, C. Trantakis, H.-E. Vitzthum, K. Kühnel, A. Raabe, F. Bootz, J. P. Schneider, F. Schmidt and J. Dietrich, "Open MRI-Guided Neurosurgery," *Acta Neurochir (Wien)*, vol. 141, pp. 455-464, 1999.

[53] J. Kettenbach, T. Wong, D. F. Kacher, N. Hata, R. B. Schwartz, P. M. Black, R. Kikinis and F. A. Jolesz, "Computer-based imaging and interventional MRI: applications for neurosurgery," *Comput Med Imaging Graph*, vol. 23, pp. 245-258, 1999.

[54] P. M. Black, E. Alexander, C. Martin, T. Moriarty, A. Nabavi, T. Z. Wong, R. B. Schwartz and F. Jolesz, "Craniotomy for Tumor Treatment in an Intraoperative Magnetic Resonance Imaging Unit," *Neurosurgery*, vol. 45, pp. 423-433, 1999.

[55] P. M. Black, T. Moriarty, E. Alexander, P. Stieg, E. J. Woodard, P. L. Gleason, C. H. Martin, R. Kikinis, R. B. Schwartz and F. A. Jolesz, "Development and Implementation of

Intraoperative Magnetic Resonance Imaging and Its Neurosurgical Applications," *Neurosurgery*, vol. 41, pp. 831-845, 1997.

[56] M. Woydt, A. Krone, N. Soerensen and K. Roosen, "Ultrasound-guided neuronavigation of deep-seated cavernous haemangiomas: clinical results and navigation techniques," *Br J Neurosurg*, vol. 15, pp. 485-495, 2001.

[57] M. M. Bonsanto, A. Staubert, C. R. Wirtz, V. Tronnier and S. Kunze, "Initial Experience with an Ultrasound-Integrated Single-Rack Neuronavigation System," *Acta Neurochirurgica*, vol. 143, pp. 1127-1132, 2001.

[58] N. Hata, T. Dohi, H. Iseki and K. Takakura, "Development of a Frameless and Armless Stereotactic Neuronavigation System with Ultrasonographic Registration," *Neurosurgery*, vol. 41, pp. 608-614, 1997.

[59] J. Koivukangas, Y. Louhisalmi, J. Alakuijala and J. Oikarinen, "Ultrasound-controlled neuronavigator-guided brain surgery," *J Neurosurg*, vol. 79, pp. 36-42, 1993.

[60] R. D. Bucholz, D. D. Yeh, J. Trobaugh, L. L. McDurmont, C. D. Sturm, C. Baumann, J. M. Henderson, A. Levy and P. Kessman, "The correction of stereotactic inaccuracy caused by brain shift using an intraoperative ultrasound device," Lecture notes in Computer Science Proceedings of the 1997 1st Joint Conference on Computer Vision, Virtual Reality, and Robotics in Medicine and Medical Robotics and Computer-Assisted Surgery, CVRMed-MRCAS'97, Grenoble, 1997.

[61] M. Strowitzki, J. R. Moringlane and W. I. Steudel, "Ultrasound-based navigation during intracranial burr hole procedures: experience in a series of 100 cases," *Surg Neurol*, vol. 54, pp. 134-144, 2000.

[62] J. Regelsberger, F. Lohmann, K. Helmke and M. Westphal, "Ultrasound-guided surgery of deep seated brain lesions," *Eur J Ultrasound*, vol. 12, pp. 115-121, 2000.

[63] J. B. A. Maintz and M. A. Viergever, "A survey of medical image registration," *Medical Image Analysis*, vol. 2, pp. 1-36, 1998.

[64] F. Maes, A. Collignon, D. Vandermeulen, G. Marchal and P. Suetens, "Multimodality image registration by maximization of mutual information," *Medical Imaging, IEEE Transactions on*, vol. 16, pp. 187-198, 1997.

[65] C. R. Maurer, Jr., J. M. Fitzpatrick, M. Y. Wang, R. L. Galloway, Jr., R. J. Maciunas and G. S. Allen, "Registration of head volume images using implantable fiducial markers," *IEEE Trans Med Imaging*, vol. 16, pp. 447-462, 1997.

[66] W. E. Lorensen and H. E. Cline, "Marching cubes: A high resolution 3D surface construction algorithm," *ACM SIGGRAPH Computer Graphics*, vol. 21, pp. 163-169, 1987.

[67] M. Levoy, "Display of surfaces from volume data," *IEEE Computer Graphics and Applications*, vol. 8, pp. 29-37, 1988.

[68] P. Lacroute and M. Levoy, "Fast volume rendering using a shear-warp factorization of the viewing transformation," in Proceedings of the 21st annual conference on Computer graphics and interactive techniques, pp. 451-458, 1994.

[69] A. Van Gelder and K. Kim, "Direct volume rendering with shading via three-dimensional textures," in Proceedings of the 1996 symposium on Volume visualization, San Francisco, California, United States, pp. 23-ff, 1996.

[70] E. LaMar, B. Hamann and K. I. Joy, "Multiresolution techniques for interactive texture-based volume visualization," IEEE Visualization, pp. 355-361, 1999.

[71] H. Pfister, J. Hardenbergh, J. Knittel, H. Lauer and L. Seiler, "The VolumePro real-time ray-casting system," in Proceedings of the 26th annual conference on Computer graphics and interactive techniques, pp. 251-260, 1999.

[72] M. Kass, A. Witkin and T. D., "Snakes: Active Contour Models," *International Journal of Computer Vision*, vol. 1, pp. 321-331, 1987.

[73] S. Osher and J. Sethian, "Fronts Propagating with Curvature Dependent Speed: Algorithms Based on Hamilton-Jacobi Formulations," *J. Comp. Physics*, vol. 79, pp. 12-49, 1988.

[74] V. Caselles, R. Kimmel and G. Sapiro, "Geodesic active contours," in Proc. Conf. Computer Vision, pp. 694-699, 1995.

[75] R. Malladi, J. A. Sethian and B. C. Vemuri, "Shape modeling with front propagation: a level set approach," *Pattern Analysis and Machine Intelligence, IEEE Transactions on*, vol. 17, pp. 158-175, 1995.

[76] T. McInerney and D. Terzopoulos, "Deformable models in medical image analysis: a survey," *Medical Image Analysis*, vol. 1, pp. 91-108, 1996.

[77] C. Xu and J. L. Prince, "Snakes, shapes, and gradient vector flow," *Image Processing, IEEE Transactions on*, vol. 7, pp. 359-369, 1998.

[78] L. Vincent and P. Soille, "Watersheds in digital spaces: an efficient algorithm based on immersion simulations," *Pattern Analysis and Machine Intelligence, IEEE Transactions on*, vol. 13, pp. 583-598, 1991.

[79] A. Mehnert and P. Jackway, "An improved seeded region growing algorithm," *Pattern Recognition Letters*, vol. 18, pp. 1065-1071, 1997.

Paper I

Multimodal image fusion in ultrasound-based neuronavigation: improving overview and interpretation by integrating preoperative MRI with intraoperative 3D ultrasound

Biomedical paper

Authors:
Frank Lindseth[1,2], MSc, Jon H. Kaspersen[1], PhD, Steinar Ommedal[1], BSc, Thomas Langø[1], PhD, Geirmund Unsgaard[3], MD, PhD, Toril A. Nagelhus Hernes[1], PhD.

Affiliation:
[1]SINTEF Unimed, Ultrasound, Trondheim, Norway.
[2]The Norwegian University of Science and Technology, Department of Computer and Information Science, Trondheim, Norway.
[3]Dept of Neurosurgery, University Hospital in Trondheim, Norway. The Norwegian University of Science and Technology, Trondheim, Norway.

Abstract

Objective: We have investigated alternative ways to integrate intraoperative 3D ultrasound images and preoperative MR images in the same 3D scene for visualizing brain shift and improving overview and interpretation in ultrasound-based neuronavigation.

Materials and Methods: A Multi-Modal Volume Visualizer (MMVV) was developed that can read data exported from the SonoWand® neuronavigation system and reconstruct the spatial relationship between the volumes available at any given time during an operation, thus enabling us to explore new ways to fuse pre- and intraoperative data for planning, guidance and therapy control. In addition, we qualified the mismatch between MRI volumes registered to the patient and intraoperative ultrasound acquired from the dura.

Results: The results show that image fusion of intraoperative ultrasound images in combination with preoperative MRI will make perception of available information easier both by providing updated (real time) image information and an extended overview of the operational field during surgery. This will assess the degree of anatomical changes during surgery and give the surgeon an understanding of how identical structures are imaged using the different imaging modalities. The present study showed that in 50% of the cases there were indications of brain shift even before the surgical procedure had started.

Conclusions: We believe that image fusion between intraoperative 3D ultrasound and preoperative MRI might improve the quality of the surgical procedure and hence also the patient outcome.

Keywords: Multimodal visualization, Image fusion, Neuronavigation, 3D Ultrasound, Intraoperative imaging, Brain shift, Image guided neurosurgery, Ultrasound-based neuronavigation, 3D display, Computer-assisted surgery, Minimally invasive surgery

Key links: www.us.unimed.sintef.no, www.atamai.com, public.kitware.com/VTK, www.mison.no

INTRODUCTION

Image guided neurosurgery, a brief overview

Modern neurosurgery has seen a dramatic change in the use of image information over the last decade. Image data from modalities like Computed Tomography (CT) and Magnetic Resonance Imaging (MRI) are increasingly being used for preoperative planning, intraoperative guidance and postoperative control, not just for diagnostics. Computer aided systems are used in order to fully take advantage of the increasing amount of information available for any given patient.

Stereotactic systems try to bridge the gap between preoperative image data (CT, MRI) and the physical object in the operating room (OR). The first systems were referred to as *frame-based* because they used specially designed frames that were attached to the patient's head both during the preoperative image scan and during surgery.[1-3] Despite the fact that these systems were highly accurate, they had and still have several disadvantages. The frames are invasive, bulky and interfere with the surgical procedure. The surgical approach is time-consuming and provides no real-time feedback of current patient anatomy.[3] With advances in sensing and computer technology a new generation of *frameless* stereotactic systems (i.e. neuronavigation systems) have been developed that try to overcome these problems without sacrificing accuracy.[4-11] Neuronavigation systems differ in the way they integrate preoperative image data with physical space and in what kind of tracking system they use to follow the surgical tools that are used (e.g. optical, magnetic, ultrasonic or mechanical). In addition, these systems vary in the way image information is controlled by various tools and displayed to the surgeon for interpretation. Although conventional navigation systems have proven to be quite useful over the last decade, these systems suffer from the fact that they only use preoperative images, making them unable to adapt to changes that occur during surgery. Thus, if the brain shifts or deforms due to drainage or surgical manipulation,[12-14] surgery guided by these images would become inaccurate.

The brain shift problem can only be solved adequately by integrating *intraoperative imaging* with navigation technology. Several intraoperative imaging modalities have been proposed. These include CT, MRI and ultrasound (US). Open CT[15, 16] and MRI[17-23] based systems, where the patient is transported into and out of the scanner, have obvious logistic drawbacks that limit the practical number of 3D scans acquired during surgery. Also, repeated use of intraoperative CT exposes both patient and personal to considerable radiation doses. Thus, the most promising alternatives in the foreseeable future are interventional MRI[24-28] and intraoperative ultrasound[29-33]. In an interventional MRI system the surgeon is operating inside the limited working space of the magnet. Choosing speed over quality it is possible to obtain close to real time 2D images defined by the position of various surgical tools in addition to updated 3D maps in minutes without moving the patient. However, these systems require high investments, high running costs, and a special operating room as well as surgical equipment.

Ultrasound, although used by some groups for several years, has just recently gained a broader acceptance in neurosurgery[34] mainly due to improved image quality and relatively low costs. The image quality and user friendliness of ultrasound have partly been achieved by optimizing and adjusting the surgical set-up[35] as well as technical scan parameters in addition to integration with navigation technology[31]. The additional real time 2D and 3D freehand capabilities, as well as real time 3D possibilities, may establish intraoperative ultrasound as the main intraoperative imaging modality in future neuroanvigation. Ultrasound may be used *indirectly* in neuronavigation to track the anatomical changes that occur, use these changes to elastically modify preoperative data and navigate according to the manipulated MRI/CT scans[32, 36], or the ultrasound images may be used *directly* as maps for navigation.[29-31, 33, 37, 38]

Even thought the direct approach is adopted and demonstrated in the present study, this should not exclude the use of preoperative MRI data during surgery, or automatically deform preoperative data to match the intraoperative anatomy detected by ultrasound when an accurate and robust method for doing this exists. The less trusted preoperative images may be useful to get information of surrounding anatomy and as an aid for interpretation of the ultrasound images (especially for inexperienced users of this modality) In order to make essential information available to the surgeon, both preoperative MRI and intraoperative ultrasound images should hence be displayed simultaneously. This gives, however, a vast amount of multimodal image information that must be handled appropriately. By combining the available data at any given time using modern medical visualization techniques, various possibilities are available for creating an optimal integrated 3D scene to the surgeon. Still, in order to achieve this we need to overcome several critical steps in future image guided surgery.

Critical steps in image guided surgery

Patient treatment using image guided surgery systems involves several important steps, of which some are more critical than others for obtaining the optimal therapy of the patient. These steps are shown in figure 1, and involve: 1) preoperative image acquisition, data processing and preoperative image visualization for optimal diagnostics as well as satisfying preoperative therapy decision and planning, 2) accurate registration of preoperative image data and visualization in the operating room (OR) for accurate and optimal planning just prior to surgery, 3) intraoperative imaging for updating images for guidance as well as intraoperative visualization and navigation for safe, efficient and accurate image guided surgery in the OR, and finally, 4) postoperative imaging and visualization for adequate evaluation of patient treatment. In the following we will give a more theoretical description of some of these steps because they are, together with intraoperative imaging, of outmost importance for understanding how optimal image guided surgery with satisfying precision may be obtained. The description is supplied by figures and images from our laboratory for a better illustration and explanation of the theoretical content.

Registration

The objective of registration is to establish a geometric transformation that relates two representations (e.g. images or corresponding points) of the same physical object.[39] It is common to distinguish between *image to image (I2I)* registration and *image to patient (physical space, reference frame, tracking system) (I2P)* registration (Fig. 2). Multimodal I2I registration makes it possible to combine structural (MRI, CT) and functional (fMRI, PET, SPECT) information for diagnosis and surgical planning from various imaging modalities. By comparing images acquired at different times (usually from the same imaging modality) I2I registration is further used for monitoring progress of a disease and postoperative follow up. I2P registration is a required step in any neuronavigation system based on preoperative images. Most registration methods can be characterized as point-based, surface-based or voxel/volume-based.[39] Point-based methods optimize the alignment of corresponding points in two images (I2I) or in one image and in physical space (I2P), and are the underlying methods for patient registration based on skull fiducials, skin fiducials or anatomical landmarks. Surface-based methods try to match corresponding surfaces. For I2I registration the two surfaces are extracted from the image data, and for I2P registration the physical space surface is either generated by sweeping over the skin with a tracked pointer or using a 3D laser camera.[40] Voxel-based methods are used for I2I registration and match two volumes by optimizing their similarity (correlation or mutual information[41] is often used). It should be mentioned that if an intraoperative image modality is available, the preoperative images could be registered to physical space by using a volume-based I2I registration between pre- and intraoperative data.

Accuracy

The overall clinical accuracy in image-guided surgery is the difference between the location of a surgical tool as indicated in the image information presented to the surgeon and where the tool tip is physically located in the patient. This accuracy determines the delicacy of the work that can be done, and is a direct result of a chain of error sources.[42] For navigation based on preoperative images the main contributors to this navigation inaccuracy are the registration process and the fact that preoperatively acquired images do not reflect the intraoperative changes that occur. Navigation based on intraoperative 3D ultrasound is associated with a similar but independent error chain, were ultrasound-probe calibration and varying speed of sound are the main contributors. No patient registration is needed for ultrasound-based guidance, which makes this kind of navigation comparable to or even better than conventional navigation in terms of accuracy even before dura is opened.[42] In addition, ultrasound based navigation will retain this accuracy throughout the operation if guidance is based on recently acquired ultrasound volumes. A mismatch between image information displayed on the computer screen and what is physically going on inside the patient's head (navigation triangle in fig. 2) can only be evaluated using well defined physical reference points in the patient, a necessity that not always is available during image guided surgery. An observed mismatch between preoperative MRI and intraoperative ultrasound images could be a direct result of the independent navigation inaccuracies of the two modalities. If a mismatch exceeds a threshold, defined by the navigation inaccuracies, we can conclude that a shift has occurred. A measure of the accuracy given by most navigation systems using preoperative MR images is often referred to as the Fiducial Registration Error (FRE), which gives the mean difference between corresponding image points and patient points. The FRE should, however, always be verified by physically touching the patient's head with a tracked pointer and making sure that physical space corresponds image space. If the two spaces match we have an estimate of the accuracy on the surface of the head, which is probably close to the accuracy inside the head (i.e. target registration error), but is only valid before the operation actually starts. On the other hand, if navigation is based on 3D ultrasound scans, reconstructed with a sound velocity matching that of the imaged objects, the accuracy will be close to what can be found in a thorough laboratory evaluation, and this navigation accuracy will be maintained throughout the operation as long as the 3D map is updated.[42]

Visualization of preoperative and intraoperative image information

In the literature there are various ways to classify the different visualization techniques that exist.[43] For medical visualization of 3D data from modalities like CT, MRI and ultrasound it is common to refer to three different approaches: *slicing, volume rendering and geometric (surface/polygon/triangle) rendering*. Slicing methods can be further sub-classed based on how the 2D slice data is generated and how this information is displayed. The sequence of slices acquired by the modality and used to generate a regular image volume is often refereed to as the *raw* or *natural* slices. From the reconstructed volume we can extract both *orthogonal* (Fig. 3A-C) and *oblique* (Fig. 3D-F) slices. Orthogonal slicing is often used in systems for pre- and post-operative visualization, as well as in intra-operative navigation systems, where the tip of the tracked instrument determines the three extracted slices (Fig. 3A). The slices can also be orthogonal relative to the tracked instrument (Fig. 3D) or the surgeons view (i.e. oblique slicing relative to the volume axis or patient), and this is becoming an increasingly popular option in navigation systems.[44]

Volume- and geometric rendering techniques are not easily distinguished. Often the two different approaches can produce similar results, and in some cases one approach may be considered both a volume rendering and a geometric rendering technique.[43] Still, volume rendering is a term used to describe a direct rendering process applied to 3D data where information exists throughout a 3D space instead of simply on 2D surfaces defined in (and often extracted from) such a 3D space. The two most common approaches to volume rendering are volumetric ray casting and 2D texture mapping. In ray casting each pixel in the image is determined by sending a ray into the volume and evaluate the voxel-data encountered along the ray using a specified ray-function (maximum, isovalue, compositing). Using 2D texture mapping, polygons are generated along the axis of the volume that is most closely aligned with the viewing direction. The data is then mapped onto these quads and projected into a picture using standard graphics hardware. The technique used to render the texture-mapped quads is essentially the same technique that is used to render geometric surface representations of relevant structures. However, the geometric representations must first be extracted from the image information. While it is possible in some cases to extract a structure and generate a 3D model of it by directly using an isosurface extraction algorithm,[45] the generation of an accurate geometric model from medical data often requires a segmentation step first. The most common surface representation is to use a lot of simple geometric primitives (e.g. triangles), though other possibilities exist.

Finally, image fusion techniques might be beneficial when using the best of both MRI and ultrasound because it is easier to perceive an integration of two or more volumes in the same scene than mentally fusing the same volumes presented in their own display windows. It also gives us the opportunity to pick relevant and needed information from the most appropriate of the available datasets. Ideally, relevant information should include not only anatomical structures for reference and pathological structures to be targeted (MRI and US tissue), but also important structures to be avoided (MRA, fMRI and US Doppler).

The present study

3D display techniques are considered to be more user friendly and convenient than 2D display, and have shown potential for improving the planning and outcome of surgery.[46-50] Rendered 3D medical image data and virtual reality visualizations have earlier been reported to be beneficial in diagnosis of cerebral aneurysms as well as in preoperative evaluation, planning and rehearsal of various surgical approaches.[51-61] However, only some studies have been reported where 3D visualizations have been brought into the operating room and have been used interactively for navigating surgical tools down to the lesion.[44, 62, 63] Additionally, the 3D scene should be continuously updated using intraoperative imaging techniques for always representing the true patient anatomy for safe and efficient surgery.

In the present study, we have developed a Multi-Modal Volume Visualizer (MMVV) for investigating alternative ways to display the image information that is available at the different stages of an operation. We have tested the module using various data sets that have been generated during the treatment of patients with brain tumors and cerebrovascular lesions in our clinic. The neuronavigation system applied during surgery uses both preoperative MRI/CT and intraoperative 3D ultrasound. The MMVV scenes were generated after surgery in order to have time to try different visualization approaches. Nevertheless, the application reconstructs the spatial relationship between all the available volumes as seen in the OR, and makes it possible to explore the optimal integration of preoperative MRI data with intraoperative 3D ultrasound data.

MATERIALS AND METHODS

3D image acquisition

Preoperative 3D MRI acquisition and patient registration

Patients included in the study were, prior to surgery, scanned by a 1.5T MRI scanner (Picker or Siemens) that acquired one or more 3D data sets (Fig. 4A) with an in plane resolution of 1.0 mm (0.78 mm for MRA) and slice thickness of 1.5 mm (1.0 mm for MRA). The MR images were transferred to the ultrasound-based neuronavigation system SonoWand® (MISON AS, Norway) (Fig. 4B), described elsewhere [31]. In the operating room the images were registered to the patient to allow conventional planning and navigation based on preoperatively acquired MR images (Fig. 4C). The registration algorithm used is based on pinpointing five corresponding skin fiducials in the image data as well as on the patient using a pre-calibrated pointer.

Intraoperative 3D ultrasound acquisition

After making the craniotomy, updated high quality 3D ultrasound maps were acquired several times during surgery using the integrated ultrasound scanner of the navigation system (Fig. 4D). The sensor-frame mounted on the ultrasound probe (5 MHz FPA probe optimized for brain surgery applications) was tracked using an optical positioning system (Polaris, Northern Digital Inc. Canada) during free-hand probe movement. The vendor determined the rigid body transformation from the sensor-frame to the ultrasound scan plane so that the position and orientation of every 2D ultrasound image could be recorded. A pyramid-shaped volume of the brain was acquired by tilting the probe approximately 80 degrees in 15 seconds. The digital images were reconstructed into a regular volume with a resolution of approximately 0.6 mm in all three directions and treated the same way as the MRI volumes (Fig. 4E). The process of ultrasound acquisition, data transfer, reconstruction and display takes less than 45 seconds for a typical ultrasound volume. Repeated 3D scans were performed when needed (as indicated by real time 2D ultrasound for example). The accuracy of ultrasound-based neuronavigation using the SonoWand® system has earlier been evaluated to be 1.4 mm on average,[42] and will be valid throughout the operation as long as the dataset used for navigation is frequently updated. However, most of the datasets used in the present study were acquired by a pre-release version of the system, with an inaccuracy not exceeding 2 mm (own laboratory results).

Integrating the different datasets into a common coordinate system

The method used to register preoperative images to the patient (I2P) in the navigation system is a point-based method that uses skin-fiducials (Fig. 4C). For a given patient all the available MRI volumes would therefore contain fiducials. These points were used to integrate all the preoperative data (MRA in addition to T1 or T2 for example) into the common coordinate system of the "master" volume using a point-based I2I registration method (Fig. 2). This made it possible to simulate preoperative planning after surgery, using the data available at this particular stage in the operation. Intraoperatively, the tracked patient reference frame was used as the common coordinate system for both pre- and intraoperative data. Preoperative data was moved into physical space by registering the "master" volume to the patient. The ultrasound volumes were acquired in the coordinate space of the tracking system and were accordingly placed correctly relative to the reference frame in the operating room. Postoperative data was not used. The visualization module (MMVV) supports different registration methods, but in the present study the registration-matrixes exported by the navigation system were used, as the aim of the study was to fuse data with the same spatial relations as seen in the OR.

Medical image fusion using the Multi-Modal Volume Visualizer (MMVV)

The multimodal image fusion application was developed as well as used on a 500 MHz PowerBook G3 computer with 384 MB RAM (ATI Rage Mobility 128 graphics card with 8 MB RAM, Mac OS X, Apple Inc.). The software was built around a set of classes from Atamai (see key links), which in turn was build on top of the visualization toolkit VTK (see key links) and the OpenGL API using the Python programming language. No preprocessing was done in order to improve the quality of the MRI and ultrasound volumes presented in this paper.

Slicing

The slicer-object implemented in the visualization module supports both orthogonal and oblique slicing relative to the volume axis. The extracted slices can be displayed in a variety of ways, where the main difference is between directly displaying the slices in a window on the screen (Fig. 3B,E) or to texture map the slices on polygons that are placed (together with other objects) in a *3D scene* that is rendered into a window (Fig. 3C,F). Figure 3B and 3E show images from the two modalities in separate windows while figure 3C and 3F show the MRI and US slices in a fused fashion. Each of the three planes can be turned on and off, and on each plane we can place slice data from any of the available volumes. It is also possible to fuse slice data from different volumes and map the resulting image onto one of the planes using compositing techniques. The user can easily cycle trough the available volumes and map corresponding slice data to a given plane, or circular rotate a volume from one of the orthogonal planes to the next. Instead of using sliders to interact with the slices, they are directly positioned by pointing, grabbing and pushing them with a mouse in the 3D scene. Figure 5A shows three different MRI volumes mapped to the same slicer-object, the bottom axial slice is taken from a T2-volume, the top right coronal slice is taken from a T1-volume and the top left sagittal slice is a fusion between the T2-volume and a MRA-volume. As we can see from the red MRA-data, every volume has its own color-table so that color as well as brightness and contrast can be adjusted individually for the slices belonging to a given volume.

Volume rendering

The volume render object developed in the present study is 2D texture based. This made it possible to generate pleasant visualizations with interactive speeds even on a notebook computer. The operator determined what to see by choosing from a set of predefined transfer functions for color and opacity that was easily adjusted to a particular dataset (fuzzy classification). Several structures within a volume can in theory be visualized using a single volume render object. However, unsegmented medical data often contains different structures occupying close to the same gray-values making it very difficult to isolate and render just the interesting structure. The volume render object therefore makes it possible to interactively cut the volume with six clipping planes. Also, many volumes only contain a single structure (e.g. the vascular tree in MRA or ultrasound flow volumes).

Geometric rendering

In order to render a geometric object the surface of the structure must first be given a geometric representation. The algorithm used to extract the MRI-tumors in the present study was based on the manual part of a semi-automatic method developed to segment structures in ultrasound volumes.[64] In an arbitrary number of the slices that went through the structure of interest, a number of control points on the tumor border were marked. Through these points a B-spline was run, and from all these parallel splines a 3D model representing the tumor surface was created. The geometric object used to represent a surface model in the 3D scene could be assigned an arbitrary color and it was possible to see inside the object, either by clipping it interactively using the bounding box of the structure (Fig. 5B), or making the model transparent.

Multimodal Image Fusion: Combining different visualization techniques with multimodal images in the same 3D scene

The MMVV module can render into multiple windows, each with its own contents and where the viewpoints in the different 3D scenes can optionally be coupled. Each window offers the possibility to place multiple slicer-, volume rendered- and geometry rendered objects together in a single 3D scene. A slicer-object can show any of the available volumes as well as different combinations of volumes on each of its three slice planes. Each volume rendered object can only visualize a single volume. If two objects are used to visualize spatially overlapping structures from different volumes artifacts may occur.[43] Implementing a single volume render object that is capable of visualizing attributed voxel data originating from multiple registered volumes can solve this. A geometrically rendered object typically shows only one structure, though multiple structures extracted from a single volume could be visualized using the hierarchical option of the geometry class. Rendering semitransparent geometry together with volume rendered structures might produce artifacts.[43] This can be fixed by sorting the geometry and the texture-mapped polygons before rendering. 3D scenes consisting of more than a single slicer-, volume render- and geometry representing object at the time was rarely used. All objects could easily be turned on and off. Direct interaction with the objects in the 3D scene was used instead of spreading a lot of controls around the rendered images. Support for stereo is build into VTK and should therefore be easy to integrate into the visualization module. However, the computer used in the current study does not support OpenGL based stereo in hardware so the option to turn on and off stereo was not used. Table 1 summarizes alternative ways to fuse the available data at a given stage in the operation using the visualization module (MMVV). Figure 5C shows a slicer-object, a volume rendered (VR) object and a geometry rendered (GR) object in the same scene. All objects use data from the same MRI volume. The slicer object has turned its coronal and sagittal slices off and the axial plane is positioned so that it slices through the tumor. The volume (grey) and geometry (red) rendered objects show the same MRI tumor. The grey VR-tumor lies like a clod around the red GR-tumor, illustrating the greater detail often achieved by direct volume rendering compared to segmented and smoothed geometry rendered objects. Figure 5D-E illustrates how multimodal information can be integrated using different combinations of slicing, VR and GR.

Clinical feasibility studies: Multimodal Visualization for optimal patient treatment

Preoperative planning and intraoperative image guidance

In the following we have chosen image data from typical clinical cases for demonstrating how multimodal imaging and visualization techniques may be used to explore essential information that is needed in the process of patient treatment. We have integrated preoperative MRI and intraoperative 3D ultrasound images in various ways due to the practical needs and availability of information in the process. Especially, we have focused on how the various display and image fusion algorithms most efficiently may solve practical problems in the various steps of preoperative planning and image guidance. For preoperative planning we have chosen various MR image data from a tumor operation. Essential information to be explored in this case was tumor location in relation to surrounding anatomy, tumor vascularisation as well as intraoperative ultrasound imaging early in the operation, before resection was initiated. In this case it was also important for the surgeon to detect any vessels that might be present inside or near the tumor, the tumor border and also to detect any shift that might be present initially in the operation. Using the MMVV software we also evaluated various solutions for visualization of brain shift as well as solutions for correction and compensation. In addition, we have focused on how to make satisfying display alternatives for following the progression of an operation and for controlling the operation at the end of the procedure. We tested various techniques for controlling the surgical procedure at the end of both tumor resections using ultrasound tissue imaging as well as controlling aneurysms surgery performed by clipsing, using ultrasound Doppler acquisation and visualization.

Clinical study to quantify the mismatch prior to surgery

In addition to visualizing the mismatch, the MMVV module can be used to quantify the spatial mismatch between volumes. This feature was used to quantify the mismatch between preoperative MRI and intraoperative 3D ultrasound at the earliest possible stage in the operation. From a total of 120 patients undergoing ultrasound-based neuronavigation from January 2000 to December 2001, 12 were randomly chosen to be included in this study. The ultrasound volumes used in the comparison were acquired right after an acoustic window through the skull was established, but before dura was opened. At this early stage the two volumes should be very similar, the main difference being that the same structure could be imaged differently due to the underlying characteristics of MRI and ultrasound. For each of these patients the two volumes (approximately aligned by the tracking system) were orthogonally sliced and fused using different splitting techniques (Fig. 6A-C). The desired axial, coronal and sagittal slice, as well as the splitting point, was adjusted using sliders. The MRI volume was then manually translated until the match with the ultrasound volume was as good as possible (Fig. 6 D-F), using structures seen in both modalities as reference (e.g. a lesion, falx, or the ventricles). The results where evaluated by a panel of three skilled operators and adjusted until consensus about the optimal match was achieved. The mismatch vector was than recorded. A conservative approach is to say that a mismatch greater than the sum of the navigation inaccuracies associated with MRI- and ultrasound based guidance is most likely caused by brain shift.

RESULTS

Multimodal image fusion in preoperative planning

Generally, multimodal image fusion has shown to be beneficial for various surgical approaches in our clinic. We have illustrated how integrated visualization may be used for planning the surgical approach in tumor surgery (Fig. 7). The conventional planning process consists of localizing the target area (Fig. 7A), which in this case is a brain tumor to be resected. Important activities will be to choose an optimal surgical approach that avoids critical structures like blood vessels (Fig. 7B,C) as well as eloquent areas (may be shown using fMRI, not shown here). This can be done in the office after preoperative MRI-data is acquired. When ultrasound is used as the intraoperative imaging modality, it is also important to plan an optimal acoustic window into the skull so that the relevant portion of the surgical field can be covered by 2D/3D ultrasound data.[35] In the OR, after the patient is positioned according to the plan and the preoperative MRI images are registered to the patient, the preoperative plan in the computer is transferred to the patient by marking the entry point and possibly a separate mini- craniotomy for the US-probe on the patient's skull. After the craniotomy is made, 3D ultrasound can be acquired and the preoperative plan can be updated to an intraoperative plan that corresponds to the true patient anatomy. Important updating features of ultrasound are blood detection (Fig. 7D,F) as well as tissue imaging (Fig 7E,F). An alternative imaging modality like ultrasound may show different or additional characteristics of anatomy and pathology than MRI, for example regarding tumor border[65] and vascularization. In addition, MRI-data with matching high quality 3D ultrasound data acquired before surgery starts was found to be the best way for inexperienced neurosurgeons to become familiar with ultrasound, interpret essential information in the images and discover how identical structures are imaged using the two modalities.

Identification, correction and quantification of brain shift.

In order to be able to use medical images for guiding surgical procedures, it is essential that the images reflect the true position of patient anatomy. The amount of brain shift should be monitored and when the shift exceeds what can be accepted for the operation at hand, preoperative MR images should not be trusted for guidance. Navigation must than be based on updated 3D ultrasound data of the target area. We present here (Fig. 8) various ways that brain shift can be visualized so that the surgeon in an easy and intuitive way can interpret this information and use the available information in a safe and efficient way for optimal surgical guidance. As can be seen from figure 8A, both modalities must be present to detect brain shift (i.e. a minimal invasive or closed procedure is performed so that the physical target area with surgical instruments will not be visible). Image fusion based on blending MRI and ultrasound together can to a certain degree reveal brain shift in the border zone (Fig. 8B). To clearly observe a mismatch we either have to split a slice in the middle of an interesting structure and put information from the two modalities on different sides (Fig. 6) or put updated ultrasound information on one slice, MRI on another and observe the intersection between the two slices (Fig. 8C,G). Alternatively we can overlay some kind of data (for example a volume rendered or segmented geometric object) from one modality on a slice from another modality (Fig. 8C-F), or based on data from one modality volume render the same object as is segmented and surface rendered from another modality (Fig. 8I). As can be seen from figure 8 a considerable mismatch is detected in the right to left direction.

Monitoring brain shift by visualizing the mismatch between pre- and intraoperative image data helps the surgeon to decide when unmodified MRI-data should be used only for overview and interpretation. Correcting and repositioning the preoperative images so that they correspond to the true patient anatomy (as monitored by intraoperative ultrasound) will greatly increase the usefulness of the MRI data during surgery. Ideally, this should be done automatically in a robust and accurate manner. Until such a method exists, only ultrasound is trusted for guidance and control, and various slicing and rendering techniques are used to fuse preoperative MRI data, that might be manually translated into a more correct position, around the ultrasound data. Figure 8 shows the mismatch before (G, I) and after (H, J) the manual correction.

In order to quantify the mismatch between similar structures recognized in both modalities at the earliest possible stage, immediately after the first ultrasound volume became available (i.e. after the craniotomy but before dura mater is opened), we used the manual method previously outlined (Fig. 6). Table 2 shows the quantitative data obtained in the present study based on a random sample of 12 patients undergoing surgical treatment in our clinic. A quantified mismatch greater then the sum of the two navigation inaccuracies is an indication of brain shift as previously explained. In the present study a mismatch indicating brain shift was detected in 50% of the cases even before the surgical procedure had started.

Surgical guidance and control

In addition to a safe approach to the surgical target area, recent reports have shown that radical resections are important for patients' outcome in the administration of brain tumors.[66] In order to achieve this it is important to know where the tumor border is and how much tumor tissue there is left. A minimum invasive procedure, where clear sight is not an option, will require some kind of image guidance. Ideally, the entire resection should be monitored by a real time 3D intraoperative modality and presented to the surgeon in the form of a 3D scene consisting of the true intraoperative positions of the surgical instruments in relation to structures to be avoided and removed. Still, much is achieved by updating the region of interest with 3D ultrasound during the procedure, and displaying preoperative data around for increased overview, as presented in figure 9. Axial and sagittal MRI-slices are used for overview, while the interesting coronal slice cuts through the tumor. The coronal slice shows preoperative MRI data (Fig. 9A), an early ultrasound volume acquired before the resection starts (Fig. 9B) and ultrasound data acquired towards the end of the operation for resection control (Fig. 9C). If we compare A) to B), or their volume rendered representations in D) and E) respectively, we can clearly see that the same tumor is imaged differently by the two modalities and that a shift is present. Looking at C) and F) there might still be some tumor tissue left before a complete radical resection is performed.

Direct volume rendering of MRA and 3D ultrasound Doppler data have proven to be quite useful for exploring complex anatomical and pathological vascular structures in the brain. High quality renderings can be generated without the need of any filtering or segmentation. We have tested this display technique for surgical guidance of both aneurysms and artery venous (AV) malformations. In figure 10 we show a 3D scene from a patient with an aneurysm, which is treated by microsurgical clipsing. Preoperative MRA is important for exploring the extension and location of the lesion for optimal preoperative planning (Fig. 10A). As in the tumor case it is important to plan the positioning of the craniotomy, not only for finding the most optimal approach to the lesion, but also for obtaining high quality intraoperative images. After the craniotomy has been made, a 3D ultrasound Doppler scan is acquired and the target area is replaced with updated ultrasound data displayed in red (Fig. 10B), while MRA-data is kept in the 3D scene for increased overview of the vascular tree. By using an axial MRA slice through the aneurysm instead of a 3D MRA rendering, the mismatch with the ultrasound Doppler angiography can easily be seen, indicating that a brain shift has occurred as in the tumor case (Fig. 10C). Zooming in on the aneurysm we can see what is to be removed and comparing D) to E) we observe how identical structures are imaged and rendered using MRA and US-Doppler, respectively. In order to confirm that the clipsing of the aneurysm was performed according to the plan, we can compare volume renderings of the aneurysm based on ultrasound acquired before (Fig. 10E) and after (Fig. 10F) clipsing. Here, 3D visualization was important both for locating the lesion as well as for controlling the vessel-anatomy and the blood flow before and after surgery.

DISCUSSION

In this paper, we have demonstrated technology that integrates various imaging modalities as well as different 2D and 3D visualization techniques that may be used for improving image guided surgery as well as preoperative planning and postoperative evaluation. The advantages of 3D display technologies have been pointed out by other research groups both due to increased overview as well as improved diagnostics and surgery planning.[47, 51-54] Although many of the commercially available systems for surgical navigation offer integrated 3D display facilities for overview and planning of the procedure, few of them have integrated intraoperative 3D imaging that can cope with brain shift during surgery. At the same time intraoperative imaging like interventional MRI and intraoperative 2D and 3D ultrasound are increasingly being presented.[13, 17, 32, 36, 66] Most 3D display technology available is, however, demonstrated on CT and MR image data because the images are of high resolution with reasonably good contrast and low noise level. Ultrasound images, which have been relatively inhomogeneous with a high noise level, are now improving in image quality and have shown promising results for 3D display using volume-rendering techniques.[44] Also, 3D visualization of intraoperative images encounters other challenges due to increased image artifacts as well as decreased image quality throughout the operation. The various approaches to obtain intraoperative 3D imaging as well as the fact that preoperative images may also be useful during navigation and not only for planning, discloses a demand for 3D display technology that can cope with the various imaging modalities used both preoperatively and intraoperatively.

Advantages and challenges using multimodal 3D visualization in the clinic

The results from the feasibility studies presented in this paper are promising. 3D visualization seems to give many advantages due to improved perception of complex 3D anatomy and easy access to more detailed information inside the 3D volume, especially in combination with 2D display techniques.

Slicing versus 3D display: Displaying slices in separate windows (Fig. 3B,E) with hair-crosses overlaid to indicate the current tool tip position, makes it possible to display many slices without obscuring other slices. The drawback is that it might be hard to handle all this information that is distributed on many separate windows. We have shown in the present study that the slices (one to three) from one to several volumes (pre-, intra- or postoperatively acquired) may be displayed together in one window, which makes it easier to interpret information. Furthermore, the ultrasound image in figure 11B can be replaced by the one in figure 11C, where MRI data from figure 11A is filled around the target area for improved overview while not obscure the updated ultrasound data. On the other hand, overlay used to aid the ultrasound interpretation often hide the information behind (Fig. 11D), and should hence be easy to turn on and off. Still, it's hard to mentally match images presented like this with current patient anatomy as seen from the surgeon's viewpoint as well as understand the orientation of the surgical tools relative to the orthogonal volume slicing. The orientation problem can be solved by integrating the 2D planes in a 3D scene (Fig. 3C,F), and manually rotate the scene until the viewpoint corresponds to the surgeon's view. This may also be controlled automatically by tracking the head movements of the surgeon in addition to tracking the surgical tools and probes. A potential problem with this approach is that some slices will be partly obscured (Fig. 3C) and that slices almost parallel to the viewing direction will be difficult to see (Fig. 3F). To minimize these problems, only relevant information should be displayed and it should be easy to turn on and off the different objects in the scene. Furthermore, the orientation of the 3D scene can be tied to the traditional 2D display of the slices so that the information is presented as close to the surgeons view as possible (Fig. 11E). Thus, when a surgeon moves the instrument to the left relative to himself, the tracked instrument will also move (approximately) left in the axial and coronal slices, while the sagittal window will display new data, extracted further to the left as seen from the surgeon.

Surface versus volume rendering: Although 2D slicing is essential for detailed information interpretation, complex 3D structures must be mentally generated based on a stack of 2D slices. This requires years of experience, and is one of the reasons why research groups now introduce various 3D display techniques in planning as well as in the operating room for surgical guidance. Computers using modern 3D rendering techniques are particularly useful for assessing complex 3D structures like the vascular tree, and to get an overview of important relations between relevant structures (e.g. infiltrating vessels in a tumor). Theoretically, it is possible to apply both volume rendering and geometric extraction techniques directly to volume data as well as to segmented data. For practical visualization of 3D MRI and ultrasound data we often experienced that it's possible to generate nice views by isolating interesting parts by clipping the volume and opacity-classify the content of the sub-volume. Another important advantage of volume rendering is that both the surface of the interesting objects as well as the inner content (e.g. tumor with cysts) may be displayed. Geometric rendering of clinically interesting structures is most successful if an intermediate segmentation step if performed first, so that an accurate surface representation can be generated. Although advanced methods for automatic or semi-automatic segmentation exist, manual methods must often be used, especially for ultrasound data. In many cases it is also necessary to verify the tumor border, for example in a low graded tumor where it is hard to delineate the border even for an experienced radiologist. Still, promising segmentation methods exists. For example the deformable models approach,[67] where a template (taken from an anatomical atlas for example) is deformed to fit new ultrasound volumes acquired during the operation. In summary, we have experienced that volume rendering is the most appropriate 3D visualization method for ultrasound data since the generation of a surface representation often requires a segmentation step, which in general is more demanding task than segmentation based on MRI. In addition, the time available for the additional segmentation step is more limited in the operating room than it is pre- or post operatively.

Future prospects

Multimodal imaging in neuronavigation: As previously stated the Multi Modal Volume Visualizer is currently used to explore different ways to integrate available image information. We plan to integrate the MMVV module with tracking technology, making it a suitable tool for direct image guided surgery in the OR. This means that the 3D scene will be controlled by surgical instruments and not only by the mouse. Virtual representations of the tracked pointers and surgical instruments, as well as the ultrasound probe with the real time 2D scan plane attached, will also be integrated in the 3D scene (Fig. 11F). By fusing the different datasets in a common scene we can compare real time 2D ultrasound to corresponding slices from MRI and ultrasound volumes in order to detect bran shift.

Real time 3D ultrasound imaging: Real-time monitoring of the position of surgical instruments in relation to the patient's current anatomy is a prerequisite for safe performance of completely image guided resections. A limitation with the real-time 2D ultrasound technique is that it is difficult to obtain a longitudinal view of the surgical instrument at all times.[35] This can only be solved by real-time 3D ultrasound. Instead of extracting slices from a recently acquired 3D ultrasound volume, the displayed real-time 2D slices from the 3D volume would include monitoring of the instrument in the image itself. In addition, it will be possible to render and integrate the real-time image data in exciting new ways. Real time 3D visualization requires real time 3D acquisition, transfer and rendering.

Automatic registration and real time updating of preoperative data: The current study makes use of preoperative MRI for surgical planning as well as for overview and interpretation during surgery. Preoperative data are registered directly to physical space, and are not modified during surgery. Though challenging, multimodal image-to-image registration[68] between MRI and the first intraoperative ultrasound volume would allow us to indirectly move preoperative data to physical space (Fig. 2). However, this will have implications in terms of accuracy because placing the MRI volumes in the patient this way will depend on the error chain associated with ultrasound-based navigation in addition to the errors of the multimodal registration process itself. Still, the present paper and earlier work[42] show that this could be favorable in terms of accuracy, since the first ultrasound volume acquired is more accurately placed in the patient than the MRI data directly registered to physical space. However, there is still a need for I2P registration to allow conventional planning based on MRI in the OR before the craniotomy for the ultrasound probe is made. A simple point-based method that uses anatomical landmarks will probably be sufficient until the acoustic window into the brain is opened. We are currently searching for optimal ways to do both I2P as well as multimodal I2I registration in an efficient, robust and user-friendly way. Surgical manipulation and resection will alter the anatomy, which may be continuously monitored using real time 2D and freehand 3D ultrasound. Preoperative MR images may be repeatedly aligned[69] (elastically) with new ultrasound data (Fig. 2), or alternatively the differences between consecutive ultrasound volumes[70] may be measured and used to update the MRI volume in sequence. The second approach will probably be the easiest as this implies a mono-modal registration between relatively similar ultrasound volumes if the time-gap between the acquisitions is not too long.

Multimodal real time image guidance: When real time 3D ultrasound and real time non-rigid registration of preoperative image data to current patient anatomy are available, as well as the integration with navigation technology has been done, complete multimodal image guided neuronavigation may be performed. Until such methods are developed, our approach is to obtain high quality intraoperative 2D and 3D ultrasound data in the target area. Preoperative MRI data may be filled around for increased overview of the surgical field as well as overlaid the ultrasound data in various ways for enhanced interpretation and assessment of brain shift.

CONCLUSION

We have developed and demonstrated clinical use of a multimodal visualization module that integrates various imaging modalities like ultrasound and MRI as well as different 2D and 3D visualization techniques that may be used for improving image guided surgery as well as preoperative planning and postoperative evaluation. The results show that image fusion of intraoperative 2D and 3D ultrasound images in combination with MRI will make perception of available information easier both by giving updated (real time) image information and an extended overview of the operational field during surgery. This will assess the degree of anatomical changes that occur during surgery and give the surgeon an understanding of how identical structures are imaged using the different imaging modalities. We believe that this might improve the quality of the surgical procedure and hence also the patient outcome.

Acknowledgments

This work was supported by The Norwegian University of Science and Technology through Strategic University Program for Medical Technology and SINTEF Unimed, through Strategic Institute Program from the Research Council of Norway, the Ministry of Health and Social Affairs of Norway, GE Vingmed Ultrasound (Horten, Norway).

References

1. Kelly PJ, Alker GJ, Goerss S. Computer-assisted stereotactic microsurgery for the treatment of intracranial neoplasms. Neurosurgery 1982;10:324-331
2. Kitchen ND, Lemieux L, Thomas DGT. Accuracy in frame-based and frameless stereotaxy. Stereotactic Functional Neurosurgery 1993;61:195-206
3. Smith KR, Frank KJ, Bucholz RD. The neurostation - A highly accurate, minimal invasive solution to frameless stereotactic neurosurgery. Computerized Medical Imaging and Graphics 1994;18:247-256
4. Roberts DW, Strohbehn JW, Hatch JF, Murrray W, Kettenberger H. A frameless stereotactic integration of computerized tomographic imaging and the operating microscope. J Neurosurg 1986;65:545-549
5. Watanabe E, Watanabe T, Manaka S, Mayanagi Y, Takakura K. Three-dimensional digitizer (neuro-navigator). Surg Neurol 1987;27:543-547
6. Kato A, Yoshimine T, Hayakawa T, Tomita Y, Ikeda T, Mitomo M, Harada K, Mogami H. A frameless, armless navigational system for computer-assisted neurosurgery. J Neurosurg 1991;74:845-849
7. Barnett GH, Kormos DW, Steiner CP, Weisenberber J. Use of a Frameless, Armless Stereotactic Wand for Brain Tumor Localization with Two-Dimensional and Three-Dimensional Neuroimaging. Neurosurgery 1993;33:674-678
8. Reinhardt HF, Horstmann GA, Gratzl O. Sonic Stereometry in Microsurgical Procedures for Deep-Seated Brain Tumors and Vascular Malformations. Neurosurgery 1993;32:51-57
9. Reinhardt H, Trippel M, Westermann B, Gratzl O. Computer aided surgery with special focus on neuronavigation. Comput Med Imaging Graph 1999;23:237-244
10. Gumprecht HK, Widenka DC, Lumenta CB. BrainLab VectorVision Neuronavigation System: Technology and Clinical Experiences in 131 Cases. Neurosurgery 1999;44:97-105
11. Dorward NL, Alberti O, Palmer JD, Kitchen ND, Thomas DGT. Accuracy of true frameless stereotaxy: in vivo measurement and laboratory phantom studies. J Neurosurg 1999;90:160-168
12. Roberts DW, Hartov A, Kennedy FE, Miga MI, Paulsen KD. Intraoperative brain shift and deformation: A quantitative analysis of cortical displacement in 28 cases. Neurosurgery 1998;43:749-760
13. Nimsky C, Ganslandt O, Cerny P, Hastreiter P, Greiner G, Fahlbush R. Quantification of, Visulaization of, and Compnsating for Brain Shift Using Intraoperative Magnetic Resonance Imaging. Neurosurgery 2000;47:1070-1080
14. Nimsky C, Ganslandt O, Hastreiter P, Fahlbusch R. Intraoperative compensation for brain shift. Surg Neurol 2001;56:357-364
15. Grunert P, Müller-Forell W, Darabi K, Reisch R, Busert C, Hopf N, Perneczky A. Basic principles and clinical applications of neuronavigation and intraoperative computed tomography. Comp Aid Surg 1998;3:166-173
16. Matula C, Rössler K, Reddy M, Schindler E, Koos WT. Intraoperative computed tomography guided neuronavigation: Concepts, efficiency, and work flow. Comp Aid Surg 1998;3:174-182

17. Tronnier V, Wirtz CR, Knauth M, Lenz G, Pastyr O, Bonsanto MM, Albert FK, Kuth R, Staubert A, Schlegel W, Sartor K, Kunze S. Intraoperative Diagnostic and Interventional Magnetic Resonance Imaging in Neurosurgery. Neurosurgery 1997;40:891-902
18. Rubino GJ, Farahani K, McGill D, Wiele B, Villablanca JP, Wang-Mathieson A. Magnetic Resonance Imaging-guided Neurosurgery in the Magnetic Fringe Fields: The Next Step in Neuronavigation. Neurosurgery 2000;46:643-654
19. Martin AJ, Hall WA, Liu H, Pozza CH, Michel E, Casey SO, Maxwell RE, Truwit CL. Brain Tumor Resection: Intraoperative Monitoring with High-Field-Strength MR Imaging-Initial Results. Radiology 2000;215:221-228
20. Kaibara T, Saunders JK, Sutherland GR. Advances in Mobile Intraoperative Magnetic Resonance Imaging. Neurosurgery 2000;47:131-138
21. Hall WA, Martin AJ, Liu H, Nussbaum ES, Maxwell RE, Truwit CL. Brain Biopsy Using High-Field Strength Interventional Magnetic Resonance Imaging. Neurosurgery 1999;44:807-814
22. Steinmeier R, Fahlbusch R, Ganslandt O, Nimsky C, Buchfelder M, Kaus M, Heigl T, Gerald L, Kuth R, Huk W. Intraoperative Magnetic Resonance Imaging with the Magnetom Open Scanner: Concepts, Neurosurgical Indications, and Procedures: A Preliminary Report. Neurosurgery 1998;43:739-748
23. Yrjänä SK, Katisko JP, Ojala RO, Tervonen O, Schiffbauer H, Koivukangas J. Versatile Intraoperative MRI in Neurosurgery and Radiology. Acta Neurochir (Wien) 2002;144:271-278
24. Black PM, Moriarty T, Alexander E, Stieg P, Woodard EJ, Gleason PL, Martin CH, Kikinis R, Schwartz RB, Jolesz FA. Development and Implementation of Intraoperative Magnetic Resonance Imaging and Its Neurosurgical Applications. Neurosurgery 1997;41:831-845
25. Black PM, Alexander E, Martin C, Moriarty T, Nabavi A, Wong TZ, Schwartz RB, Jolesz F. Craniotomy for Tumor Treatment in an Intraoperative Magnetic Resonance Imaging Unit. Neurosurgery 1999;45:423-433
26. Kettenbach J, Wong T, Kacher DF, Hata N, Schwartz RB, Black PM, Kikinis R, Jolesz FA. Computer-based imaging and interventional MRI: applications for neurosurgery. Comput Med Imaging Graph 1999;23:245-258
27. Seifert V, Zimmermann M, Trantakis C, Vitzthum H-E, Kühnel K, Raabe A, Bootz F, Schneider JP, Schmidt F, Dietrich J. Open MRI-Guided Neurosurgery. Acta Neurochir (Wien) 1999;141:455-464
28. Moriarty TM, Quinones-Hinojosa A, Larson PS, Alexander E, Gleason PL, Schwartz RB, Jolesz FA, Black PM. Frameless Stereotactic Neurosurgery Using Intraoperative Magnetic Resonance Imaging: Stereotactic Brain Biopsy. Neurosurgery 2000;47:1138-1146
29. Bonsanto MM, Staubert A, Wirtz CR, Tronnier V, Kunze S. Initial Experience with an Ultrasound-Integrated Single-Rack Neuronavigation System. Acta Neurochirurgica 2001;143:1127-1132
30. Woydt M, Krone A, Soerensen N, Roosen K. Ultrasound-guided neuronavigation of deep-seated cavernous haemangiomas: clinical results and navigation techniques. Br J Neurosurg 2001;15:485-495
31. Gronningsaeter A, Kleven A, Ommedal S, Aarseth TE, Lie T, Lindseth F, Langø T, Unsgård G. SonoWand, An ultrasound-based neuronavigation system. Neurosurgery 2000;47:1373-1380

32. Hata N, Dohi T, Iseki H, Takakura K. Development of a Frameless and Armless Stereotactic Neuronavigation System with Ultrasonographic Registration. Neurosurgery 1997;41:608-614
33. Koivukangas J, Louhisalmi Y, Alakuijala J, Oikarinen J. Ultrasound-controlled neuronavigator-guided brain surgery. J Neurosurg 1993;79:36-42
34. Kelly PJ. Comments to: Neuronavigation by Intraoperative Three-dimensional Ultrasound: Initial Experience during Brain Tumor Resection. Neurosurgery 2002;50:812
35. Unsgaard G, Gronningsaeter A, Ommedal S, Hernes TAN. Brain operations guided by real-time 2D ultrasound: New possibilities as a result of improved image quality - Surgical approches. Neurosurgery 2002;In Press
36. Bucholz RD, Yeh DD, Trobaugh J, McDurmont LL, Sturm CD, Baumann C, Henderson JM, Levy A, Kessman P. The correction of stereotactic inaccuracy caused by brain shift using an intraoperative ultrasound device. Lecture notes in Computer Science Proceedings of the 1997 1st Joint Conference on Computer Vision, Virtual Reality, and Robotics in Medicine and Medical Robotics and Computer-Assisted Surgery, CVRMed-MRCAS'97. Grenoble, 1997
37. Regelsberger J, Lohmann F, Helmke K, Westphal M. Ultrasound-guided surgery of deep seated brain lesions. Eur J Ultrasound 2000;12:115-121
38. Strowitzki M, Moringlane JR, Steudel WI. Ultrasound-based navigation during intracranial burr hole procedures: experience in a series of 100 cases. Surg Neurol 2000;54:134-144
39. Maintz JBA, Viergever MA. A survey of medical image registration. Medical Image Analysis 1998;2:1-36
40. Maurer CR, Jr., Fitzpatrick JM, Wang MY, Galloway RL, Jr., Maciunas RJ, Allen GS. Registration of head volume images using implantable fiducial markers. IEEE Trans Med Imaging 1997;16:447-462
41. Maes F, Collignon A, Vandermeulen D, Marchal G, Suetens P. Multimodality image registration by maximization of mutual information. Medical Imaging, IEEE Transactions on 1997;16:187-198
42. Lindseth F, Langø T, Bang J, Hernes TAN. Accuracy evaluation of a 3D ultrasound-based neuronavigation system. Comp Aid Surg 2002, Submitted November 2001
43. Schroeder W, Martin K, Lorensen B. The Visualization Toolkit: An Object-Oriented Approach To 3D Graphics. 2 ed: Prentice Hall, 1997
44. Hernes TAN, Ommedal S, Lie T, Lindseth F, Langø T, Unsgaard G. Stereoscopic Navigation-controlled Display of Preoperative MRI and Intraoperative 3D Ultrasound in Planning and Guidance of Neurosurgery: New technology for minimally invasive image guided surgery approaches. Minimally Invasive Neurosurgery 2002:In Press
45. Lorensen WE, Cline HE. Marching Cubes: A High Resolution 3D Surface Construction Algorithme. Computer Graphics 1987;21:163-169
46. Gronningsaeter A, Lie T, Kleven A, Mørland T, Langø T, Unsgård G, Myhre HO, Mårvik R. Initial experience with stereoscopic visualisation of three-dimensional ultrasound data in surgery. Surgical Endoscopy 2000;14:1974-1078
47. Hayashi N, Endo S, Shibata T, Ikeda H, Takaku A. Neurosurgical simulation and navigation with three-dimensional computer graphics. Neurosurgical Research 1999;21

48. Psiani LJ, Comeau R, Davey BLK, Peters TM. Incorporation of stereoscopic video into an image-guided neurosurgery environment. IEEE-EMBC 1995:365-366
49. Peters TM, Comeau RM, Psiani L, Bakar M, Munger P, Davey BLK. Visualization for image guided neurosurgery. IEEE-EMBC 1995:399-400
50. Glombitza G, Lamade W, Demiris AM, Göpfert MR, Mayer A, Bahner ML, Meinzer HP, Richter G, Lehnert T, Herfarth C. Virtual planning of liver resection: image processing, visualization and volumetric evaluation. Int. J. of Medical Informatics 1999;53:225-237
51. Harbaugh RE, Schlusselberg DS, Jeffrey R, Hayden S, Cromwell LD, Pluta D, English RA. Three-dimensional computer tomograpic angiography in the preoperative evaluation of cerebrovascular lesions. Neurosurgery 1995;36:320-326
52. Hope JK, Wilson JL, Thomson FJ. Three-dimensional CT angiography in the detection and characterization of intracranial berry aneurysms. Am J. Neuroradiol 1996;17:437-445
53. Nakajima S, Atsumi H, Bhalerao AH, Jolesz FA, Kikinis R, Yoshimine T, Moriarty TM, Stieg PE. Computer-assisted surgical planning for cerebrovascular neurosurgery. Neurosurgery 1997;41:403-409
54. Muacevic A, Steiger HJ. Computer-assisted resection of cerebral arteriovenous malformation. Neurosurgery 1999;45:1164-1171
55. Pflesser B, Leuwer R, Tiede U, Höhne KH. Planning and rehearsal of surgical interventions in the volume model. Medicine Meets Virtual Reality, IOS Press 2000:29-264
56. Soler L, Delingette H, Malandain G, Ayache N, Koehl C, Clemet JM, Dourthe O, Marescaux J. An automatic virtual patient reconstruction from CT scans for hepatic surgical planning. Medicine meets virtual reality, IOS press, 2000
57. Hans P, Grant AJ, Laitt RD, Ramsden RT, Kassner A, Jackson A. Comparison of three-dimensional visualization techniques for depicting the scala vestibuli and scala Tympani of the cochlea by using high resolution MR imaging. Am J. Neuroradiol 1999;20:1197-1206
58. Kato Y, Sano H, Katada K, Ogura Y, Hayakawa M, Kanaoka N, Kanno T. Application of three-dimensional CT angiography (3D-CTA) to cerebral aneurysms. Surg Neurol 1999;52:113-122
59. Masutani Y, Dohi T, Yamane F, Iseki H, Takakura K. Augmented reality visualization system for intravascular neurosurgery. Computer aided surgery 1998;3:239-247
60. Vannier MW. Evaluation of 3D imaging. Critical reviews in diagnostic imaging, CRC press LLC 2000;41:315-378
61. Anxionnat R, Bracard S, Ducrocq X, Trousset Y, Launay L, Kerrien E, Braun M, Vaillant R, Scomazzoni F, Lebedinsky A, Picard L. Intracranial aneurysms: Clinical value of 3D digital substraction angiography in terapeutic decision and endovascular treatment. Radiology 2001;218:799-808
62. Walker DG, Kapur T, Kikinis R, Yezzi A, Zollei L, Bramley MD, Ma F, Black P. Automatic segmentation and its use with an electromagnetic neuronavigation system. Abstract presentet at the 12th World Congress of neurosurgery, Sydney Australia 2001:16-20
63. Wilkinson EP, Shahidi R, Wang B, Martin DP, Adler JR, Steinberg GK. Remote-rendered 3D CT angiography (3DCTA) as an intraoperative aid in cerebrovascular neurosurgery. Computer Aided Surgery 1999;4:256-263

64. Kaspersen JH, Langø T, Lindseth F. Wavelet based edge detection in ultrasound images. J Ultrasound Med Biol 2001;27:89-99
65. Selbekk T, Unsgård G, Ommedal S, Muller T, Torp S, Myhr G, Bang J, Hernes TAN. Neurosurgical biopsies guided by 3D ultrasound – comparison of image evaluations and histopathological results. In: Lemke HU, Vannier MW, Inamura K, Farman AG, Doi K, Reiber JHC, eds. Computer Assisted Radiology and Surgery (CARS). Vol. 1. Paris, France: Spinger, 2002:133-138
66. Wirtz CR, Knauth M, Staubert A, Bonsanto MM, Sartor K, Kunze S, Tronnier VM. Clinical Evaluation and Follow-up Results for Intraoperative Magnetic Resonance Imaging in Neurosurgery. Neurosurgery 2000;46:1112-1122
67. Xu C, Prince JL. Snakes, shapes, and gradient vector flow. Image Processing, IEEE Transactions on 1998;7:359-369
68. Roche A, Pennec X, Malandain G, Ayache N. Rigid registration of 3-D ultrasound with MR images: a new approach combining intensity and gradient information. Medical Imaging, IEEE Transactions on 2001;20:1038-1049
69. Pennec X, Ayache N, Roche A, Cachier P. Non-rigid MR/US registration for tracking brain deformations. Medical Imaging and Augmented Reality, 2001. Proceedings. International Workshop on. EPIDAURE, Inst. Nat. de Recherche en Inf. et Autom., Sophia Antipolis, France: Practical, 2001:79-86
70. Shekhar R, Zagrodsky V. Mutual information-based rigid and nonrigid registration of ultrasound volumes. Medical Imaging, IEEE Transactions on 2002;21:9-22

			Preoperative MRI						Intraoperative ultrasound		
									Time$_1$		Time$_n$
			T1	T2	PD	Angio	fMRI	MRSI	Tissue	Doppler	
W$_1$ Window$_1$ (3D-scene$_1$ / View-point$_1$)	Ortho Sliced	A							T		
		C	T								
		S		O							
	Volume Rendered (VR)					V				V	
	Geometry Rendered (GR)			T							
W$_m$											

Table 1: Datasets and visualization techniques in various combinations. Many volumes, originating from both pre- and intraoperative acquisitions, which can be visualized in a variety of ways, offer a lot of options. However, only the relevant structures for a given operation (type and phase) should be shown. And these structures should be extracted from the most appropriate volume (considering things like image quality and importance of updated information), and visualized in an optimal way (both individually and in relation to each other). The content of the table summarizes the situations illustrated in figure 7F, where the most interesting structures are the tumor (T) and the vessels (V), and the other objects are used for overview (O).

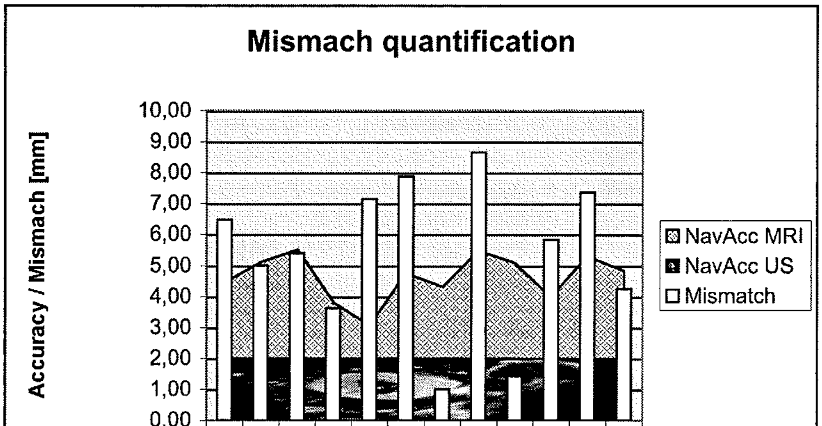

	1	2	3	4	5	6	7	8	9	10	11	12
NavAcc MRI	2,4	3	4	2	1	3	2	3	3	2	3	3
NavAcc US	2,0	2,0	2,0	2,0	2,0	2,0	2,0	2,0	2,0	2,0	2,0	2,0
Mismatch	6,4	5,0	5	4	7	8	1,0	9	1	6	7	4

Table 2: Results from clinical mismatch analysis. If the mismatch between preoperative MRI and intraoperative ultrasound is greater then the sum of the independent navigation inaccuracies we have an indication of brain shift. In the present study, this happened in six of the twelve cases where the mismatch was quantified. This means that in approximately 50% of the cases we can expect to find considerable shifts even in the early stage of an operation.

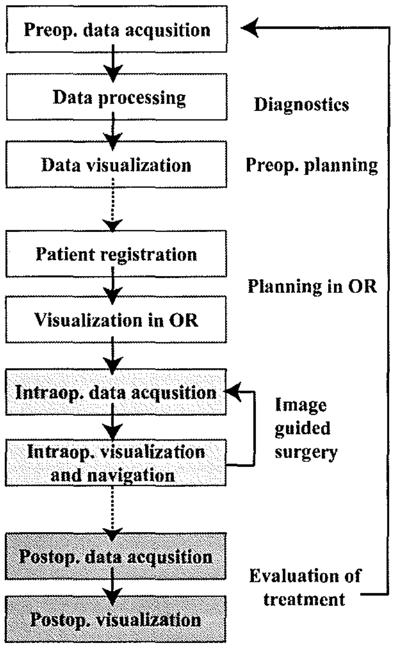

Figure 1: Important steps in image guided surgery. 1) Preoperative data acquisition and planning. 2) Patient registration and planning in the OR. 3) Intraoperative data acquisition and navigation. 4) Postoperative control of treatment.

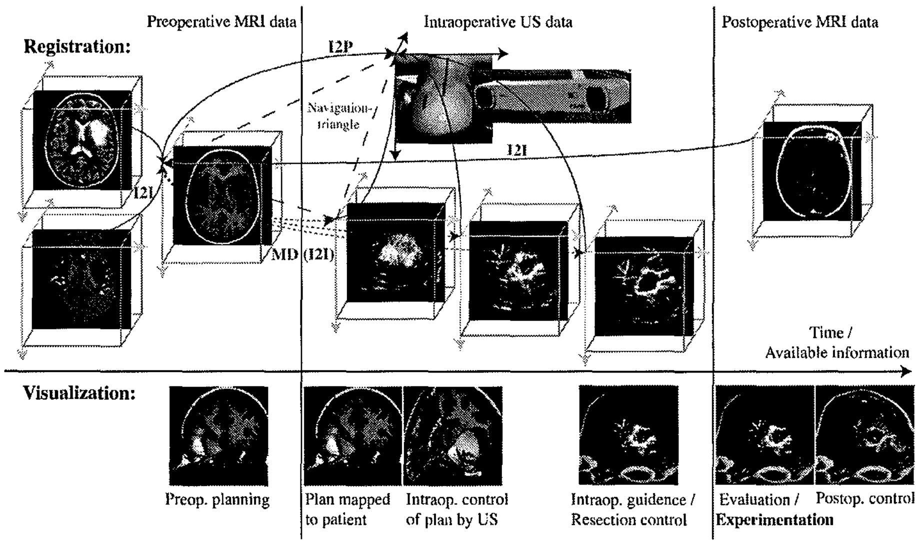

Figure 2: Registration of preoperative images to each other (I2I reg.) for diagnostics and planning in the office, and to the patient (I2P reg.) for intraoperative planning and guidance in the OR. Acquisition and reconstruction of ultrasound volumes are performed relative to the reference frame of the tracking system so that registration is not required. The navigation triangle symbolizes the fact that the accuracies involved in navigation based on preoperative MRI and intraoperative ultrasound are independent and that an observed mismatch between the two modalities not necessarily implies brain shift. Visualizations at the different stages in the operation can be simulated by experimenting with the data available at that stage.

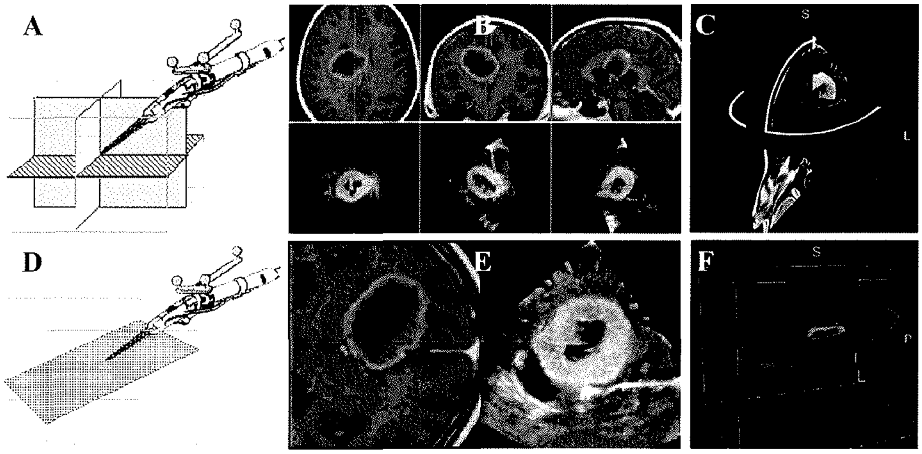

Figure 3: Generating and displaying slice data. Orthogonal (A) or oblique (D) slices relative to the volume axis can be controlled by a surgical tool (intraop.) or by a mouse (pre- and postop.). The extracted slices can be displayed directly in a window (B, E), or texture-mapped on polygons in a 3D scene and rendered into a window (C, F).

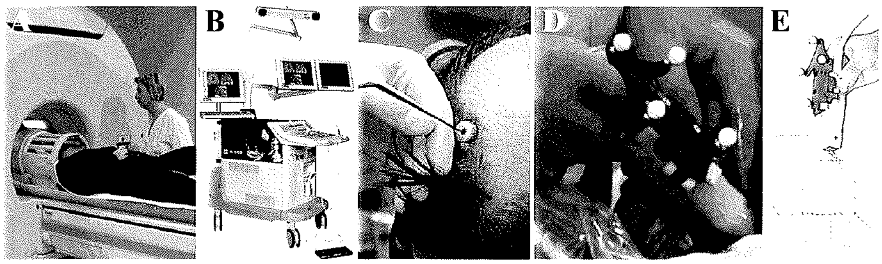

Figure 4: 3D image acquisition. A) Prior to surgery the patient is scanned, and one or more MRI datasets are generated. B) Preoperative MRI data are transferred to the navigation system in the OR, and registered to the patient (C). High quality ultrasound images are acquired when needed (D), and the tracked digital images are reconstructed into a regular volume (E) that is automatically registered and can be treated the same way as the MRI volumes in the navigation system.

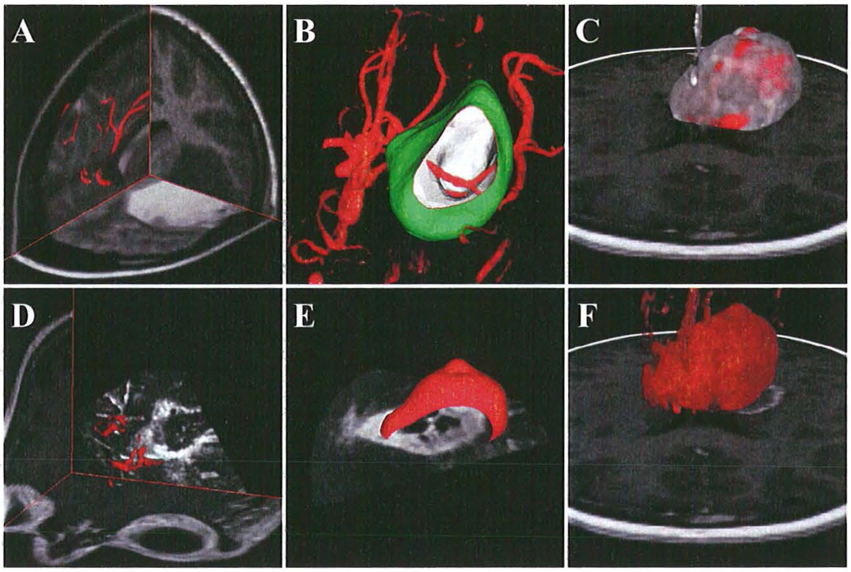

Figure 5: Integrating different visualization techniques and modalities (D-F) in the same 3D scene. A) A slicer object where each of the three orthogonal planes shows a different MRI-volume (T1, T2 and T2 fused with MRA). B) Volume rendered (VR) arteries from an MRA-volume (VR-MRA-arteries in red) in the same 3D scene as a geometric rendered (GR) tumor extracted from a T2-MRI-volume (GR-T2-tumor in green). C) The same MRI-tumor is GR (in red) as well as VR (white fog), illustrating the grater detail often achieved with the letter technique. In addition, an axial MRI-slice is displayed where the tumor is located and improves the overview. D) An intraoperative coronal US-slice (as well as VR-US-Doppler-vessels) integrated with axial and sagittal MRI-slices. Visualizing the mismatch between pre- and intraoperative data using a GR-MRI-tumor together with a US-slice trough the same tumor (E) and a MRI-slice together with a VR-US-tumor (F).

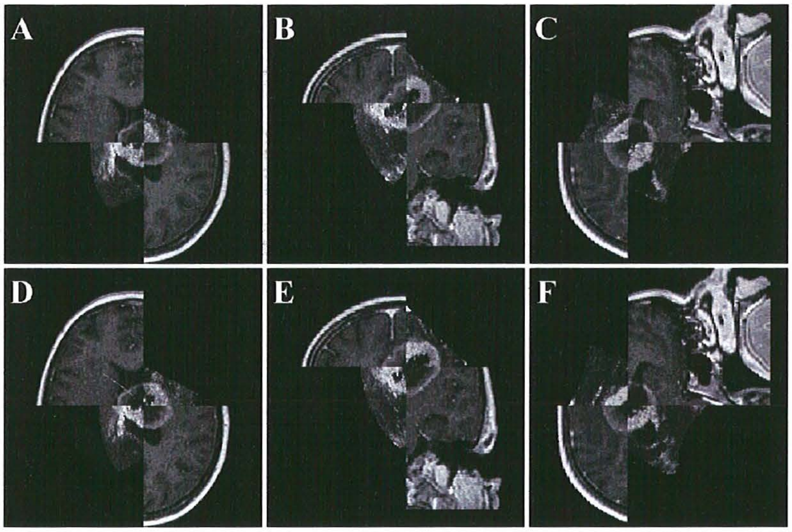

Figure 6: Manual quantification of mismatch. Three orthogonal slice-plans are displayed. Each plane is split in the middle of an interesting structure and the different regions of the plane are assigned data from the two modalities (A-C). The MRI-volume is then translated until the mach with the ultrasound volume is as good as possible using the eye for adjustments (D-F). The length of the shift vector can then be calculated.

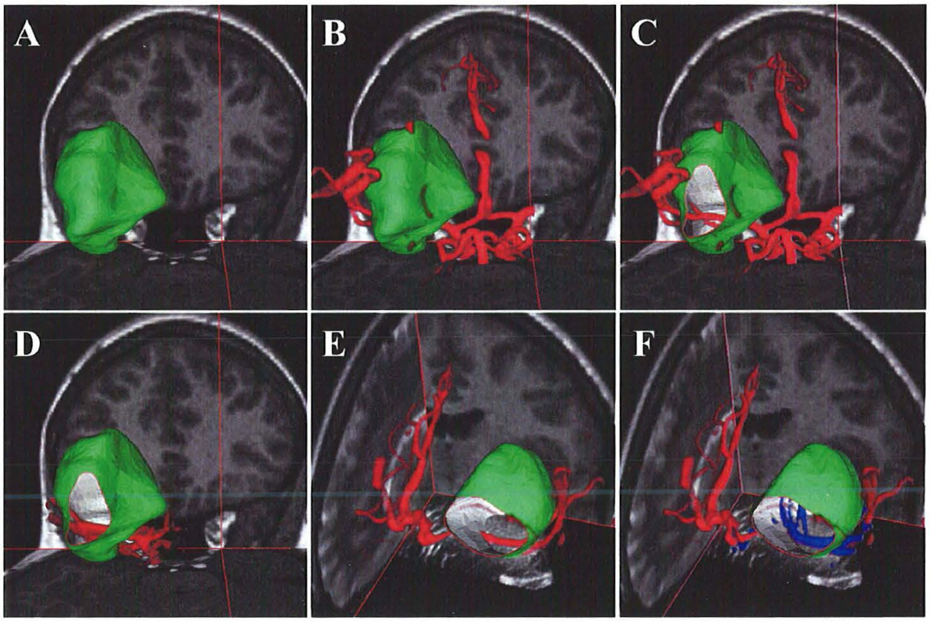

Figure 7: Preoperative planning in the office based on MRI (A-C) as well as in the OR based on both MRI and updated ultrasound (D-F). A) Localization of the target, i.e. the green GR T2-MRI tumor seen in front of the axial and coronal T1-MRI slices used for overview. B) Search for the optimal surgical approach that avoids important structures, e.g. the VR MRA vessels seen in red. C) Infiltrating vessels complicating the surgical procedure (revealed by cutting into the tumor). The plan is update with intraoperative ultrasound data to make sure that vessel locations (D shows VR-Power-Doppler-US vessels in red) and the tumor border (E shows an axial US slice) are correctly displayed. F) Use of updated ultrasound data when available (VR-US vessels in blue as well as an axial US slice) and preoperative MRI data around for improved overview.

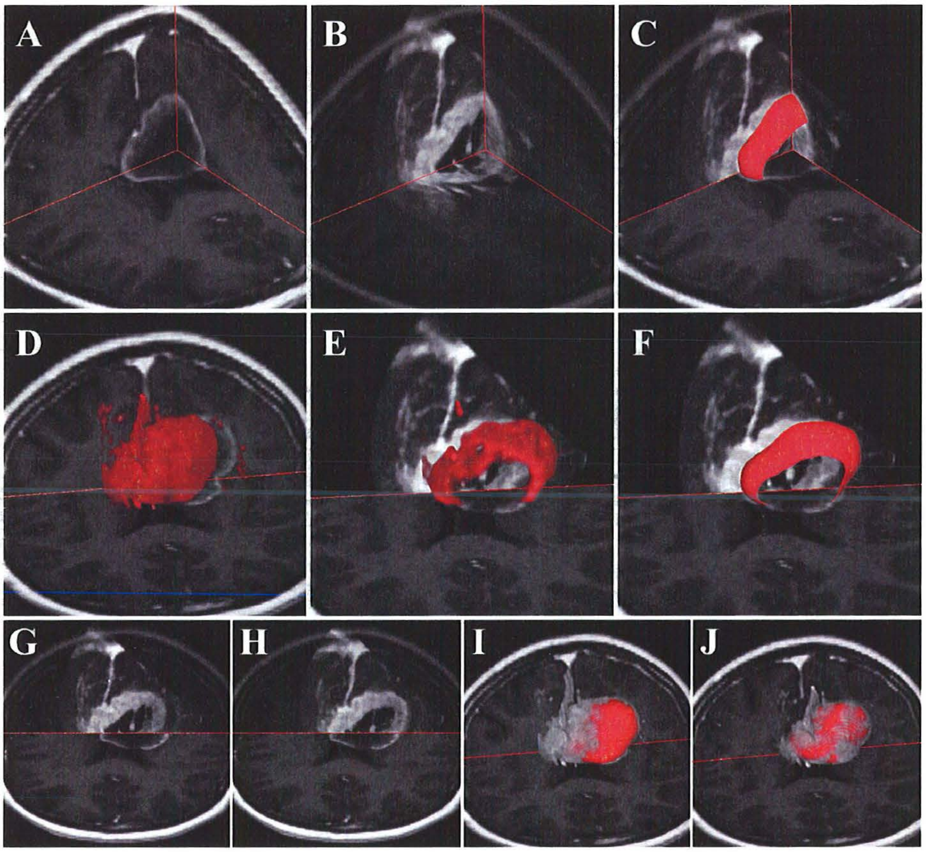

Figure 8: Identification and correction of brain shift using mulimodal image fusion. A) Orthogonal MRI-slices cut through the target area. B) Intraoperative ultrasound is shown transparent and overlaid existing MRI slices. C) Axial MRI slice, sagittal US slice and blended coronal slice in addition to a MRI-segmented tumor that is given a geometric representation (GR-MRI-tumor in red). Mismatch is seen between a MRI-slice and a VR-US-tumor in red (D), between an US-slice and a VR-MRI-tumor in red (E), between an US-slice and a GR-MRI-tumor in red, between a MRI-slice and a US-slice (G) and between a VR-US-tumor in gray and a GR-MRI-tumor in red. H and J are mismatch corrected views of G and I, respectively.

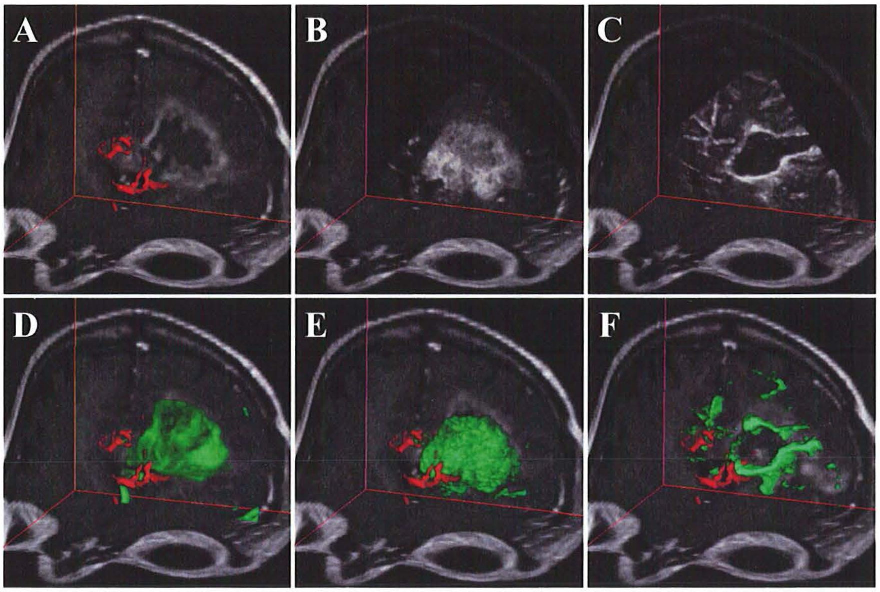

Figure 9: Multimodal imaging for guiding a tumor operation with resection control. A) A coronal MRI-slice cuts through the target area (VR-US-flow in red). The coronal slice is replaced by the corresponding first US-slice (B), and a slice extracted from one of the last 3D Ultrasound volumes acquired (C). D, E and F are volume rendered representations of A, B and C, respectively. As can be seen from C and F there might be some tumor tissue left.

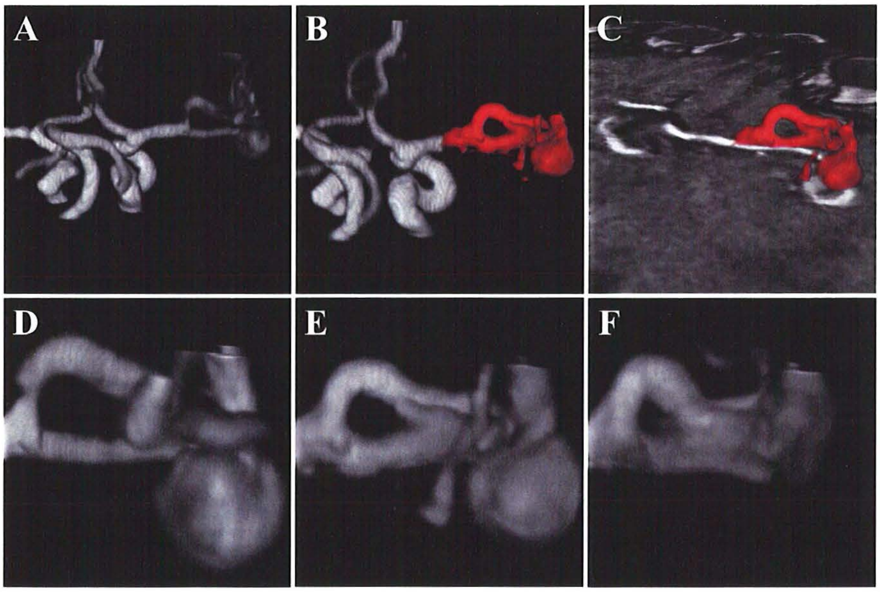

Figure 10: 3D displays for improved aneurysm operation with clipsing control. A) VR-MRA-aneurysm for overview. B) The target area is replaced with updated ultrasound data (VR-US-flow-aneurysm in red). C) The mismatch between the preoperative MRA-slice through the aneurysm and the intraoperative VR-US-flow- aneurysm in red is clearly visible. Zoom in on the VR-MRA-aneurysm (D), and the VR-US-flow-aneurysm before (E) and after clipsing (F).

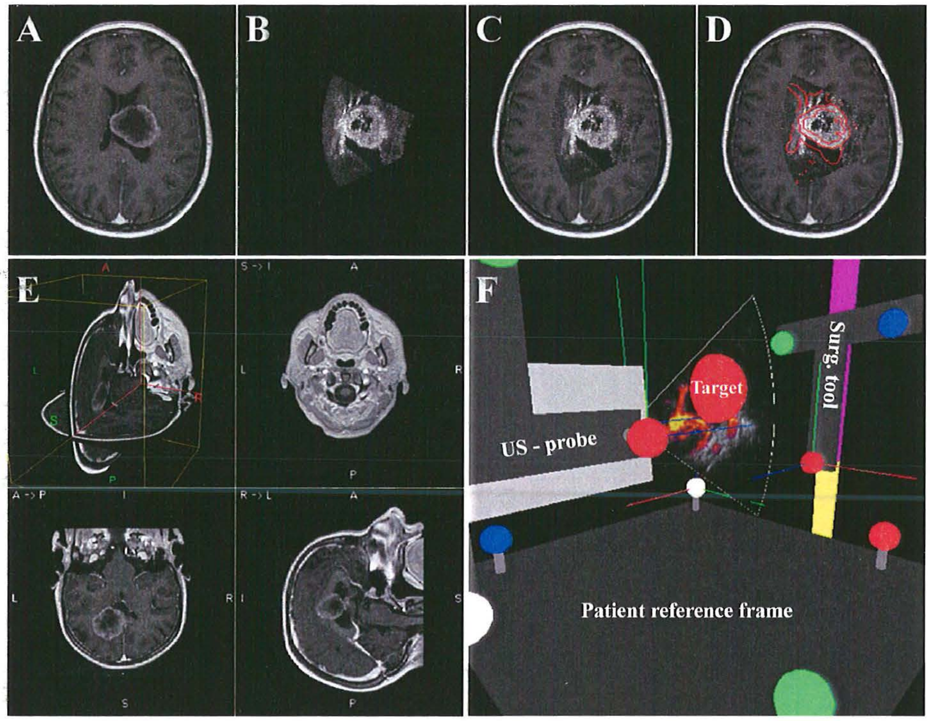

Figure 11: The ultrasound image in B can be replaced by C where MRI-data from A is filled around the US-data without obscuring the updated map of the target area at the same time as improved overview is achieved. Overlay as an aid for interpretation as well as brain shift assessment will partly hide the data behind and should therefore be easy to turn on and off (D). Traditional display of orthogonal slices coupled to the viewpoint in the 3D scene (E). When the 3D scene is rotated to simulate that the surgeon is looking at the patient from a different direction, the 2D display of the slices follow in discrete steps (each slice has two sides and each side can be rotated in steps of 90 degrees) to approximately match the surgeon's view of the patient. F) Virtual navigation scene. Four objects can be seen: 1) the patient reference frame used by the tracking system, 2) an ultrasound probe with real time ultrasound data (both tissue and flow) mapped onto the virtual scan-sector, 3) the target, which could be extracted from preoperative data and given a geometric representation, and 4) a surgical tool with and attached tracking frame.

Paper II

TOOL NAVIGATION IN ULTRASOUND-GUIDED INTERVENTIONS

Technical Note:

Authors:
Thomas Langø[1], Frank Lindseth[1,2], Geir Arne Tangen[1], Jon Harald Kaspersen[1], Steinar Ommedal[1], Toril A Nagelhus Hernes[1]

Affiliation:
[1]SINTEF Unimed, Ultrasound, Trondheim, Norway
[2]The Norwegian University of Science and Technology, Department of Computer and Information Science, Trondheim, Norway

Abstract

We describe novel methods for navigating surgical instruments during real time 2-D ultrasound-guided surgery. The methods provide the surgeon with complete and direct visual information about the position and orientation of the ultrasound image relative to the surgical tool. This means that the surgeon easily can adjust either the orientation of the ultrasound probe or the surgical tool in order to obtain an optimal view of the tool at all times in the real time 2-D image. This is important for safe and accurate patient treatment. The method requires a tracking device on both the tool and the probe; it also requires that both the probe and tool have been calibrated. The probe calibration procedure establishes the position and orientation of the ultrasound image relative to the tracking device attached to the probe. Similarly, the tool calibration calculates the tip location and orientation relative to the origin of the tracking device attached to the tool. The tool tip and the tracking device attached to the tool must constitute a rigid body. The method can easily be expanded to include preoperative image data and segmented structures or models.

Keywords: tool navigation, ultrasound imaging, surgical navigation, ultrasound-guided surgery

INTRODUCTION

Image-guided surgery is commonly conducted by the use of preoperative images, such as magnetic resonance images (MRI) or computerized tomography (CT) data. These preoperative images can very accurately provide information of anatomy if no significant changes occur during surgery. However, during surgery many different factors may affect tissue movement, and hence cause changes that are not reflected in the images acquired prior to the surgical procedure. In neurosurgery these changes are often referred to as the brain shift problem (Bucholz et al. 1997; Hata et al. 1997; Hirschberg and Unsgaard 1997; Koivukangas et al. 1993; Trobaugh et al. 1994). This movement or shifting of anatomical structures as the procedure progresses is mainly caused by removal of tumor tissue, drainage of cerebrospinal fluid, and gravity as the patient might be positioned differently than what was the case during acquisition of the preoperative images. To continuously work with images reflecting the true patient anatomy, intraoperative imaging modalities have been introduced. These include real time 2-D ultrasound imaging (Unsgaard et al. 2002), repetitive 3-D ultrasound imaging (Unsgaard et al. 2002), intraoperative MRI (Hadani et al. 2001; Kettenbach et al. 1999; Samset and Hirschberg 1999), or intraoperative CT (Grunert et al. 1998; Matula et al. 1998). Some operating theaters use a combination of preoperative MRI and intraoperative ultrasound where the ultrasound images are used to identify and quantify the brain shift (Erbe et al. 1996) and/or to warp the preoperative images so that they reflect the true position of organs during surgery (Bucholz et al. 1997).

In recent years, another possibility has been presented; real time 2-D ultrasound in combination with repetitive 3-D ultrasound acquisitions using a position sensing system to track the position and orientation of the images (Gronningsaeter et al. 2000; Hata et al. 1997). The preoperative MRI or CT images are used mainly for preoperative planning and to get an overview of the anatomical area of interest. A major advantage of intraoperative ultrasound-guided navigation in surgery is the ability to do repetitive 3-D imaging (up to approximately 10 times) during the surgical procedure without prolonging the operation time considerably, and thus continuously work with a 3-D data set that has recently been updated according to possible changes in the brain anatomy (Gronningsaeter et al. 2000; Unsgaard et al. 2002). Hence, real time 2-D and recently acquired 3-D ultrasound images are used to monitor the progress of the operation. A limitation with this and other techniques is that it often can be difficult to obtain a real time view of the tip portion of the tool (longitudinal cross section view) in the 2-D image (Unsgaard et al. 2002). Furthermore, it can be difficult to coordinate the handling of both the ultrasound probe and the tool at the same time. It would be of benefit to the operator if the position and orientation of the tool always could be seen in relation to the real time image plane (and hence, important anatomic structures). If the instrument can not be seen in the image, it would be valuable to know how to adjust the ultrasound probe (or tool) to obtain a visualization of the tip of the tool. This is important to ensure safe and accurate interventions, e.g. in minimally invasive surgery. Furthermore, it is relevant for several interventional tasks such as image-guided biopsy sampling, where the operator needs to see the instrument (biopsy forceps) in the real time image to know where the biopsy sample is taken. Some ultrasound scanners have a built-in biopsy guidance system (e.g. System FiVe®, GE Vingmed Ultrasound, Norway). This means that a biopsy adapter is attached to the ultrasound probe and a calculated path in the 2-D image is indicated on the monitor due to the angle of incision imposed by the attached biopsy adapter. The problem with this approach is that the tool might bend out of the 2-D image plane, and due to the coupling of the probe and instrument, the operator is unable to adjust the probe or the tool orientation to obtain a better view.

We have developed a tool navigation technique that may run as a stand-alone application or in conjunction with an image-based navigation system. The module provides the surgeon with a direct and intuitive view (display) of the position and orientation of the surgical tool and the ultrasound real time 2-D image, correctly oriented relative to each other in space. This view simplifies navigation of the tool and anatomic changes in the vicinity of the tool is directly monitored in the real time ultrasound image. In addition, details about the distance and angle between the image and the tool tip can be displayed. The display can be seen from any position, e.g. from the surgeon's point of view or from the ultrasound probe or tool. In this paper, we describe the application and present examples. In the discussion, we explore the potentials of the tool navigator by inclusion of other data/objects, such as preoperative or intraoperative 3-D data or segmented objects from 3-D data.

METHODS

Equipment

We used an in-house navigation system based on an optical tracking system (Polaris®, Northern Digital, Canada). The tracking system consists of a processing unit and two cameras (Fig. 1a) that emit infrared light and register the reflected light from small spheres arranged in a specific geometric configuration on a frame attached to the instruments to be tracked (Fig. 1b-c). The ultrasound probe was a phased array probe with 5 MHz center frequency connected to a high-end digital ultrasound scanner (System FiVe®, GE Vingmed Ultrasound, Norway) (Fig. 1d).

Calibration of ultrasound probe and surgical tool

The tool navigation techniques presented in this paper are based on position measurements from tracking devices attached to the probe and tool (Fig. 1b-c). The ultrasound image plane coordinate system is set up with the origin at the top center of the image with the z-axis pointing along the middle of the image in the radial direction (Fig 1e). A probe calibration procedure determines the transformation between the image plane coordinate system and the coordinate system of the tracking device attached to the probe. An accurate calculation of this transformation is of crucial importance for: 1) A 3-D reconstruction that preserves true anatomical shape and size in 3-D freehand ultrasound acquisitions, and 2) Navigation where the absolute position and orientation of the 2-D real time image is needed. Hence, an accurate probe calibration is an important parameter for accurate and safe patient interventions. The probe used in this study was calibrated using an image alignment method with a custom built phantom (Langø 2000). The main idea of the method is to align the image plane with a thin and planar structure with known physical dimensions and points. The known points of the phantom is first accurately measured relative to a reference frame attached to the phantom. By pinpointing the corresponding points in image space, two sets of points are achieved that are matched using a least squares error minimization approach for fitting two point sets (Arun et al. 1987). From this matching the probe calibration transformation is obtained. The calibration matrix $M_{tdp \leftarrow ui}$ (Fig. 1e) is applicable in general since the probe and tracking device constitute a rigid body.

The pointer was calibrated by accurate measurements of the tip relative to the tracking device (origin) attached to the pointer shaft. The pointer was built such that the z-axis of the tracking device coordinate system is oriented along the longitudinal pointer axis tip direction (the z-axis of the tip coordinate system) (Fig. 1e).

Distance and angle between tool tip and ultrasound plane

The shortest distance between the tool tip and the image plane is the perpendicular projection from the tool tip onto the image plane. Let A be the tool tip, at a perpendicular distance d from the image plane. The image plane is spanned out by the three points P, Q, and R (Fig. 2). The perpendicular distance *d* can then be calculated as (Edwards and Penny 1990):

$$d = \frac{\left|\overrightarrow{AP} \cdot \overrightarrow{AQ} \times \overrightarrow{AR}\right|}{\left|\overrightarrow{PQ} \times \overrightarrow{PR}\right|} \tag{1}$$

The angle of interest is the angle ϕ between the distal part of the tool and the line represented by the perpendicular projection of the extended tool line $\vec{T}$ onto the image plane as shown in Fig. 2. This angle, which is always between 0° and 90°, is represented by the angle α in Fig. 2. This angle is given by

$$\alpha = \cos^{-1}\left\{\frac{\vec{T} \cdot \overrightarrow{u_x}}{\left|\vec{T}\right|}\right\}, \quad \vec{u}_x = \frac{\overrightarrow{PR} \times \overrightarrow{PQ}}{\left|\overrightarrow{PR} \times \overrightarrow{PQ}\right|} \tag{2}$$

We must distinguish between three situations: 1) The tool is pointing completely or partially along the negative *x*-axis of the image plane ($\alpha > 90°$, which is the case illustrated in Fig. 2), in which case the angle must be decreased by 90° to obtain the desired angle ϕ; 2) The tool is pointing completely or partially along the positive *x*-axis of the image plane ($\alpha <$ 90°), in which case ϕ is equal to 90° minus α (Eq. 2); 3) The tool is pointing perpendicularly at the *x*-axis ($\alpha = 90°$), in which case the angle ϕ is equal to 0°, i.e., the tool is parallel with the image plane. With these calculations, we are able to tell whether the tool is pointing towards the sensor frame side of the probe or vice versa.

RESULTS FROM VIRTUAL NAVIGATION EXPERIMENTS

We have implemented and tested the virtual navigation scene with the three objects described above (pointer, ultrasound probe, and real time 2-D ultrasound image). All the objects are always correctly localized relative to each other, the objects can be turned on and off as needed (e.g. if an object blocks free sight to interesting structures and other objects), the viewpoint or camera position can be set at any point in the scene, and the objects can be modeled arbitrarily realistic. The most useful views are probably the surgeon's view (Fig. 3a-b) and the tool (Fig. 3c-d) or probe view (Fig. 3e-f). In the surgeon's view, the whole scene is viewed at a distance and all the objects are seen as they would if the patient was transparent to the operator (and if the ultrasound image could be seen in front of the probe in physical space). Since we used a simple set-up in a water bath, we have included photos of the scene taken from the same position as the view point of the virtual camera in the scene display. The tool view displays the scene from the distal part of the tool (Fig. 3c) or from the tip of the tool (Fig. 3d). In one type of probe view (Fig. 3e), the virtual camera of the scene is placed at a distance from the image plane, looking perpendicular onto the image plane at all times. This means that the complete ultrasound 2-D real time image can always be viewed in the scene during navigation. In another probe view, the ultrasound plane can be viewed from the distal part of the probe with the probe object removed from the scene (Fig. 3f). This view makes it easy to see the distance between the image plane and the tool tip (Fig. 3f shows the tool tip in the plane).

All views can be flipped to move the view point to the opposite side of the scene. In addition, the virtual camera distance from the image plane can be set by the operator. The scene display can also be zoomed in and out to capture special details or include all objects.

The supplement graphic bar display shown in Fig. 4 (third column) can be explained by exploring cases of the probe view in Fig. 3f. In Fig. 4a-e the graphic bar display shows detailed information about the distance and angle between the image and tool. The graphic display is continuously updated from the calculations of angle and distance as described above. This navigator module is most useful when views *a-e* in Fig. 3 are used. In particular, this graphic bar (and the numeric values) can prove useful as free sight to the tool tip might be blocked by other objects (tools or image data). The vertical blue bar in the middle is the distance indicator. This indicator has a fixed color and grows in width from the middle to one side according to the distance measure d (Eq. 1) and the sign of the dot product in Eq. 2. One of the areas to the side of the distance indicator is used to indicate the angle, the side used depending on the sign of the dot product in Eq. 2. The angle is indicated by the color of the area. We have used a color scale ranging from light yellow to dark red for this information. All color schemes can be set according to preferences by the operator. The operator also has the option of changing the maximum distance to be indicated by the navigator module. The bar can be flipped if the surgeon switches position from one side of the patient to the other so that left and right in the display keeps its meaning. The color bar and distance and angle information numbers can easily be used for fine tuning of the position of the tool after navigation using the virtual scene.

DISCUSSION

We believe that the virtual scene navigation module will be of great value for minimally invasive surgery, either as an additional feature in conventional navigation systems for surgery or as a stand-alone application. We expect that the method will simplify and improve interventional procedures (e.g. performing biopsies) by providing essential information and an intuitive display of the location and orientation of the tool in relation to the real time 2-D image on the ultrasound scanner.

The accuracy of the tool calibration, the probe calibration, and the inherent position tracking accuracy of the system will determine the accuracy of the virtual scene display and the navigation bar. It has previously been found that probe calibration constitutes the largest error source in neuronavigation for an ultrasound-based system (Lindseth et al. 2002), but the error was found to be approximately 1 mm. The corresponding value for the tool calibration is probably smaller, and has been found to be 0.6 mm for a similar pointer and tracking device configuration as used in this study (Chassat and Lavallée 1998). The errors from the tracking system itself is approximately 0.35 mm according to the vendor. A direct visual inspection of the accuracy (qualitative) is available when using the navigator display. The degree of match between the model of the tool and the actual tool in the real time 2-D ultrasound image can be evaluated by using the navigator. Optimal accuracy means that the tool model will obstruct the view of the ultrasound image of the tool, and only the noise around the tool should be visible. The information in the supplement navigation bar can even be included in the tool model in the navigation scene. The blue color distance bar can be superimposed onto the tip of the tool, while the angle code can be visualized on the distal part of the tool. This makes it even easier to see how far from the ultrasound image, the tool actually is located at all times.

The virtual navigation scene can easily be expanded to include other objects than the simple tool, probe, and ultrasound image as used in our set-up. By performing a registration (Maintz 1996) of preoperative images (e.g. MRI/CT) to the patient or to intraoperative data (e.g. ultrasound), these data can be included in the same scene display. Extracted objects or models based on these preoperative data can also be used in the scene, e.g. segmented tumors or abdominal aortic aneurysm (AAA) model as the example in Fig. 5 shows. If preoperative images are used, the registration accuracy will influence the accuracy of display of objects based on these images. The introduction of preoperative data into the navigation scene means that it is possible to detect, visually, shifts in anatomy relative to the preoperative data (Fig. 5b). This, in turn, implies that the method can be used as a follow-up control method to see how the anatomy or implants change over time, since objects extracted from image data can be stored and included in the scene at a later time with updated 3-D image data (and segmented objects). It can further be used to confirm correct placement of e.g. an AAA graft by using the real time 2-D ultrasound image in conjunction with a segmented or modeled representation of an implanted graft. In addition, inclusion of more objects in the scene, means that we must develop effective ways of displaying all the different information. We have developed multimodal image visualization methods (Lindseth et al. 2002) and will incorporate these methods in the tool navigation module to achieve one integrated 3-D scene display that includes all interesting information (where the various parts/objects can be turned on or off as needed). Others have implemented guidance systems for interventional imaging using integrated visualization based on preoperative data and segmented objects (Gering et al. 1999). However, we believe that to make interventional procedures safer and more accurate, there is a need for real time imaging. In our opinion, ultrasound is the best alternative for this, when considering cost, ease of use, image quality, and real time imaging capabilities (2-D and 3-D).

Today a modern high-end digital ultrasound scanner is capable of making approximately 20 high quality images per second, assuming a wide sector (≥ 90°) with scanning depths of approximately 10 cm. By reducing the sector width and the spatial resolution, it is probably possible to achieve as many as several hundred scans per second (depending on scan depth). This means that a limited 3-D sector may be scanned with several 3-D volumes per second. Real time 3-D imaging will make it possible to see the moving surgical instrument and tissue directly in the scene in relation to the surrounding structures. Nevertheless, with the limited sector scan size of ultrasound compared to MR and CT, we believe it would still be beneficial to have a virtual representation of the entire tool as well as other objects (tools or segmented objects from MR/CT images) embedded in the same scene as the image data (Lindseth et al. 2002). Finally, with high demands for resolution and scan depth, one will probably have to cope with repetitive 3-D acquisitions for a while to come.

CONCLUSION

In conclusion, we have developed a navigation module to simplify navigation of tools in relation to real time 2-D ultrasound images in minimal invasive patient interventions. The method can easily be expanded to include preoperative 3-D data and segmented objects by using registration techniques. The main advantage of the method is the ease of navigating tools into the real time 2-D ultrasound image. Furthermore, the navigation display is intuitive and easy to understand. The method presents an augmented visualization of the operating scene in a display that can be viewed from anywhere. In addition, the distance and angle between the real time 2-D ultrasound image plane and the tip of the tool from position tracking information can be used for documentation purposes (e.g. biopsy sampling position) or fine tuning of the position of the tool or the ultrasound probe.

ACKNOWLEDGEMENTS

This work was supported by grants from the Research Council of Norway through the Strategic University Program in Medical Technology at the Norwegian University of Science and Technology (NTNU), the Strategic Institute Program at SINTEF Unimed, and the Norwegian Ministry of Health and Social Affairs.

REFERENCES

Arun KS, Huang TS, and Blostein SD. Least-squares fitting of two 3-D point sets. IEEE Trans Pattern Anal Machine Intell, 1987;PAMI-9:698-700.

Bucholz RD, Yeh DD, Trobaugh J, McDurmont LL, Sturm CD, Baumann C, Henderson JM, Levy A, and Kessman P. Correction of stereotactic inaccuracy caused by brain shift using an intraoperative ultrasound device. Lecture Notes in Computer Science Proceedings of the 1997 1st Joint Conference Computer Vision, Virtual Reality and Robotics in Medicine and Medical Robotics and Computer-Assisted Surgery, CVRMed-MRCAS'97, Grenoble, 1997;1205:459-466.

Chassat F, and Lavallée S. Experimental protocol of accuracy evaluation of 6-D localizers for computer-integrated surgery: Application to four optical localizers. Lecture notes in Computer Science, Medical Image Computing and Computer-Assisted Intervention - MICCAI'98, Springer-Verlag, Berlin, 1998;1496:277-284.

Edwards CH, and Penny DE. Calculus and analytic geometry. Englewood Cliffs, N.J., USA, Prentice-Hall, 1990.

Erbe H, Kriete A, Jödicke A, Deinsburger W, and Böker DK. 3D-ultrasonography and image matching for detection of brain shift during intracranial surgery. Computer Assisted Radiology, CAR '96, Paris, France, Elsevier Science, 1996:225-230.

Gering DT, Nabavi A, Kikinis R, Grimson WEL, Hadani N, Everett P, Jolesz F, and Wells WM. An integrated visualization system for surgical planning and guidance using image fusion and interventional imaging. Medical Image Computing and Computer-Assistes Intervention (MICCAI), Cambridge, England, Springer, 1999

Gronningsaeter A, Kleven A, Ommedal S, Aarseth TE, Lie T, Lindseth F, Langø T, and Unsgård G. SonoWand, An ultrasound-based neuronavigation system. Neurosurgery, 2000;47:1373.

Grunert P, Müller-Forell W, Darabi K, Reisch R, Busert C, Hopf N, and Perneczky A. Basic principles and clinical applications of neuronavigation and intraoperative computed tomography. Comp Aid Surg, 1998;3:166-173.

Hadani M, Spiegelman R, Feldman Z, Berkenstadt H, and Ram Z. Novel, compact, intraoperative magnetic resonance imaging-guided system for conventional neurosurgical operating rooms. Neurosurgery, 2001;48:799-809.

Hata N, Dohi T, Iseki H, and Takakura K. Development of a frameless and armless stereotactic neuronavigation system with ultrasonographic registration. Neurosurgery, 1997;41:608-613.

Hirschberg H, and Unsgaard G. Incorporation of ultrasonic imaging in an optically coupled frameless stereotactic system. Acta Neurochir Suppl Wien, 1997;68:75-80.

Kettenbach J, Wong T, Kacher DF, Hata N, Schwartz RB, Black PM, Kikinis R, and Jolesz FA. Computer-based imaging and interventional MRI: applications for neurosurgery. Comput Med Imaging Graph, 1999;23:245-258.

Koivukangas J, Louhisalmi Y, Alakuijala J, and Oikarinen J. Ultrasound-controlled neuronavigator-guided brain surgery. J Neurosurg, 1993;79:36-42.

Langø T. Ultrasound guided surgery: Image processing and navigation. Doctoral thesis, Norwegian University of Science and Technology, Trondheim, Norway, 2000.

Lindseth F, Kaspersen JH, Ommedal S, Langø T, Unsgaard G, and Hernes TAN. Multimodal image fusion in ultrasound-based neuronavigation: Improving overview and interpretation by integrating preoperative MRI with intraoperative 3D ultrasound. Comp Aid Surg, 2002;Submitted

Lindseth F, Langø T, Bang J, and Hernes TAN. Accuracy evaluation of a 3D ultrasound-based neuronavigation system. Comp Aided Surg, 2002; 7:197-222

Maintz JBA. Retrospective registration of tomographic brain images. PhD, Utrecht University, Utrecht, Nederland, 1996.

Matula C, Rössler K, Reddy M, Schindler E, and Koos WT. Intraoperative computed tomography guided neuronavigation: Concepts, efficiency, and work flow. Comp Aid Surg, 1998;3:174-182.

Samset E, and Hirschberg H. Neuronavigation in intraoperative MRI. Comp Aided Surg, 1999;4:200-207.

Trobaugh JW, Richard WD, Smith KR, and Bucholz RD. Frameless stereotactic ultrasonography: Method and applications. Comput Med Imaging Graph, 1994;18:235-246.

Unsgaard G, Gronningsaeter A, Ommedal S, and Hernes TAN. Brain operations guided by real-time 2D ultrasound: New possibilities due to improved image quality. Neurosurgery, 2002;51:402-412.

Unsgaard G, Ommedal S, Muller T, Gronningsaeter A, and Hernes TAN. Neuronavigation by intraoperative 3D ultrasound, Initial experiences during brain tumor resections. Neurosurgery, 2002;50:804-812.

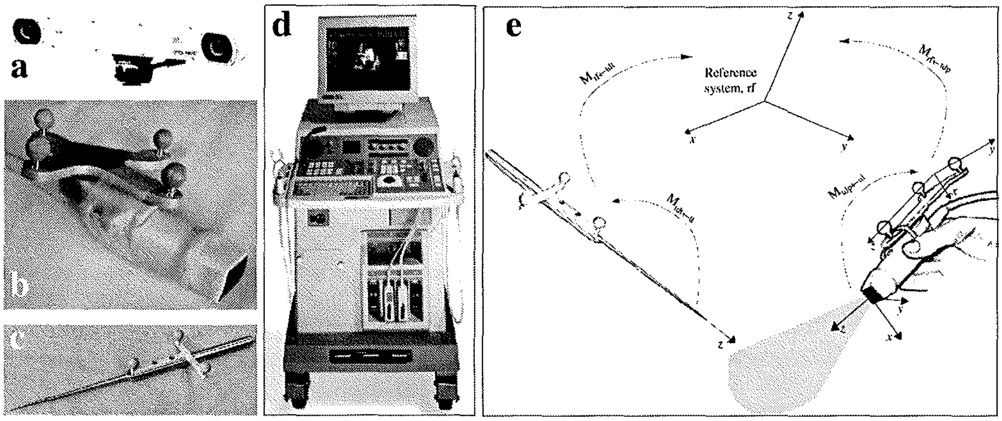

Fig. 1. Equipment. a) Optical tracking system Polaris® (Northern Digital Inc., Canada). b) 5 MHz phased array ultrasound probe. c) Pointer with attached tracking device. d) Ultrasound scanner System FiVe ® (GE Vingmed Ultrasound, Norway). e) Definitions of coordinate systems and transformations. The probe calibration matrix is denoted $M_{tdp\leftarrow ui}$, while $M_{tdt\leftarrow tt}$ is the tool calibration matrix. $M_{rf\leftarrow tdp}$ and $M_{rf\leftarrow tdt}$ are the transformations measured by the position tracking system. *tdp* denotes the coordinate system of the tracking device on the probe, *ui* the coordinate system of the ultrasound image, *tdt* the coordinate system of the tracking device on the tool, *tt* the tool tip coordinate system, and *rf* the reference.

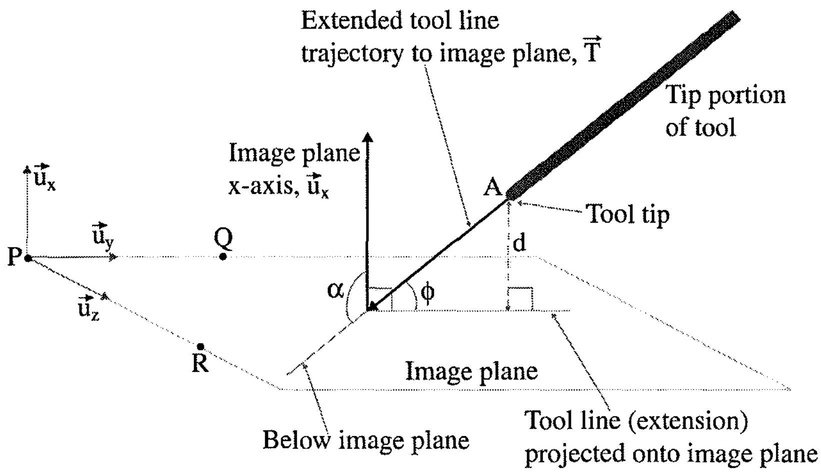

Fig. 2. Illustration of the distance d between the tool tip and image plane and the angle ϕ between the distal part of the tool and the image plane. $\vec{u}_x$ is a unit vector along the x-axis of the image plane (perpendicular to the plane). P is the image plane origin, Q is a point along the y-axis of the image plane, and R is a point along the z-axis of the image plane. Numerical values for A, P, Q, and R are available from position tracking measurements.

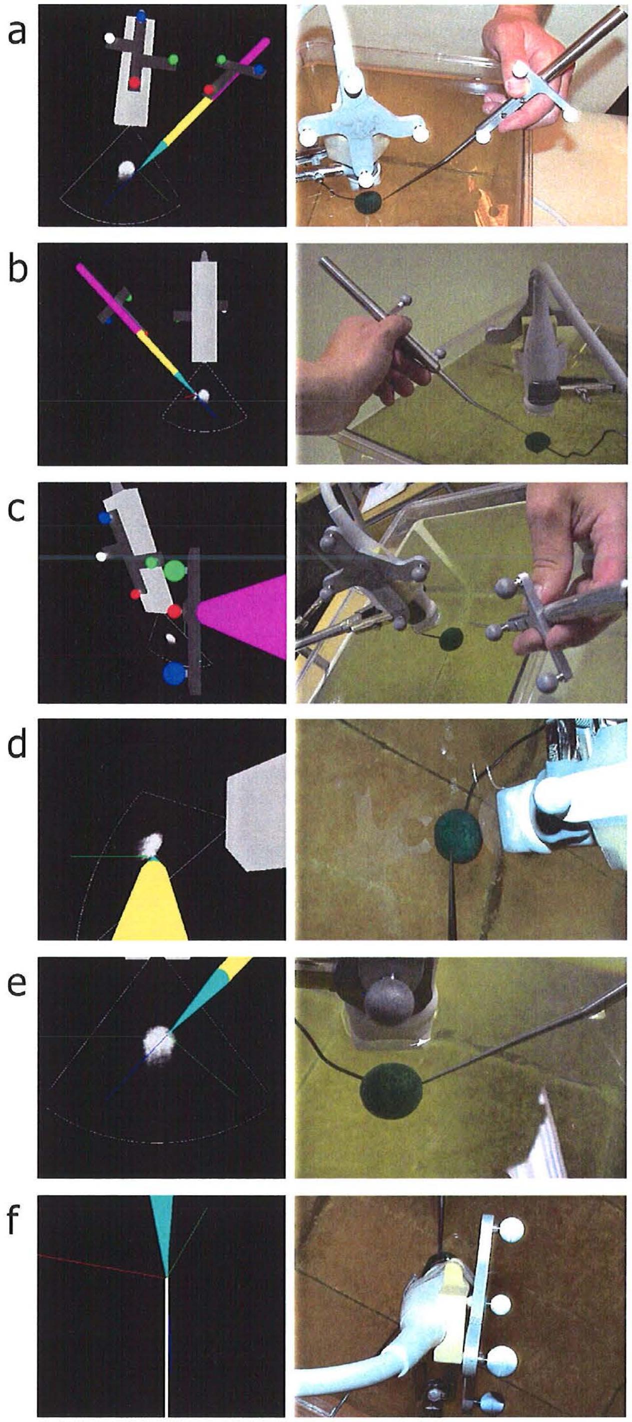

Fig. 3. Virtual navigation scene display with corresponding photos from a water tank set-up. a-b) Surgeon's view from both sides of the scene. c-d) Tool view from the distal part of the tool (c) and from the tip of the tool (d). e) Probe view, i.e. view normal to ultrasound image. f) Probe view from distal part of the probe with probe object removed from scene. In this probe view (f), the image plane is the vertical thin line, i.e. the image plane is perpendicular to the view window.

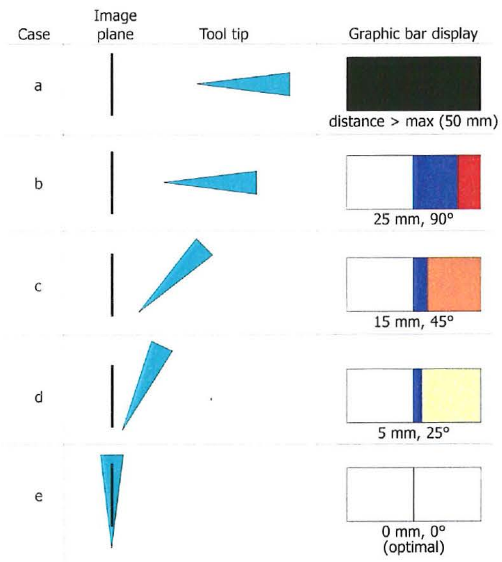

Fig. 4. The graphic bar display module showing five cases of the set-up in Fig. 3f. The blue (fixed color) bar in the middle indicates the distance parameter *d* (Eq. 1). a) If the tool and image are separated by more than a preset distance, the entire bar is black. The angle ϕ (Eq. 2) is coded using a color range from b) red (90 angle between the tool tip and the image plane) through c) orange and d) yellow, to e) white (optimal alignment, i.e. the tip portion of the tool is in the image plane).

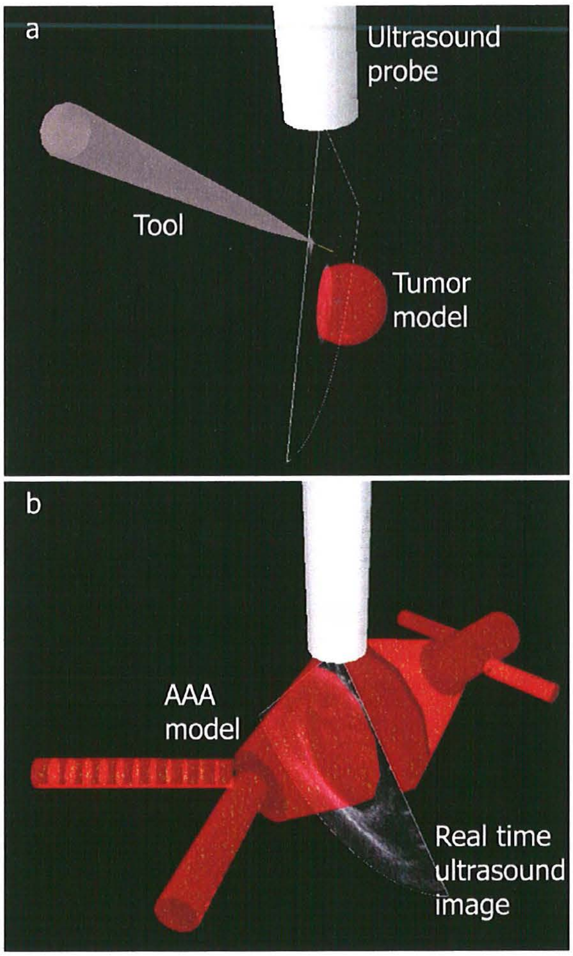

Fig. 5. Two examples of how the navigation module can be used to fuse preoperative images, real time intraoperative imaging, and segmented objects. This fusion makes it easy to detect and/or visualize shifts in the anatomy that have occurred. a) This scene shows a similar display to what was shown in Fig. 3, but with a transparent 3-D model tumor representing a segmented object from preoperative images. b) The scene shows a model of an abdominal aortic aneurysm (AAA) with an overlaid real time ultrasound image from a patient with AAA (surgeon's view). The model has been made transparent to reveal details in the relative position and orientation of the AAA and the model object.

Paper III

Biomedical Paper

Accuracy Evaluation of a 3D Ultrasound-Based Neuronavigation System

Frank Lindseth, M.SC., Thomas Langø, PH.D., Jon Bang, PH.D., and Toril A. Nagelhus Hernes, PH.D.
SINTEF Unimed, Ultrasound (F.L., T.L., J.B., T.A.N.H.), and the Norwegian University of Science and Technology, Department of Computer and Information Science (F.L.), Trondheim, Norway

ABSTRACT
We have investigated the 3D navigation accuracy of a frameless ultrasound-based neuronavigation system (SonoWand®) for surgical planning and intraoperative image guidance. In addition, we present a detailed description and review of the error sources associated with surgical neuronavigation based on preoperative MRI data and intraoperative ultrasound. A phantom with 27 precisely defined points was scanned with ultrasound by various translation and tilt movements of the ultrasound probe (180 3D scans in total), and the 27 image points in each volume were located using an automatic detection algorithm. These locations were compared to the physically measured locations of the same 27 points. The accuracy of the neuronavigation system and the effect of varying acquisition conditions were found through a thorough statistical analysis of the differences between the two point sets. The accuracy was found to be 1.40 ± 0.45 mm (arithmetic mean) for the ultrasound-based neuronavigation system in our laboratory setting. Improper probe calibration was the major contributor to this figure. Based on our extensive data set and thorough evaluation, the accuracy found in the laboratory setting is expected to be close to the overall clinical accuracy for ultrasound-based neuronavigation. Our analysis indicates that the overall clinical accuracy may be as low as 2 mm when using intraoperative imaging to compensate for brain shift. Comp Aid Surg 7:197–222 (2002).

Key words: **accuracy evaluation; computer-assisted surgery; neuronavigation; 3D ultrasound; neurosurgery**
Key links: **http://www.us.unimed.sintef.no/; http://www.mison.no/**

INTRODUCTION

Several commercial three-dimensional (3D) navigation systems for image-guided surgery are available today, and are being used routinely in neurosurgery.[1–6] The expected benefits from such systems are improved and easier understanding of 3D orientation and anatomy, more confident surgeons, more precise surgical planning and interventions, reduction of residual tumor volumes (i.e., more radical tumor resections), reduced operation times, and better patient outcomes.[7–17]

Conventional systems based on preoperative data such as magnetic resonance imaging (MRI) and computed tomography (CT) scans will not reflect the true anatomy of the patient, as changes in

Received October 19, 2001; accepted September 24, 2002.

Address correspondence/reprint requests to: Thomas Langø, SINTEF Unimed Ultrasound, 7465 Trondheim, Norway. E-mail: Thomas.Lango@sintef.no

Published online in Wiley InterScience (www.interscience.wiley.com). DOI: 10.1002/igs.10046

anatomy occur during a surgical procedure. Systems based on intraoperative MRI or intraoperative ultrasound can, to a certain degree, compensate for these changes by updating the 3D map of the patient during surgery. In an interventional MRI system, the surgeon is operating inside the magnet, and by choosing speed over quality he is able to obtain one image per second.[18] On the other hand, neuronavigation systems based on intraoperative ultrasound are becoming more accepted due to improved image quality and real-time 2D and 3D freehand capabilities, as well as future real-time 3D possibilities.[19,20] There are two different ways of using 3D ultrasound to obtain a map that corresponds to the anatomy at all times. In the first, the surgeon uses ultrasound indirectly to track the anatomical changes that occur, then uses these changes to elastically deform the preoperative image data. Navigation is then undertaken with reference to the manipulated preoperative MRI/CT data.[4] In the second approach, direct navigation is conducted according to the ultrasound data itself.[1] The system investigated in the present study uses the latter approach.

The delicacy, precision, and extent of the work that the surgeon can perform based on image information rely on the surgeon's confidence in the overall clinical accuracy and the anatomic or pathologic representation. The overall clinical accuracy in image-guided surgery is a measure of the difference between the apparent location of a surgical tool relative to some structure as indicated in the image information presented to the surgeon, and the actual location of the tool relative to that same structure in the patient. This accuracy is difficult to assess in a clinical setting, due to the lack of fixed and well-defined landmarks inside the patient that can be reached accurately by a pointer. It is therefore common practice to estimate the system's overall accuracy in a controlled laboratory setting using precisely built phantoms.[21–23] To make a conclusion on the potential clinical accuracy, the differences between the clinical and laboratory settings must be carefully examined.

Several investigators have estimated the accuracy of navigation systems for surgery.[6,21–25] Although much has been written about conventional neuronavigation systems, the literature on accuracy measurements of ultrasound-based neuronavigation is sparse. Hata et al.[4] reported a root-mean-square (RMS) error of 3.1 mm, with standard deviation 2.5 mm, at a depth of 10 mm from the transducer. These numbers represent the difference between the position of a phantom point in one MRI scan and its position in several ultrasound scans. Similarly, Comeau et al.[26] reported an error of less than 1.3 mm when mapping an ultrasound image pixel to its homologous MRI pixel, as measured on a custom-built phantom. Hartov et al.[23] performed a phantom error analysis of a 3D ultrasound-based neuronavigation system, and reported an overall error of 2.96 ± 1.85 mm when locating features in ultrasound images.

More information is available on navigation systems based on preoperative MRI, and the studies cover a broad range of different positioning systems, various commercially available navigation tools, and imaging and registration techniques, as well as setup and measurement techniques. A common way of assessing the overall accuracy has been to use a rigid and precise phantom/head model in the laboratory and measure the registration accuracy. Typical results for skin fiducial-based registrations are in the order of 2 mm[27] or better.[28,29] Registration based on anatomical landmarks typically yields poorer accuracy.[27,29] Other groups have measured the accuracy in a clinical setting where fiducials and/or the skin surface have been used. For fiducial registration, mean error results of 1.6 mm,[30] 2.51 mm,[6] and approximately 2 mm[31] have been found. Other reported mean error results are 3.03 mm for surface-fit registration,[6] and 3.4 mm using facial landmarks.[30]

However, a perfect match on the skin surface does not necessarily imply a perfect match deep inside the brain. Rotation errors in the registration procedure may be difficult to discover, and may result in significant errors at the skull base. Schaller et al.[5] performed measurements inside the brain using landmarks such as the internal table of the skull, the falx, the tentorium, or the clinoid processes. They reported errors in the order of 3 mm. This approach is interesting, but it is difficult to obtain a precise measurement in more than one or two dimensions, and the number of measurements in one patient will be sparse.

To gain a better understanding of the relationship between laboratory and clinical accuracy, we will describe and compare the most relevant error sources associated with neuronavigation based on preoperative MRI and the error sources associated with neuronavigation based on intraoperative 3D ultrasound. Navigation based on preoperative MRI is well established and more frequently used compared to interventional MRI. Furthermore, the analysis includes patient registration based on skin fiducials, with some comments on other registration methods. Apart from these restrictions, the description of MRI error sources is intended to be general. Similarly, the section on ultrasound error sources

Table 1. Error Chain Associated with Neuronavigation Based on Preoperative MRI Data

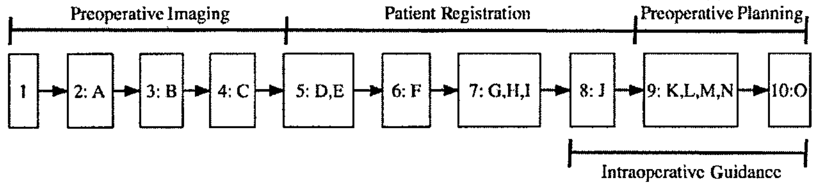

	Action items		Error sources	Error magnitude (mm) <1	1–2	>2
1	Glue fiducials to skin					
2	Position patient in MR-scanner	A	Skin/fiducial slide			√*
3	Perform 3D MRI	B	Geometric distortion in MR data	√[34]	√[34]	√[32]
4	Load images and generate volume	C	Quantization in volume reconstruction	√*		
5	Position patient on operating table	D	Brain shift due to gravity			√[46]
		E	Skin/fiducial slide due to gravity			√*
6	Mark fiducials in MR images	F	Fiducial identification		√*	√[6,27]
7	Touch fiducials with pointer	G	Skin/fiducial slide due to pointer pressure			√*[27]
		H	Position system and pointer tip definition	√[24,35]		
		I	Pointing	√*	√[47]	
8	Match images to patient	J	Matching algorithm	√*		
9	Point and reconstruct images with overlaid colored cross	K	2D image extraction	√*		
		L	Quantization, colored cross	√*		
		M	Interpretation	√*		
		N	Position system and tool tip definition	√[35]		
10	Surgery and brain movements	O	Discrepancy between anatomy and images		√*[48]	√*[45,48]

In the error magnitude columns, a star (*) indicates that the error value is based on our own experience and algorithm tests, while the numbers refer to the list of references.

covers the general steps necessary for ultrasound-based neuronavigation. In both sections, however, the cited error magnitudes are based on a combination of the available literature and our own experience during 7 years of ultrasound-based image-guidance in neurosurgery.

Error Sources Associated with Neuronavigation Based on Preoperative MRI

Preoperative imaging. Fiducials are glued to the skin of the patient (action item 1 in Table 1). The patient is then positioned in the MRI scanner on his/her back (action item 2). The normal procedure in our hospital is to stabilize the head with bitemporal padding and a strap across the forehead. The fiducials can easily slide several millimeters during the procedure and cause a significant error (error source A in Table 1). We normally place five fiducials on the patient, but we avoid the back part of the head/skull and exclude the padding and strap to minimize this error. A 3D MRI scan is performed (3), and a digital data set is acquired. Inhomogeneities of the magnetic field and nonlinear gradients cause geometric errors (error source B) between the true anatomy and the image information. We have no documentation for this error in our MRI system. However, Sumanaweera et al.[32] reported values in the order of 2 mm for the average difference between the true patient anatomy and the anatomy represented by MR images when no actions are taken to correct for MR field distortions. The selected slice thickness and distance between consecutive slices will also affect the accuracy.[33,34] The images are transferred to the navigation system and organized into a regular 3D volume (4). If the original images have a different pixel resolution and image distance than the specified voxel resolution of the regular 3D volume (which is normally not the case), this process will introduce a small quantization/interpolation error (C).

Patient registration. Next, the patient is placed on the operating table and the position reference frame is attached to the head frame (5). Brain shift due to gravity can occur (D), especially if the head orientation is different from that in the MRI scanner. This effect is often accounted for in functional stereotaxy. The skin and fiducials can also slide and deviate several millimeters from their original position in the MRI scanner due to gravity and/or manipulation during positioning of the head in the head frame (E). This effect is probably most pronounced for elderly people.

The next step in the procedure is to register the position of the fiducials in the 3D data set by a manual or automatic method (6). This process is subject to operator errors and possibly algorithm/quantization errors depending on the slice distance and zoom factor (magnification) of the images in which the operator is supposed to pinpoint the fiducials (F). A pointer is used to mark the fiducials, and hence register the patient relative to the preoperative image data (7). The fiducials/skin can again slide several millimeters[27] due to the applied pointer pressure (G), and the position system is subject to a certain error in the measurement and calculation of the pointer tip position (H).[24,35] The operator normally attempts to point at the center of the fiducial, but this procedure may also be subject to a pointing error (I), depending on the fiducial type being used.

A matching algorithm is then applied to find a best match, i.e., a transformation between the patient space and image space (8). Both direct and iterative minimization algorithms exist. For point (fiducial or anatomical)-based registration, the accuracy will depend on the chosen implementation and the number of points used (J).

In the error chain of Table 1, we consider point (fiducial)-based patient registration only, as this method is used in our clinic, and is also frequently used by others. Another common method is surface-based patient registration, in which a surface map of the head/face is created by sweeping the skin with a 3D spatial digitizer, or by imaging a projected light pattern with an array of video cameras. The surface map is then registered to, for example, the preoperative MRI or CT data by minimizing some form of cost function. Some studies have shown that, in neurosurgery, the errors for fiducial-based methods are smaller than the errors for surface-fitting and anatomical landmark-based methods.[6,27,30,31] However, for other surgical applications, such as ENT surgery, surface point registration techniques have proven reliable and robust, with reported errors as small as 1.5 mm.[36]

Preoperative planning. A pointer or other calibrated surgical instrument/tool is applied to the skin surface or within the brain to perform image-guided planning. The navigation system will reconstruct a 2D image from the 3D volume and draw a cross in the images at a location given by the tool (9). This process is subject to an interpolation error from 3D to 2D data (K), a quantization error in the positioning of the cross in the images (L), and an operator-dependent interpretation error when the surgeon is supposed to position the cross at a desired point in the image space (M). The tool tip is now supposed to be located exactly at the spot on the patient that is indicated by the crosshairs in the images. However, this will rarely happen in practice due to the error in measuring and estimating the tool tip position (N), as well as the contribution of the other error sources listed above.

Intraoperative guidance. The last action item on the list is the actual surgery in the brain (10). Most procedures will cause a certain amount of brain shift, and possibly a deformation of normal and pathologic structures. These changes may easily cause a discrepancy between the image space (3D MRI) and the patient space in the order of several millimeters or even centimeters (O).

Error Sources Associated with Neuronavigation Based on 3D Intraoperative Ultrasound

The following is a description of the general steps necessary when performing ultrasound-based neuronavigation, as outlined in Table 2. The action item and error source numbering is continued from Table 1.

The craniotomy is planned, and in some cases a separate minicraniotomy is made for the ultrasound probe. The skull is opened and the first 3D ultrasound scan is acquired for further planning. However, before 3D free-hand ultrasound imaging can begin, a probe calibration procedure must be performed to determine the position and orientation of the scan-plane relative to the sensor attached to the ultrasound probe (action item 11 in Table 2). Various algorithms exist for probe calibration (see, e.g., the work by Langø[37] or Prager et al.[38]). The possible error in this transformation (P) has been investigated by others[37–39] for various probe calibration methods, and will also be evaluated in this study. Prior to ultrasound imaging in the operating room, the ultrasound probe is covered with a thin sterile drape and the position sensor frame is attached to the probe housing (12). Proper design of the adapter glued to the probe housing and the sensor frame ensures a small or negligible repeatability error associated with this process, even through the sterile drape (Q).

A 3D ultrasound volume is then acquired using a position system to track the position and orientation of the probe (13). The probe is tilted ~90° in ~15 s to acquire ~200 images from the volume of interest in the brain. This process is subject to errors in tracking of the position sensor attached to the probe (R), errors in the synchroni-

Table 2. Error Chain Associated with Neuronavigation Based on Intraoperative Ultrasound

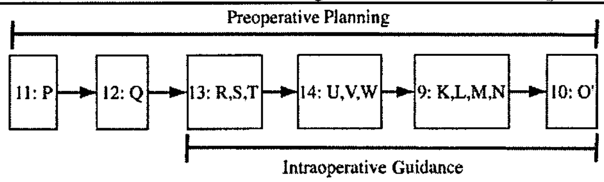

	Action items		Error sources	Error magnitude (mm) <1	1–2	>2
11	Probe calibration	P	Sensor to scan plane transformation		√[38,39]	√*[37–39]
12	Mount position sensor	Q	Sensor attachment repeatability	√*		
13	Acquire 3D ultrasound data	R	Position sensor tracking	√[35,49]		
		S	Synchronization between position data and images	√*		
		T	2D image position discretization	√*		
14	Load images and reconstruct volume: 3D scan conversion	U	Sound speed value		√*	
		V	Grid resolution/interpolation algorithms	√*		
		W	Finite thickness of ultrasound plane		√	
9	Point and reconstruct images with overlaid colored cross	K	2D image extraction	√*		
		L	Quantization, colored cross	√*		
		M	Interpretation	√*		
		N	Position system and tool tip definition	√*[35]		
10	Surgery and brain movements	O′	Brain shift (between repetitive 3D ultrasound acquisitions)	√*	(√)*	

In the error magnitude columns, a star (*) indicates that the error value is based on our own experience and algorithm tests, while the numbers refer to the list of references.

zation between the positioning data and the images (S), and uncertainty in the positioning of each 2D scan plane due to the finite time required for the acquisition of one image relative to the continuous probe movement during scanning (T).

The images with position tags are transferred to the navigation computer and reconstructed (scan-converted) into a regular 3D volume (14) with a certain grid resolution. This process is subject to geometric errors caused by the difference between the real speed of sound in the brain and that assumed in the algorithm (U), and by interpolation errors in the 3D scan conversion procedure, in combination with the selected 3D grid resolution (V). Furthermore, the ultrasound plane actually has a finite thickness, which implies an additional position uncertainty for the elements in the acquired image. The error may be associated with various stages in Table 2 (probe calibration, data acquisition, volume reconstruction). We have chosen to consider this error source as part of the 3D reconstruction error (W). The magnitude of this uncertainty varies with the probe type and the distance from the probe. The value listed in Table 2 is an estimated average over the depth range of interest in our experiment for the actual probe used.

Surgical planning can then start by moving the pointer over the skin surface. Again, the position of the pointer determines which images are displayed on the monitor and the position of the cross in the images (9). The error sources associated with this process are the same as for MRI-based navigation (K, L, M, and N).

An important advantage of ultrasound-guided navigation is the ability to do repetitive 3D imaging during surgery and thus work with a data set that has recently been updated according to possible changes in the brain anatomy. The error or discrepancy between the images and the anatomy during surgery (O′, 10) will therefore be small or negligible.

The use of ultrasound does not require any patient registration, because throughout the operation all ultrasound volumes are acquired in the same coordinate system as the one in which navigation is performed. Hence, error sources associated with patient registration are excluded from the ultrasound error chain.

It should be mentioned that, in our clinic, preoperative data (MRI, CT) is routinely used for planning and throughout the surgical procedure for overview purposes. These data must therefore be registered to physical space through a patient registration procedure, as described in the previous section. Hence, the error chains associated with placing the MRI or CT volumes and the ultrasound volumes in the patient will be independent. We apply ultrasound repeatedly during surgery to obtain updated and detailed images of the area of interest in the brain. Tumor resections are often performed using 3D ultrasound alone, with preoperative MRI/CT data being used only for planning purposes, for example, for the craniotomy.[40] An alternative registration approach is to match the MRI/CT data directly to the ultrasound data by volume-to-volume registration. This implies that the errors related to placing the MRI/CT volumes in the patient depend on the ultrasound error chain, in addition to the errors of the multimodal registration process. The latter option is not used in our clinic, and, to our knowledge, the procedure is still only used for research purposes elsewhere.

Scope of the Work

The overall clinical accuracy of a navigation system will be determined by the contribution from each of the individual error sources described in Tables 1 and 2. The net effect will not be the sum of all the error sources, but rather a stochastic contribution from all terms. In ultrasound-based navigation, error sources M and O′ (Table 2) are affected by the user, while the remaining sources are under the control of the system vendor. In MRI-based navigation, the user and procedure affect error sources A–G, M, and O (Table 1), while the remaining six error sources are under the control of the vendor (H–L and N).

The purpose of this study was to perform a 3D accuracy evaluation of an ultrasound-based navigation system in the laboratory setting to obtain an estimate of the potential overall clinical accuracy of ultrasound-based neuronavigation. Error sources P–W in Table 2 are included in this analysis, although Q and W cannot be quantified from our data.

MATERIALS AND METHODS

Navigation System

The SonoWand® system (MISON AS, Trondheim, Norway)[1] is a neuronavigation system that differs from conventional neuronavigation systems by being integrated with a built-in high-performance digital ultrasound scanner for updating the 3D map during surgery. The system comprises a computer for image processing and navigation and an optical 3D position tracker (camera system). The single-rack system is shown in Figure 1(a). A direct link between the ultrasound scanner and the navigation computer provides rapid transfer of 3D ultrasound data. The system can function as a conventional ultrasound scanner, as a conventional neuronavigation system based on MRI or CT images, or, more importantly, as a combined system in which full use is made of the features and advantages of preoperative MRI and intraoperative 3D ultrasound. The system thus enables the surgeon to navigate directly by means of intraoperative 3D ultrasound.

The navigation software can import MRI or CT data, perform patient registration using fiducials or anatomical landmarks, and display navigation images on the monitor in the same manner as conventional neuronavigation systems. In addition, the system measures the position of the ultrasound probe and tags images from the ultrasound scanner with positions from the optical tracker. The ultrasound probe with the attached position-sensor frame is shown in Figure 1(b). The position of the ultrasound image relative to the sensor frame is determined through a probe calibration procedure. A scan conversion algorithm is performed on the 3D ultrasound data to convert it into a regular volume that is handled by the navigation software in a similar fashion to the preoperative MRI and CT volumes. The system supports various navigation features and display options.

Wire Phantom

The ultrasound volumes studied in this article were acquired by scanning a precisely built wire phantom. A schematic drawing of the phantom is shown in Figure 2. The phantom is made of aluminum, and has four infrared-reflecting spheres mounted as references for the camera positioning system. Eighteen polyester wires of diameter 0.3 mm are mounted inside the phantom, with spring loadings to keep the wires straight. The wires are parallel to either the reference frame's X- or Y-axis. They form 27 wire crosses in a cubic pattern, with vertical separation of 0.5 mm between the wire center axes at each cross. All the wire crosses lie within a volume of dimensions $5 \times 5 \times 5$ cm.

The positions of all the wire crosses and the four reflecting spheres have been physically measured on a machining table, with an accuracy of 0.1 mm in all directions. These positions were then transformed into the reference coordinate system used by the position tracker. This is the coordinate system in which the ultrasound volumes are reconstructed.

Experimental Setup, Data Acquisition, and Volume Reconstruction

An overview of the data flow and the experimental setup is shown in Figure 3 (refer to this figure for the next three sections).

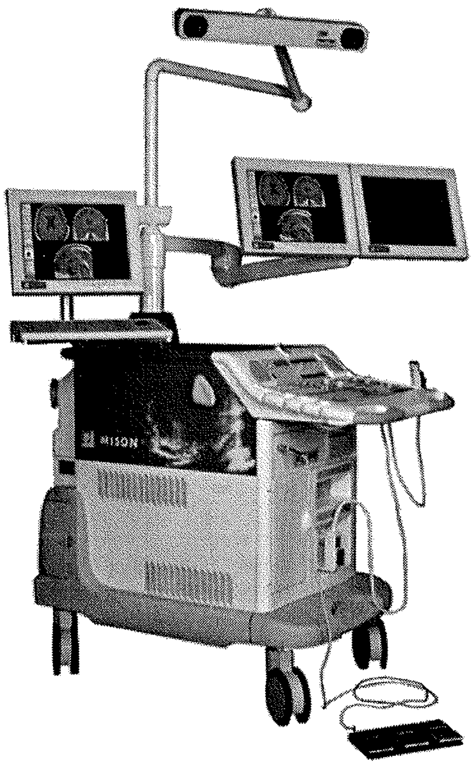

(a)

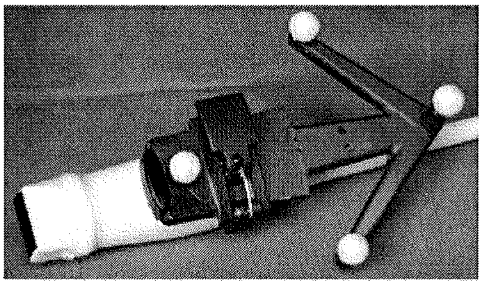

(b)

Fig. 1. (a) The single-rack ultrasound-based neuronavigation system (SonoWand®, MISON AS, Norway) with the position tracking system attached to an adjustable arm (Polaris®, Northern Digital, Canada). (b) Ultrasound probe (5 MHz FPA) with an attached position-sensor frame and reflecting spheres.

The wire phantom was immersed in water and scanned using a 5-MHz flat phased array ultrasound probe with an attached position sensor [Fig. 1(b)]. The probe was mounted in a rigid holder for practical reasons (overall stability; good repetition of scans; full coverage of all wire crosses in all scans), but the scanning was done by manually pulling or tilting the holder. As far as possible, the scanning motion was performed smoothly and at a constant speed, taking approximately 25 s to cover the total distance (~10 cm). The ultrasound images were acquired at a constant frame rate (six frames/s), typically yielding 150 images per scan. These images are thus somewhat irregularly spaced throughout the volume, but the typical distance between consecutive images is 0.6 mm for translation scans and from 0.03 mm near the probe to ~1.3 mm far from the probe for tilted scans. Scans were performed parallel to the phantom's *X*- and *Y*-axes and diagonally. Both translation scans and tilts were performed for each direction. A total of 180 scans were performed for the system evaluation (Table 3).

The highly accurate[35] optical 3D tracking system (Polaris®, Northern Digital Inc., Ontario, Canada) monitored the positions of the phantom and the probe from various distances and elevation angles above the horizontal. Figure 4 shows the experimental setup from above and from the side, while the specific numbers are given in Table 3. The five camera positions were chosen as: (1) the optimal distance (1.8 m) specified by the vendor, combined with an elevation angle (45°) that en-

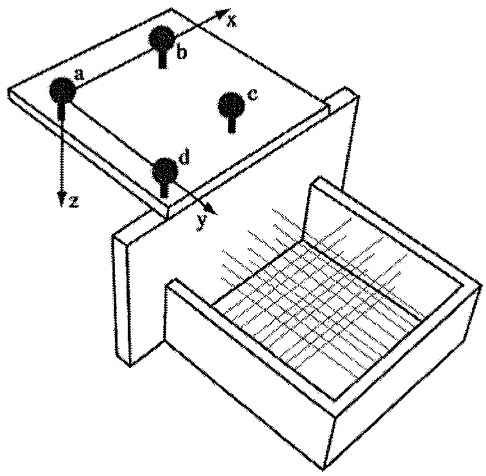

Fig. 2. The wire cross phantom. The four spheres (a–d) constitute the reference frame for the optical positioning system. The dimensions of the cube defined by the 27 wire crosses are 5 × 5 × 5 cm.

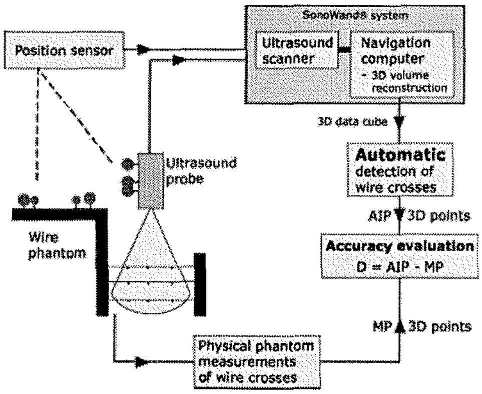

Fig. 3. Measurement setup and data flow. The position sensor tracks the wire phantom and the ultrasound probe during image acquisition. The automatic algorithm identifies the positions of the wire crosses (*AIP*) in the reconstructed volume. We compare *AIP* to the physically measured positions of the wire crosses (*MP*) to assess the accuracy of the whole 3D ultrasound-based navigation system.

sured good visibility of both the phantom's reference frame and the probe's tracking frame; and (2)–(5) reasonable variations in distance and elevation around position 1, based on vendor specifications and typical clinical use. The distances between the position cameras and the reference frame were measured to within ±10 cm accuracy, and the elevation to within ±2°. The phantom and probe were oriented such that all scans were made directly towards or away from the cameras.

High image quality is assured in the SonoWand system by using the raw digital data (not video-grabbing) from the built-in ultrasound scanner. Scanner settings such as frequency, depth, sector width, and frames per second were tuned to achieve a satisfactory view of the wires in the water bath on the scanner monitor. We scan-converted all volumes with voxels of 0.65 × 0.65 × 0.65 mm. This resulted in volumes having sizes from 6 to 24 megabytes, depending mainly on the acquisition time and scan distance. Sample ultrasound images from a reconstructed volume of a tilt scan are shown in Figure 5.

Important parameters in the reconstruction process are probe calibration to determine the position of the image relative to the position sensor attached to the probe; synchronization of position and image data; the speed of sound in water used in the scan conversion; and the desired output resolution measured in mm/voxel. We measured the temperature of the water bath containing the phantom to determine the sound speed, following the tabulated data of Duck[41] to set a proper value. Both the probe calibration method and the synchronization procedure used in the SonoWand system are proprietary to the vendor, and the details are unknown to us. Nevertheless, the effects of these parameters on the system accuracy can still be evaluated from our experiments (see the Discussion section).

Automatic Detection of Wire Crosses

The wire crosses were detected in the ultrasound volumes by an automatic procedure.[42] A small data cube was extracted around the expected position of each cross, accessible from the physical measurements. The cube was then correlated with a template cube of the same size, containing a model description of the wire cross. This model descrip-

Table 3. Overview of Camera Positions and Acquisition Conditions Used for the 180 Scanned Volumes

	Camera position	1	2	3	4	5
	Distance/Elevation	1.87 m/45.5°	1.48 m/44.7°	1.82 m/35.3°	1.79 m/61.9°	2.08 m/44.9°
Acquisition	Translation, +*X*	1, 2, 3	13, 14, 15	25, 26, 27	37, 38, 39	49, 50, 51
	Translation, −*X*	4, 5, 6	16, 17, 18	28, 29, 30	40, 41, 42	52, 53, 54
	Tilt, +*X*	7, 8, 9	19, 20, 21	31, 32, 33	43, 44, 45	55, 56, 57
	Tilt, −*X*	10, 11, 12	22, 23, 24	34, 35, 36	46, 47, 48	58, 59, 60
	Translation, +diag	61, 62, 63	73, 74, 75	85, 86, 87	97, 98, 99	109, 110, 111
	Translation, −diag	64, 65, 66	76, 77, 78	88, 89, 90	100, 101, 102	112, 113, 114
	Tilt, +diag	67, 68, 69	79, 80, 81	91, 92, 93	103, 104, 105	115, 116, 117
	Tilt, −diag	70, 71, 72	82, 83, 84	94, 95, 96	106, 107, 108	118, 119, 120
	Translation, +*Y*	121, 122, 123	133, 134, 135	145, 146, 147	157, 158, 159	169, 170, 171
	Translation, −*Y*	124, 125, 126	136, 137, 138	148, 149, 150	160, 161, 162	172, 173, 174
	Tilt, +*Y*	127, 128, 129	139, 140, 141	151, 152, 153	163, 164, 165	175, 176, 177
	Tilt, −*Y*	130, 131, 132	142, 143, 144	154, 155, 156	166, 167, 168	178, 179, 180

Three repeated scans were made for each camera position and acquisition method. The volumes were scanned during a 10-h session, and are numbered 1–180 in chronologic order.

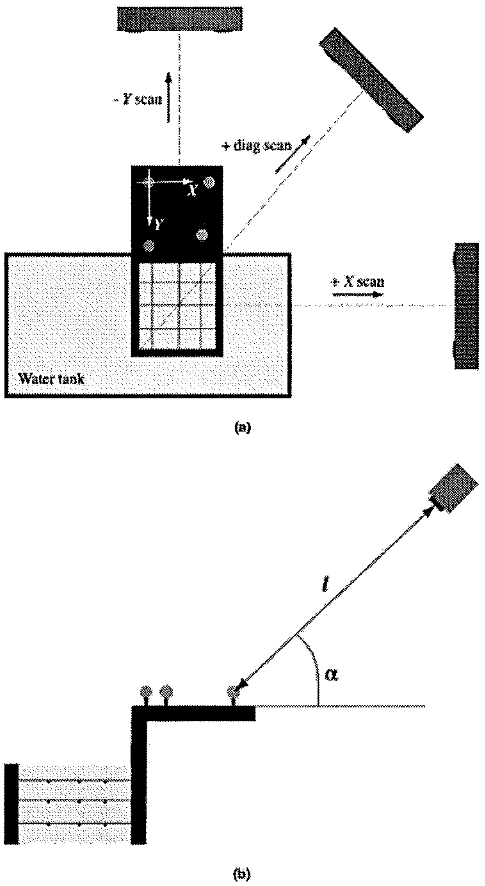

Fig. 4. Experimental setup during scanning of the phantom. (a) View from above. The figure indicates three different camera positions, i.e., for scans along the *X*- and *Y*-axes, and along the diagonal of the phantom. (b) View from the side. The elevation angle α from the horizontal plane and the distance l are given in Table 3.

tion is defined through a number of parameters, and we used the optimal parameter setting found earlier.[42] The location of the correlation maximum was used to find the actual position of the wire cross in the ultrasound volume.

Statistical Analysis

The physical position measurements of the wire crosses performed on the machining table were considered true values. The positions found from the 3D ultrasound scans were then compared to the true values through a statistical analysis. We denote the image points $AIP_{p,v}$ (*Automatic Image Points,* p = point 1 . . . 27, v = volume 1 . . . 180) and the true values MP_p (*Measured Points,* p = point 1 . . . 27). These points are all described in the same coordinate system, i.e., the reference system used by the position tracker.

Subtracting one data set from another we get 27 residual vectors in 3D space for each of the 180 volumes, i.e., a total of 4,860 3D error vectors:

$$D_{p,v} = \mathrm{AIP}_{p,v} - \mathrm{MP}_p \qquad (1)$$

The Euclidian lengths of these vectors are:

$$d_{p,v} = \|D_{p,v}\| = \sqrt{D_{p,v}(X)^2 + D_{p,v}(Y)^2 + D_{p,v}(Z)^2} \qquad (2)$$

From the error vectors, or any subset of the vectors, we may calculate the vector mean and standard deviation:

$$\bar{D} = \frac{1}{N_p \cdot N_v} \cdot \sum_p^{N_p} \sum_v^{N_v} D_{p,v} \qquad (3)$$

$$\sigma_D = \sqrt{\frac{1}{N_p \cdot N_v - 1} \sum_p^{N_p} \sum_v^{N_v} (D_{p,v} - \bar{D})^2} \qquad (4)$$

where N_p and N_v are the number of wire crosses and volumes in the data set, respectively. Similarly, we find the mean and standard deviation of the vector lengths as:

$$\bar{d} = \frac{1}{N_p \cdot N_v} \sum_p^{N_p} \sum_v^{N_v} d_{p,v} \qquad (5)$$

$$\sigma_d = \sqrt{\frac{1}{N_p \cdot N_v - 1} \sum_p^{N_p} \sum_v^{N_v} (d_{p,v} - \bar{d})^2} \qquad (6)$$

The end points of the vectors $D_{p,v}$ describe a cloud of points in three dimensions. If the cloud is not centered at the origin, there is a bias in the error estimate, given by $\bar{D}$. The measurements may be considered accurate if the bias $\bar{D}$ and the spread σ_D are both small. The parameter $\bar{d}$ is a single number describing the overall accuracy of the system, i.e., the value represents the mean distance between a point in physical space and the corresponding point in ultrasound image space. We also present d_β percentiles, where β% (β = 50 or 95) of all the observed values are below d_β.

To examine whether varying factors (e.g.,

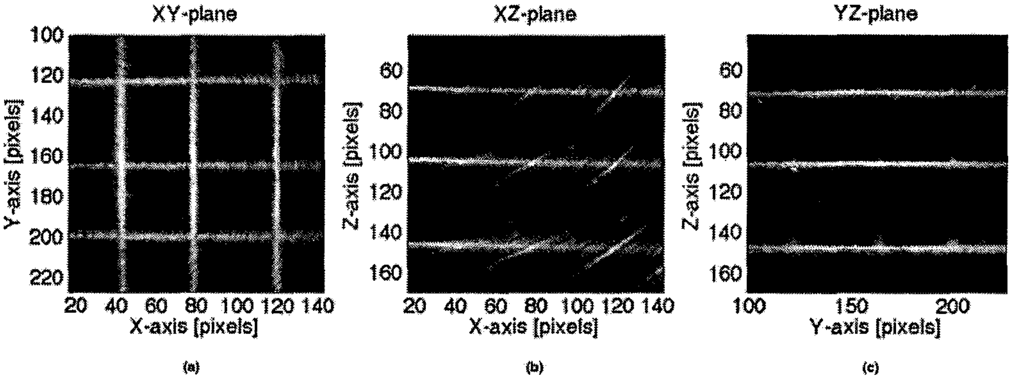

Fig. 5. Sample ultrasound images (three orthogonal views) from a tilted (+X direction) 3D scan of the phantom.

acquisition conditions like camera position) had significant influence upon the accuracy, we performed an analysis of variance (ANOVA) on the data. A thorough description of this technique can be found in statistical textbooks.[43] The basic principle is that the data material is grouped into several subsets, one for each level of the factor being considered. The variance between the groups is then compared to the variance within each group, according to well-defined algorithms. The comparison is quantified by one calculated parameter, the so-called p value, which will be discussed below.

In the present context, we shall restrict ourselves to only one response variable, namely accuracy in terms of $\bar{d}$. This response variable is modeled as a sum of contributions from the various data subsets, plus a residual error term. The application of the standard ANOVA technique assumes that the residual error obeys a normal distribution, and this assumption holds well for our data set, as can be seen from a histogram plot of $\bar{d}$. We shall apply a multiway ANOVA analysis, which allows us to identify interaction between several factors, in addition to the main effects of each single factor. The analysis will be applied throughout to balanced data sets and subsets, i.e., sets containing the same number of elements.

Our initial assumption (null hypothesis) is that the factors do not affect the accuracy. In other words, the between-groups variation should not differ from the within-groups variation. Whether this is so is determined by the p value, which can be interpreted as "the probability of obtaining the given data material provided that the null hypothesis is true." Thus, a p value close to zero indicates that we can conclude—at significance level p—that the null hypothesis was wrong and must be rejected, and that the investigated factor or interaction has significant influence on the accuracy.

RESULTS AND INTERPRETATION

Results for All 180 Volumes

The 4,860 individual error vectors $D_{\mathrm{p,v}}$ are plotted as projections onto the XY-, XZ-, and YZ-planes in Figure 6. This plot clearly shows the bias and spread of the data set. The bias $\bar{D}$ (3) (offset of center of gravity) is (−0.21 mm, 0.90 mm, 0.27 mm), while the standard deviation of each component is (0.88 mm, 0.50 mm, 0.43 mm).

The X, Y, and Z components, and the length d of the individual error vectors D are calculated and then averaged over each volume (27 individual vectors). The results are shown in Figure 7, where the volume numbers 1 through 180 follow the chronological order listed in Table 3. Rulers are included to show the acquisition conditions of each volume.

As an overall result, d averaged over all volumes yields $\bar{d}$ = 1.40 mm, with a standard deviation of σ_d = 0.45 mm. In both Figures 6 and 7, we notice biases and systematic variations that suggest that the error vectors are not purely stochastic according to a normal distribution. On the contrary, the figures indicate significant systematic errors that are strongly correlated to the acquisition conditions. An overall impression of the results can be gained from the following observations on Figure 7:

1. The results are fairly consistent within each group of three repeated volumes.
2. The results typically cluster into groups cor-

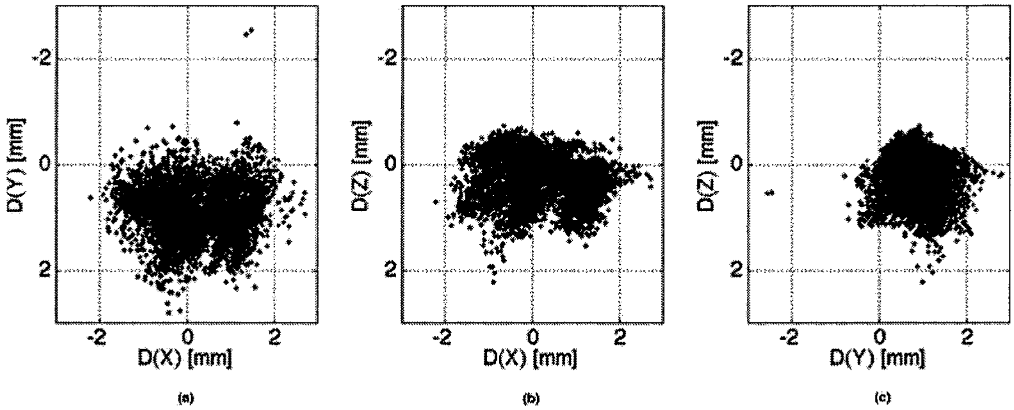

Fig. 6. Projections of individual error vectors D ($27 \times 180 = 4{,}860$ vectors) onto the XY-, XZ-, and YZ-planes.

responding to the series of translation or tilt scans.

3. Scan orientation (X/Diagonal/Y scans) and camera position show some correlation with the results; however, these trends are not unambiguous.
4. The $D(X)$ and $D(Y)$ components are quite irregular; some jumps and trends seem to correlate with the rulers, while other trends do not. The $D(Z)$ component is more clearly related to the translation/tilt ruler division. At the same time, an overall drift term seems to be superimposed on this component.
5. d varies in a rather complex manner with camera position and acquisition method, due to its dependence upon $D(X)$, $D(Y)$, and $D(Z)$.

Figure 8 shows the histogram of the 4,860 individual lengths, and the accumulated histogram. The 50 and 95% percentile values are 1.35 and 2.12 mm, respectively. The maximum d in the whole data set was 2.99 mm.

As a check of the system repeatability, we group all three volumes scanned at the same acquisition conditions. The average d for each volume is plotted in Figure 9. Within each group of three volumes, we use the $\max(d) - \min(d)$ difference as a measure of the repeatability. The average of this difference over all 60 groups is 0.10 mm. Being an order of magnitude smaller than the variation between the groups, this number indicates that the overall repeatability of the system is good.

Although the features observed in Figures 6 through 9 are, in general, correlated to the acquisition scheme, the relations cannot be determined directly from this overview. We shall therefore investigate the effects of single factors and their interactions on the accuracy by performing an ANOVA on the appropriate subsets (see next section). Furthermore, the extensive data set enables us to search for the underlying error sources that cause the systematic variations. This will be covered in the Discussion.

Results for Data Subsets

The extensive data set allows us to investigate how various camera positions and acquisition conditions affect the accuracy by analyzing appropriate subsets of the data (ANOVA). We first consider interaction results of the multiway ANOVA applied to the following factors: camera distance/camera elevation; scan orientation (X, diagonal, or Y scans); translation versus tilt scanning; and scanning towards versus away from the camera. As our experimental setup (Table 3) does not cover all possible combinations of camera distance and elevation, we analyze the effect of distance versus acquisition parameters (data set A; camera positions 1, 2, and 5) separately from the effect of elevation versus acquisition parameters (data set B; camera positions 1, 3, and 4). Each of these analyses thus involves 3/5 (2,916 points) of the total data set. We will classify the results against the 5% significance level (effect is significant when $p < 0.050$; not significant when $p > 0.050$).

The ANOVA results are listed in Table 4. The results for data sets A and B are fairly similar. In both cases, we find a significant three-factor interaction between camera distance (elevation), scan orientation, and translation/tilt. All two-factor com-

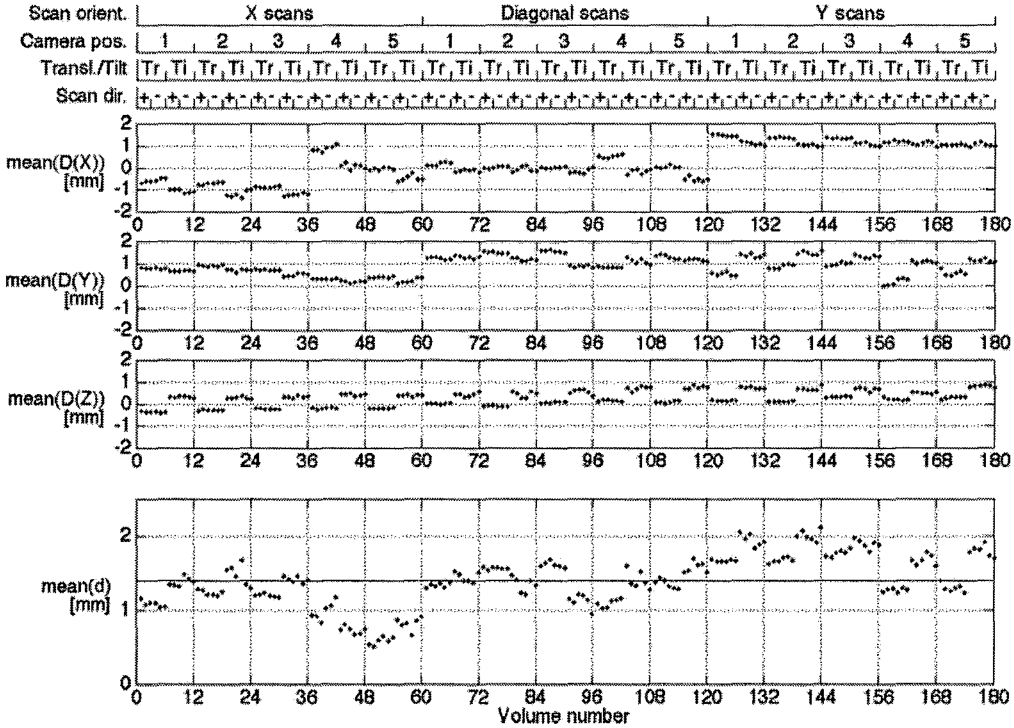

Fig. 7. *X*, *Y*, and *Z* components, and length *d*, of the average error vector $\bar{D}$ for each of the 180 volumes. The average *d* over all volumes ($\bar{d}$ = 1.40 mm) is shown by the horizontal line in the lowest plot. The volumes are numbered and presented in the order they were measured. The four rulers at the top indicate the acquisition conditions for each volume, in accordance with Table 3. The smallest interval (subdivision of the "Scan dir." ruler) represents the repetition of three volumes under identical scanning conditions.

binations of the same three factors, and the single factors themselves, also have significant effect on the accuracy. The fourth factor, scan direction, shows no effect in data set A, neither alone nor in combination with other factors. In data set B, however, scan direction gives a significant effect in combination with translation/tilt and in the four-factor interaction, but not otherwise. This may be

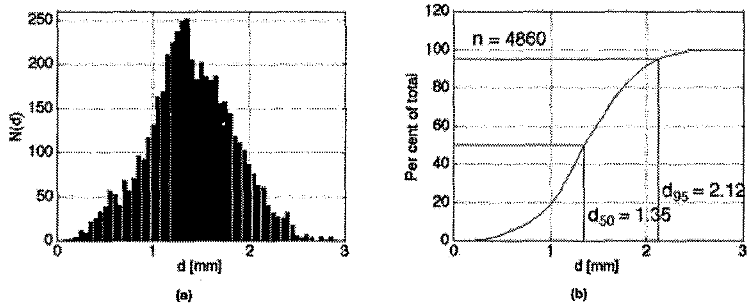

Fig. 8. (a) Histogram of all 27 × 180 = 4,860 error vector lengths *d*. (b) Cumulated histogram with the 50 and 95% percentiles indicated.

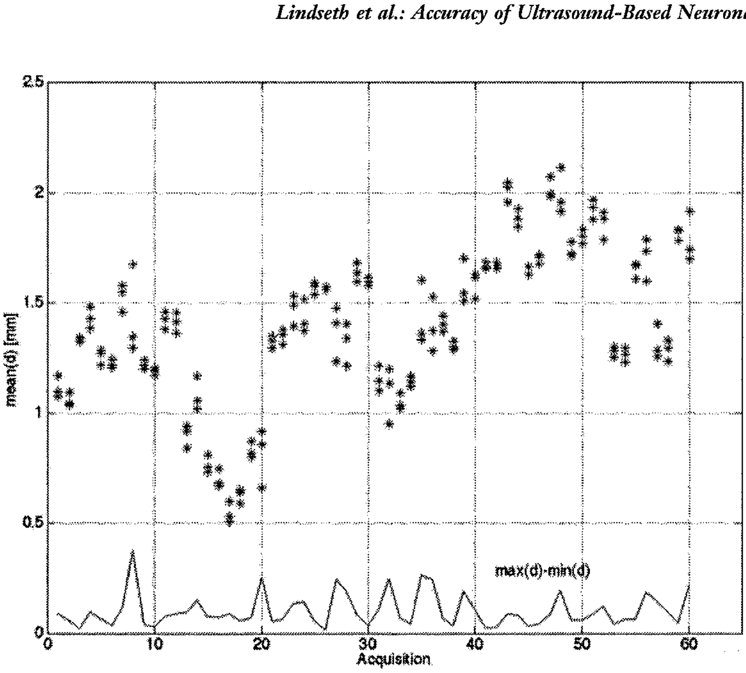

Fig. 9. System repeatability, characterized by the error vector lengths, for all 180 volumes. The three volumes taken under the same acquisition conditions are plotted at the same abscissa value (star symbol). From left to right, the volume groups are displayed in chronologic order, i.e., volumes 1–3, 4–6, 7–9, etc. (cf. Table 3). For each volume group, max(d) − min(d) was calculated, and this difference is shown by the solid line. The mean difference is 0.10 mm.

related to the way the volume is actually scanned during translation or tilt (see the comments on Table 7 for details), or possibly to the time-tagging effect (see Discussion section), but the latter will be shown to be rather small.

Because the accuracy results depend strongly upon the combination of camera distance/elevation, scan orientation, and translation/tilt, we present interaction plots in Tables 5 (data set A) and 6 (data set B). In both cases, the following trends seem to dominate (although exceptions do occur):

Table 4. Results of Multiway ANOVA for Data Set A (Variation of Camera Distance versus Acquisition Parameters) and Data Set B (Variation of Camera Elevation versus Acquisition Parameters)

Factor/interaction	A: Cam = Camera Distance	B: Cam = Camera Elevation
ScanOrient (scan orientation)	<.001	<.001
Cam	<.001	<.001
TraTi (translation/tilt)	<.001	<.001
ScanDir (scan direction)	.154	.885
ScanOrient*Cam	<.001	<.001
ScanOrient*TraTi	<.001	<.001
ScanOrient*ScanDir	.713	.426
Cam*TraTi	<.001	<.001
Cam*ScanDir	.941	.069
TraTi*ScanDir	.396	.021
ScanOrient*Cam*TraTi	<.001	<.001
ScanOrient*Cam*ScanDir	.247	.546
ScanOrient*TraTi*ScanDir	.528	.668
Cam*TraTi*ScanDir	.625	.247
ScanOrient*Cam*TraTi*ScanDir	.077	<.001

The table lists p-values for the single factors and interactions.

Table 5. The Significant (p < .050) Three-Factor Interactions for Data Set A: Camera Distance, Scan Orientation, and Translation/Tilt

a) Translation scans.

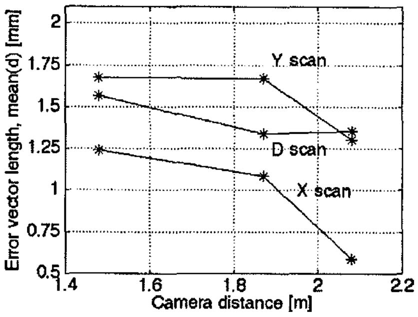

b) Tilt scans.

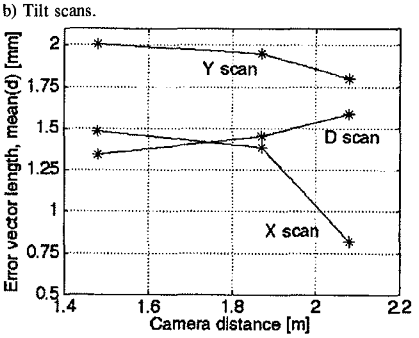

	Camera position (distance, m)		
Scan orientation	2 (1.48)	1 (1.87)	5 (2.08)
a) Translation scans.			
X	1.24	1.09	0.59
Diagonal	1.57	1.34	1.35
Y	1.68	1.67	1.30
b) Tilt scans.			
X	1.48	1.38	0.82
Diagonal	1.35	1.45	1.59
Y	2.01	1.95	1.80

The table lists $\bar{d}$ for each specific combination of the three factors.

1. X scans give better accuracy than Y scans, with diagonal scans somewhere between.
2. Increased camera distance or elevation improves the accuracy.
3. Translational scans give better accuracy than tilt scans.

To facilitate the comprehension of the main (single-factor) effects, Table 7 presents the effects of varying camera distance, camera elevation, scan orientation (X, diagonal, or Y), translation versus tilt scan, scan direction (towards or away from the camera), and the distance from the probe. Due to the balanced experiment design, $\bar{d}$values for selected factors in Table 7 can be found simply by averaging over the superfluous dimensions of Tables 5 and 6. The additional information presented in Table 7 is spread (σ_D) and range (d_{95}), as well as factors not included in Tables 5 and 6. The results confirm that all these factors except scanning direction have a significant effect on the accuracy, as seen from the low p values.

When comparing the camera positions, we assume approximate equality between the distances for positions 1, 3, and 4 (1.8 m), and between the elevations for positions 1, 2, and 5 (45°) (cf. Table 3). Of the five investigated camera positions, the combination of 1.8 m distance and 62° elevation gives the best accuracy (lowest $\bar{d}$). Tables 7a and b confirm the previous result that increased distance and increased elevation may improve the accuracy, within the limits of the position tracker. The effect of the camera position is discussed further in the section below entitled *Implications for Clinical Use of the System.*

As already revealed from Tables 5 and 6, the scan orientation has significant influence upon the accuracy, with X scans yielding the best results. This is confirmed by Table 7c.

Table 6. The Significant ($p < .050$) Three-Factor Interactions for Data Set B: Camera Elevation, Scan Orientation, and Translation/Tilt

a) Translation scans.

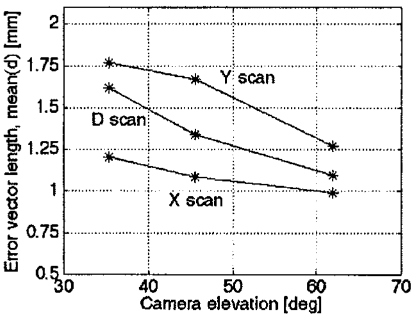

Scan orientation	Camera position (elevation, deg.) 3 (35.3)	1 (45.5)	4 (61.9)
X	1.20	1.09	0.99
Diagonal	1.62	1.34	1.10
Y	1.77	1.67	1.27

b) Tilt scans.

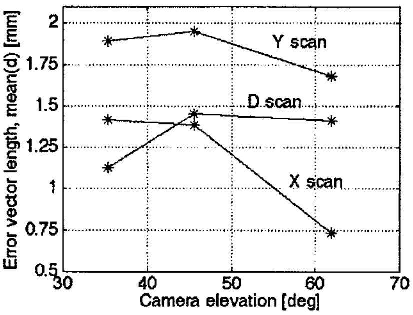

Scan orientation	Camera position (elevation, deg.) 3 (35.3)	1 (45.5)	4 (61.9)
X	1.42	1.38	0.73
Diagonal	1.13	1.45	1.41
Y	1.89	1.95	1.68

The table lists $\bar{d}$ for each specific combination of the three factors.

Tables 7d through f confirm that the accuracy is better for translation scans than for tilt scans. This is to be expected, because all wire crosses in our phantom are imaged rather close (<9 cm) to the probe in translation scans, thus reducing the effect of the lateral image resolution degrading with distance from the probe. The distance between the probe and the farthest wire crosses may have been in the order of 12 cm during tilt scans. In addition, the tilt movement implies low resolution (spatial sampling) normal to the image plane at large distances from the probe compared to the translation movement. These arguments are supported by Table 7g, which shows the actual degradation of accuracy with distance from the probe.

When comparing translation and tilt results, it should also be kept in mind that tilting is the dominating 3D acquisition method in the clinical situation.

The effect of scanning direction is exploited in Tables 7e and f. Here, the translation and tilt scans are separated because they differ with respect to the interpretation of "direction." During a translation scan, the probe and the ultrasound plane both move either towards or away from the cameras. However, the rotational movement during a tilt scan causes the ultrasound plane to approach the cameras when the probe moves away, and vice versa. The scan directions stated in Tables 7e and f refer to the motion of the probe. The results show that the scanning direction itself has negligible effect. See, however, the section of the Discussion entitled *Time tagging* for further details.

As already mentioned, Table 7g confirms that the accuracy degrades with distance from the probe, due to reduced resolution as a function of depth, particularly for the type of sector-scanning probe used here.

Table 7. Effect on Accuracy of Varying Acquisition Conditions (ANOVA Results for Single Factors)

Camera distance	n	$\bar{d}$	σ_d	d_{95}
1.5 m	972	1.55	0.37	2.21
1.8 m	972	1.48	0.39	2.11
2.1 m	972	1.24	0.52	2.07

a) Effect of varying camera distance. Camera elevation angle was constant at 45°

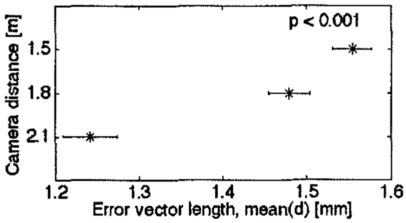

Camera elevation	n	$\bar{d}$	σ_d	d_{95}
35°	972	1.50	0.41	2.21
45°	972	1.48	0.39	2.11
62°	972	1.20	0.42	1.87

b) Effect of varying camera elevation. Camera distance was constant at 1.8 m

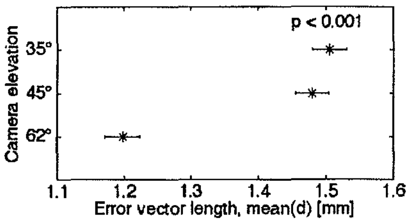

Orientation of scan	n	$\bar{d}$	σ_d	d_{95}
X	1620	1.10	0.40	1.74
Diagonally	1620	1.39	0.34	2.01
Y	1620	1.70	0.38	2.29

c) Effect of scan orientation.

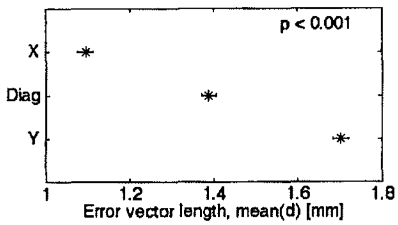

Acquisition type	n	$\bar{d}$	σ_d	d_{95}
Translation	2430	1.32	0.42	2.00
Tilt	2430	1.47	0.46	2.17

d) Effect of translation versus tilt scan.

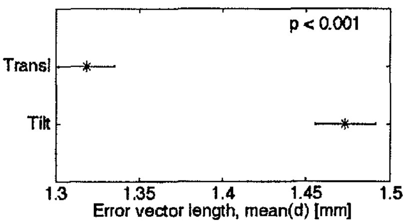

Table 7. Effect on Accuracy of Varying Acquisition Conditions (ANOVA Results for Single Factors) (cont'd.)

e) Effect of scanning towards versus away from the camera (translation scans).

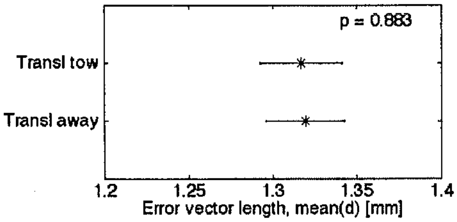

Scan direction	n	$\bar{D}$	$\bar{d}$	σ_d	d_{95}
Transl towards	1215	0.36, 0.88, 0.00	1.32	0.43	2.01
Transl. away	1215	0.42, 0.82, 0.01	1.32	0.42	1.99

f) Effect of scanning towards versus away from the camera (tilt scans).

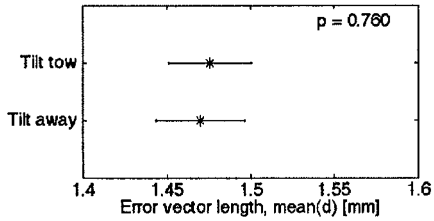

Scan direction	n	$\bar{D}$	$\bar{d}$	σ_d	d_{95}
Tilt towards	1215	0.01, 0.95, 0.53	1.48	0.44	2.13
Tilt away	1215	0.05, 0.96, 0.55	1.47	0.47	2.22

g) Effect of depth inside the phantom.

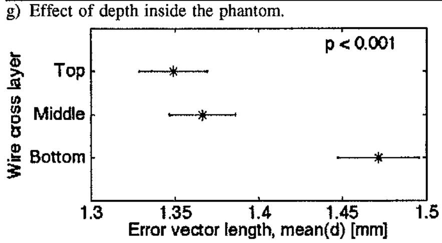

Wire layer (vertical distance from probe)	n	$\bar{d}$	σ_d	d_{95}
Top (4.0 cm)	1620	1.35	0.42	2.05
Middle (6.5 cm)	1620	1.37	0.41	1.99
Bottom (9.0 cm)	1620	1.47	0.50	2.28

The plots show $\bar{d}$ within each group, and the 95% confidence interval on $\bar{d}$, which is equal to $\pm 1.96 \cdot \sigma_d/\sqrt{n}$ for a normal distribution. n is the number of points in each group, and p is a measure of the effect of each factor (low p means significant effect). All D and d values are given in millimeters. All acquired data are used in Tables c through g, while data subsets A and B (each covering three out of five camera positions) are used in Tables a and b, respectively.

DISCUSSION

Error Sources

From the total of 4,860 points, we have obtained an overall laboratory accuracy of 1.40 mm. However, it is obvious that only a minor fraction of this number should be attributed to random noise. First, the correlation between accuracy and acquisition conditions is revealed graphically in Figures 6 and 7, and by the ANOVA analysis (Tables 4 through 7). Second, the repeatability test (Fig. 9) shows that the random contribution is typically one order of magnitude less than the overall variations.

We therefore assume that the results are greatly influenced by systematic error sources, and will investigate this in detail. We consider the potential error sources listed in Table 8 to be the most important in this context (cf. also Table 2). The table also shows how each error source would individually affect the results under varying acquisition conditions. Thus, we may identify the error

Table 8. Possible Error Sources and Their Expected Effect under Various Scan Configurations

Error source	Action: Rotate probe (and scan) 90° about probe's axis	Action: Scan in opposite direction
Bias in automatic method	No effect	No effect
Time tagging	Effect rotates 90°	Sign change
Sound speed	No effect on axial beam	No effect
Other geometric distortion (scan conversion effect)	Depends on distortion type	No effect
Probe calibration	Effect rotates 90°	No effect

sources of greatest influence by investigating appropriate data subsets for these effects.

Bias in Automatic Method

The automatic method for locating the wire crosses in the images has been thoroughly tested, and was found to be as accurate as any human operator.[42] In the present study, the resolution of the reconstructed volume is the same (0.65 mm/voxel), and we apply the "optimal" algorithm parameters from the previous work. The automatic method is therefore expected to be unbiased, and to have an accuracy of 0.25 voxels (=0.16 mm).[42]

However, because we now have an entirely new data set, acquired by a different ultrasound scanner, we confirm the applicability of the automatic method and its parameter settings by running the following test. A total of 12 reconstructed volumes were selected, one for each acquisition condition (randomized over repetition number and camera position—see Table 3). We then designed a computer program that looped through each volume and presented each of the 27 wire crosses on the screen in three orthogonal projections, together with the automatic method's results as shown by the hair crosses. Three skilled operators judged these images independently, classifying each wire cross according to whether he/she agreed or disagreed with the automatic results. The criterion for agreement was that the hair cross should be within one voxel of what the operator considered to be the "correct" wire cross location.

The combined results of the three independent operators (total of $12 \times 27 \times 3 = 972$ cases) indicated that 97.8% of crosses (951 cases) were in agreement with the operator's opinion, whereas 2.2% (21 cases) were not. These findings confirm our statement that the automatic method is as precise as any human operator, and hence has no significant bias.

Time Tagging

By time tagging, we mean synchronization of the position data and the image before reconstructing the volume. Position data and ultrasound data will not be recorded exactly simultaneously, so a time lag (positive or negative) will occur between these data sets. The time lag is constant for a particular scanning setup. In a dynamic scanning session, the time lag converts into a spatial offset between the "true" image position and the position recorded by the position sensor. The offset is ideally proportional to probe velocity. Hence, reversing the scanning direction should give a sign change in the offset component along the scanning direction. We will therefore investigate our data for such direction-dependent errors.

We compare only translation scans along the X- or Y-axis, because, for these cases, time-tagging errors give offsets in only one component. Table 9 summarizes the results. As expected for the scans in the X direction, only the X component of D is affected by the change of direction. $D(X)$ is directed away from the camera, and has the largest magnitude when scanning towards the camera. The same effect—measured relative to the camera position—is seen for the scans in the Y direction. This indicates that incorrect time tagging may account for an offset of half the difference, i.e., approximately 0.06 mm at the specified scanning speed.

The results thus indicate that time-tagging errors may have contributed to the overall accuracy, but only as a minute error source. The contribution itself is small and relatively insignificant compared to the standard deviations listed in Table 9. Furthermore, the effect is not seen as a sign change around zero, but merely as a fluctuation around a considerable offset value, which must then be attributed to other error sources.

Speed of Sound

Using the correct sound speed is crucial for obtaining the correct geometry of the reconstructed volume. The water tank used in the study was filled more than 3 days before the measurements were performed; hence, the water could be assumed to be degassed. During the data acquisition (10 h), we monitored the air temperature close to the tank using a standard thermometer with resolution of 0.5°C. The temperature was kept in the range 25.5–27.0°C throughout, corresponding to theoretical values for the sound speed in water of 1,498.0–1,501.9 m/s.[41] Note that this variation in sound

Table 9. Effect on Accuracy of Reversing the Scan Direction

Acquisition	n	$\bar{D}(X)$, $\bar{D}(Y)$, $\bar{D}(Z)$	$\sigma_D(X)$, $\sigma_D(Y)$, $\sigma_D(Z)$
$+X$ scan (camera at $+X$)	405	−0.32, 0.63, −0.24	0.65, 0.33, 0.18
$-X$ scan (camera at $+X$)	405	−0.21, 0.64, −0.25	0.75, 0.33, 0.19
$+Y$ scan (camera at $-Y$)	405	1.29, 0.57, 0.22	0.43, 0.45, 0.15
$-Y$ scan (camera at $-Y$)	405	1.28, 0.69, 0.22	0.46, 0.40, 0.16

Only translation scans parallel to the wires (X and Y directions) are considered. n is the number of points included in the analysis. All D values are given in millimeters.

speed is much smaller than the variations one may expect in a clinical situation due to variation in tissue types (see below).

For volume reconstruction, we used a constant sound speed of 1,499.3 m/s. The maximum deviation from this value was thus 1.6 m/s, giving a percentage uncertainty of maximum 0.11% (1.6/1,499.3). This implies a stretching or compression of the volume in the beam direction by 0.16 mm at a distance of 15 cm (maximum sector depth). However, these numbers are extreme values. Considering typical temperature fluctuations and averaging over the whole imaged volume, we expect the sound speed variation to account for far less than 0.1 mm.

We also note that an incorrect value for the sound speed should mainly affect the Z component of the error vector D, for the given probe orientation and acquisition protocol. However, Figures 6 and 7 show that the largest discrepancy typically occurred in the Y component. This confirms that variation in the sound speed was not a significant source of error in our experiment.

It is appropriate here to comment on the drift term observed on the $D(Z)$ component in Figure 7. Considering translation and tilt scans separately, the increase in $D(Z)$ over 10 h is approximately 0.6 mm. We are unable to give a satisfactory explanation for the drift. From the above discussion, it is unlikely that this is a sound speed effect caused by temperature variation, because such a variation would only account for errors in the order of 0.1 mm. We have also considered the effect of microbubbles in the water, assuming that the water was not completely degassed at start of the measurement session. Due to repeated exposure to the ultrasound, such bubbles might be gradually removed from the water, thus altering the bulk sound speed. However, our analysis shows that decreasing the amount of free gas would cause $D(Z)$ to decrease with time, i.e., the opposite of the observed effect.

Other Geometric Distortion Effects

By visual inspection, we observe no obvious geometric distortions in the reconstructed volumes. Unfortunately, we do not have access to the details of the 3D scan conversion algorithms. However, a simple test for geometric consistency is to check the dimensions of the reconstructed volume against the true dimensions of the phantom.

The imaged phantom contains 27 wire crosses in a $3 \times 3 \times 3$ cubic pattern, where the distances between the wires are known to an accuracy of ~0.1 mm.[42] For the two outer layers of crosses, the nominal distance is found by averaging over the nine coordinate differences. We calculate the same distance for each processed volume (27 automatically located wire cross positions), and further average the results over all 180 volumes. The differences between these distances are thus a measure of the stretching/compression of the reconstructed volume. The results are listed in Table 10. Compared to the nominal dimensions, the reconstructed volumes are, on an average, expanded along the X- and Z-axes and compressed along the Y-axis, the X discrepancy being the largest. Considering each distance as the difference between two stochastically independent numbers, it is appropriate to divide by $\sqrt{2}$ to find the bias of a single layer (single point). This gives an average bias of $|\Delta X| = 0.21$ mm, $|\Delta Y| = 0.05$ mm, and $|\Delta Z| = 0.05$ mm for the reconstructed volume compared to the phantom's physical dimensions. The average bias vector has a length of 0.22 mm. Considering only the mean value, we know from the discussion above that the variation in sound speed does not account for a discrepancy of this magnitude. In any case, the sound speed would primarily affect the Z dimension of the volume, while the observed effect is largest in the horizontal plane. The spread around the mean values are also relatively high (note also that the manufacturing uncertainty in wire cross locations is excluded). An extensive study would thus be needed to determine whether the observed discrepancy is significant and, if so, whether it might be due to (for example) the 3D scan conversion algorithm. We have not pursued this topic further, because, after all, the observed discrepancy in geometric dimensions may only account for a minor fraction of the total error of 1.4 mm.

Table 10. Comparison of Nominal Distances between Wire Cross Planes, and Distances Found in Reconstructed Ultrasound Volumes

Wire cross planes	Nominal distance (mm) in phantom (n = 9)	Distance (mm) in ultrasound volumes (n = 1620)
Xfront–Xback	50.04 ± 0.10	50.34 ± 0.51
Yfront–Yback	50.05 ± 0.08	49.98 ± 0.39
Ztop–Zbottom	50.03 ± 0.08	50.10 ± 0.25

Means and standard deviations are based on the n coordinate differences included in each analysis; the manufacturing uncertainty in physical wire locations is not included.

Probe Calibration

Incorrect probe calibration implies that an image point will be displaced from its "true" position. This displacement is constant in the ultrasound plane's coordinate system. Thus, if the probe is shifted/rotated, the same shift/rotation occurs to the displacement.

We exploit this feature by comparing results obtained from all translation scans, sorted according to scanning direction (X, Y, or diagonally). We need to compare the error vectors D in the ultrasound plane's coordinate system, which is X_{us} (normal to image), Y_{us} (lateral image coordinate), Z_{us} (radial or depth image coordinate), as shown in Figure 10. The error vectors must therefore be transformed from the phantom's coordinate system X, Y, Z. One step in this transform involves the transform between the probe system X_{pr}, Y_{pr}, Z_{pr} and the ultrasound system X_{us}, Y_{us}, Z_{us}. This is, by definition, the unknown probe calibration. However, for the present purpose, a sufficient approximation is to assume no rotation between these systems, such that $X_{us} = X_{pr}$, $Y_{us} = Y_{pr}$, $Z_{us} = Z_{pr}$. With this approximation, the relations between the phantom's system and the ultrasound plane's system are:

(1) Scans in the X direction [Fig. 10(a)]

$$X_{us} = -X \quad Y_{us} = -Y \quad Z_{us} = Z \tag{7}$$

(2) Scans in the diagonal direction [Fig. 10(b)]

$$X_{us} = (-X + Y)/\sqrt{2} \quad Y_{us} = (-X - Y)/\sqrt{2} \quad Z_{us} = Z \tag{8}$$

(3) Scans in the Y direction [Fig. 10(c)]

$$X_{us} = Y \quad Y_{us} = -X \quad Z_{us} = Z \tag{9}$$

The results of these transformations are listed in Table 11. In the ultrasound plane's coordinate system, the average D vectors become (0.27, −0.63, −0.24) for the X scans, (0.80, −1.01, 0.05) for the diagonal scans, and (0.63, −1.29, 0.22) for the Y scans. Despite some discrepancies (note also the relatively large standard deviations in Table 11), we observe a certain consistency between these offset vectors. The mean of the vectors in the (X_{us}, Y_{us}, Z_{us}) system is (0.57, −0.98, 0.01), which has a length of 1.13 mm.

This analysis indicates that erroneous probe calibration is a major contributor to the system error in the present study. To confirm this further, we used the mean (X_{us}, Y_{us}, Z_{us}) vector as compensation to the original data set by converting it back

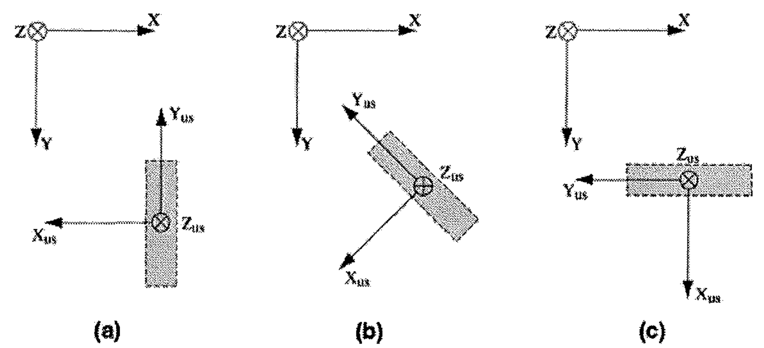

Fig. 10. Coordinate systems for the phantom (X, Y, Z) and ultrasound plane (X_{us}, Y_{us}, Z_{us}) viewed from above. The dashed rectangle indicates the probe orientation during the scan. (a) Scans in the X direction; (b) scans in the diagonal direction; (c) scans in the Y direction.

Table 11. Effect on Accuracy of Rotating the Probe and Scan Direction

Acquisition	n	$\bar{D}(X)$, $\bar{D}(Y)$, $\bar{D}(Z)$	$\sigma_D(X)$, $\sigma_D(Y)$, $\sigma_D(Z)$	Transform from X, Y, Z to X_{us}, Y_{us}, Z_{us}	$\bar{D}(X_{us})$, $\bar{D}(Y_{us})$, $\bar{D}(Z_{us})$
All X scans	810	−0.27, 0.63, −0.24	0.70, 0.33, 0.18	Equation 7	0.27, −0.63, −0.24
All diagonal scans	810	0.15, 1.28, 0.05	0.43, 0.43, 0.19	Equation 8	0.80, −1.01, 0.05
All Y scans	810	1.29, 0.63, 0.22	0.45, 0.43, 0.16	Equation 9	0.63, −1.29, 0.22

Only translation scans are considered. (X, Y, Z) is the reference frame's (phantom's) coordinate system, while (X_{us}, Y_{us}, Z_{us}) is the coordinate system of the ultrasound image plane. n is the number of points included in the analysis. All D values are given in millimeters.

into the reference system (X, Y, Z) (using separate conversion for the X, Y, and diagonal scanning directions, by inversion of the above relations), and subtracting it from the respective data subsets. Although the compensation vector was derived from only the translation scans, and thus is not, strictly speaking, valid for the tilt scans, we applied the compensation to the whole data set. The average error vector length $\bar{d}$ was 0.84 mm after compensation, compared to 1.40 mm before compensation.

For certain probe calibration procedures, the finite width of the ultrasound plane [classified as reconstruction error (W) in Table 2] may influence the calibration accuracy. However, we cannot say whether this is so in the present case, because the details of the procedure used in the neuronavigation system studied here are unavailable to us. This also implies that we are unable to suggest improvements to the procedure.

Accuracy When Compensating for Systematic Error Sources

The systematic error effects discussed above imply that the reconstructed volume is positioned with an offset relative to the physical volume. This offset may be compensated for by moving the reconstructed volume until the residual $\bar{d}$ attains a minimum value. We have done this for each of the 180 volumes, using standard point set registration algorithms (translational and rotational motion). After this compensation, the $\bar{d}$ over all volumes becomes 0.37 mm. Additional uniform scaling of the translated and rotated volumes gives negligible improvement, while nonuniform scaling brings $\bar{d}$ down to 0.26 mm.

These numbers result from individual offset compensation and therefore cannot be achieved by a common correction to all reconstructed volumes. However, they confirm that the volume is fairly accurately reconstructed with respect to geometric proportions. In addition, they give an indication of the overall (random) noise level in our experimental design.

Implications for Clinical Use of the System

Differences in Acquisition Conditions between Laboratory and Clinic

In this work, we have evaluated the neuronavigation system in a controlled laboratory setting. It is, however, important to understand how this setting differs from the clinical situation to assess the overall clinical accuracy of the system.

In the clinical situation, 3D volumes are typically acquired by tilted scans. We also made linear translation scans, because such volumes allow for easier analysis of various effects. It should be noted that tilted scans give slightly poorer accuracy than translation scans (Table 7d).

The camera position relative to the reference and probe frames is also important. According to the manufacturer of the positioning system, the best performance is obtained when the frames face the cameras directly. This was impossible in our laboratory setting, because the reference frame affixed to the wire phantom is horizontal. This probably accounts for the improvement in accuracy as the cameras are raised higher (Table 7b), although the probe frame visibility is simultaneously degraded. Our evaluation includes five different camera positions to cover the situation where the cameras may be moved during an operation. However, it can be expected that the accuracy will improve if the frames and cameras are optimally positioned in the clinical situation. We get an indication of this by considering only the tilted scans for the "best" camera position, which gives an average error vector length $\bar{d}$ = 1.28 mm; σ_d = 0.45 mm (camera position 4; distance 1.8 m and 62° elevation).

Sensor Frame Attachment/Probe Calibration

Ideally, one unique position sensor should be permanently attached to one unique ultrasound probe before calibration in the factory. However, this option represents practical difficulties in that most ultrasound probes cannot be sterilized, while the position-sensor frame can. Alternatively, both devices can be covered by sterile drapes, but this may interfere with the view of the cameras.

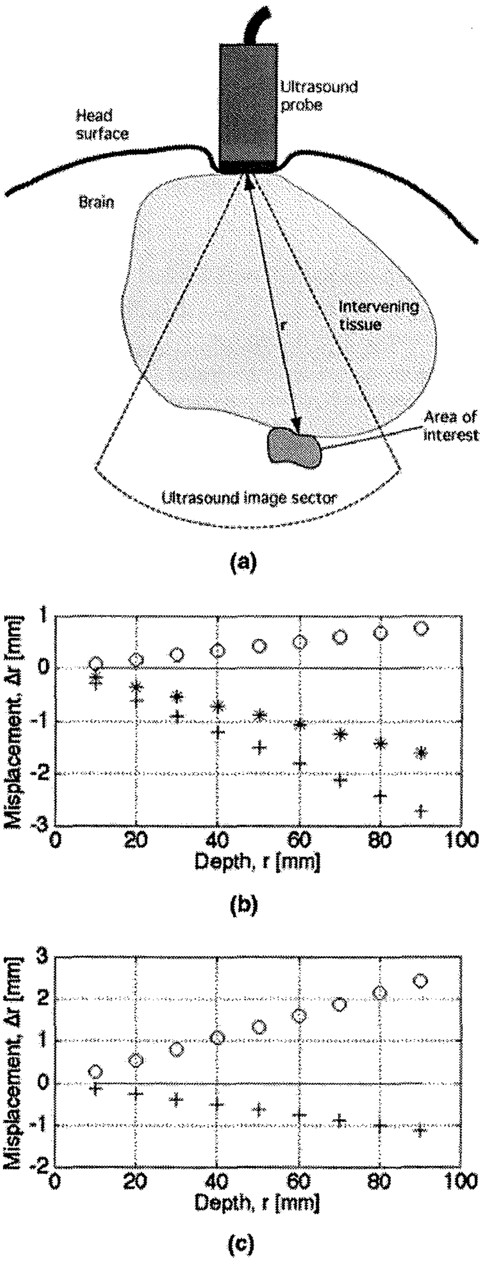

Fig. 11. Idealized model to illustrate the effect of using erroneous sound speed in volume reconstruction. (a) Ultrasound imaging of the area of interest in the brain at a distance r from the probe. (b) The error in radial distance due to volume reconstruction with a sound speed of 1,540 m/s (average value for soft tissue), when the true sound speed in intervening tissue is 1,527 m/s (cyst, circle symbols), 1,568 m/s (average in normal brain, star symbols), or 1,588 m/s (meningioma, plus symbols). (c) Similar to (b), but with 1,568 m/s (average in normal brain) used for volume reconstruction. The true sound speed in the intervening tissue is 1,527 m/s (cyst, circle symbols) or 1,588 m/s (meningioma, plus symbols).

To our knowledge, there is still no good solution to this problem for optical tracking systems, but current strategies include two methods: (a) calibration of any probe to any position sensor inside the operating room using a special ultrasound calibration phantom and algorithm; or (b) calibration of one particular probe to one particular position sensor in the laboratory or factory, using a special adapter that ensures repetitive and precise attachment between the two, even through a sterile probe drape. The latter option allows neither the probe nor the position-sensor adapter to be replaced without returning both to the factory for new calibration. The neuronavigation system investigated here is based on the latter solution to give the vendor better control over the accuracy.

Sound Speed Variation in the Brain

For the human brain, the average value for the sound speed at 37°C and 5 MHz is 1,568 m/s.[44] The average value for soft human tissue is 1,540 m/s.[41] Some variation exists between different tissue types; it can be as low as 1,504 m/s for tumor cysts at 22°C, and as high as 1,569 m/s for a certain type of meningioma at 20°C.[41] Temperature coefficients for acoustic velocity are sparse, but for human fetal brain the coefficient has been estimated to be 1.5 m/(s · °C) for the temperature range 24–37°C.[41] Assuming this coefficient for cysts and meningiomas, the sound speed at 37°C becomes approximately 1,527 m/s and 1,588 m/s, respectively.

We illustrate how the sound speed may affect the accuracy in a practical situation with the idealized example shown in Figure 11(a). The area of interest is located a constant distance r from the probe at the surface of the brain. We consider three types of intervening tissue: cyst with sound speed 1,527 m/s; meningioma with sound speed 1,588 m/s; or normal brain tissue with sound speed 1,568 m/s. A displacement error occurs if the image is reconstructed with a sound speed differing from the true value. This error, at depth r, is given by

$$\Delta r = \left\{ \frac{v_{sc}}{v} - 1 \right\} r \qquad (10)$$

where v is the true sound speed, and v_{sc} is the sound speed used for reconstruction (scan conversion). We have calculated Equation (10) as a function of distance r for two cases of scan-conversion sound speed: using the average sound speed of soft human tissue (1,540 m/s), or using the average sound speed of brain tissue (1,568 m/s). The results are shown in Figure 11(b) and (c), respectively.

It should be mentioned that these examples represent extreme cases, because the intervening tissue during imaging is seldom only cystic or a meningioma. Nevertheless, for the smaller values of r, the plot may have practical implications.

Table 12. Overall Clinical Accuracy of an Ultrasound-Based Neuronavigation System

Laboratory accuracy (tilt scans, one camera position)	1.3 mm
+ Calibration and position tracking of rigid surgical tool	0.6 mm
+ Interpolation 2D slice from 3D/tool cross indication	0.1 mm
= Overall laboratory accuracy	1.4 mm
+ Sound speed uncertainty	0.5–3 mm
+ Brain shift	1–10 mm
+ Interpretation of images on monitor	0.5 mm
= Overall clinical accuracy	1.9–10.6 mm

The magnitude of the error numbers is discussed in the text. The numbers are summed as stochastically independent contributions ($\sqrt{\Sigma(\ldots)^2}$).

Overall Clinical Accuracy

As stated previously, the most important parameter for the surgeon is the overall clinical accuracy. Although this parameter is difficult to assess, we believe that an estimate can be made, based on our laboratory evaluation and a thorough understanding of the significant additional error sources that occur in the clinical setting. In neuronavigation based on preoperative MRI, the laboratory accuracy may be well controlled, with the clinical accuracy being considerably worse due to error sources like patient registration and brain shift during surgery. For neuronavigation based on intraoperative ultrasound, however, data registration is superfluous, and the brain shift can be kept small by repeated image acquisition. Hence, the overall clinical accuracy is likely to be closer to the overall laboratory accuracy. This is further supported by the ultrasound modality being less susceptible to user- and procedure-dependent error sources than MRI. We will therefore estimate the overall clinical accuracy of the neuronavigation system used in this study based on our laboratory results. This calculation is summarized in Table 12.

Our starting point is the laboratory accuracy for all tilt scans at the best camera setting, because this configuration is considered to be most relevant in the clinical situation (see the earlier section entitled *Differences in acquisition conditions between laboratory and clinic*). Our study does not include calibration and tracking errors for a rigid pointer or surgical tool, which are in the order of 0.6 mm.[35] Furthermore, we have not considered errors associated with the extraction and presentation of a 2D image from the 3D volume. However, such errors should be rather small for a system using good interpolation routines and a high-resolution monitor.

By adding these error numbers, we obtain an estimate of the overall laboratory accuracy. The error sources are assumed to be stochastically independent. Hence, their contributions are added on a sum-of-squares basis.

For a rigid phantom, the overall laboratory accuracy may be better for an MRI system than for the ultrasound-based system, mainly due to the probe calibration needed for ultrasound-based navigation. However, in the clinical setting, the MRI option will require a registration based on invasive skull fiducials to be comparable to the laboratory (phantom) accuracy. The registration process is unnecessary when using ultrasound.

The main error sources for the ultrasound system in the clinical situation—sound speed variation and brain shift—have already been discussed in detail. The sound speed range indicated in Table 12 is based on Figure 11. The brain-shift error may be negligible if the 3D maps are frequently updated (zero when using real-time 3D ultrasound), whereas the error increases when the update is done at longer intervals. The extreme situation would be where the surgery is based on a single ultrasound volume acquired before the operation starts. However, even in this case, the situation is favorable compared to preoperative MRI. For example, when performing a craniotomy, the brain shift may be as large as 1 cm,[45,46] and this kind of error will be eliminated by using ultrasound. The problem of brain shift during the operation can also be reduced by using intraoperative MRI.

The surgeon's interpretation of the images will be individual and subjective, and the accuracy will depend on the monitor's size and resolution, in addition to the image resolution and contrast. Hence, no exact number can be given for this error. However, we estimate that an accuracy in the order of 0.5 mm should be attainable.

When summing these contributions, again as stochastically independent sources, we obtain an estimated overall clinical accuracy for the ultrasound system of ~2 mm under favorable conditions, i.e., when the sound speed used in the scanner is close to the average sound speed in the imaged tissue and the ultrasound volumes are frequently updated. The need for updating can be determined by real-time 2D imaging. If these conditions are not met, the accuracy becomes poorer.

CONCLUSION

We have evaluated the 3D navigation accuracy of an ultrasound-based neuronavigation system, using a wire phantom in a laboratory setup. A total of 180 scans of the phantom were performed under various acquisition conditions. The laboratory accuracy was found to be 1.40 ± 0.45 mm. Detailed analysis of the data indicates that inappropriate probe calibration is the main error source in this study.

The differences between our setup and the clinical situation have been discussed. The overall clinical accuracy for ultrasound-based neuronavigation is expected to be close to the overall laboratory accuracy. This is partly due to the fact that patient registration is unnecessary. In addition, intraoperative ultrasound imaging may eliminate the brain-shift problem, which is the potentially largest source of error.

ACKNOWLEDGMENT

This work was supported by grants from the Research Council of Norway through the Strategic University Program in Medical Technology at the Norwegian University of Science and Technology (NTNU), the Strategic Institute Program at SINTEF Unimed, and the Norwegian Ministry of Health and Social Affairs. We wish to thank the Laboratory for Fine Mechanics at SINTEF Unimed in Trondheim, Norway, for making the equipment necessary for this study, especially the main phantom, and also for providing indispensable measurements. We also thank Geir Arne Tangen, M.Sc. (SINTEF Unimed) for valuable contributions to the laboratory set-up, and John S. Tyssedal (Associate Professor, Department of Mathematical Sciences, NTNU, Trondheim, Norway) for helpful suggestions on the ANOVA analysis. We wish to thank MISON AS and the Department of Neurosurgery at the University Hospital in Trondheim, Norway, for providing us with access to the neuronavigation system evaluated in this study, and, in particular, we thank Åge Grønningsæter (MISON AS) for helpful discussions.

REFERENCES

1. Gronningsaeter A, Kleven A, Ommedal S, Aarseth TE, Lie T, Lindseth F, Langø T, Unsgård G. SonoWand, an ultrasound-based neuronavigation system. Neurosurgery 2000;47(6):1373–1380.
2. Gumprecht HK, Widenka DC, Lumenta CB. BrainLab Vector Vision neuronavigation system: technology and clinical experiences in 131 cases. Neurosurgery 1999;44(1):97–105.
3. Hadani M, Spiegelman R, Feldman Z, Berkenstadt H, Ram Z. Novel, compact, intraoperative magnetic resonance imaging-guided system for conventional neurosurgical operating rooms. Neurosurgery 2001;48(4): 799–809.
4. Hata N, Dohi T, Iseki H, Takakura K. Development of a frameless and armless stereotactic neuronavigation system with ultrasonographic registration. Neurosurgery 1997;41(3):608–613.
5. Schaller C, Meyer B, van Roost D, Schramm J. Image guided microsurgery with a semifreehand neuronavigational device. Comp Aid Surg 1997;2(3–4):162–171.
6. Sipos EP, Tebo SA, Zinreich SJ, Long DM, Brem H. In vivo accuracy testing and clinical experience with the ISG Viewing Wand instrumentation application. Neurosurgery 1996;39(1):194–204.
7. Eljamel MS. Frameless stereotactic neurosurgery: two steps towards the holy grail of surgical navigation. Stereotact Funct Neurosurg 1999;72(2–4): 125–128.
8. Gumprecht H, Trost HA, Lumenta CB. Neuroendoscopy combined with frameless neuronavigation. J Neurosurg 2000;14(2):129–131.
9. Knauth M, Witz CR, Tronnier VM, Aras N, Kunze S, Sartor K. Intraoperative MR imaging increases the extent of tumor resection in patients with high-grade gliomas. AJNR Am J Neuroradiol 1999;20:1642–1646.
10. Paleologos TS, Wadley JP, Kitchen ND, Thomas DGT. Clinical utility and cost-effectiveness of interactive image-guided craniotomy: Clinical comparison between conventional and image-guided meningioma surgery. Neurosurgery 2000;47(1):40–48.
11. Reinhardt H, Trippel M, Westermann B, Gratzl O. Computer aided surgery with special focus on neuronavigation. Comput Med Imaging Graph 1999;23(5):237–244.
12. Roessler K, Ungersboeck K, Aichholzer M, Dietrich W, Goerzer H, Matula C, Czech T, Koos WT. Frameless stereotactic lesion contour-guided surgery using a computer-navigated microscope. Surg Neurol 1998; 49:282–289.
13. Seifert V, Zimmermann M, Trantakis C, Vitzthum H-E, Kühnel K, Raabe A, Bootz F, Schneider J-P, Schmidt F, Dietrich J. Open MRI-guided neurosurgery. Acta Neurochir 1999;141(5):455–464.
14. Steinmeier R, Fahlbusch R, Ganslandt O, Nimsky C, Buchfelder M, Kaus M, Heigl T, Lenz G, Kuth R, Huk W. Intraoperative magnetic resonance imaging with the Magnetom open scanner: concepts, neurosurgical indications, and procedures. A preliminary report. Neurosurgery 1998;43(4):739–748.
15. Wadley J, Dorward N, Kitchen N, Thomas D. Pre-

operative planning and intra-operative guidance in modern neurosurgery: a review of 300 cases. Ann R Coll Surg Engl 1999;81(4):217–225.
16. Wirtz CR, Albert FK, Schwaderer M, Heuer C, Staubert A, Tronnier VM, Knauth M, Kunze S. The benefit of neuronavigation for neurosurgery analyzed by its impact on glioblastoma surgery. Neurol Res 2000;22: 354–360.
17. Zakhary R, Keles E, Berger MS. Intraoperative imaging techniques in the treatment of brain tumors. Curr Opin Oncol 1999;11:152–156.
18. Samset E, Hirschberg H. Neuronavigation in intraoperative MRI. Comp Aid Surg 1999;4(4):200–207.
19. Fenster A, Downey DB. 3-D ultrasound imaging: a review. IEEE Eng Med Biol 1996;15(6):41–51.
20. Nelson TR, Pretorius DH. Three-dimensional ultrasound imaging. Ultrasound Med Biol 1998;24(9):1243–1270.
21. Cartellieri M, Kremser J, Vorbeck F. Comparison of different 3D navigation systems by a clinical "user." Eur Arch Otorhinolaryngol 2001;258:38–41.
22. Dorward NL, Alberti O, Palmer JD, Kitchen ND, Thomas DGT. Accuracy of true frameless stereotaxy: in vivo measurement and laboratory phantom studies. J Neurosurg 1999;90:160–168.
23. Hartov A, Eisner SD, Roberts DW, Paulsen KD, Platenik LA, Miga MI. Error analysis for a free-hand three-dimensional ultrasound system for neuronavigation. Neurosurg Focus 1999;6(3):Article 5.
24. Kaus M, Steinmeier R, Sporer T, Ganslandt O, Fahlbusch R. Technical accuracy of a neuronavigation system measured with a high-precision mechanical micromanipulator. Neurosurgery 1997;41(6):1431–1436.
25. Wirtz CR, Kanuth M, Hassfeld S, Tronnier VM, Albert FK, Bonsanto MM, Kunze S. Neuronavigation—first experiences with three different commercially available systems. Zentralbl Neurochir 1998;59:14–22.
26. Comeau RM, Sadikot AF, Fenster A, Peters TM. Intraoperative ultrasound for guidance and tissue shift correction in image-guided surgery. Med Phys, 2000; 27(4):787–800.
27. Helm PA, Eckel TS. Accuracy of registration methods in frameless stereotaxis. Comp Aid Surg 1998;3(2): 51–56.
28. Kall B, Goerss SJ, Stiving SO, Davis DH, Kelly PJ. Quantitative analysis of a noninvasive stereotactic image registration technique. Stereotact Funct Neurosurg 1996;66:69–74.
29. Smith KR, Frank KJ, Bucholz RD. The NeuroStation™—a highly accurate, minimally invasive solution to frameless stereotactic neurosurgery. Comp Med Imaging Graph 1994;18(4):247–256.
30. Villalobos H, Germano IM. Clinical evaluation of multimodality registration in frameless stereotaxy. Comp Aid Surg 1999;4(1):45–49.
31. Sandemann DR, Patel N, Chandler C, Nelson RJ, Coakham HB, Griffith HB. Advances in image-directed neurosurgery: preliminary experience with the ISG Viewing Wand compared with the Leksell G frame. Br J Neurosurg 1994;8:529–544.
32. Sumanaweera TS, Adler JR, Napel S, Glover G. Characterization of spatial distortion in magnetic resonance imaging and its implications for stereotactic surgery. Neurosurgery 1994;35(4):696–704.
33. Maciunas RJ, Galloway RL, Latimer JW. The application accuracy of stereotactic frames. Neurosurgery 1994;35(4):682–695.
34. Walton LB, Hampshire A, Forster DMC, Kemeny AA. A phantom study to assess the accuracy of stereotactic localization, using T1-weighted magnetic resonance imaging with the Leksell stereotactic system. Neurosurgery 1996;38(1):170–178.
35. Chassat F, Lavallée S. Experimental protocol of accuracy evaluation of 6-D localizers for computer-integrated surgery: Application to four optical localizers. In: Wells WM, Colchester A, Delp S, editors: Proceedings of First International Conference on Medical Image Computing and Computer-Assisted Intervention (MICCAI'98), Cambridge, MA, October 1998. Lecture Notes in Computer Science 1496. Berlin: Springer, 1998. p 277–284.
36. Schmerber S, Chassat F. Accuracy evaluation of a CAS system: laboratory protocol and results with 6D localizers, and clinical experiences in otorhinolaryngology. Comp Aid Surg 2001;6:1–13.
37. Langø T. Ultrasound guided surgery: Image processing and navigation. Doctoral thesis, Norwegian University of Science and Technology, Trondheim, Norway, 2000.
38. Prager RW, Rohling RN, Gee AH, Berman L. Rapid calibration for 3-D freehand ultrasound. Ultrasound Med Biol 1998;24(6):855–869.
39. Prager RW, Rohling RN, Gee AH, Berman L. Automatic calibration of 3-D free-hand ultrasound. Technical report: CUED/F-INFENG/TR 303. Department of Engineering, Cambridge University, UK, 1997.
40. Unsgård G, Ommedal S, Muller T, Gronningsaeter A, Hernes TAN. Neuronavigation by intraoperative 3D ultrasound: initial experiences during brain tumor resections. Neurosurgery 2002;50(4):804–812.
41. Duck FA. Physical Properties of Tissue. A Comprehensive Reference Book. London: Academic Press Ltd., 1990.
42. Lindseth F, Bang J, Langø T. A robust and automatic method for evaluating the accuracy in 3D ultrasound-based navigation. Manuscript under review.
43. Box GEP, Hunter WG, Hunter JS. Statistics for Experimenters: An Introduction to Design, Data Analysis, and Model Building (chapter 6). New York: John Wiley & Sons, 1978.
44. Kremkau FW, Barnes RW, McGraw CP. Ultrasonic attenuation and propagation speed in normal human brain. J Acoust Soc Am 1981;70:29–38.
45. Nimsky C, Ganslandt O, Cerny S, Hastreiter P, Greiner G, Fahlbusch R. Quantification of, visualization of, and compensation for brain shift using intraoperative magnetic resonance imaging. Neurosurgery 2000;47(5):1070–1080.

46. Roberts DW, Hartov A, Kennedy FE, Miga MI, Paulsen KD. Intraoperative brain shift and deformation: A quantitative analysis of cortical displacement in 28 cases. Neurosurgery 1998;43(4):749–760.
47. Maurer CR, Fitzpatrick JM, Wang MY, Galloway RL, Maciunas RJ, Allen GS. Registration of head volume images using implantable fiducial markers. IEEE Trans Med Imaging 1997;16(4):447–462.
48. Hill DLG, Maurer CR, Maciunas RJ, Barwise JA, Fitzpatrick JM, Wang MY. Measurement of intraoperative brain surface deformation under a craniotomy. Neurosurgery 1998;43(3):514–528.
49. Khadem R, Yeh C, Sadeghi-Tehrani M, Bax MR, Johnson JA, Welch JN, Wilkinson EP, Shahidi R. Comparative tracking error analysis of five different tracking systems. Comp Aid Surg 2000;5(2):98–107.

Paper IV

Probe calibration for freehand 3D ultrasound reconstruction and surgical navigation

Authors:
Frank Lindseth[1, 2], Geir Arne Tangen[1], Thomas Langø[1], Jon Bang[1]

Affiliation:
[1]SINTEF Unimed, Ultrasound, Trondheim, Norway
[2]The Norwegian University of Science and Technology, Department of Computer and Information Science, Trondheim, Norway

Abstract

Ultrasound probe calibration is an important requirement for correct freehand 3D ultrasound reconstruction and accurate surgical navigation based on ultrasound. The probe calibration procedure establishes the rigid body transformation between the ultrasound scan plane (image) and an attached tracking device. A regular volume can then be reconstructed from the tracked images. Real-time 2D, as well as motorized and 2D-array based 3D ultrasound will also require probe calibration when used in an integrated navigation scene. We propose two new methods for probe calibration, one alignment-based, and one based on freehand scanning. In addition, we use an established method for comparison. For all three methods we have developed novel algorithms for robust and automatic identification of image points. Three different ultrasound probes are used for assessment and a new evaluation method based on automatically extracted features in reconstructed volumes is used as our main quality measure. The freehand method performed best with a navigation accuracy of 0.62 mm for one of the probes. This indicates that sub-millimeter accuracy can be achieved in ultrasound-based surgical navigation when a precise probe calibration is performed.

Key Words: Ultrasound probe calibration, freehand 3D ultrasound reconstruction, ultrasound-based surgical navigation, image guided therapy, phantom study, accuracy evaluation, automatic point detection, image processing

INTRODUCTION

Three-dimensional (3D) tracking of 2D ultrasound images involves determination of the position and orientation of the 2D images with respect to a given 3D coordinate system. Several medical applications require such tracking; 3D ultrasound-based visualization in neurosurgery, (Gronningsaeter et al. 2000; Hartov et al. 1999), multimodal image registration such as 3D ultrasound to magnetic resonance (MR) images or X-ray or single photon emission computed tomography (CT or SPECT) (Gobbi et al. 2000; Gobbi et al. 1999; Lindseth et al. 2002b.; Pagoulatos et al. 1999a; Péria et al. 1995), ultrasound-guided radiation therapy (Bouchet et al. 2001), diagnostic volume measurements and analysis (Barry et al. 1997; Rohling et al. 1998), in vivo cardiac valve reconstructions (Berg et al. 1999), and breast cancer surgery guided by 3D ultrasound (Sato et al. 1998).

Regardless of the choice of tracking technology (e.g. optical, magnetic, acoustical, mechanical), a probe calibration has to be performed before tracking is feasible. Calibration of an ultrasound probe is the process of determining the mathematical transformation between the position and orientation of the coordinate system of the 2D ultrasound image and the 3D coordinate system of the tracking device attached to the probe shaft. Finding this transformation matrix is probably one of the most challenging and critical tasks regarding accuracy in 3D freehand ultrasound imaging (Lindseth et al. 2002a; Lindseth et al. 2002c.) and in particular 3D reconstructions that preserves true anatomic shape and size.

The probe calibration can be done once in the factory or laboratory under controlled conditions, so that the result does not depend on an arbitrary operator. This leaves the system vendor in control of the accuracy. Ideally, one unique tracking device should be permanently attached to one unique ultrasound probe before calibration in the factory. But for sterile use of ultrasound, this option represents practical difficulties in that most ultrasound probes cannot be sterilized, while the tracking devices often can. Both devices can alternatively be covered by sterile drape, but this may hinder free sight to the cameras (optical tracking). Current solutions to this problem include: 1) Calibration of any probe to any position sensor inside the operating room using a special ultrasound calibration phantom and fast algorithms; or 2) Calibration of one particular probe to one particular position sensor in the laboratory or factory, using a special adapter that ensures repetitive and precise attachment between the two, even through sterile probe drape. This option does not allow for replacement of neither the probe nor the tracking device adapter without returning both to the factory for new calibration.

Theory

The probe calibration transformation is a 2D matrix defined by three translation offsets (t_x, t_y, t_z), and three angular rotations (α, β, γ);

$$CM_{td \leftarrow ui} = T(t_x, t_y, t_z) \cdot R_z(\alpha) \cdot R_y(\beta) \cdot R_x(\gamma)$$

$$= \begin{bmatrix} 1 & 0 & 0 & t_x \\ 0 & 1 & 0 & t_y \\ 0 & 0 & 1 & t_z \\ 0 & 0 & 0 & 1 \end{bmatrix} \cdot \begin{bmatrix} \cos\alpha & -\sin\alpha & 0 & 0 \\ \sin\alpha & \cos\alpha & 0 & 0 \\ 0 & 0 & 1 & 0 \\ 0 & 0 & 0 & 1 \end{bmatrix} \cdot \begin{bmatrix} \cos\beta & 0 & \sin\beta & 0 \\ 0 & 1 & 0 & 0 \\ -\sin\beta & 0 & \cos\beta & 0 \\ 0 & 0 & 0 & 1 \end{bmatrix} \cdot \begin{bmatrix} 1 & 0 & 0 & 0 \\ 0 & \cos\gamma & -\sin\gamma & 0 \\ 0 & \sin\gamma & \cos\gamma & 0 \\ 0 & 0 & 0 & 1 \end{bmatrix}$$

(1)

The coordinate systems (*ui* = ultrasound image; *td* = tracking device) and the transformations are shown in Fig. 1. The transformation is written with homogeneous coordinates (fourth row is [0 0 0 1]) to handle both translation and rotation with one single matrix multiplication. The equation above can be deduced by multiplying the four matrixes: R_x; rotation by γ about the x-axis, R_y; rotation by β about the y-axis, and R_z; rotation by α about the z-axis, T; translation by t_x, t_y, and t_z, respectively.

The calibration parameters can be crudely estimated by external measurements of the probe and the attached tracking device. However, this estimate will have low accuracy for several reasons. Firstly, the origin of the ultrasound image system may be located inside the probe housing, and may vary from one probe to another. Secondly, the orientation of the ultrasound plane is basically unknown, and this will affect the rotational parameters in the matrix. Thirdly, in magnetic tracking systems, the tracking device's origin cannot be defined exactly. For these reasons, a commonly used approach for probe calibration is to image a phantom with known physical properties and dimensions.

The majority of probe calibration methods found in the literature can be categorized into three different classes; 1) Single point methods based on targeting single points or lines, 2) 2D alignment methods based on 2D imaging of thin planar structures, and 3) Freehand methods based on scanning certain 3D structures (typically string phantoms). A brief description of each of these classes, with reference to publications describing them in detail, is outlined below. Common for all methods is the acquisition of ultrasound images of known structures (dimension and physical properties such as speed of sound) submerged in either water or tissue equivalent media. The imaged structures are either known through accurate measurements of the phantom or by measuring the specific points interactively using e.g. a calibrated pointer. The processing of the acquired data is more or less common for all methods.

Single point methods

The majority of published works on probe calibration uses some type of single point method. These methods are based on acquisition of several 2D ultrasound images of some point target like crossed wires (Barry et al. 1997; Detmer et al. 1994; Hartov et al. 1999; Leotta et al. 1995; Leotta et al. 1997; Prager et al. 1997; Prager et al. 1998), small spheres/beads/pins (Legget et al. 1998; Pagoulatos et al. 1998; Pagoulatos et al. 1999a; State et al. 1994), or fastening the probe and simply moving the target point into different locations in the imaging plane (Muratore and Galloway 2001). A three-wire scanning method has also been suggested (Prager et al. 1997; Prager et al. 1998), in which three wires are arranged orthogonally in a water bath and both the origin and the wires themselves are scanned. However, the accuracy of the method depends on the orthogonality and straightness of the wires. In addition, the wires must be scanned separately and which wire is scanned must be kept track of during data acquisition. The advantage of this method over e.g. cross-wire technique is mainly that it is easier to scan the length of a wire than it is to keep the image focused at a point from various positions.

The target points in single point methods are usually located in water, but some groups have used tissue equivalent media (Pagoulatos et al. 1998) to avoid sound speed estimations and scaling issues for the 2D ultrasound images. The target is imaged from several distances and orientations. To facilitate imaging from a variety of positions (not just from the surface in a water tank set-up), different solutions have been suggested, such as embedding the target point inside a cylinder (Leotta et al. 1997) or balloon (Legget et al.

1998; Pagoulatos et al. 1998). The points in the ultrasound images are usually found by manual detection. The accuracy of single point methods depends on the accuracy of marking the points in the images, the alignment of the scan plane with the point structure, and the accuracy of determination of the physical coordinates of the target point. In addition, the resolution of 2D ultrasound imaging is an important factor, in particular the lateral and elevation direction resolution (Fig. 1).

Another method in this category is probe calibration based on detection of lines. It is much easier to detect lines than points in ultrasound images due to the presence of noise. Hence, methods based on line detection are better suited for automatic processing. The membrane method (Langø 2000), the single-wall method (Prager et al. 1998), and the Cambridge phantom method (Prager et al. 1997; Prager et al. 1998) are all based on detection of lines, and then extraction of points from these lines (hence, they can be categorized as single point methods). The main idea of the single-wall method is to let the bottom of the water tank constitute the xy-plane of the reconstruction system. The bottom of a water bath is imaged from different directions and the line in each image defining the bottom is detected. Points from this edge are used in the further processing and transformation calculations. One problem with this method is the specular reflection that causes a low intensity echo at oblique scan angles. This can to a certain degree be compensated for by roughening the surface of the bottom, as suggested by the authors (Prager et al. 1997; Prager et al. 1998). Another problem is that it is difficult to determine the true position of the floor in the images based on the reflected signal intensity. This is due to the strong reverberations from the bottom, which appear as a tail in the reflected intensity signal. These drawbacks are compensated for in the membrane method (Langø 2000). The latter method uses a thin nylon membrane submerged in water to avoid the problems of specular reflections at oblique scan angles and tail echoes. Nevertheless, the membrane method suffered from poor accuracy, probably due to movements of the membrane during probe scanning/movement and registration of the membrane position.

The Cambridge method (Prager et al. 1998) uses a specially designed phantom and a clamping device that fits to the phantom without being rigidly locked to it. By mounting the probe in the clamp, the operator may scan the phantom with the necessary degrees of freedom. During scanning, the clamp restricts the relative motion between the probe and the phantom and thus guarantees optimal imaging conditions. The method thus requires a precision-made phantom and clamp, and involves somewhat cumbersome procedures for probe mounting.

2D alignment methods

Only a few publications have suggested 2D alignment-based methods for probe calibration (Langø 2000; Péria et al. 1995; Sato et al. 1998; Welch et al. 2000). The main idea of these methods is to align the 2D ultrasound plane with a thin membrane (Langø 2000; Sato et al. 1998; Welch et al. 2000) in a water bath containing known points (e.g. corners and edges of a jagged membrane). The points are either accurately measured in advance or marked by using a pointer, as for the single point methods. The main difference from the single point methods is the more difficult alignment procedure. This is the procedure of making sure that the ultrasound 2D plane and the thin membrane structure of the phantom coincide in space. The ultrasound image is in fact not really a 2D plane, but has finite thickness. This makes the process of aligning the image with the phantom membrane tedious and often the probe can be moved considerably without affecting the view on the ultrasound monitor. Nevertheless, the method is attractive since only one image is needed to calibrate the probe.

Freehand methods

Recently, several methods based on freehand scanning have been proposed, typically using string phantoms (Bouchet et al. 2001; Gobbi et al. 1999; Liu et al. 1998; Pagoulatos et al. 1999b; Pagoulatos et al. 2001; Welch et al. 2002). The main difference from the previously mentioned methods is the fact that the user can hold and move the probe by freehand and no alignment with structures is required (neither single points nor membranes). The methods in their simplest form require only one or a few images. However, for most of the methods it is a simple task acquiring several hundred images to increase accuracy. The strings in the phantoms are arranged in patterns that make it possible to perform automatic image analysis, while some claim random string configurations for their method (Welch et al. 2002). Two different groups use string phantoms where the wires are arranged in *N* (Pagoulatos et al. 2001) or *Z* (Bouchet et al. 2001) shapes (depending on the view direction) and the basic idea is that, due to the specific geometry, relative distances between points in the ultrasound image uniquely determine the physical coordinates of some of these points. The simplest phantom in this group is a pyramidal string phantom (Liu et al. 1998) with three strings stretched across a water tank to form a triangular pyramid. This phantom was then scanned from the top and from geometrical knowledge of the pyramid it is possible to determine, from the 2D ultrasound images showing three dots each, where on the pyramid the image was acquired. The authors concluded that the error due to the thickness of the ultrasound scan plane in two other single point methods (Detmer et al. 1994; Legget et al. 1998) was significantly reduced.

Approaches for probe calibration based on image registration techniques has also been suggested (Blackall et al. 2000). The term registration is typically used when the two coordinate systems are completely independent of each other, while calibration is used when the coordinate systems are rigidly connected. In registration-based calibration, 2D ultrasound images of a calibration phantom are matched (mutual information) to a volume (MRI or CT) of the same phantom.

MATERIALS AND METHODS

In this study we have used three custom made phantoms to evaluate different methods for ultrasound probe calibration. Two methods were based on alignment. These involved imaging a single point for the Bead method and imaging a vertical plane of wire crosses for the Diagonal method. The last method, the Pyramid method, was based on freehand scanning of a phantom made up of N structures.

An overview of the experimental set-up and the data flow is shown in Fig. 2. Our ultrasound scanner tagged each ultrasound image frame with position data delivered from an optical tracking system. The resulting data (ultrasound image with position data) were imported into a computer for further processing. The processing consists of two main parts: one for the generation of probe calibration matrixes and one for 3D evaluation of previously generated probe calibration matrixes. The generation of the probe calibration matrixes started with 2D reconstruction (scan conversion) of the raw digital ultrasound data, transforming it into a regular 2D image. The next processing step was automatic detection of points in the images based on the selected method (Bead, Diagonal or Pyramid). The physical coordinates of the same points were measured during phantom design. These two point sets were matched using a least squares error minimization approach (Arun et al. 1987). From this matching procedure, the probe calibration transformation matrix was attained.

The evaluation sequence started with a translation scan of the Diagonal phantom (27 wire crosses). The evaluation scans were reconstructed into a regular volume using the matrixes attained by the different calibration methods. The coordinates of the 27 wire crosses in the generated volumes were automatically detected. These image points were then compared to the physically measured wire crosses to evaluate the effect of using different calibration matrixes in the reconstruction process (Lindseth et al. 2002a). We also evaluated the probe calibration matrixes using more traditional quality measures.

Calibration phantoms

All three phantoms were made of aluminum and had four infrared reflecting spheres mounted as a reference frame for the optical tracking system. The position tracking software reported positions/orientations relative to this reference frame. The physical measurements of the phantoms were made in the same coordinate system.

Bead phantom

A vertical pole is mounted on the phantom frame (Fig. 3A). On top of this pole is a needle pin with a round head (Fig. 3B). The head of the needle forms a well-defined point that can easily be visualized in an ultrasound image.

Diagonal phantom

18 polyester wires with diameter 0.2 mm are mounted inside the Diagonal phantom, with spring loadings to keep the wires straight (Fig. 3C). The wires are parallel to the X- or Y-axis of the reference frame. They form 27 wire crosses with vertical separation 0.5 mm. All wire crosses lie within the cubic volume with dimensions 5^3 cm^3. The position of all wire crosses and the four reflecting spheres have been physically measured with an accuracy of 0.1 mm in all directions.

Pyramid phantom

Like the Diagonal phantom, the Pyramid phantom consists of a frame with polyester wires mounted internally (Fig. 3D). The internal wire configuration is shown in Fig. 4. The front and back walls of the phantom are connected with parallel wires through the corresponding front and back wall holes. In addition, diagonal (intermediate) wires are stretched from the front to the back wall in the direction indicated by the arrows.

The wire configuration inside the phantom is designed to allow for automatic detection of image points by the algorithm described later. We have adapted the design suggested by (Pagoulatos et al. 2001). The basic element of the wiring configuration is the N structure made up of three straight wires as shown in Fig. 4A. In the phantom reference coordinate system, the wires' end points A, B, C, and D are known, while the crossings P, Q and R with the ultrasound plane are unknown since the position of the plane itself is unknown. However, P is determined in the phantom coordinate system by the following set of equations (subscripts correspond to the points in Fig. 4A):

$$
\begin{aligned}
x_P &= x_B + k\cdot(x_C - x_B)\\
y_P &= y_B + k\cdot(y_C - y_B)\\
z_P &= z_B + k\cdot(z_C - z_B)
\end{aligned}
\tag{2}
$$

where k is the ratio of distance BP to distance BC. Since the phantom is built with wires AB and CD parallel, the triangles BPQ and CPR are similar such that

$$
k = \frac{|BP|}{|BC|} = \frac{|QP|}{|QR|} \tag{3}
$$

Points P, Q and R can be identified in the ultrasound image (Fig. 4C), and thus we can calculate the distances QP and QR. Insertion of (3) in (2) then gives the phantom reference coordinates of point P.

The phantom consists of a series of such N structures. To be applicable for a fair selection of probes (small and large footprint; linear and sector), the design was guided by the following criteria:

Narrow wire spacing near the top (small probes)

Increasing wire spacing with depth (to accommodate for lower image resolution at greater depth, especially for sector probes)

The distance between the front and back walls should allow for freehand scanning; at the same time, it should be small enough that the angles ABC and BCD are sufficiently large (the accuracy degrades as these angles decrease).

Acquisition of calibration and evaluation data

For acquisition of ultrasound data we have used a high-end ultrasound scanner (System FiVe, GE Vingmed, Norway). Tracking data was supplied by an optical tracking system (Polaris®, Northern Digital Inc., Canada). The optical tracking camera was mounted looking down on our working area at approximately 60 elevation and 2 m distance. This set-up agreed with the recommendations of the manufacturer.

The phantoms were immersed in water and were scanned using the three ultrasound probes that are shown in Fig. 5.

With one exception, we acquired images of all three phantoms with all three probes, according to the protocol shown in Table 1. The exception is the intraoperative (ILA) probe, which could not image the Diagonal phantom appropriately due to the small footprint.

For scanning of the Bead phantom, we manually aligned the probe for optimal imaging of the needle's head, judged visually from the display on the scanner. This was repeated several times, changing the position and the orientation of the probe so that all degrees of freedom were explored. For each probe position, we recorded an image that was transferred to the computer. The number of images for each probe is listed in Table 1.

For the Diagonal method we aligned the probe with a vertical plane of wire crosses (the main diagonal of the Diagonal phantom). Nine wire crosses were visible for the FPA probe, and six for the FLA probe. As already mentioned, the ILA probe could not be used on this phantom. Table 1 shows the number of acquired images. A new probe alignment was performed for each image.

The intended use of the Pyramid method is to perform a continuous scan covering all the possible degrees of freedom, followed by automatic detection of the image points. However, in order to obtain a reasonable number of significantly different images, and thus be able to compare with the other two methods, we recorded single images also for the Pyramid method (Table 1).

The data were transferred to the processing computer through an Ethernet connection to the scanner. Our software application then performed a reconstruction (scan conversion) of the ultrasound data into a geometrically correct 2D ultrasound image. Transducer sector data (number of beams, number of samples, sector angle etc) and the speed of sound in the scanned material (water) were used as input during this scan conversion. The transducer sector data were read from the digital scanner file. The temperature of the water was measured before doing the scans of the phantoms. The temperature could then be converted to the speed of sound in water using tabulated data (Duck 1990).

We also performed 3D scans of the Diagonal phantom to be used for the accuracy evaluation of the probe calibration matrixes. This was done by mounting the probe in a rigid holder for repeatability and overall stability purposes, and translating this holder parallel to the wires. We made two volume recordings of the 27 wire crosses for each of the three ultrasound probes. Since the FLA and ILA probes did not cover the full width of the Diagonal phantom, we had to do several scans to cover the full volume for these two probes. For the FLA probe one volume scan consisted of two translation scans, one scan covering two vertical planes of wire crosses and one scan covering the last vertical plane of wire crosses. For the ILA probe, one volume scan consisted of three translation scans, each covering one of the three vertical planes of wire crosses. This gives the number of evaluation scans listed in Table 1.

Calculation of the probe calibration matrix

A single probe calibration matrix $CM_{td \leftarrow ui}$ was generated in the following way: for the particular probe and method combination, draw randomly the amount of input data needed from the calibration pool given in Table 1 (the amount of data needed will be investigated). In each of these images, find the ultrasound image coordinates (an automatic method is described below) of all the points that can be identified as calibration points ($IP_{ui}^{p,i}$; superscript p,i denotes point p in image i). Next, transform the measured points MP_{rf}^{p} from physical reference coordinates rf into tracking device coordinates td by using the inverse of the tracking matrix $TM_{rf \leftarrow td}^{i}$. The rigid body transformation that minimizes the mean Euclidian distance between the two homologous points sets $IP_{ui}^{p,i}$ and $MP_{td}^{p,i}$ will be the probe calibration matrix $CM_{td \leftarrow ui}$:

$$CM_{td \leftarrow ui} = \underset{CM'}{\arg\min} \sum_{p,i} \left\| CM' \cdot IP_{ui}^{p,i} - MP_{td}^{p,i} \right\|, \quad MP_{td}^{p,i} = \left(TM_{rf \leftarrow td}^{i} \right)^{-1} \cdot MP_{rf}^{p} \tag{4}$$

The matrix is calculated using a direct point set minimization technique (Arun et al. 1987). Iterative minimization techniques also exist (Prager et al. 1998). The results are checked for mirror solutions (Prager et al. 1998).

Automatic detection and identification of image points

The Bead method

Automatic detection of the bead in an ultrasound image is complicated by the presence of other high-intensity areas like the bead's support bin and pole, multiple reflections, or noise. The algorithm therefore detects a number of intensity peaks (typically four) and evaluates each of them against the following criteria:

1. The peak intensity I_0 should exceed 230 (pixel intensity values range from 0 to 255).
2. The peak intensity should exceed 80% of the maximum detected intensity.
3. The peak's vertical extension M (distance between $0.3*I_0$ – points vertically in image) should be 3-6 mm.
4. The peak's horizontal extension N (distance between $0.3*I_0$ – points horizontally in image) should be 3-6 mm.
5. The intensity integrated over the area defined by M and N should exceed 0.1 of the image's total intensity.
6. Within the area defined by M and N we calculate the intensity centroid. This point should not lie farther than 0.75 mm from the intensity peak position originally detected.

Each intensity peak is assigned a numerical value with respect to each criterion. This value is 1 when the criterion is fulfilled, and decays linearly to 0 over a suitable range outside the criterion acceptance region. In addition to the six criteria, the peak lying highest in the image (closest to the probe) gets an additional score of 1, the next highest peak scores 0.5, and the third highest peak scores 0.25. The total rating for one intensity peak is found by summation of the scores with respect to each criterion plus the extra credit to peaks close to the probe. Optionally, the relative influence of each criterion can be adjusted by applying different weighting factors; however, initial testing showed that a flat weighting was appropriate for our data. The intensity peak with maximum total rating is taken as a detection of the bead. The centroid found in criterion 6 is used as the location, since these coordinates are relatively insensitive to pixel noise.

The Diagonal and Pyramid methods

Fig. 6 shows the flowchart for automatic detection of points in the Diagonal and Pyramid methods. The algorithm is based on the fact that images of the phantom will contain a set of points with a known geometric relation between them. In the Diagonal phantom, these points are the wire crosses on the main diagonal, while in the Pyramid phantom, the points are the parallel wires of all N structures. This known or ideal geometry, represented by distances (in mm) and directions between any pair of points, is stored on a geometry file that is specific for each probe and acquisition session. After loading of an ultrasound image and the corresponding geometry file, the image resolution is used to convert the ideal geometry from mm to pixels.

A possible detection of one point – in the following termed candidate point – is found by searching a selected area of the image for an intensity peak. This candidate point is not accepted unless it is confirmed by a sufficient number of neighbours. By the term "neighbour" we mean other high-intensity peaks in the image, at locations relative to the candidate point that agree with the ideal geometry. The search for neighbours is done by repetitively superimposing the ideal geometry onto the ultrasound image. In the first superposition, the candidate point is assumed to be point 1 of the ideal geometry. To compensate for sideways tilting of the probe during data acquisition, the ideal geometry is rotated in the image plane in finite steps. Intensity peaks above a specified threshold at locations corresponding to the ideal geometry are counted as neighbours of the candidate point for this particular superposition. The search is then repeated with the candidate point as point 2 of the ideal geometry, then as point 3, and so on, and the number of neighbours is recorded for each case. A mutual cross-checking is also performed to ensure that the candidate point was not a spurious noise peak. The superposition of the ideal geometry that yields the maximum number of neighbours is taken as the valid detection.

The acceptance criterion is that the maximum number of neighbours exceeds a pre-set threshold that depends on the actual probe and the image size. If necessary, the search procedure will start from the beginning, searching another area of the image for a new candidate point. If, at the end, the acceptance criterion is not met, a warning is displayed for the image being analyzed. Reasons for this kind of failure may be too few wires being included in the image, too low intensity at some wires, or incorrect ideal geometry description. However, testing has shown that the algorithm works satisfactorily on realistic images with both probe tilting within reasonable limits and moderate amounts of noise.

When the acceptance criterion is met, the positions of the detected points are fine-tuned by a two-step procedure. Firstly, the detected points are replaced by the ideal geometry mask, which is translated and rotated slightly to find the position that maximizes the sum-of-intensities at the ideal geometry points. Secondly, the intensity centroid is calculated over a finite area at each position. The area size is derived from the extension of each intensity peak. If the displacement of the centroid from the ideal geometry is less than typically seven pixels, the centroid coordinates are taken as the final position; otherwise, the ideal geometry position is used. The first step thus guarantees that the overall geometry of the detected point set agrees with the ideal geometry, while the second step allows for small local deviations from the ideal geometry.

The above algorithm completes the task of automatic point detection for the Diagonal method. It is also used to detect the parallel wires in the Pyramid method (points Q and R in Fig. 4). The intermediate wires in the Pyramid phantom are detected using the a priori knowledge that these points lie on the straight lines connecting specific pairs of parallel wires. To detect these points, we apply a search mask that weighs down the region outside this connecting line and the regions close to the end points. The specific design of this mask is derived from the extent of the two parallel wire points. Within the masked region, the maximum intensity above a predefined threshold is taken as the intermediate wire, and the position is fine-tuned to the centroid coordinates as described above. Finally, the location is projected onto the straight line, to guarantee consistent results if the points Q and R are interchanged. This projection typically means a lateral displacement by less than one pixel, and thus has minor impact on the results.

Evaluation

The quality of the different calibration methods was assessed using several criteria. Both evaluation of volumes reconstructed from 3D evaluation scans (Table 1) and more established evaluation (Blackall et al. 2000; Prager et al. 1998) were performed. The quality measures are:

3D Navigation Accuracy (3D NA)
3D Distance Reconstruction Accuracy (3D DRA)
3D Registration Accuracy (3D RA)

Calibration Reproducibility (CR)
Point Reconstruction Accuracy (PRA)

The 3D quality measures are defined by:

$$\Delta_{rf}^{3D\,NA} = \underset{p,v}{mean}\left\{\left\| VM_{rf \leftarrow uv}^{v} \cdot IP_{uv}^{p,v} - MP_{rf}^{p} \right\|\right\} \tag{5}$$

$$\Delta_{rf}^{3D\,DRA} = \underset{pi\ \ pj,v}{mean}\left\{\left\| \left\| VM_{rf \leftarrow uv}^{v} \cdot IP_{uv}^{pi,v} - VM_{rf \leftarrow uv}^{v} \cdot IP_{uv}^{pj,v} \right\| - \left\| MP_{rf}^{pi} - MP_{rf}^{pj} \right\| \right\|\right\} \tag{6}$$

$$\Delta_{rf}^{3D\,RA} = \underset{p,v}{mean}\left\{\left\| RM_{rf \leftarrow uv}^{v} \cdot IP_{uv}^{p,v} - MP_{rf}^{p} \right\|\right\} \tag{7}$$

The volume matrix $VM_{rf \leftarrow uv}^{v}$ for volume v transforms an image point $IP_{uv}^{p,v}$ (point p in volume v) given in ultrasound volume (*uv*) coordinates into the reference frame (*rf*) where the gold standard MP_{rf}^{p} has been accurately measured. The volume matrix is generated during the reconstruction. $RM_{rf \leftarrow uv}^{v}$ is the registration matrix that matches the two points sets *IP* and *MP* by translation and rotation (Arun et al. 1987).

The navigation accuracy is crucial when reconstructed ultrasound data is used in image guided surgical approaches. 3D NA measures this by comparing the extracted and transformed points directly to the gold standard. We therefore consider 3D NA to be the best quality measure, and will use it extensively throughout the evaluation. The other quality measures are given for comparison and completeness when appropriate.

3D DRA and 3D RA measures how accurately an imaged object can be geometrically reconstructed using 3D freehand ultrasound. 3D DRA compares the Euclidian distance between two points in image space (transformed into the common *rf* coordinate system) with the distance between the points in physical space. We calculate the distances between corresponding points in the outermost wire cross layers of the phantom (nine point pairs in each direction), since these distances are likely to show the largest discrepancies. The evaluation of direction-dependent measures will also reveal possible anisotropic reconstruction problems. 3D RA measures how well the extracted evaluation point set can be matched to the gold standard by translation and rotation only (i.e., without scaling). It can be represented by a single number by averaging over all points within the volume.

The last two quality measures are defined by:

$$\Delta_{td}^{CR} = \underset{j,k}{mean}\left\{\left\| CM_{td \leftarrow ui}^{j} \cdot IP_{ui}^{virtual} - CM_{td \leftarrow ui}^{k} \cdot IP_{ui}^{virtual} \right\|\right\} \tag{8}$$

$$\Delta_{rf}^{PRA} = \underset{p,i}{mean}\left\{\left\| TM_{rf \leftarrow td}^{i} \cdot CM_{td \leftarrow ui} \cdot IP_{ui}^{p,i} - MP_{rf}^{p} \right\|\right\} \tag{9}$$

CR measures how well a given probe calibration method repeats when performed on a new set of images. Δ_{td}^{CR} is the Euclidian distance between the two transformations j and k of the same virtual image point $IP_{ui}^{virtual}$. To comply with previously published work (Blackall et al. 2000; Prager et al. 1998), we use $IP_{ui}^{virtual}$ = (0, 20, 40)mm. The measure can be calculated for any pair of calibrations.

PRA is a measure of how well a point p in image i maps to the gold standard using the calibration matrix under test and the appropriate tracking matrix. In this manner, PRA is the 2D equivalent to 3D NA. The points used in the PRA evaluation can either originate from a separate 2D evaluation data set especially acquired for this purpose, or from the pool of calibration data. We used the last approach for practical reasons, and calculated the PRA based on three subsets of the calibration pool: a) the whole pool; b) just the data used in the calibration; and c) the data not used in the calibration.

The evaluation was divided into three steps. First we established the practical amount of data needed in a typical probe calibration. We did this by considering 3D NA as a function of the amount of calibration data that goes into the calculation of the calibration matrixes. This was done for the FPA probe, and for all three calibration methods. We used ten steps along the horizontal axis with increments of 5, 1, and 1 frame for the Bead, Diagonal, and Pyramid methods, respectively. The needed data at each step were randomly drawn from the pool of calibration data given in Table 1. This was independently repeated three times at each step, and all the generated matrixes were used to reconstruct each of the two 3D evaluation scans for the FPA probe, giving a total of 180 evaluation volumes (3 methods * 10 steps * 3 repetitions * 2 scans). The results for the FPA probe were then used for the FLA and ILA probes in the following evaluation steps.

In the second step, we compared the various calibration methods by evaluating the quality measures described above. For each of the probe / method combinations we calculated 15 calibrations, each based on the amount of data found in the first step. The needed data were randomly drawn from Table 1.

In the third step, we used the probe calibration quality measures 3D NA and 2D CR to evaluate the automatic method for identification of image points, versus doing this identification manually. We performed this evaluation on the best probe/method combination (i.e., the combination with lowest 3D NA) identified in the previous step. For this probe/method combination we chose three of the 15 calibrations, one approximately equalling the mean 3D NA, one extreme below, and one extreme above the mean. For each of the three input data sets four human experts manually identified the same image points as the automatic calibration method. The operators could freely zoom in and out to the level desired on each point. This generated twelve manual matrixes that were treated the same way as the three automatic matrixes, and the performance of all 15 matrixes were compared.

RESULTS

Automatic point identification

The result of running the automatic point identification algorithm on a random frame from Table 1 for each of the eight possible probe / method combinations are shown in Figs. 7 through 9. The results are overlaid the images. For the Pyramid method both parallel wires points and intermediate wire points in the N structures are shown. Table 2 gives the number of identified points in each of the calibration images listed in Table 1. When a range is indicated, all the possible calibration points are not identified in all the images, and the first number is the minimum number of points found in any of the images for a given probe / method combination. The percentages of identified points are also included in Table 2.

Establishing the amount of data needed for a calibration

Fig. 10 shows 3D NA as a function of the number of frames (images) used for the probe calibration. The solid black curve is the average over three repeated calibrations, each evaluated on two 3D volumes. The individual results are shown by the six coloured curves. The general trend is that the accuracy improves as more calibration data is used in the calculations for all three methods. Also, the variations between identical calibrations applied to different 3D evaluation scans (curves with same colour) are small. This indicates that the overall stability of the system / evaluation method is good, and that observed differences greater than this can be attributed to the probe calibration alone. The effects of different calibrations are easily observed when these calibrations are based on a small number of frames. These discrepancies approach the effect caused by different evaluation volumes when more calibration data are used.

Acquiring and processing the data can be time consuming, especially for alignment based methods with manual identifications of image points, and there is no point in adding more data if this doesn't improve the accuracy and stability of generated matrixes. For the further evaluation we will use the number of images listed in Table 3. These numbers are practical compromises based on extracted information from Fig. 10, the time needed to generate a larger pool of data than that given in Table 1, especially for the Bead and Diagonal methods, and the desire to use approximately the same number of data (i.e. points) for each of the probe / method combinations.

By including increasingly more input data for the probe calibration, the accuracy will approach a value that we term the asymptotic accuracy. This value can be estimated from the solid black curves in Fig. 10. It can also be estimated by using all available input data (Table 1), and averaging over all the evaluation volumes. The results, which are listed in Table 4, support the impression of Fig. 10 that the Pyramid method is asymptotically the most accurate.

To investigate the effect of field of view, we made a separate series of 20 acquisitions with 9 cm imaging depth of the FPA probe, such that the three lowest N structures of the Pyramid phantom fell outside the image. From this data set, we calculated and evaluated probe calibration matrixes the same way as for the ordinary FPA / Pyramid combination. The results are shown by the dotted black curve in Fig. 10. The difference between the solid and dotted lines at 1-2 frames cannot be fully explained by the variation between the individual curves. A possible explanation is that, in a single image, the lowest points are smeared out and therefore more difficult to locate exactly. However, when averaging over several images, such points will help stabilizing the ultrasound image plane and thus improving the probe calibration accuracy, as indicated by the asymptotic behaviour of the curves.

Assessment of the three calibration methods using different ultrasound probes

The results of applying the five quality measures on the 15 calibrations for each of the eight probe / method combinations can be seen in Table 5. The number of observations, mean, standard deviation, minimum, and maximum values are given for each quality measure. Results for all three probes are listed in the same table to ease the comparison between the probes.

As can be seen from the mean 3D NA measures the general tendency is that the Pyramid method is slightly better then the Diagonal method, while the Bead-method appears to be the least accurate calibration method. The asymptotic accuracies listed in Table 4 confirm these findings, and suggest further that the numbers in Table 5 may be somewhat improved by using more input data for the calibration. Table 6 presents the results of an analysis-of-variance (ANOVA) calculation on the 3D NA numbers of Table 5. We find significant differences between the three calibration methods for all cases except between the Diagonal and Pyramid methods applied to the FPA probe.

In Fig. 11 each of the 15 calibrations has been evaluated on the upper, middle, and lower wire layers of the evaluation volumes. This is done for each of the eight probe /

calibration method combinations. In some cases, we observe large variation between the layers, and this may be due to smearing, in particular of the lowest evaluation points (typically seen for the FLA/Diagonal and the FLA/Pyramid combinations; cf. Fig. 8B). The extreme values of calibrations 2 and 6 for the ILA/Pyramid combination are obviously caused by erroneous detection of evaluation points in the middle wire layer (the lowest layer attainable for this probe). The variation between calibrations can be seen directly when the layer variation is small. An example is the FPA/Pyramid combination, which indicates that more than three frames should be used in each calibration (cf. Fig. 10).

By allowing for translation and rotation of the reconstructed volume, the 3D RA acts as a lower limit to the 3D NA. From Table 5 we can see that the 3D RA is around 0.5 mm for all probes and methods. Consequently, one might conclude that the potential is greatest for improving the probe / method combinations with the largest 3D NA numbers. However, it should be noted that the 3D RA numbers are not based on matching the same number of points for the different probes as only the wire crosses contained in a single evaluation volume are matched.

The 3D DRA for the FPA probe is 0.15, 0.10 and 0.16 mm for the Bead, Diagonal and Pyramid methods, respectively. Analyzing the directional dependency of these numbers, we find considerable discrepancies in the lateral image direction (around 0.5 mm for all three methods), and very small contributions in the other two directions (0.05 mm for Bead and Diagonal, 0.02 mm for Pyramid). For the ILA probe, the lateral direction discrepancy could not be calculated; otherwise this probe shows the same trends. Again the smearing effect is assumed to be the reason, in combination with an automatic evaluation algorithm that may not be optimal for all wire crosses in the evaluation volume. For the FLA, the 3D DRA is larger, and shows less directional dependency.

The mean CR values are smallest for the Diagonal method. This is probably because this method constrains the images to be quite similar if they are properly aligned with the phantom. The Bead and Pyramid methods show very similar CR values.

The PRA is around 0.8 mm for the FPA and FLA probes when the Bead and Diagonal methods are used. The Pyramid method performance is worse, especially for the FPA-probe. This might be explained by the deep localization of the lower N structures, and hence the increased smearing here. The ILA / Bead performance is also relatively poor. The results shown in Table 5 are based on using the whole calibration pool for PRA evaluation. Using the two subsets described above gave almost the same results.

Manual versus automatic point identification of calibration data

We evaluated the automatic point identification method versus manual point identification for three calibrations of the FPA probe using the Pyramid phantom. The three calibrations were chosen based on the 3D NA performance shown in Fig. 11, and comprised an "average" case (calibration #2), a "good" case (#7), and a "poor" case (#10). The images used for these calibrations were presented to four skilled operators, who independently identified the calibration points manually. We thus obtained four manual matrixes and one automatic matrix for each calibration case, i.e. a total of 15 matrixes (twelve manual and three automatic). All matrixes were evaluated by two of the measures described earlier: calibration repeatability (CR), and 3D navigation accuracy (3D NA).

Fig. 12A shows CR between all combinations of the 15 matrixes. The result diagram is by definition symmetric and has zeros on the main diagonal. Each group of 5x5 numbers located on the main diagonal compares calibrations that differ only by the way the image points were identified. For all three data sets, these numbers indicate good consistency between the four manual sets, and also fairly good agreement with the automatic method. The groups of 5x5 numbers away from the main diagonal compare calibrations performed with different images as input. For these cases, CR is somewhat increased, thus indicating that the effect of identifying image points automatically or manually is less significant than the choice of input images for the calibration.

Fig. 12B shows the 3D NA for each of the 15 matrixes. Each matrix was used to scan convert the two evaluation data sets, and the results are averaged over all wire crosses and both evaluation volumes. The results indicate that the variations between manual operators are rather small, also for different sets of input images, whereas the automatic method gives larger variations. The reason may be that the operators detected all points, whereas the automatic method may have missed some of the deepest situated points.

DISCUSSION

Pool of calibration data

The protocol used to evaluate the different calibration methods in this study was a compromise between what ideally could be done and what was practically possible. We are confident that the result presented gives a valid picture of what could be shown with a more extensive protocol. Ideally, the acquisition protocol should be organized into pre-defined catergories like translation, rotation, and relative position between tracking system, phantom, and probe. This would enable us to select (by random drawing within each category) an input data set for each calibration, that was balanced with respect to these categories. For practical reasons, we had to lump the input data together and draw randomly from the entire pool without knowledge of the acquisition conditions of each image. A consequence is that different calibrations may be "biased" with respect to the categories, in particular when few frames are used, and this may increase the variation between the calibrations. This can probably be observed when we use just a few frames in Fig. 10, as well as in Fig. 11. The results indicate that more frames should be used in the calculations of the 15 calibrations for each of the eight probe / method combinations, both in terms of stability and accuracy, especially for the Pyramid method. On the other hand, our protocol might cause the same frame to be used in different calibrations, and this will have the opposite effect of reducing the variation between calibrations.

The acquisition for the Pyramid method is not based on aligning the scan-plane with some phantom-structure and can therefore be used to generate large amounts of calibration data. We used approximately the same amount of data for each method in order to allow for comparison. Acquiring more data for the Bead and Diagonal methods would be very time-consuming as three probes were used. Furthermore, we acquired individual frames for the Pyramid method in order to make sure that we explored the necessary degrees of freedom. Acquisition of a sequence of frames by intelligent freehand movement of the probe is possible, but this would require an algorithm that extracts the 10 % or so of the frames that were significantly different.

Also, more evaluation scans could be used in the 3D evaluation. This would have a profound impact on the workload as each calibration matrix is used to reconstruct each of the evaluation scans. As most of the needed processing steps are automated this would mainly require additional CPU hours (approximately 800 evaluation volumes are processed in the present study). However, as long as we know that two different evaluation scans that are acquired, reconstructed and processed the same way essentially gives the same results (Lindseth et al. 2002a), we only need a small number of 3D freehand scans.

Automatic algorithm

The automatic algorithms for point detection are designed to be robust with respect to acquisition procedures and image noise, and as far as possible independent of the actual probe. The high percentage of successful detections (Table 2) and the correspondence between evaluation results when using manual (average 0.7 mm; Fig. 12) and automatic point detection (average 0.8 mm; Fig. 11) indicate that the algorithms work as intended.

For the Bead method, we verified that the bead center is represented by the peak's centroid in the image, by stretching a surgical thread (diameter approximately 0.2 mm) through the ultrasound plane. The image of this thread was a well-defined spot. By using the thread as a marker in the vicinity of the bead, we observed that the physical extension of the bead coincided well with the image. For the Diagonal and Pyramid phantoms the concern should be even lower, because the wires have smaller dimensions and are more transparent to ultrasound than the bead.

For the Pyramid method the image geometry may not correspond exactly to the ideal geometry. In a typical experimental set-up, tilting or rotation of the probe may cause the distances between physical structures to increase by up to 4% in the images. This is accounted for by using a search region of some finite extent at the potential neighbour locations. The ideal geometry cannot be stretched accordingly, as this would require knowledge of the position tagging of the image, which is unavailable at this processing step. Image distortion due to uncertainty in sound velocity is assumed to be negligible compared to the effects of probe tilting.

Evaluation of probe calibration methods

Of the five quality measures discussed in this report, we consider the 3D NA to be the most important, because it measures the effect of probe calibration on reconstruction and navigation accuracy. A favourable 3D NA score implies that the internal geometric properties (3D DRA and 3D RA) of the reconstructed volume are accurate, and that the volume is correctly positioned in space. The ANOVA results (Table 6) show that the Pyramid method is the best method with respect to 3D NA. Only for the FPA probe, the Diagonal method is comparable to the Pyramid method. However, the asymptotic accuracy (Table 4) confirms that the Pyramid method performs best.

The reproducibility of a probe calibration method may also be an important feature. Considering the CR column of Table 5, it appears that the Diagonal method should be preferred. The good reproducibility for this method is probably a direct consequence of the strict alignment procedure.

Comparison with result presented by other groups

The performance of the calibration methods presented in this study compares favourably with equivalent measures reported previously in other studies of calibration techniques for freehand 3D ultrasound (Blackall et al. 2000; Prager et al. 1998). Quality measures for probe calibration based on reconstructed ultrasound volumes have not been reported earlier. 3D NA and 3D DRA are the volume equivalents to the more common image measures point (PRA) and the distance (DRA) reconstruction accuracy defined by Blackall (Blackall et al. 2000). Even though the measures are not directly comparable as a result of this, the numbers are similar, especially when considering the subset results for the 3D DRA measure. However, comparing values with other groups should be done with caution. The measured performance will depend on the scanning protocol, the type of tracking system, the quality of the ultrasound equipment and the amount of data used in a calibration.

CONCLUSION

We have developed two new methods for probe calibration. The Diagonal method is alignment-based while the Pyramid method is a freehand method. In addition, we have implemented a traditional alignment-based Bead method for comparison. We have further developed a novel algorithms for robust and automatic identification of image points. For evaluation we used a new method that extracts features from reconstructed 3D volumes, in addition to more traditional quality measures. The calibration methods were applied to three different ultrasound probes. We have investigated calibration accuracy as a function of the amount of input data used to calculate the calibration matrixes.

The results, quantified in terms of 3D Navigation Accuracy, showed that the Pyramid method performed slightly better than the Diagonal method and considerably better than the Bead method. In particular, the Pyramid method was superior to the other two methods with respect to the asymptotic accuracy, where the probe calibration is based on all available input data. Being both freehand and automatic, the Pyramid method is ideally suited for handling such large data sets.

The asymptotic accuracy for one of the probes was 0.62 mm and this indicates that sub-millimetre accuracy can be achieved in ultrasound-based surgical navigation.

ACKNOWLEDGEMENTS

This work was supported by grants from the Research Council of Norway through the Strategic University Program in Medical Technology at the Norwegian University of Science and Technology (NTNU), from the Strategic Institute Program at SINTEF Unimed, and from the Norwegian Ministry of Health and Social Affairs.

We wish to thank the Laboratory for Fine Mechanics at SINTEF Unimed, Trondheim, Norway, for making necessary equipment used in this study and also for providing indispensable measurements.

REFERENCES

Arun KS, Huang TS, and Blostein SD. Least-squares fitting of two 3-D point sets. IEEE Trans Pattern Anal Machine Intell, 1987;PAMI-9:698-700.

Barry CD, Allott CP, John NW, Mellor PM, Arundel PA, Thomson DS, and Waterton JC. Three-dimensional freehand ultrasound: image reconstruction and volume analysis. Ultrasound Med Biol, 1997;23:1209-1224.

Berg S, Torp H, Martens D, Steen E, Samstad S, Høivik I, and Olstad B. Dynamic three-dimensional freehand echocardiography using raw digital ultrasound data. Ultrasound Med Biol, 1999;25:745-753.

Blackall JM, Rueckert D, Maurer CRJ, Penney GP, Hill DLG, and Hawkes DJ. An Image Registration Approch to Automated Calibration for Freehand 3D Ultrasound. MICCAI 2000, Springer, 2000:462-471.

Bouchet LG, Meeks SL, Goodchild G, Bova FJ, Buatti JM, and Friedman WA. Calibration of three-dimensional ultrasound images for image-guided radiation therapy. Phys Med Biol, 2001;46:559-577.

Detmer PR, Bashein G, Hodges T, Beach KW, Filer EP, Burns DH, and Strandness DEJ. 3D ultrasonic image feature localization based on magnetic scanhead tracking: In vitro calibration and validation. Ultrasound Med Biol, 1994;20:923-936.

Duck FA. Physical properties of tissue. A comprehensive reference book. London, UK, Academic Press Ltd., 1990.

Gobbi DG, Comeau RM, Lee BKH, and Peters TM. Integration of intra-operative 3D ultrasound with pre-operative MRI for neurosurgical guidance. Proc 22nd Ann Int Conf IEEE Eng Med Biol Soc, Chicago, IL, USA, 2000;3:1738-1740.

Gobbi DG, Comeau RM, and Peters TM. Ultrasound Probe Tracking for Real-Time Ultrasound/MRI overlay and visualization of Brain Shift. Medical Image Computing and Computer Assisted Intervention - MICCAI'99, 1999:1679:1920-1927.

Gronningsaeter A, Kleven A, Ommedal S, Aarseth TE, Lie T, Lindseth F, Langø T, and Unsgård G. SonoWand, An ultrasound-based neuronavigation system. Neurosurgery, 2000;47:1373.

Hartov A, Eisner SD, Roberts DW, Paulsen KD, Platenik LA, and Miga MI. Error analysis for a free-hand three-dimensional ultrasound system for neuronavigation. Neurosurg Focus, 1999;6:Article 5 (12 pages).

Langø T. Ultrasound guided surgery : Image processing and navigation. Ph.D, Norwegian University of Science and Technology, Trondheim, 2000.

Legget ME, Leotta DF, Bolson EL, McDonald JA, Martin RW, Li X-N, Otto CM, and Sheehan FH. System for quantitative three-dimensional echocardiography of the left ventricle based on a magnetic-field position and orientation sensing system. IEEE Trans Biomed Eng, 1998;45:494-504.

Leotta DF, Detmer PR, Gilja OH, Jong J-M, Martin RW, Primozich JF, Beach KW, and Strandness EDJ. Three-dimensional ultrasound imaging using multiple magnetic tracking systems and miniature magnetic sensors. Proc IEEE Ultraso Symp, Seattle, WA, USA, 1995;2:1415-1418.

Leotta DF, Detmer PR, and Martin RW. Performance of a miniature magnetic position sensor for three-dimensional ultrasound imaging. Ultrasound Med Biol, 1997;23:597-609.

Lindseth F, Bang J, and Langø T. A robust and automatic method for evaluating the accuracy in 3D ultrasound-based navigation. Manuscript in review., 2002a

Lindseth F, Kaspersen JH, Ommedal S, Langø T, Unsgaard G, and Hernes TAN. Multimodal image fusion in ultrasound-based neuronavigation: Improving overview and interpretation by integrating preoperative MRI with intraoperative 3D ultrasound. Manuscript in review., 2002b.

Lindseth F, Langø T, Bang J, and Hernes TAN. Accuracy evaluation of a 3D ultrasound-based neuronavigation system. Manuscript in review., 2002c.

Liu J, Gao X, Zhang Z, Gao S, and Zhou J. A new calibration method in 3D ultrasonic imaging system. Proc 20th Ann Int Conf IEEE Eng Med Biol Soc, Hong Kong, China, 1998;2:839-841.

Muratore DM, and Galloway LJ. Beam calibration without a phantom for creating a 3-D freehand ultrasound system. Ultrasound Med Biol, 2001;27:1557-1566.

Pagoulatos N, Edwards WS, Haynor DR, and Kim Y. Calibration and validation of free-hand 3D ultrasound systems based on DC magnetic tracking. Proc SPIE Conf Image Display, Medical Imaging, San Diego, CA, USA, 1998;3335:59-71.

Pagoulatos N, Edwards WS, Haynor DR, and Kim Y. Interactive 3-D registration of ultrasound and magnetic resonance images based on a magnetic position sensor. IEEE Trans Inf Technol Biomed, 1999a;3:278-288.

Pagoulatos N, Haynor DR, and Kim Y. Fast calibration for 3D ultrasound imaging and multimodality image registration. Proc IEEE, 1st Joint BMES/EMBS Conference (Serving Humanity, Advancing Technology), Atlanta, GA, USA, 1999b;2:1065.

Pagoulatos N, Haynor DR, and Kim Y. A fast calibration method for 3-D tracking of ultrasound images using a spatial localizer. Ultrasound Med Biol, 2001;27:1219-1229.

Péria O, Chevalier L, François-Joubert A, Caravel J-P, Dalsoglio S, Lavallée S, and Cinquin P. Using a 3D position sensor for registration of SPECT and US images of the kidney. Proc Computer Vision, Virtual Reality Robotics Surgery, 1995:23-29.

Prager RW, Rohling RN, Gee AH, and Berman L. Automatic calibration for 3-D free-hand ultrasound. England, Cambridge University, Engeneering Department, 1997:1-27.

Prager RW, Rohling RN, Gee AH, and Berman L. Rapid calibration for 3-D freehand ultrasound. Ultrasound Med Biol, 1998;24:855-869.

Rohling RN, Gee AH, and Berman L. Automatic registration of 3-D ultrasound images. Ultrasound Med Biol, 1998;24:841-854.

Sato Y, Nakamoto M, Tamaki Y, Sasama T, Sakita I, Nakajima Y, Monden M, and Tamura S. Image guidance of breast cancer surgery using 3-D ultrasound images and augmented reality visualization. IEEE Trans Med Imaging, 1998;17:681-693.

State A, Chen DT, Tector T, Brandt A, Chen H, Ohbuchi R, Bajura M, and Fuchs M. Case study: Observing a volume rendered fetus within a pregnant patient. Proc IEEE Conf Visualization, Wahington, DC, USA, 1994;Oct 17-21:364-368.

Welch JN, Bax M, Mori K, Krummel T, Shahidi R, and Maurer CRJ. A fast and accurate method of ultrasound probe calibration for image-guided surgery. Proc 16th Int Congress Computer Aided Radiology and Surgery (CARS), Paris, France, Springer, 2002:1078.

Welch JN, Johnson JA, Bax M, Badr R, and Shahidi R. A real-time freehand 3D ultrasound system for image-guided surgery. Proc IEEE Ultraso Symp, San Juan, Puerto Rico, 2000;2:1601-1604.

		Calibration scans			3D evaluation scans
		Bead	Diagonal	Pyramid	
Probes	FPA	60 images	22 images	15 images	2 volumes
	FLA	64 images	24 images	18 images	4 volumes
	ILA	61 images	-	39 images	6 volumes

Table 1. Pool of ultrasound data used for calibration and evaluation.

		Bead	Diagonal	Pyramid
Probes	FPA	1 (100%)	7-9 (>91%)	9-12 (>85%)
	FLA	1 (100%)	5-6 (>99%)	5-7 (>96%)
	ILA	1 (100%)	-	3 (100 %)

Table 2. The number of automatically identified points in the images used for calibration. If two numbers are listed for any of the probe / method combinations, all points were not identified in all the calibration images. The numbers in parenthesis is the total percentage of identified points in all images. The percentage for the FPA/Pyramid combination was 100% for a new set of 20 images with reduced depth (lower three N structures not visible).

		Bead	Diagonal	Pyramid
Probes	FPA	15	3	3
	FLA	15	3	3
	ILA	15	-	6

Table 3. The number of images used for probe calibration for the different methods and probes. The ILA/Pyramid combination uses six images, as only three calibration points are covered by each image.

		Bead	Diagonal	Pyramid
Probes	FPA	0.90 mm	0.79 mm	0.62 mm
	FLA	1.43 mm	1.20 mm	0.92 mm
	ILA	1.75 mm	-	1.25 mm

Table 4. Asymptotic 3D navigation accuracy. All the calibration images given in Table 1 were used to calculate the calibration matrixes.

		3D NA			3D DRA			3D RA			CR			PRA		
		Bead	Diag	Pyra	Bead	Diag	Pyra	Bead	Diag	Pyra	Bead	Diag	Pyra	Bead	Diag	Pyra
FPA probe	# obs.	810	810	810	810	810	810	30	30	30	105	105	105	900	2715	2295
	Mean	1.00	0.84	0.81	0.15	0.10	0.16	0.48	0.48	0.43	0.63	0.38	0.55	0.79	0.86	1.52
	St.dev	0.39	0.36	0.43	0.30	0.30	0.33	0.16	0.07	0.06	0.39	0.17	0.29	0.39	0.46	1.35
	Min	0.38	0.07	0.07	-0.79	-1.04	-0.66	0.30	0.34	0.31	0.08	0.03	0.06	0.11	0.06	0.05
	Max	3.11	1.98	2.29	1.00	0.79	0.94	0.86	0.64	0.55	1.72	0.89	1.31	2.83	3.20	9.22
FLA probe	# obs.	810	810	810	810	810	810	60	60	60	105	105	105	960	2145	1830
	Mean	1.48	1.24	1.15	0.23	0.26	0.25	0.53	0.57	0.54	0.62	0.44	0.63	0.73	0.77	1.03
	St.dev	0.35	0.71	0.43	0.51	0.46	0.45	0.13	0.09	0.13	0.38	0.25	0.36	0.41	0.43	0.84
	Min	0.73	0.08	0.35	-2.91	-1.10	-1.53	0.28	0.35	0.31	0.03	0.05	0.08	0.06	0.05	0.03
	Max	3.27	3.99	3.90	2.02	2.02	1.83	0.79	0.71	0.87	1.61	1.30	1.46	2.44	3.01	5.50
ILA probe	# obs.	540		540	450		450	90		90	105		105	915		1755
	Mean	1.80		1.33	0.09		0.04	0.51		0.47	1.86		1.73	1.67		1.15
	St.dev	0.32		0.79	0.49		0.50	0.15		0.21	1.21		1.18	0.92		0.91
	Min	1.00		0.09	-1.56		-1.75	0.21		0.20	0.21		0.11	0.11		0.05
	Max	2.94		4.29	2.11		1.55	0.85		1.18	5.69		4.31	5.53		5.66

Table 5. Evaluation of the Bead, Diagonal, and Pyramid methods using five different quality measures: 3D Navigation Accuracy (3D NA); 3D Distance Reconstruction Accuracy (3D DRA); 3D Registration Accuracy (3D RA); Calibration Reproducibility (CR); and Point Reconstruction Accuracy (PRA). The results are based on 15 calibrations, each containing the number of images given in Table 3. Except for the number of observations, the listed numbers are given in millimeters. The mean 3D NA measures are shaded as these are considered to be the most important figures. The results for the three probes used in the evaluation are listed in the same table to ease the comparison.

	p Bead - Diagonal	p Bead - Pyra	p Diagonal - Pyra	p Bead – Diagonal - Pyra
FPA probe	< 0.01	< 0.01	0.22	< 0.01
FLA probe	< 0.01	< 0.01	< 0.01	< 0.01
ILA probe	-	< 0.01	-	-

Table 6. Comparison of probe calibration methods by a analysis-of-variance (ANOVA). Each group contains 810, 810, and 540 observations, respectively. Further statistics (mean and standard deviation) are given in Table 5.

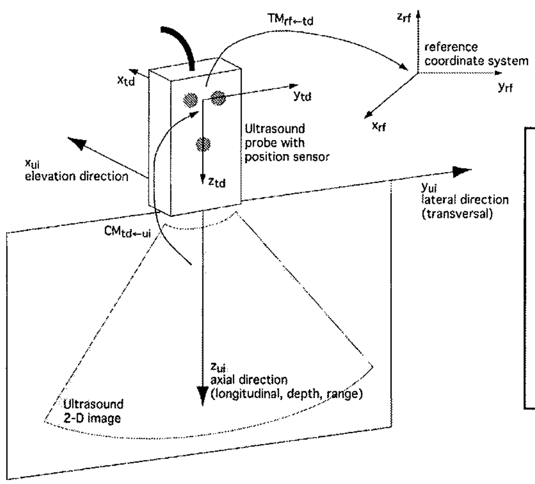

Fig. 1. The various coordinate systems involved in probe calibration. The probe calibration matrix is given by $CM_{td \leftarrow ui}$, while $TM_{rf \leftarrow td}$ signifies the tracking device measurements. Index *ui* represents the ultrasound image, *td* is the tracking device coordinate system, and *rf* is the reference system (often denoted world coordinate system in the literature).

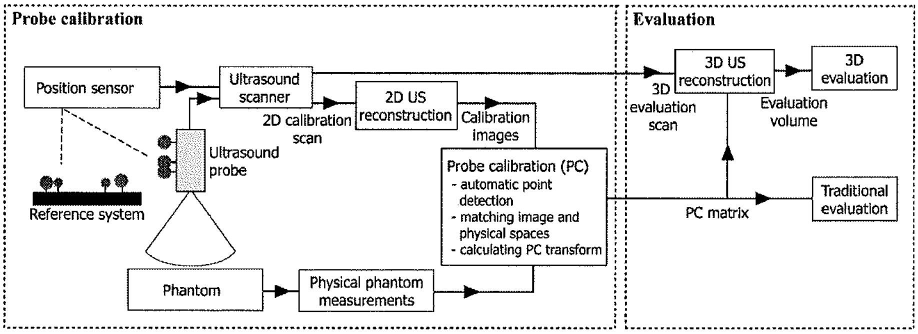

Fig. 2. Experimental setup and dataflow. Ultrasound data were tagged with position and orientation during acquisition. Both 2D calibration data and 3D evaluation data were acquired. Calibration images were matched with the physical phantom measurements in order to generate probe calibration matrixes. The calibration matrixes were then used to reconstruct the ultrasound volumes used in the 3D evaluation.

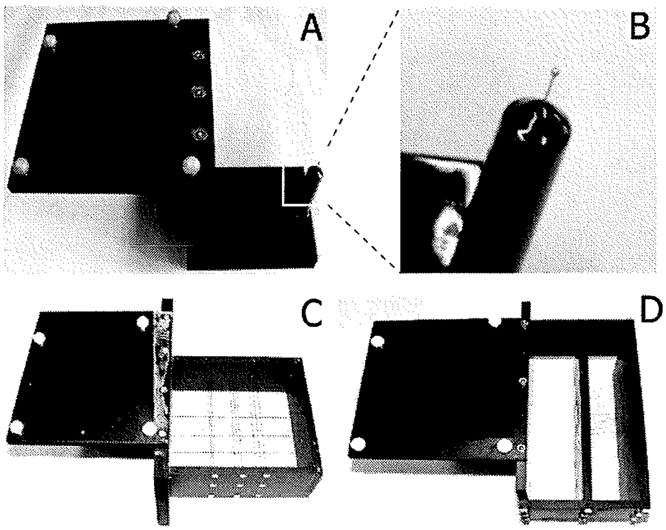

Fig. 3. The three phantoms used for acquiring probe calibration data in this study: the Bead phantom (A), the Diagonal phantom (C), and the Pyramid phantom (D). B) shows a close-up of the Bead phantom. Scans of the Diagonal phantom were also used for volume evaluation of the resulting probe calibration matrixes.

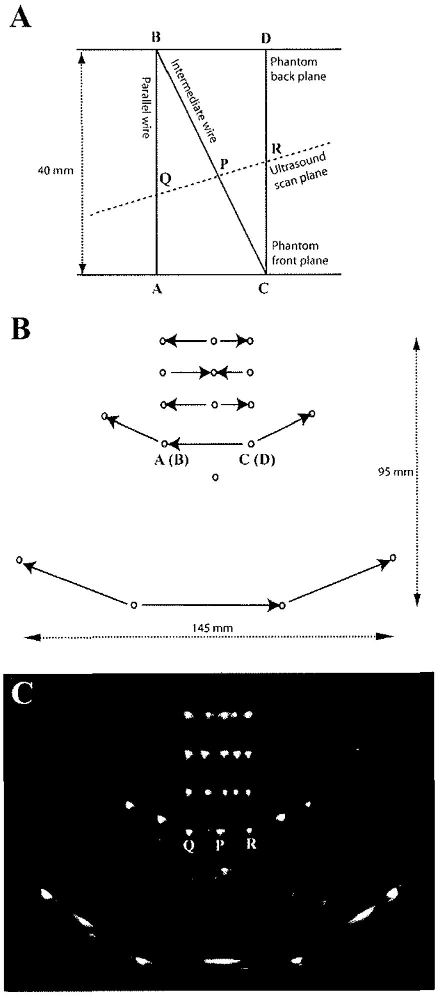

Fig. 4. Wire configuration of the Pyramid phantom. A) Top view of the phantom showing one N structure that consists of three wires. The ultrasound scan plane will intercept these wires in the points P, Q, and R. B) Front view of the phantom showing the twelve N structures. The circles represent holes in the phantom walls. One N structure is indicated with the parallel wires at points A (B) and C (D). The intermediate wires are represented by arrows, which point from the phantom's front wall to the back wall. C) An image of the Pyramid phantom using the FPA probe, with points P, Q, and R indicated, corresponding to figure A). From each of the twelve N structures the points P are extracted and used in the probe calibration.

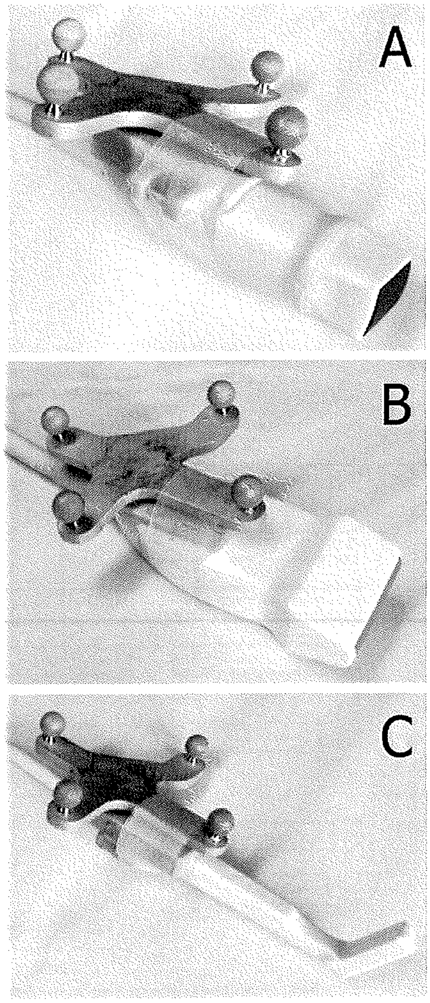

Fig. 5. The three ultrasound probes used in the study with optical tracking device attached. A) 5MHz Flat Phased Array (FPA), B) 10 MHz Flat Linear Array (FLA). C) 10 MHz Intraoperative Linear Array (ILA).

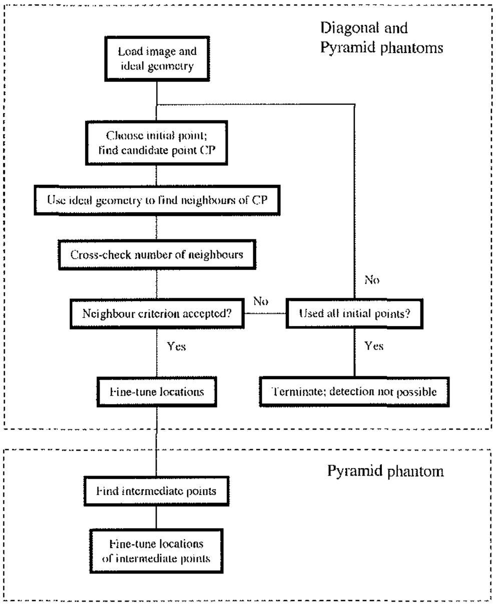

Fig. 6. Overall flowchart for automatic detection and identification of point sets in the ultrasound images that were used for calibration.

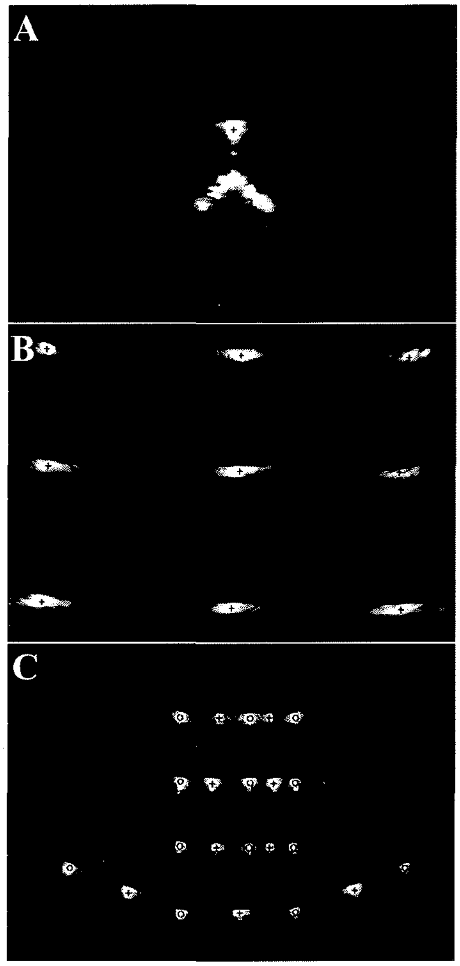

Fig. 7. Examples of ultrasound images from the FPA probe, with automatic point identification results overlaid. A) The Bead phantom (detection marked by +). B) The Diagonal phantom (detections marked by +). C) The Pyramid phantom (parallel wires marked by o, intermediate wires by +). The lowest N structures are outside the image due to zooming.

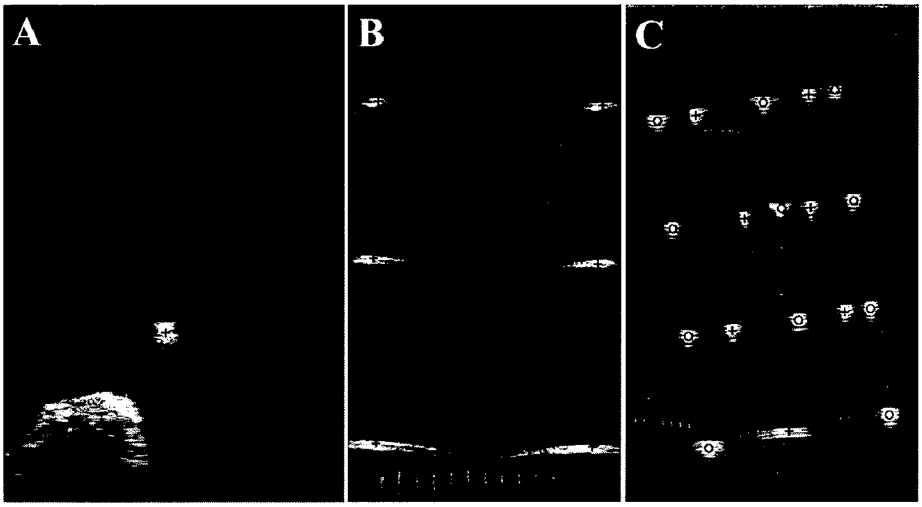

Fig. 8. Examples of ultrasound images from the FLA probe, with automatic point identification results overlaid. A) The Bead phantom (detection marked by +). B) The Diagonal phantom (detections marked by +). C) The Pyramid phantom (parallel wires marked by o, intermediate wires by +). B) and C) show the entire image that could be obtained with this probe.

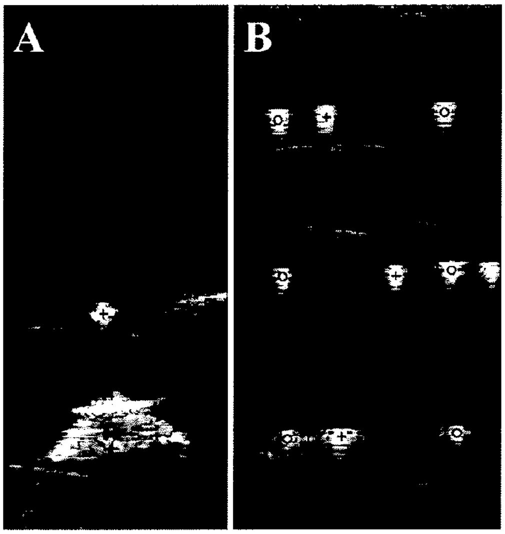

Fig. 9. Examples of ultrasound images from the ILA probe, with automatic point identification results overlaid. A) The Bead phantom (detection marked by +). B) The Pyramid phantom (parallel wires marked by o, intermediate wires by +). B) shows the entire image that could be obtained with this probe. The Diagonal method could not be applied due to the small footprint of the ILA probe.

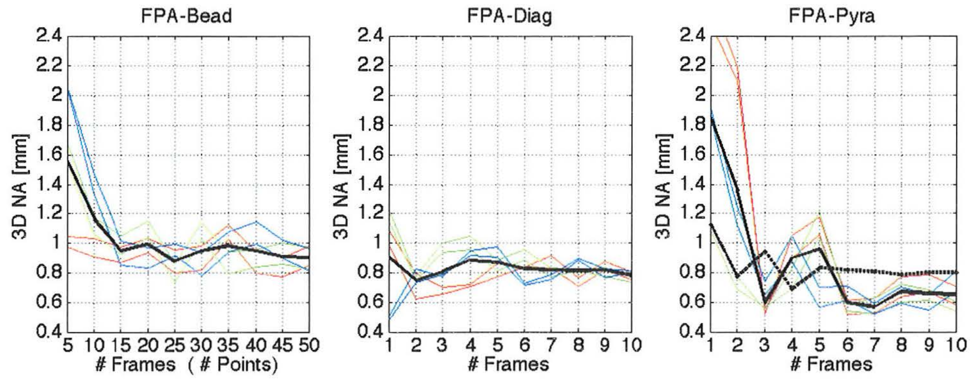

Fig. 10. 3D Navigation Accuracy (3D NA) as a function of the number of frames (images) used in the calibration for each of the three methods using the FPA probe. For a given number of images used as input three calibrations were calculated (red, green and blue curves) and each of these were used to reconstruct the two evaluation scans for the FPA probe (two curves for each color). The solid black curve represents the mean of all six curves. The dotted black curve for the Pyramid method shows the effect of reducing the depth for the FPA probe so that the calibration images did not cover the lower three N structures (i.e., the calibration images looked like Fig. 7C instead of Fig. 4C).

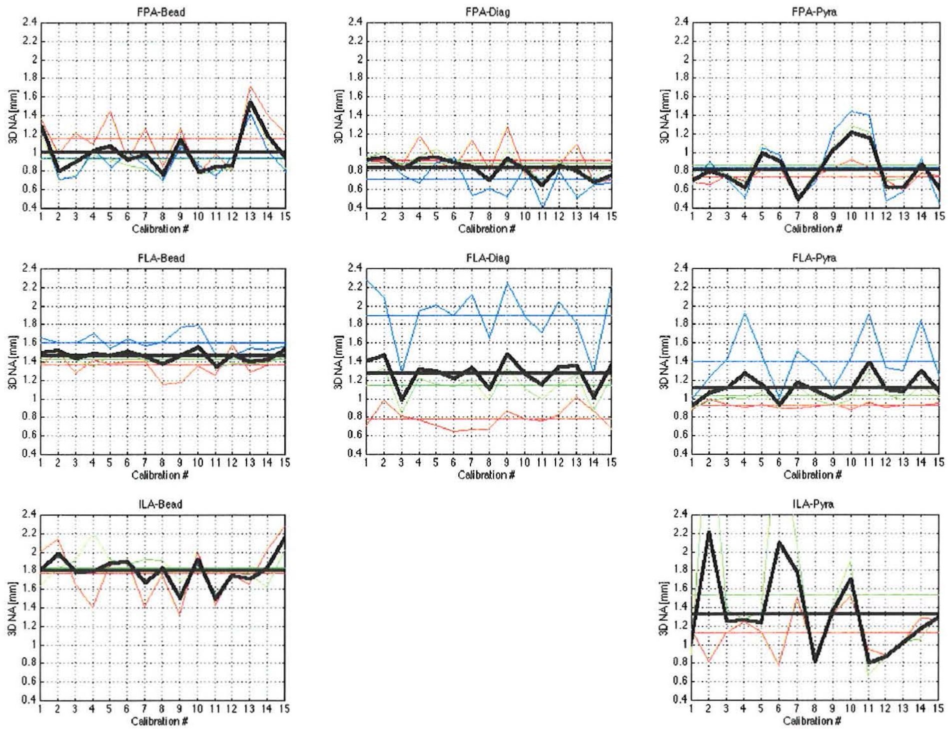

Fig. 11. 3D Navigation Accuracy (3D NA) as a function of calibration number for each of the eight probe / method combinations that were evaluated. The red, green and blue curves represent evaluation of the upper-layer, middle-layer and lower-layer subsets, respectively. The black curve represents all three layers, and the horizontal lines represent the mean over all 15 calibrations for the respective curves. The calibrations for the different probes are used to reconstruct all the evaluation scans available for the actual probe (Table 1).

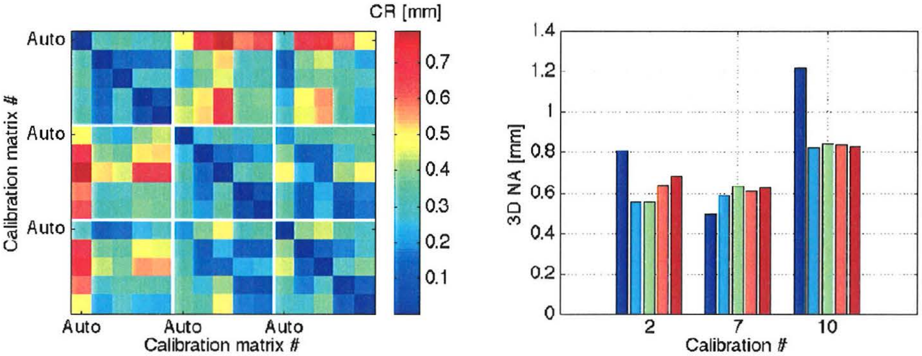

Fig. 12. Evaluation of manual versus automatic identification of image points. The analysis is done for the FPA/Pyramid combination. A) CR values (colour coded) between all combinations of 15 calibration matrixes. The first five matrixes are based on one calibration data set (#2 in Fig. 11), the next five on another set (#7), and the last five on a third set (#10). Within each group of five, the first matrix was generated by automatic point identification, as indicated in the diagram. B) 3D NA evaluation of the 15 calibration matrixes. The matrixes are arranged in the same order as in figure A (calibration data sets #2, #7, and #10; the first within each group is generated by automatic point identification).

Paper V

A ROBUST AND AUTOMATIC METHOD FOR EVALUATING THE ACCURACY IN 3D ULTRASOUND-BASED NAVIGATION

Authors:
Frank Lindseth[1,2], Jon Bang[1], Thomas Langø[1]

Affiliation:
[1]SINTEF Unimed, Ultrasound, Trondheim, Norway
[2]The Norwegian University of Science and Technology, Department of Computer and Information Science, Trondheim, Norway

Abstract

We present a robust and automatic method for evaluating the 3D navigation accuracy in ultrasound-based image-guided systems. The method is based on a precisely built and accurately measured wire phantom and an automatic 3D template matching by correlation algorithm. We investigate the accuracy and robustness of the algorithm and also address optimization of algorithm parameters. Finally, we apply the method to an extensive data set from an in-house ultrasound-based navigation system. To evaluate the method, eight skilled observers identified the same crosses manually, and the average over all observers constitute our reference data set. We found no significant differences between the automatic and the manual method, and the average distance between the point sets for one particular volume (27 point pairs) was 0.27±0.17 mm. Furthermore, the spread of the automatically determined points compared to the reference set was lower than the spread for any individual operator. This indicates that the automatic algorithm is more accurate than manual determination of the wire-cross locations, in addition to being faster and non-subjective. In the application example we used a set of 35 3D ultrasound scans of the phantom under various acquisition configurations. The accuracy, represented by the mean distance between automatically determined wire-cross locations and physically measured locations, was found to be 1.34±0.62 mm.

Key Words: 3D ultrasound imaging, navigation, accuracy, phantom study, template matching, correlation

INTRODUCTION

In image guided surgery, established imaging techniques like conventional magnetic resonance imaging (MRI) and computer tomography (CT) provide high quality 3D data for surgical planning and overview of the patient's anatomy during the operation. However, significant anatomical changes may occur during the operation. E.g. in neurosurgery, the brain shift may be of the order of 1-6 mm even before starting the surgical resection (Hill et al. 1998), and up to a few centimeters during the course of the operation (Nimsky et al. 2000; Roberts et al. 1998). Alternative approaches like intraoperative MRI have been developed for detecting and monitoring such changes as surgery proceeds (Hadani et al. 2001; Nimsky et al. 2001; Tronnier et al. 1997; Wirtz et al. 1997). However, this is a costly and time-consuming option, which may have considerable impact on the workflow of many standard operation procedures.

Intraoperative ultrasound offers real-time capabilities at relatively low cost, and with relatively small impact on established operation routines. Furthermore, the image quality is now satisfactory for navigation purposes (Gronningsaeter et al. 2000). For these reasons, we see an increased application of ultrasound imaging during surgical interventions, either used for morphing or warping preoperative MRI or CT data (Bucholz et al. 1997; Comeau et al. 2000), or as an independent monitoring option (Gronningsaeter et al. 2000; Hartov et al. 1999). Real-time 2D imaging and repetitive 3D scans will probably be dominating features in first generation ultrasound-based navigation systems, while real-time 3D imaging may be available in second and third generation systems (Fenster and Downey 1996; Nelson and Pretorius 1998).

The delicacy, precision, and extent of the work the surgeon can perform based on image information, rely on his/her confidence in the overall clinical accuracy and the anatomical or pathological representation. The overall clinical accuracy in image-guided surgery is the difference between where a surgical tool is located relative to some structure as indicated in the image information presented to the surgeon and where the tool is actually located relative to the same structure in the patient. This accuracy is difficult to assess in a clinical setting, due to the lack of fixed and well-defined landmarks inside the patient that can be reached accurately by a pointer. Common practice is therefore to estimate the system's overall accuracy in a controlled laboratory setting using precisely built phantoms (Cartellieri et al. 2001; Dorward et al. 1999; Hartov et al. 1999). In order to conclude on the potential clinical accuracy, the differences between the clinical and the laboratory settings must be carefully examined.

To assess the accuracy of an ultrasound-based navigation system, a precisely built phantom designed for ultrasound scanning may be used. Physical positions of structures/points inside the phantom can be accurately measured and compared to the corresponding positions in image space (determined from a 3D ultrasound volume). However, there is no definite way of identifying such points in image space. A commonly used technique is manual marking, which for example is applied in patient-to-image registration (Helm and Eckel 1998; Maurer et al. 1997; Sipos et al. 1996; Villalobos and Germano 1999). However, manual marking is tedious and often requires a skilled operator. Advantages of an automated procedure are rapid execution so that an extensive evaluation can be performed, and avoidance of subjective influence upon the results.

Template matching by correlation is a well-established technique (Atallah 2001; Didon and Langevin 1995; Prasad and Iyengar 1995; Remagnino et al. 1994), but we have found few publications that apply this technique on 3D medical data, or in particular on 3D ultrasound data. Examples of correlation of preprocessed multimodal data sets are CT-to-MR registration (Van den Elsen et al. 1995) and ultrasound-to-MR registration (Porter et al.

2001). Furthermore, 3D correlation has been used for registration of several preprocessed ultrasound volumes to each other, in order to reduce the noise by averaging (Rohling et al. 1998).

We have developed a robust and automatic method for evaluating the accuracy in 3D ultrasound-based navigation. The paper presents the method and an evaluation of the accuracy and the robustness of the algorithm. This is done by comparing its results to a reference data set created by manual picking (average of several skilled operators' individual opinion). Furthermore, the algorithm applies a set of parameters, and we evaluate the sensitivity of the correlation result to variations in these parameters and determine the optimal parameter setting. Finally, we demonstrate the method's application to quantification of the accuracy in 3D ultrasound-based navigation using an extensive data set acquired with our in-house navigation system tailored for vascular and laparoscopic surgery.

MATERIALS AND METHODS

Experimental set-up and data acquisition

An overview of the measurement set-up and data flow is shown in Fig. 1. Within the reconstructed ultrasound volume, the automatic algorithm determines the points *AIP* (Automatic Image Points). The physically measured points are termed *MP* (Measured Points), while we use the symbol *MIP* (Manual Image Points) for the wire cross points manually picked by the observers. In the accuracy evaluation we compare *AIP* to *MIP* to assess the accuracy of the algorithm, and *AIP* to *MP* to determine the accuracy of the 3D ultrasound navigation system as an application example.

The ultrasound volumes studied in this article were acquired by scanning a precisely built wire phantom. A photo of the phantom with overlaid axis is shown in Fig. 2. The phantom is made of aluminum, and has four infrared-reflecting spheres mounted as reference for the camera positioning system. 18 polyester wires with diameter 0.3 mm are mounted inside the phantom, with spring loadings to keep the wires straight. The wires are parallel to either the reference frame's *X*- or *Y*-axes. They form 27 wire crosses in a cubic pattern with vertical separation 0.5 mm between the wire center axes at each cross. All wire crosses lie within a volume with dimensions 5^3 cm^3. The positions of all wire crosses have been physically measured relative to the reference frame, with an accuracy of 0.1 mm in all directions.

The wire phantom was submerged in water and scanned using a 4-8 MHz phased array ultrasound probe with an attached position sensor. The probe was mounted in a rigid holder to ensure overall stability; however, the scanning motion was done manually. Scans were performed parallel to the phantom's *X*- and *Y*-axis, and diagonally. Both translation scans and tilts were performed for each direction. A total of 36 scans were performed for the application test (Table 1).

An optical tracking system (Polaris, Northern Digital Inc., Ontario, Canada) monitored the positions of the phantom and the probe from a distance of ~1.8 m, and an elevation of 45° above the horizontal plane (optimal conditions for the camera system with respect to the experiment design). The phantom and the probe were oriented such that all scans were made directly towards or away from the cameras.

High image quality was assured by using digital data (not video-grabbing) from a digital ultrasound scanner (System FiVe, GE Vingmed Ultrasound, Horten, Norway). Images were tagged with position data in the scanner and transferred to a computer, where the 3D ultrasound volume was reconstructed. Scanner settings like frequency, depth, sector width, and frames per second were tuned to achieve a satisfactory view on the scanner monitor of the wires in the water bath. We reconstructed all volumes with 0.65^3 mm^3 sized voxels. This resulted in volumes having sizes from 7 to 32 megabytes depending mainly on acquisition time, scan distance, and whether the acquisition was done by tilting or translating the probe. The wire crosses identified in the image volumes can be positioned in the same coordinate system as the physical wire crosses since both were measured relative to the reference frame attached to the phantom.

Important parameters in the reconstruction process are: probe calibration to determine the position of the image relative to the position sensor attached to the probe; synchronization of position and image data; the speed of sound in water used in the scan conversion; and the desired output resolution measured in millimeter per voxel. The effects of resolution and speed of sound are addressed in this paper.

For the evaluation of the automatic method, we shall mainly consider two scanned volumes: one translation scan diagonally across the phantom (volume #15), and one tilt scan parallel to the *Y*-axis (volume #33). Volume #15 is chosen since the ultrasound imaging of the wires is generally good and homogeneous throughout the entire volume, thus yielding a volume of high quality for visual determination of the wire crosses. Sample images of volume #15 are shown in Fig. 3. In volume #33, the varying angle and the long distance from the probe to the farthest wires make the reconstructed volume less homogeneous and thus more difficult to interpret visually. It is therefore expected to be more challenging for the automatic algorithm as well. All volumes are considered in the application test section of this paper for a quantification of our in-house ultrasound-based navigation system.

We know of no 'gold standard' procedure for establishing the 'true' positions of the wire crosses in the images. The physically measured coordinates cannot be used as reference when evaluating the automatic method as such, since any discrepancy might include irrelevant effects due to the volume acquisition and reconstruction procedures. We have therefore chosen to use as reference the average of wire cross coordinates identified manually in the ultrasound volumes by several skilled observers. This procedure is reasonable also from a clinical point of view, as the surgeon's confidence in the system is based on visual interpretation of the ultrasound images. The manual procedure comprised projecting three orthogonal cross-sectional images (like Fig. 3) from the volume onto the screen. The operator was then free to move each image plane through the volume, and zoom in or out, in order to determine the 'optimal' location of each wire cross by visual judgment. Although the image planes could only be presented in steps corresponding to the volume's voxel resolution, the operator's decision on the wire cross location was done with 0.1 voxel resolution. The images and overlaid lines were updated continuously, in response to the operator searching for the 'optimal' wire cross location.

Eight skilled observers performed the manual procedure individually. The identification and selection of all 27 wire crosses in one volume typically had a duration of 45 minutes. The eight sets of 27 locations were then averaged, resulting in the reference set of manually determined image points (MIP_p, $p \in [1,27]$).

Automatic algorithm

We use a standard correlation technique to match an ultrasound subvolume containing a wire cross to a synthetic template. The choice of this technique was guided by several factors. Firstly, the wires are well aligned with the coordinate system used in both subvolumes. Hence, rotation and skewness will not represent significant problems over typical subvolume dimensions, unless probe calibration is an important error source, which we consider is not the case here. Secondly, the structure irregularities typically seen in reconstructed ultrasound volumes forced us to choose a method utilizing all available information in the ultrasound subvolume simultaneously, rather than a method working locally inside the subvolume. Thirdly, fast execution turned out to be essential, due to the application to data sets containing up to 5000 points (Lindseth et al. 2002). This requirement led us to reject iterative methods, and also to choose the Fourier implementation of the correlation method (see below).

The ultrasound subvolume was chosen with equal dimensions (number of voxels) in all directions, and it will therefore be referred to as the ultrasound cube (*UC*). This cube is extracted around an initial point in the reconstructed ultrasound volume. *UC* should contain only one wire cross with both wires clearly visible in order to conclude that the right correlation point is found. As initial location of UC we used the physically measured points (MP_p) transformed into the ultrasound volume's coordinate system.

A synthetic template cube *TC* of the same size as UC is then generated. The intention is that the synthetic description should resemble the ultrasound image of the wires, not the physical wires themselves. Inside TC, each wire is modeled as a cylindrical object, as depicted in Fig. 4(a). The intensity is assumed to decrease gradually in the wire's radial direction according to a predefined profile, and to be constant along the wire's axis. The cross-sectional profile (equi-intensity curve) is in general elliptic, reflecting the ultrasound field's radial and lateral resolution. The location and width of the wire may be varied as discussed in the following. Two such cylindrical structures, with axes parallel to the *X*- and *Y*-axes respectively, are finally superimposed to give the actual template cube.

The 3D correlation procedure determines the displacement in *X*-, *Y*-, and *Z*-directions of *TC* with respect to *UC*. With *i, j,* and *k* being the coordinates of a general voxel, the correlation is defined by

$$\Gamma_{UC-TC}(m,n,r) = \sum_{i,j,k} UC(i,j,k)TC(i-m, j-n, k-r) \tag{1}$$

for a particular displacement *m,n,r* of *TC*. The displacement for optimal correlation is thus the *m,n,r* triplet where the maximum of Γ_{UC-TC} is found. This triplet can then be converted into the physical (millimeter scale) displacement using the predefined voxel size. The set of wire cross locations found in this way by the automatic algorithm is denoted AIP_p, $p \in [1,27]$.

For large *UC* and *TC* the calculation of Γ_{USC-TC} using (1) is rather time consuming. We therefore implemented the correlation via its Fourier space equivalent

$$\Gamma_{UC-TC} = FFT_{3D}^{-1}\{FFT_{3D}\{UC\} \cdot (FFT_{3D}\{TC\})^*\} \tag{2}$$

where $FFT_{3D}\{...\}$ is the 3D fast Fourier transformation operator, $FFT_{3D}^{-1}\{...\}$ is the inverse transform, and $(\ldots)^*$ denotes complex conjugation. The Fourier space implementation in (2) works most efficiently when the dimensions of the cubes are 2^n with integer n. Computer memory limitations restrict us to use cube sizes up to 64^3 voxels (after zero padding). In some cases, smaller sizes must be used to ensure that only one wire cross lies within *UC*. This restriction may be set automatically, based on the actual voxel size and the wire separation in the phantom. The effect of the cube size on the accuracy of the algorithm will be addressed in this article.

To improve the accuracy in the determined displacement, we did an interpolation in the resulting correlation volume Γ_{UC-TC}. The interpolation is done hierarchically, to a resolution of 0.5/0.25/0.125 voxels and so on. The accompanying increase in computation time puts a practical limit to the achievable resolution. The subvoxel resolution on m, n, and p has been fixed to 0.25 voxels in the work presented here.

We assume that the synthetic model of the wire cross is sufficiently similar to the ultrasound data to give reliable correlation results. However, the details of the synthetic description may affect the overall performance of the algorithm. We investigate this by varying a number of template parameters:

The 1D intensity profile: Gaussian or rectangular (see Fig. 4(b))
The wire width: fixed or derived from the ultrasound data
The vertical separation between the two wires

Table 2 lists the template cube's parameter ranges investigated in this study. For the 'fixed' option, all combinations of horizontal wire width, vertical wire width, and wire separation were run. Note that the horizontal widths and the vertical heights of the two wires are the same to keep the number of parameter combinations at a reasonable level. This gives a test structure, and a result set, of size $12 \cdot 6 \cdot 7 = 504$ for the 'fixed Gaussian' option and $20 \cdot 10 \cdot 4 = 800$ for the 'fixed rectangular'. For each of these cases, we ran the automatic algorithm with a cube size of both 32^3 voxels and 64^3 voxels.

As shown in Fig. 4(b), the wire width ΔX (ΔY, ΔZ) equals the exact width of the rectangular profile, and the 2σ-width of the Gaussian profile. The tails of the Gaussian thus makes it effectively broader than ΔX, and this explains the difference in selected parameter ranges in Table 2. Furthermore, the width and separation parameters are given in voxels, since this is the unit used by the correlation algorithm. For user-friendliness, these parameters might have been specified in millimeters; however, the fundamental restriction on cube size ($=2^n$) is specified in voxels, and the distinction becomes important only when comparing volumes of different resolutions (*RESULTS AND INTERPRETATION; Effect of varying resolution*).

We have also investigated an adaptive algorithm for generation of the template cube. In this case, the synthetic wire width and separation are derived from the ultrasound cube at each wire cross, and will thus vary over the set of crosses. The *UC* wire profile is found by projecting the cube in various directions (averaging over the other dimensions). Applying a threshold to this profile, we obtain an estimate of the 'true' wire width, and this estimate is used to generate the *TC* wire. The main parameter is now the threshold, and we investigate the effect of tuning this threshold. The adaptive algorithm is restricted to using a Gaussian wire profile in the template cube.

One run consists of correlating the template cube and the ultrasound cube at each of the 27 wire crosses of one volume in sequence. Typical execution time for one run on a Power Macintosh G4 450 MHz computer was 45 seconds when the 32^3 cube was used, and 4-5 minutes using the 64^3 cube. There was no significant difference in execution time between the 'fixed' and 'adaptive' options.

Statistical analysis

Comparing the data sets:

After measuring the wire crosses of the phantom physically, manually pinpointing the same crosses in volumes #15 and #33 by eight operators, and running the automatic algorithm on all the acquired ultrasound volumes, we have the following datasets:

MP_p Measured Points, point $p \in [1,27]$

$MIP_{p,v,o}$ Manual Image Points, operator $o \in [1,8]$ for volume v=15 or 33

$AIP_{p,v}$ Automatic Image Points, volume $v \in [1,36]$ (except v=26, see Table 1)

In addition, we average $MIP_{p,v,o}$ over all operators to get the manually established reference:

$MIP_{p,v}$ Manually determined reference Image Points, v=15 or 33

Ideally, all these datasets should be equal when measured in a common reference system. However, subtracting one dataset from another we get 27 residual vectors in 3D space for each volume ($v \in [1,36]$) and operator ($o \in [1,8]$ for v=15 or *33*).

For the evaluation of the automatic matching algorithm the interesting residuals to consider are the differences between the automatic data sets and the manual reference sets (volumes #15 and #33)

$$D_p = AIP_p - MIP_p \tag{3}$$

When we use the method to evaluate the accuracy of a navigation system we are interested in the errors between the measured physical points and the automatically detected image points: $E_{p,v} = AIP_{p,v} - MP_p$,for all volumes $v \in [1,36]$ as well as for subgroups of the data.

The error differences D_p and $E_{p,v}$ consists of 27 or 945 3D vectors, respectively, and for each of these vectors we can calculate the Euclidian lengths given by

$$d_p = \|D_p\| = \sqrt{D_p(X)^2 + D_p(Y)^2 + D_p(Z)^2} \tag{4}$$

$$e_{p,v} = \|E_{p,v}\| = \sqrt{E_{p,v}(X)^2 + E_{p,v}(Y)^2 + E_{p,v}(Z)^2} \tag{5}$$

Difference vectors (D_p is used below but the formulas are equally applicable for $E_{p,v}$):

The difference vectors D_p will be three-variant normally distributed when the components $\left(D_p(X)\ D_p(Y)\ D_p(Z)\right)^T$ are normally distributed. This is a reasonable assumption in our case and will be shown later. The two most obvious measures derived from the differences vectors D_p are the sample mean vector $\overline{D}$ and the sample covariance matrix S_D, which are unbiased estimators for the true mean vector (μ_D) and the covariance matrix (Johnson and Wichern 1992):

$$\overline{D} = \frac{1}{n}\sum_{p=1}^{n} D_p \tag{6}$$

$$S_D = \frac{1}{n-1}\sum_{p=1}^{n}\left[\left(D_p - \overline{D}\right)\left(D_p - \overline{D}\right)^T\right] \tag{7}$$

We will also consider the confidence ellipsoids for D_p. Contours of constant density for the 3D normal distribution are ellipsoids defined by all $D_p^{'}$ such that (Johnson and Wichern 1992)

$$\left(D_p^{'} - \overline{D}\right)^T S_D^{-1}\left(D_p^{'} - \overline{D}\right) = \chi_3^2(\alpha) \tag{8}$$

where $\chi_3^2(\alpha)$ is the upper $(100\alpha)th$ percentile of a chi-square distribution with 3 degrees of freedom. These ellipsoids will contain (1-α)·100% of the probability, be centered at $\overline{D}$ and have axes $\pm\sqrt{\chi_3^2 \cdot \lambda_i} \cdot \vec{e}_i$, where $\left(\lambda_i , \vec{e}_i\right)$ are the eigenvalue-eigenvector pairs for S_D ,$i = 1,2,3$. The eigenvectors of the covariance matrix give the directions of the ellipsoid's main axes, while the eigenvalues are the squared lengths of the axes in a 1σ ellipsoid. Theoretically, if D_p obeys a 3D normal distribution, 20%, 74% and 97% of all points should lie within the 1σ, 2σ, and 3σ ellipsoids, respectively. To confirm our assumption that the actual data (D_p) obey a 3D normal distribution, we determine the fraction of observations that lies inside the ellipsoids found from (8).

Finally, we can reach valid conclusions about the true mean vector μ_D using Hotelling's T^2 statistics (Johnson and Wichern 1992)

$$T^2(\mu_{D0}) = n\left(\overline{D} - \mu_{D0}\right)^T S_D^{-1}\left(\overline{D} - \mu_{D0}\right) \tag{9}$$

where μ_{D0} is the test vector that is investigated in order to see whether it is a plausible value for the true mean vector μ_D. This can be formulated as a hypothesis test:

$$H_0 : \mu_D = \mu_{D0} \quad \text{against} \quad H_1 : \mu_D \quad \mu_{D0} \tag{10}$$

Once $\overline{D}$ and S_D are observed, the test becomes: Reject, at significance level α, the null hypothesis H_0 in favor of the two-sided alternative hypothesis H_1, if

$$T^2(\mu_{D0}) > \frac{(n-1)\cdot p}{(n-p)} \cdot F_{p,n-p}(\alpha) = Q(\alpha) \tag{11}$$

where $F_{p,n-p}(\alpha)$ is the upper $(100\alpha)th$ percentile of the $F_{p,n-p}$ distribution with p and $n-p$ degrees of freedom (p=3 dimensions and n=27 residual vectors in our case). $Q(\alpha)$ is introduced only to simplify the notation. If H_0 is not rejected, we conclude that μ_{D0} is a plausible value for the true mean vector. However, this is not the only plausible value: the (1-α)·100% confidence ellipsoid for μ_D is the set of all μ_{D0} values such that:

$$T^2(\mu_{D0}) \leq Q(\alpha) \tag{12}$$

Before T^2 ($\overline{D}$ and S_D) is observed this is a random ellipsoid that will contain the true μ_D with probability (1-α). Observing a large numbers of intervals, (1-α)·100% of them will in fact contain the true and unknown mean difference vector μ_D. From the well-known correspondence between acceptance regions for tests and confidence ellipsoids we have that the conclusion ' Do not reject $H_0 : \mu_D = \mu_{D0}$ at level α ' is equivalent to 'μ_{D0} lies in the (1-α)·100% confidence ellipsoid for μ_D'.

Error vector lengths ($e_{p,v}$ is used below but the formulas are equally applicable for d_p):

The lengths $e_{p,v}$ will be Rayleigh distributed when the components $\left(E_{p,v}(X)\ E_{p,v}(Y)\ E_{p,v}(Z)\right)^T$ are normally distributed (Papoulis 1984). Important measures are the unbiased sample mean and standard deviation. However, for the sake of completeness, we shall evaluate the following measures:

Sample mean: $$\bar{e} = \frac{1}{27 \cdot 35}\sum_{p=1}^{27}\sum_{v=1}^{35} e_{p,v} \tag{13}$$

Sample STD: $$s_e = \sqrt{\frac{1}{(27 \cdot 35) - 1} \cdot \sum_{p=1}^{27}\sum_{v=1}^{35}\left(e_{p,v} - \bar{e}\right)^2} \tag{14}$$

RMS value: $$e_{RMS} = \sqrt{\frac{1}{27 \cdot 35}\sum_{p=1}^{27}\sum_{v=1}^{35} e_{p,v}^2} \tag{15}$$

β percentiles: e_β : where β % of all the observed $e_{p,v}$ lie below e_β (16)

Maximum value: $$e_{\max} = \max\left(e_{p,v}\right) \tag{17}$$

The error measure $\bar{e}$ (or $\bar{d}$) is useful in the manner that it is possible to present a single number characterizing the system (or algorithm). Some authors prefer the RMS value and hence we have included this. Nevertheless, the vector $\bar{E}$ (or $\bar{D}$) presents not only a value but also the direction in space of the error measure, which may be useful in determining whether the system error has a certain bias, i.e. an offset in a certain direction.

RESULTS AND INTERPRETATION

Evaluation of Automatic Algorithm

Manual determination of the reference set:

In order to assess the variability between the operators, the individually picked points were compared to the reference set (MIP_p) generated by averaging over all the operators. Hence we are looking at the difference set $D_{p,o} = MIP_{p,o} - MIP_p$, and we will use the similarity measure $\bar{d}$ (13) for comparison.

Averaging over both operators and points we found the mean difference $\bar{d}$ between an individual operator and the reference set to be 0.40±0.29 mm (Fig. 5). The individual operators agreed with the average value to within ±0.2 mm (Fig. 5(a)). Furthermore, Fig. 5(b) shows that the variability increased with depth, from ca. 0.25 mm in the top layer ($p \in [1,9]$) to more than 0.5 mm in the lowest layer ($p \in [19,27]$). This can be expected from the increased smearing effect of the ultrasound beam.

In Fig. 6 we show zoomed images through a wire cross. Overlaid on the images are shown projections of the reference location (vertical and horizontal lines), the physically measured point, the eight individual operators marks, and the automatically detected point. Although having a certain variability among the operators (Fig. 5), we consider the average over all operators to be the best wire cross position estimate available, and hence use this as the reference when evaluating the automatic algorithm.

Optimization of algorithm parameters:

The variation and definition of the template cube parameters can be found in Table 2, and a detailed description of the parameters was presented in *METHODS; Algorithm.* For a specific parameter setting, the automatic algorithm finds the point set $AIP_p(L,P,dX,dZ,Zsep)$, $p \in [1,27]$. This set is compared to the reference set MIP_p, $p \in [1,27]$ by calculating the difference vectors

$$D_p = AIP_p(L,P,dX,dZ,Zsep) - MIP_p \tag{18}$$

For comparing the individual parameter settings we use the similarity measure $\bar{d}$ (13). Table 3 summarizes the 'optimal' parameter settings for the diagonal translation scan (volume #15) and the tilt scan (volume #33). We note that:

- Min($\bar{d}$) is almost the same (0.25-0.31 mm) for all cases.
- The 'optimal' parameter setting is essentially the same for all cases.
- Cube size 32 gives essentially the same results as cube size 64. (As mentioned earlier, the 32^3 cube runs considerably faster.)
- Gaussian profiles give slightly lower min($\bar{d}$) than rectangular profiles. The max($\bar{d}$) values are also better.

The adaptive approach resulted in $\bar{d}$ ranging from approximately 1.1 mm for volume #15 to 1.9-2.2 mm (depending on threshold setting) for volume #33, i.e. considerably higher values than for the results of the fixed Gaussian and rectangular template profiles. An explanation for this is that the adaptive option typically yields wide synthetic wires for the deeper situated layers. Wide wires imply a poorly defined correlation maximum, thus increasing the chances of having an incorrect offset in the resulting displacement. This leads to an overall degradation in the method's accuracy, manifested in increased values of $\bar{d}$. By using synthetic wires considerably narrower than the ultrasound images of the wires, the maximum of the ultrasound images is found with better precision. The optimization results obtained with the fixed option support this conclusion.

Based on these results and considering the fact that a typical edge in an ultrasound image is closer to a Gaussian than to a rectangular profile, we use the following settings for the algorithm when performing the further analysis in this paper:

Wire description:	*Fixed*
Wire profile P:	*Gaussian*
Cube size L:	*32 voxels*
Wire width (hor.) $\Delta X = \Delta Y$:	*2 voxels*
Wire width (vert.) ΔZ:	*1 voxel*
Wire separation:	*0 voxels*

Accuracy of automatic method:

An important characteristic of the automatic algorithm is its ability to find the 'true' positions of the wire crosses in the ultrasound volumes. This is evaluated through the difference vectors D_p, $p=1\ldots27$ (3), using the optimal parameter setting determined above. These vectors for volume #15 are shown in three orthogonal projections in Fig. 7. The sample mean vector (6) is $\bar{D} = (-0.035\ \ 0.011\ \ 0.003)^T$ mm, and the mean length (13) is $\bar{d} = 0.27 \pm 0.17$ mm. The corresponding number for volume #33 is $\bar{d} = 0.30 \pm 0.22$ mm. Fig. 7 also shows the projections of the ellipsoids found from (9). The 1σ half axis lengths are $a = 0.268$ mm, $b = 0.156$ mm, and $c = 0.076$ mm. Table 4 compares the theoretical $k\sigma$-ellipsoids for constant confidence levels (for a 3D normal distribution) to the actual fraction of observed points within these ellipsoids, for several values of k. The table indicates that our data is in reasonable agreement with the assumption of a 3D normal distribution. Note that the discrepancy is partly due to the uncertainty in actual fraction that arises from the limited number of points (one volume; n=27).

Using our observations the conclusion of the hypothesis test in (9)-(12) with a test value of $\mu_{D0}^T = (0\,0\,0)^T$ is that the null hypothesis should not be rejected at significance level $\alpha = 0.5$, because the statistic $T^2 = 0.673$ is less than $Q(0.5) = 2.639$ and not greater (12). This means that the test value μ_{D0} is a plausible value for the unknown true mean vector, and that the data shows no evidence that the automatic algorithm for picking image points is any different from the manual average over all operators at any significance level $\alpha < 0.5$.

This can also be seen from the $(1\text{-}\alpha)\cdot 100\%$ confidence ellipsoids (11)-(12) for μ_D in Fig. 8. The innermost black ellipsoid projection is the 50% interval, and every test vector μ_{D0} contained in this ellipsoid will not reject the null hypothesis at significance level $\alpha < 0.5$. The crosses indicate our test vector, the null vector. The outermost confidence ellipsoid (99.9%) is well within a ±0.1 mm range in the Z-direction, but considerably larger in the X- and Y-directions.

It is further interesting to compare the performance of the automatic algorithm to the performance of a human operator. Keeping the average over manually picked points as the reference set, we repeat the eigenvalue analysis in (9) for each of the individual operators. Choosing a confidence level (eg. 20%) we now have an ellipsoid for each of the operators as well as for the automatic algorithm. The size of such an ellipsoid will be a direct measure of the spread in the given data set relative to the reference set. The volume of an ellipsoid is given by

$$V = \frac{4\pi}{3} \cdot a \cdot b \cdot c \qquad (19)$$

where a, b, and c are the lengths of the ellipsoid's half axes. The results listed in Table 5 indicate that the automatic algorithm is closer to the reference set than are any of the individual operators.

Application Example

Accuracy of navigation system:

The main application for our automatic method is accuracy evaluation of a neuronavigation system (Lindseth et al. 2002). This includes the accuracy and quality of the data acquisition and volume reconstruction procedures, which were irrelevant for the characterization of the automatic algorithm described above. We shall now demonstrate the intended application, using the total set of 35 valid volumes acquired with our in-house ultrasound navigation system. Volume #26 did not cover the entire span of the wire cross cube and hence was omitted from further analysis. An overview of the volumes is shown in Table 1.

The reference is now the set of physically measured coordinate values MP_p, $p \in [1,27]$. Scanning, volume reconstruction, and application of the automatic algorithm yield a data set $AIP_{p,v}$ for each volume v ($p \in [1,27]$; $v \in [1,36]$). From the error vectors $E_{p,v} = AIP_{p,v} - MP_p$ as well as the vector lengths $e_{p,v}$ various characteristic figures can be calculated.

The endpoints of the $E_{p,v}$ vectors are shown in three projections in Fig. 9, while the 945 (27·35, see Table 1) distances $e_{p,v}$ are plotted in the histogram shown in Fig. 10(a), together with the normalized cumulative curve in Fig. 10(b). $\bar{e}$ was found to be 1.34±0.62 mm, while e_{95} = 2.46 mm, and $\bar{E} = (0.547\ \ 0.646\ \ -0.099)^T$ mm, indicating a small bias. The results from the calculation of the various parameters in (13)-(17) are listed in Table 6. For comparison, we have also calculated the parameters for the single volumes considered during evaluation of the algorithm: the diagonal translation scan; volume #15 and the tilted scan; volume #33, as well as for individual layers. The latter results indicate a small increase in error with depth, thus reflecting the inherent resolution of the ultrasound technique.

System repeatability:

The repeatability of the system, i.e. the navigation system's ability to reproduce a 3D point location in image space as determined by our automatic method, was measured by calculating the largest difference for all sets of three repetitions of the acquisitions. The average over all such differences was 0.23 mm.

Effect of varying resolution:

The ability of the automatic method to identify the wire crosses correctly might be expected to depend upon the resolution of the reconstructed volume. We investigate this dependence by applying the automatic method to a volume reconstructed with several different resolutions (volume #1). This volume was chosen because it would not exceed computer memory limitations even after high-resolution scan conversion. The variation of the results from the automatic method as a function of resolution of the reconstructed volume is presented in Fig. 11, which shows $\bar{e}$ derived from the automatic point set AIP_p at varying resolution and the set of physically measured points MP_p. We found that the automatic method is almost insensitive to the resolution of the ultrasound volume. Note, however, that this analysis was done with the constant synthetic wire width given in voxel units (cf. *METHODS; Algorithm*), implying that the wire width (in millimeters) varies.

Effect of varying speed of sound:

The speed of sound is an important parameter in scan conversion. The value is well controlled in our laboratory setting (water), but will vary more in a clinical setting. To investigate the sensitivity of the accuracy to this parameter, we perform a model calculation using our automatic method. We scan converted one volume (#1) using different values for speed of sound. We used 1485 m/s as the expected value (at 21°C in water (Duck 1990)) and changed this value in steps of ±3%, ±5%, and ±10%, i.e. speed of sound ranging from 1336 m/s to 1633 m/s, resulting in seven volumes in all. The automatic wire cross detection algorithm was performed on all volumes and $\bar{e}$ (13) was calculated. The result is plotted in Fig. 12(a). We also determined the mean *X*-, *Y*- and *Z*-components of $\bar{E}$ (6) and plotted these in Fig. 12(b). It can be seen that the largest error, naturally, appears in the *Z*-direction, which is identical to the beam direction for the center beam in each of the 2D images for this translation acquisition. This model illustration shows the importance of using the correct value for the speed of sound when imaging in a clinical situation.

DISCUSSION

The data sets used here (two ultrasound volumes for method evaluation; 35 volumes for application demonstration; each volume containing 27 points) are considered sufficiently large and diverse to reveal the method's potentials. This also indicates that our automatic method is robust with respect to the varying image quality. The robustness is confirmed by the resolution variation example, and by the insensitivity to small variations in template parameter setting and in initial positioning of the ultrasound cube within each volume.

We find negligible bias in the results of the automatic method compared to the reference data sets in image space. In addition, the applicability of the method to navigation system accuracy evaluation is confirmed by the numbers shown in Fig. 13. When compared to the physically measured point set MP, our method gives essentially the same results as the manual method, for both volumes #15 and #33. We have further shown that the method is more accurate (lower spread) and considerably faster than even a skilled human operator, as well as being non-subjective. For these reasons, we believe the proposed method is superior to methods involving human interaction.

The reference data set is established from manual identification of points in the ultrasound volume. This eliminates error sources associated with the volume reconstruction process, which is irrelevant when evaluating the automatic method's accuracy. The accuracy of the method is limited by the accuracy in the location of the correlation maximum (the resolution 0.25 voxel typically equals 0.15 mm). In a system evaluation setting, the accuracy of the physically measured phantom points (presently ~0.1 mm) must also be considered.

We have only considered the identification of separate points. Thus, geometric distortion of the volume due to reconstruction errors is not detected. However, our method should be able to analyze also geometric distortions, due to the well-defined and accurately measured spatial extension of the phantom. This ability may be applicable also to imaging modalities other than ultrasound.

We have attempted to design a laboratory set-up that resembles a clinical setting. For example, the internal phantom size defined by the wires (5^3 cm^3) is comparable to a typical surgical volume, and the manual scanning procedure and the scan times (typically 18-24 seconds) are also realistic.

In the application test on our in-house navigation system, there are several other error sources than those associated with the algorithm and the phantom. These include probe calibration (determining the image position and orientation relative to the position sensor attached to the probe), position reading and synchronization (tagging each image with the correct position data), and the volume reconstruction process (interpolation, speed of sound). The resulting system error includes all these factors. The main differences between our experimental set-up and the clinical setting are the accuracy associated with determining the correct slice through an ultrasound volume using a calibrated instrument, and greater variance in the speed of sound.

We developed the automatic method for in-depth accuracy evaluation of 3D ultrasound-based navigation systems, which is the main application. We have conducted such a study on a commercial system for neurosurgery (Lindseth et al. 2002). However, since the total procedure (scan + data transfer + volume reconstruction + automatic algorithm) takes less than five minutes, the method may also be used in the operating room for the purpose of system validation prior to surgery. Furthermore, we are presently running a study on probe calibration, in which we use the automatic method for evaluation and comparison of several probe calibration techniques.

CONCLUSION

We have developed a novel method for automatically assessing the accuracy of 3D ultrasound-based navigation systems. The method applies a correlation-based template matching algorithm that identifies the location well-defined structures in ultrasound volumes. The present implementation is designed for a precisely built wire phantom with 27 wire crosses within a volume of 5^3 cm^3.

We found no significant difference between the results of our new method and a reference data set, which was established by averaging several manual identifications of the same wire crosses. In addition, the new method is faster and more accurate than a skilled human operator, as well as being fully automatic and thus non-subjective. Investigation of volume reconstruction parameters, like resolution, showed that the method is also robust with respect to the ultrasound volume quality. Due to the non-interactive algorithm and the high execution speed, the method is especially suited for analyzing large amounts of data (many volumes).

We demonstrated the application of the method on an extensive set of ultrasound volumes, scanned by our in-house navigation system under various acquisition conditions. We have further applied the method in the accuracy evaluation of a commercial ultrasound-based navigation system. These results are published elsewhere. The method can also be used to evaluate the performance of one probe calibration method to another (work in progress).

ACKNOWLEDGEMENTS

This work was partly supported by grants from the Research Council of Norway through the Strategic University Program in Medical Technology at the Norwegian University of Science and Technology, the Strategic Institute Program at SINTEF Unimed, and the Norwegian Ministry of Health and Social Affairs.

We wish to thank the Laboratory for Fine Mechanics at SINTEF Unimed in Trondheim, Norway, for making necessary equipment used in this study, especially the wire phantom, and also for providing indispensable measurements. We also thank Toril A Nagelhus Hernes, SINTEF Unimed Ultrasound, for helpful discussions during preparation of the manuscript.

REFERENCES

Atallah MJ. Faster image template matching in the sum of the absolute value of differences measures. IEEE Trans Image Proc, 2001;10:659-663.

Bucholz RD, Yeh DD, Trobaugh J, McDurmont LL, Sturm CD, Baumann C, Henderson JM, Levy A, and Kessman P. The correction of stereotactic inaccuracy caused by brain shift using an intraoperative ultrasound device. Lecture notes in Computer Science Proceedings of the 1997 1st Joint Conference on Computer Vision, Virtual Reality, and Robotics in Medicine and Medical Robotics and Computer-Assisted Surgery, CVRMed-MRCAS'97, Grenoble, 1997

Cartellieri M, Kremser J, and Vorbeck F. Comparison of different 3D navigation systems by a clinical "user". Eur Arch Otorhinolaryngol, 2001;258:38-41.

Comeau RM, Sadikot AF, Fenster A, and Peters TM. Intraoperative ultrasound for guidance and tissue shift correction in image-guided surgery. Med Phys, 2000;27:787-800.

Didon JP, and Langevin F. Registration of MR images: from 2D to 3D, using a projection based cross correlation method. IEEE 17th Annual Conference, Engineering in Medicine and Biology Society, 1995;1:489 - 490.

Dorward NL, Alberti O, Palmer JD, Kitchen ND, and Thomas DGT. Accuracy of true frameless sterotaxy: in vivo measurement and laboratory phantom studies. J Neurosurgery, 1999;90:160-168.

Duck FA. Physical properties of tissue. A comprehensive reference book. London, UK, Academic Press Ltd., 1990.

Fenster A, and Downey DB. 3-D ultrasound imaging: A review. IEEE Engineering in Medicine and Biology, 1996;15:41-51.

Gronningsaeter A, Kleven A, Ommedal S, Aarseth TE, Lie T, Lindseth F, Langø T, and Unsgård G. SonoWand, An ultrasound-based neuronavigation system. Neurosurgery, 2000;47:1373.

Hadani M, Spiegelman R, Feldman Z, Berkenstadt H, and Ram Z. Novel, compact, intraoperative magnetic resonance imaging-guided system for conventional neurosurgical operating rooms. Neurosurgery, 2001;48:799-809.

Hartov A, Eisner SD, Roberts DW, Paulsen KD, Platenik LA, and Miga MI. Error analysis for a free-hand three-dimensional ultrasound system for neuronavigation. Neurosurg Focus, 1999;6:Article 5 (12 pages).

Helm PA, and Eckel TS. Accuracy of registration methods in frameless stereotaxis. Comp Aided Surg, 1998;3:51-56.

Hill DLG, Maurer CR, Maciunas RJ, Barwise JA, Fitzpatrick JM, and Wang MY. Measurement of intraoperative brain surface deformation under a craniotomy. Neurosurgery, 1998;43:514-528.

Johnson RA, and Wichern DW. Applied multivariate statistical analysis. Englewood Cliffs, NJ, Prentice-Hall International, Inc., 1992.

Lindseth F, Langø T, Bang J, and Hernes TAN. Accuracy evaluation of a 3D ultrasound-based neuronavigation system. Comp Aided Surg, 2002;In Press

Maurer CR, Fitzpatrick JM, Wang MY, Galloway RL, Maciunas RJ, and Allen GS. Registration of head volume images using implantable fiducial markers. IEEE Trans Med IMaging, 1997;16:447-462.

Nelson TR, and Pretorius DH. Three-dimensional ultrasound imaging. Ultrasound Med Biol, 1998;24:1243-1270.

Nimsky C, Ganslandt MD, Kober H, Buchfelder M, and Fahlbusch R. Intraoperative magnetic resonance imaging combined with neuronavigation: a new concept. Neurosurgery, 2001;48:1082 - 1091.

Nimsky C, Ganslandt O, Cerny S, Hastreiter P, Greiner G, and Fahlbusch. Quantification of, visualization of, and compensation for brain shift using intraoperative magnetic resonance imaging. Neurosurgery, 2000;47:1070-1080.

Papoulis A. Probability, random variables, and stochastic processes. Singapore, McGraw-Hill, 1984.

Porter BC, Rubens DJ, Strang JG, Smith J, Totterman S, and Parker KJ. Three-dimensional registration and fusion of ultrasound and MRI using major vessels as fiducial markers. IEEE Transactions on Medical Imaging, 2001;20:354 - 359.

Prasad L, and Iyengar SS. High performance algorithms for object recognition problem by multiresolution template matching. IEEE Proc Seventh Int Conf Tools Artificial Intell, 1995:362-365.

Remagnino P, Brand P, and Mohr R. Correlation techniques in adaptive template matching with uncalibrated cameras. SPIE Vol. 2356 Vision Geometry III, 1994;2356:252 - 263.

Roberts DW, Hartov A, Kennedy FE, Miga MI, and Paulsen KD. Intraoperative brain shift and deformation: A quantitative analysis of cortical displacement in 28 cases. Neurosurgery, 1998;43:749-760.

Rohling RN, Gee AH, and Berman L. Automatic registration of 3-D ultrasound images. 6th International Conference on Computer Vision, 1998:298 - 303.

Sipos EP, Tebo SA, Zinreich SJ, Long DM, and Brem H. In vivo accuracy testing and clinical experience with the ISG Viewing Wand instrumentation application. Neurosurgery, 1996;39:194-204.

Tronnier VM, Wirtz CR, Kanuth M, Lenz G, Pastyr O, Bonsanto MM, Albert FK, Kuth R, et al. Intraoperative diagnostic and interventional magnetic resonance imaging in neurosurgery. Neurosurgery, 1997;40:891-902.

Van den Elsen PA, Maintz JBA, Pol E-JD, and Viergever MA. Automatic registration of CT and MR brain images using correlation of geometrical features. IEEE Trans. on Medical Imaging, 1995;14:384 - 396.

Villalobos H, and Germano IM. Clinical evaluation of multimodality registration in frameless sterotaxy. Comp Aided Surg, 1999;4:45-49.

Wirtz CR, Bonsanto MM, Kanuth M, Tronnier VM, Albert FK, Staubert A, and Kunze S. Intraoperative magnetic resonance imaging to update interactive navigation in neurosurgery: Method and preliminary experience. Comp Aided Surg, 1997;2:172-179.

Tables

Wire phantom/camera set-up	Volume #	Scan type
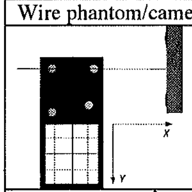	1-3	Translation positive X-axis
	4-6	Translation negative X-axis
	7-9	Tilt positive X-axis
	10-12	Tilt negative X-axis
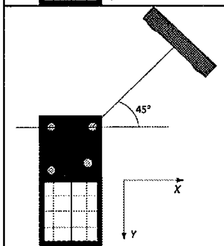	13-15	Translation positive diagonal
	16-18	Translation negative diagonal
	19-21	Tilt positive diagonal
	22-24	Tilt negative diagonal
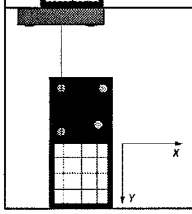	25-27	Translation positive Y-axis
	28-30	Translation negative Y-axis
	31-33	Tilt positive Y-axis
	34-36	Tilt negative Y-axis

Table 1. Ultrasound volumes acquired for the application and algorithm tests. Volume #15 and #33 were used in the algorithm evaluations. Volume #26 was omitted from all calculations since it did not cover all wire crosses.

Synthetic wire description	Fixed		Adaptive
Wire profile P	Gaussian	Rectangular	Gaussian
Cube size L	32, 64	32, 64	32
Wire width (hor.) $\Delta X = \Delta Y$	1-12, step 1	1-20, step 1	Threshold: 0.1-0.9, step 0.1
Wire width (vert.) $\Delta Z_1 = \Delta Z_2$	1-6, step 1	1-10, step 1	
Wire separation (vert.) $Zsep$	0-3, step 0.5	0-3, step 1	
Total number of runs	1008	1600	9

Table 2. Test matrix for parameter optimization. The cube size, wire width, and separation are in voxel units.

Synthetic description	min(d_p)	Setting for min(d_p)			d_p for chosen setting	max(d_p)
		$\Delta X = \Delta Y$	ΔZ	$Zsep$		
Fixed Gaussian (L=32)	0.27 (0.29)	2 (3)	1 (1)	0 (0)	0.27 (0.30)	1.67 (1.54)
Fixed rectangular (L=32)	0.29 (0.31)	4 (6)	1 (2)	0 (0)	0.30 (0.38)	3.88 (3.98)
Fixed Gaussian (L=64)	0.30 (0.28)	2 (9)	1 (2)	0 (0)	0.30 (0.32)	1.98 (1.57)
Fixed rectangular (L=64)	0.31 (0.30)	2 (6)	1 (2)	0 (0)	0.31 (0.38)	4.20 (3.94)

Table 3. Minimum d values in millimeter, and parameter setting with respect to d_p. Results from diagonal translation scan; volume #15 and volume #33 (in parenthesis).

Theoretical confidence level (3D normal distribution)	50%	75%	90%	95%	99%	99.9%
Scale factor k ($k\sigma$-ellipsoid)	1.54	2.03	2.50	2.79	3.36	4.04
Actual fraction within $k\sigma$-ellipsoid (#15)	59.3	77.8	92.6	96.3	96.3	100.0
Actual fraction within $k\sigma$-ellipsoid (#33)	44.4	81.5	92.6	96.3	100.0	100.0

Table 4. Confidence levels (3D) for theoretical $k\sigma$-ellipsoids, for various values of k (Johnson and Wichern 1992). This is compared to the actual fraction of our data set falling within the $k\sigma$-ellipsoid (ultrasound volumes #15 and #33).

Operator	Volume of 1σ-ellipsoid (mm^3)	V(operator)/V(AIP_p)
AIP	0.0133	1.00
1	0.0719	5.41
2	0.0153	1.15
3	0.0411	3.09
4	0.0261	1.96
5	0.1185	8.91
6	0.0520	3.91
7	0.0671	5.05
8	0.0151	1.14

Table 5. Spread in automatic data set AIP_p, and in eight individual operators's data sets, relative to the reference data set MIP_p. The spread is represented by the volumes of the 1σ-ellipsoids calculated from the covariance matrix for each data set. Greater volumes correspond to greater spread. The last column presents all volumes normalized by the AIP_p volume.

	n	$\bar{e}$	e_{STD}	e_{RMS}	e_{50}	e_{95}	e_{max}
Diagonal translation (vol. # 15)	27	1.24	0.41	1.30	1.13	1.98	2.09
Tilt parallel to *Y*-axis (vol. # 33)	27	2.29	0.60	2.37	2.14	3.53	3.76
All volumes, layer 1	315	1.21	0.56	1.33	1.10	2.14	2.99
All volumes, layer 2	315	1.31	0.60	1.44	1.23	2.29	2.97
All volumes, layer 3	315	1.52	0.66	1.66	1.42	2.61	3.84
All volumes	945	1.34	0.62	1.48	1.25	2.46	3.84

Table 6. Comparison of similarity measures between automatically detected points and physically measured points (all numbers in mm). N is the total number of point pairs.

Figures

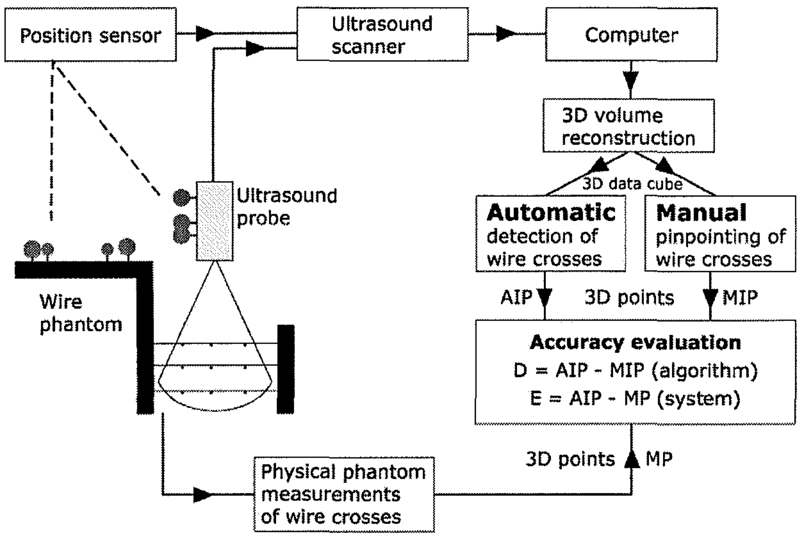

Fig. 1. Measurement set-up and data flow. The position sensor registers the wire phantom and the ultrasound probe during image acquisition. Ultrasound data and position data are input to the computer, which reconstructs the 3D volume. The algorithm identifies the positions of the wire crosses (*AIP*) in this volume. For evaluation, the wire crosses are also identified manually in the same reconstructed volume (*MIP*). We also compare *AIP* to the physically measured positions of the wire crosses (*MP*), to assess the accuracy of the whole 3D ultrasound-based navigation system.

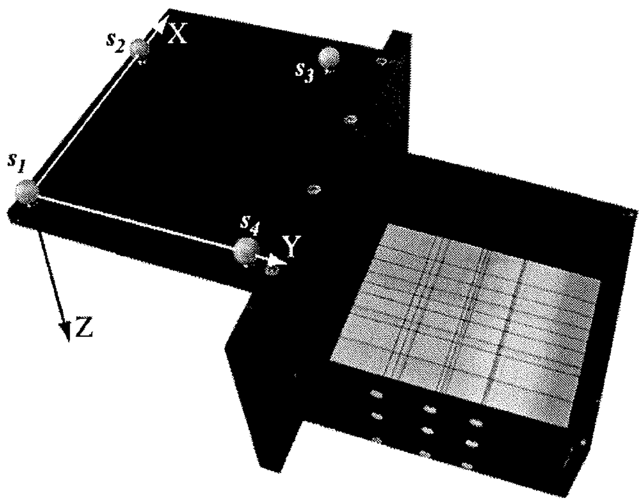

Fig. 2. The wire cross phantom. The four spheres s_i, i=1-4, constitute the reference frame for the optical positioning system.

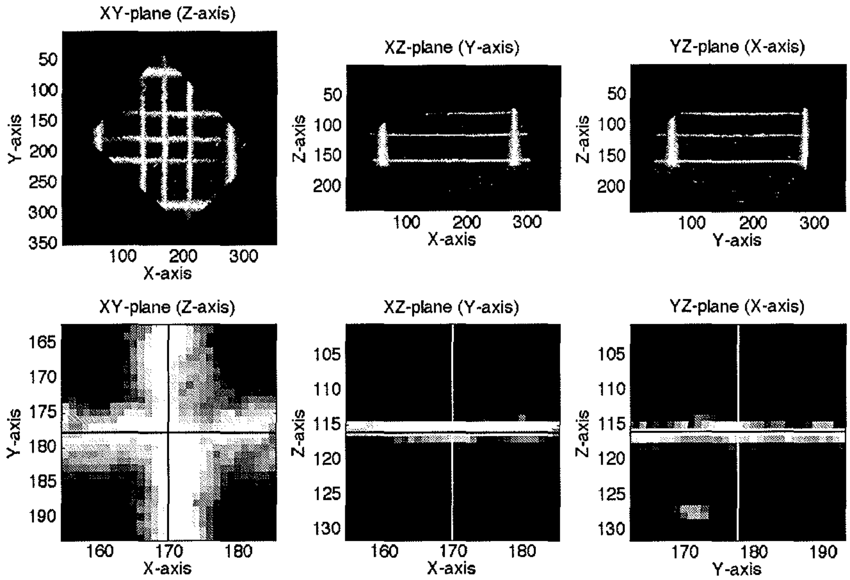

Fig. 3. Orthogonal slices through the ultrasound volume (#15) after 3D reconstruction. Top line: The strong echoes at the edges are from the phantom aluminum side plates. The nine wire crosses at the middle layer are seen in the first slice. Bottom line: Example of zooming in on one wire cross for manual determination of the location. The cross-hairs indicate the selected location. All numbers are in voxel units.

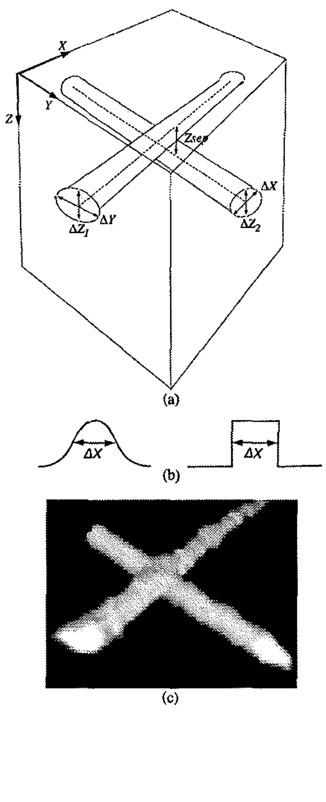

Fig. 4. (a) Illustration of template cube (synthetic model of wire cross) with model parameters. (b) Gaussian and rectangular wire profiles. (c) A rendered projection of an ultrasound volume of one wire cross.

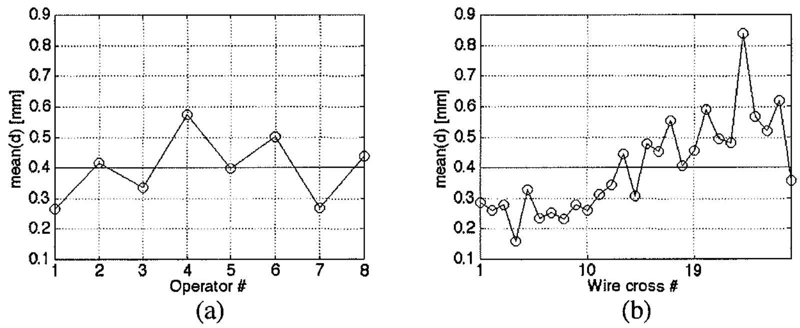

Fig. 5. Results from manual detection of wire crosses in volume #15. The distances d are defined as the deviation of each operator's opinion $MIP_{p,o}$ from the average MIP_p over all eight operators. (a) Results for each operator, averaged over the whole volume (27 crosses). (b) Results for each wire cross, averaged over all operators. The straight lines indicate the mean over all operators and points: $\bar{d}$=0.40 mm.

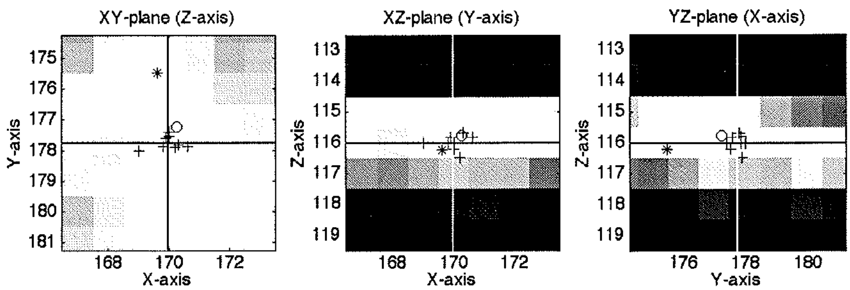

Fig. 6. High-resolution excerpt from volume #15 at the center wire cross location. Superimposed on the orthogonal images are projections of the physically measured points MP_p (*), the automatic procedure's results AIP_p (o), the eight operators' markings $MIP_{p,o}$ (+), and the reference position MIP_p (vertical and horizontal lines). All numbers are in voxel units.

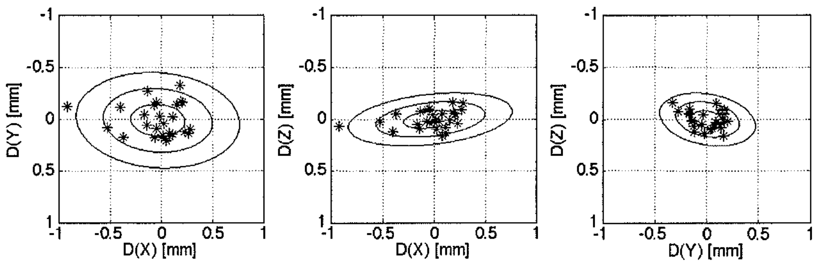

Fig. 7. Spread of automatic points AIP_p relative reference points MIP_p, plotted as stars in three orthogonal projections (in millimeter) for volume #15. The projections of the 1σ (smallest), 2σ, and 3σ (largest) ellipsoids corresponding to the covariance matrix of $D_p = AIP_p - MIP_p$ are shown as solid lines. For a normally distributed D_p in 3D space, these ellipsoids represent 20%, 74%, and 97% confidence surfaces, respectively.

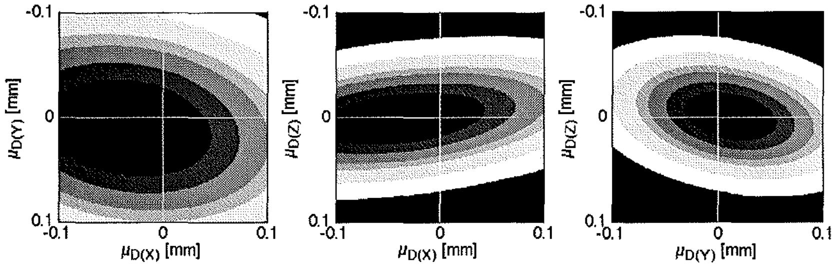

Fig. 8. Three orthogonal slices through the confidence ellipsoids of 50% (innermost), 75%, 90%, 95%, 99% and 99.9% for the true difference between manually and automatically picked points μ_D for volume #15. The cross shows our test vector $\mu_{D0}{}^T = (0\,0\,0)^T$.

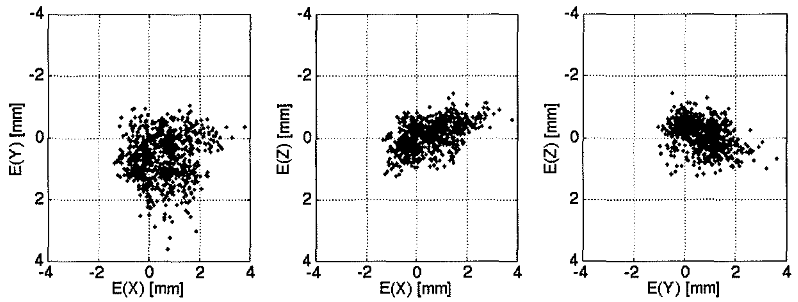

Fig. 9. 2D projection plots of endpoints of the 945 error vectors $E_{p,v}$.

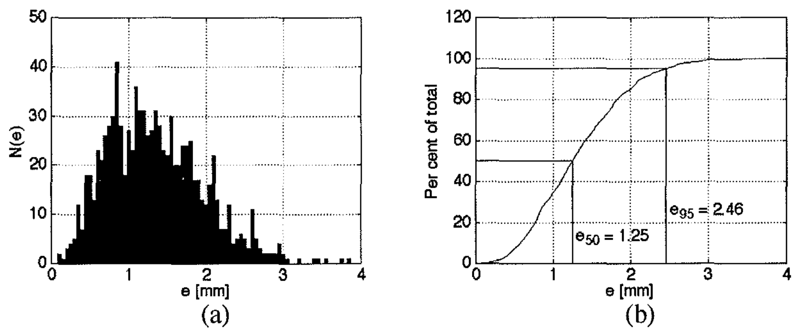

Fig. 10. (a) Histogram for lengths ($e_{p,v}$) of error vectors ($E_{p,v}$) between $AIP_{p,v}$ and MP_p, for v=1...36. The total number of error distances is 945. (b) Cumulated histogram (normalized to 100%) with the percentile values e_{50} = 1.25 mm and e_{95} = 2.46 mm indicated.

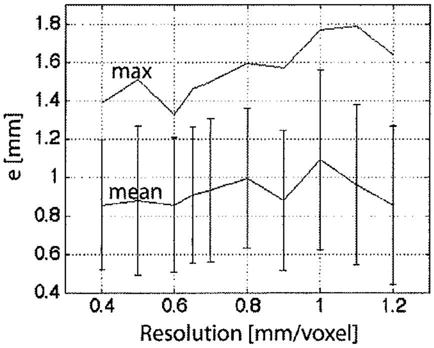

Fig. 11. $\bar{e}$ and $\max(e_{p,v=1})$ as a function of resolution of the reconstructed volume (volume #1). The error bars represent ±1 standard deviation.

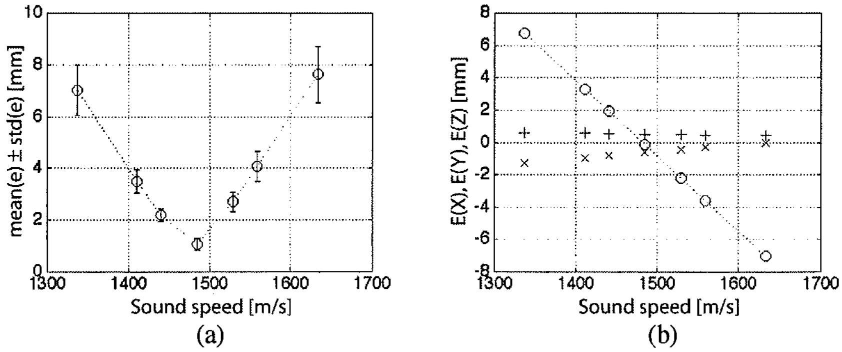

Fig. 12. (a) $\bar{e}$ (o) and standard deviation s_e (error bars) for volume #1 scan converted with 7 different values for the speed of sound (1485m/s ±3%, ±5%, and ±10%). (b) Plot of the *X*- (+), *Y*- (×), and *Z*-components (o) of $\overline{E}$.

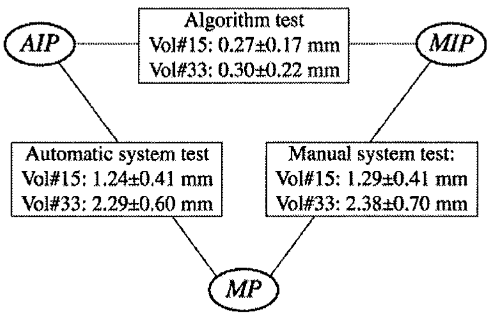

Fig. 13. Mean error vector lengths between the 27-point data sets *AIP*↔*M I P*, *AIP*↔*M P*, and *MIP*↔*MP*, for volumes #15 and #33.

Paper VI

Stereoscopic Navigation-controlled Display of Preoperative MRI and Intraoperative 3D Ultrasound in Planning and Guidance of Neurosurgery

New technology for minimally invasive image guided surgery approaches

Authors:

Toril A. Nagelhus Hernes[1], PhD, Steinar Ommedal[1], BSc, Torgrim Lie[1], MSc, Frank Lindseth[1], MSc, Thomas Langø[1], PhD, Geirmund Unsgaard[2], PhD

[1] SINTEF Unimed, Ultrasound Dept., N-7465 Trondheim, NORWAY

[2] Dept of Neurosurgery, University Hospital in Trondheim, The Norwegian University of Science and Technology, N-7465 Trondheim NORWAY

ABSTRACT

Objective: This paper demonstrates a method that brings together three essential technologies for surgery planning and guidance: *Neuronavigation systems, 3D visualization techniques* and *intraoperative 3D imaging technologies*. We demonstrate the practical use of an in-house interactive stereoscopic visualization module that is integrated with a 3D ultrasound based neuronavigation system.

Materials and methods: A stereoscopy volume visualization module has been integrated with a 3D ultrasound based neuronavigation system, which also can read preoperative MR and CT data. The various stereoscopic display modalities, such as "cut plane visualization" and "interactive stereoscopic tool guidance" are controlled by a pointer, a surgical tool or an ultrasound probe. Interactive stereoscopy was tested in clinical feasibility case studies for planning and guidance of surgery procedures.

Results: By orientating the stereoscopic projections in accordance to the position of the patient on the operating table, it is easier to interpret complex 3D anatomy and to directly take advantage of this 3D information for planning and surgical guidance. In the clinical case studies, we experienced that the probe controlled cut plane visualization was promising during tumor resection. By combining 2D and 3D display, interpretation of both detailed and geometric information may be achieved simultaneously. The possibilities of interactively guiding tools in a stereoscopic scene seemed to be a promising functionality for use during vascular surgery, due to specific location of certain vessels.

Conclusion: Interactive stereoscopic visualization improves perception and enhances the ability to understand complex 3D anatomy. The practical benefit of 3D display is increased considerably when integrated with surgical navigation systems, since the orientation of the stereoscopic projection corresponds to the orientation of the patient on the operating table. Stereoscopic visualizations work well on MR and CT images, although volume rendering techniques are especially suitable for intraoperative 3D ultrasound image data.

Key words: Image guided Neurosurgery - stereoscopic visualization - 3D ultrasound based neuronavigation – 3D display – computer assisted surgery – minimally invasive image guided surgery – cerebrovascular surgery – tumor resection - intraoperative imaging – virtual reality

INTRODUCTION

Computer assisted systems, as neuronavigation technology, are now increasing in number on the market (1). These systems have shown to be powerful since the surgical tools may be tracked by positioning systems and the surgeon may hence navigate the tools into the brain based on image information only (2,3,4). However, most of the commercially available neuronavigation systems frequently monitor only 2D slices of preoperative 3D images, a technique that may have limitations for interpreting and understanding the complex 3D geometric anatomy and pathology of the brain during surgery. Various 3D display techniques may be considered as more user friendly than 2D display, more convenient and have potential of improving the planning and outcome of surgery (5,6,7,8,9). Rendered 3D medical image data and virtual reality visualizations have earlier been reported to be beneficial in diagnosis of cerebral aneurysms as well as in preoperative evaluation, planning and rehearsal of various surgical approaches (10,11,12,13,14,15,16,17,18,19,20). However, only some studies have been reported where these 3D visualizations have been brought into the operating room and have been used interactively for navigating surgical tools down to the lesion (21,22).

Although the use of navigation technology is increasing in neurosurgery, most of the available systems have practical limitations due to the lack of an intraoperative imaging modality providing the surgeon with *updated* image information, monitoring dynamic changes that occur during surgery. Both MR, CT and ultrasound have been presented as alternative intraoperative imaging modalities having different advantages, benefits and drawbacks in the practical clinical set up. However, all the modalities have shown to be useful for monitoring the progression of the operation, coping with brain shifts that occur during surgery (23,24,25) as well as for controlling the resection at the end of surgery (26,27,28,29,30).

In this paper we describe technology that integrates three important tools that we believe will improve neurosurgical outcome: 1) Navigation technology, 2) 3D visualization and 3) intraoperative 3D ultrasound imaging. We demonstrate how interactive stereoscopic 3D visualization may be integrated with navigation technology and hence be used directly for guiding surgical procedures. The stereoscopic projections are based on intraoperative 3D ultrasound updates as well as on corresponding preoperative MR images. We have tested the integrated stereoscopic display module in several clinical cases with promising results. In this paper we present images that demonstrate the technology from three of the cases. We believe that the stereoscopic module has potential for improving the surgeon's interpretation of complex 3D anatomy and when used in conjunction with 2D display, the technology will increase the user friendliness of navigation technology and improve the outcome of future image guided surgery.

MATERIALS AND METHODS

Stereoscopy

The stereoscopic display is created by generating two perspective projections, one for each eye according to a simple ray casting technique. Each of the projections are generated using a semitransparent volume rendering method, where high intensity objects in the volume, like blood vessels, have low transparency and thus will hide more distant objects. The voxel values are mapped directly to color and opacity through continuous functions, avoiding strict classification algorithms. Each pixel in the projection image is generated as a function of all the voxel values through the image volume along the beam from the observer position (31). The stereoscopic images may be presented on a CRT screen by alternating the left and right eye views 120 times per second or by simple red/blue projections on conventional monitors. The 3D rendered speed is highly dependent on the image volume size and geometry. Typical 3D image volumes of ultrasound are 15-20 Mbytes in our cases. However, a frame rate of 5 stereoscopic projections per second is obtained using a resolution of 128 x 96 pixels in each projection. Stereoscopic projections with high resolution are used for interactive navigation in the operating theatre. The stereoscopy software runs on a medium cost computer (Power Macintosh, G4, Apple, USA).

Navigation equipment and 3D imaging technology

Navigation and ultrasound equipment: A combined prototype system utilizing features of both navigation technology (own developed software and SonoWand, MISON AS, Trondheim, Norway) and intraoperative ultrasound imaging (System FiVe, GE Vingmed Ultrasound, Horten, Norway) integrated with an optical tracking system (Polaris, Northern Digital, Canada) was used in the present study (26,32). The camera (figure 1A) reads the position of the patient reference frame (figure 1B), the pointer (figure 1E), surgical instruments such as CUSA (figure 1F) or biopsy forceps (figure 1D) or the ultrasound probe (figure 1C).

Preoperative MR and intraoperative 3D ultrasound images for stereoscopic display: 3D MR images with high resolution (Picker or Siemens 1.5 T, figure 2A) and a slice thickness of 1.5 mm are registered to the patient using fiducial markers (figure 2B). Both 3D tissue images as well as CT or MR angiographies generating a 3D volume of the vascular tree of the brain are used. A 4-8 MHz Flat Phased Array (FPA) probe (figures 1C, 2C) with optimal focusing properties at 3-6 cm is used and the scanner factory set-up and the clinical set-up have been optimized for brain surgery applications as previously described (26,32). The ultrasound power Doppler modus is used for acquiring intraoperative 3D angiographies of the vessels in the brain. The probe is tilted at angles of approximately 80 degrees by free hand movement for 15 seconds over the anatomical area of interest. The pyramid-shaped 3D data sets are transferred to the navigation computer and reconstructed to a 3D volume as shown in figure 2C. No patient registration is needed for the 3D ultrasound volumes since they are acquired in the same coordinate system as the navigation is performed. After 3D acquisition, the ultrasound probe can be removed from the working area and image guidance can be performed based on the acquired 3D volumes.

Conventional neuronavigational control: The position of the surgical tools or pointer, determines which images to be displayed on the navigation monitor. This makes it possible to steer the tools down to the lesion guided by 3D images. Corresponding slices from preoperative MR and intraoperative ultrasound volumes are displayed simultaneously as shown in figure 2D-I. Display modalities are: *1) Orthogonal slices*:

three orthogonal 2D slices from each 3D volume orientated either in relation to the surgical tool or due to the position the patient as axial, sagittal or coronal slices (figure 2D,G). 2) *Single "anyplane" slices*: one slice from each volume defined by the position of the surgical tool (figure 2E,H) or 3) *Stereoscopic projections*: one stereoscopic projection generated from each 3D volume (figure 2F,I). Slices or projections from the 3D ultrasound volumes are displayed according to the orientation of the surgical tool and are not limited by the scan plane of the ultrasound probe.

Interactive stereoscopy by neuronavigational control

Instrument driven stereoscopy: The stereoscopic projection is controlled interactively using a pointer, a surgical tool or an ultrasound probe, which all act as virtual hand held cameras (figure 3A). The projection view may then easily and interactively be changed and makes it possible for the surgeon to interpret 3D information from any angle during planning and surgery guidance.

Cut plane visualization: The image volume used for generating the stereoscopic projections may be virtually decreased (figure 3B) by excluding parts of the 3D volume defined by a 2D plane ("cut plane"), perpendicular to the pointer (figure 3C) or according to the scan plane of the ultrasound probe (figure 3E). The cut plane makes it possible to virtually inspect the inside of an object or volume, simultaneously as more detailed information in the cut plane may be displayed.

Probe controlled stereoscopic cut plane display: When the ultrasound probe is used for defining the cut plane in the stereoscopic projection as shown in figure 3E, additional detailed information in the cut plane is easily obtained from the real time 2D ultrasound image. This makes it possible to interactively stereoscopically "see" inside the preacquired 3D volumes simultaneously as detailed information in the cut plane is achieved. In addition, the corresponding tissue 2D slice ("anyplane") from the preceding 3D ultrasound volumes may be displayed simultaneously.

Guidance of surgical tools by stereoscopic display: When the most optimal projection is generated, the projection may be frozed, and the position of the tool inside the patient is stereoscopically displayed as a small sphere in the projection view (figure 3D). This marker varies in size and position due to location of the tool tip inside the patient. The pointer or tool can then be navigated directly down to a specific location in the patient based on the stereoscopic view.

Both the stereoscopic cut plane visualization and the stereoscopic tool guidance display modalities are demonstrated in feasibility case studies; during surgery of a patient with a tumor (metastasis) and during two other cases, both with cerebral aneurysms.

RESULTS

Integration of stereoscopy with navigation technology makes it easier to benefit from 3D display

In all the case studies, stereoscopy made it easier to understand 3D anatomy. In addition, we experienced that 3D display was easier to use directly for planning and guidance when integrated with navigation technology as compared to stand-alone 3D visualization equipment. The orientation of the stereoscopic projections was intuitive due to the patient's position on the operating table. Figure 4 shows how the stereoscopic view in a novel and a low cost way is realized in the operating room. The operating team is using red blue glasses in order to get tree dimensional perception of the structures in the brain. The monitors are easily moved in order to get the 3D view in an optimal distance to the surgeon during image guidance of the instruments.

Interactive stereoscopic cut plane visualization; simultaneous interpretation of detailed 2D information and 3D geometry

During planning and surgery guidance, both 3D and more detailed information inside an object is needed. We experienced that the stereoscopic cut plane visualization technique was especially useful for giving detailed monitoring of important information as well as for giving adequate understanding of complex 3D anatomy, since the method integrates conventional display techniques (2D slices) and 3D visualization techniques. The cut plane makes it possible to virtually inspect the inside of an object or volume, since the projection is based on volume rendering techniques, which take care of information inside an object. Figure 5 shows results from two of the case studies, were stereoscopic cut plane display were used. Figure 5A-F is from a tumor resection. When the cut plane in the stereoscopic projection is defined far in front of the tumor the surgeon will get an overview of the location of the lesion due to surrounding anatomy as shown from preoperative MRI (figure 5A) and from corresponding intraoperative 3D ultrasound images (figure 5D). However, no information or characteristics from inside the tumor are given. The cut plane may, however, be changed interactively by moving the relevant instrument to be in the middle of the tumor (or using an offset) as shown in figure 5B (MR) and 5E (corresponding stereoscopic projection as B, but based on intraoperative 3D ultrasound). In this case the cut plane volume visualization technique was especially useful for interpreting the difference in nature of MR and ultrasound modalities in imaging tumor border and characteristics. A thick border of tumor tissue, surrounding necrotic or cystic material inside the tumor, not distinctly visualized in the MR images, was clearly visualized in the ultrasound cut plane projection (figure 5E). Even more detailed information was obtained by displaying corresponding tissue slices from the preacquired 3D MR (figure 5C) and intraoperative 3D ultrasound (figure 5F) volumes in addition to the stereoscopic cut plane view.

Stereoscopic display was especially important for understanding and interpreting the complex 3D geometry of a pathological vascular three. Stereoscopic *cut plane* visualization was tested in one of the aneurysms operations (figure 5G-I). By positioning a cut plane of the stereoscopic projection exactly where the aneurysm is located (aneurysm on top in all images G-I), the vessels located in front of the cut plane are excluded from the stereoscopic display and will not complicate the 3D geometric understanding of the vascular three behind the cut plane (stereoscopic cut plane from MRA, figure 5H). Simultaneous display of corresponding anyplane angiographies of MRI (figure 5G) and ultrasound power Doppler (figure 5I) as the stereoscopic cut plane projection (figure 5H) gave more detailed information of the aneurysm. The intraoperative ultrasound power Doppler anyplane slice (figure 5I) correlated well with the corresponding slice from the preoperative 3D MR angiography volume (figure 5G). By controlling the cut plane projection using the ultrasound probe, real time monitoring of blood flow in the aneurysm was performed simultaneously as interactively controlling the stereoscopic cut plane view. This made it possible to detect any changes that occurred during surgery both due to location of the vessels as well as blood flow inside the vessels.

Interactive stereoscopic tool-guidance

The stereoscopic view was found to be especially useful for interpreting the complex anatomy of the blood vessels in the brain and to localize abnormal anatomy as shown in figure 6A, where two aneurysms (middle, top in image) are easily detected using stereoscopic display of MRA. The projection displayed on the monitor, could be interactively zoomed in and out as well as viewed from any directions to get more detailed information about aneurysm size, location and surroundings. After making a craniotomy and exploring one of the aneurysms for direct visible sight, interactive stereoscopic display was tested for navigating the pointer down to the aneurysm. The most optimal stereoscopic projection was frozen, and the pointer position was displayed in the projection as a small sphere. The pointer was interactively navigated down to gently touch the aneurysm as shown in the stereoscopic projection in figure 6B. The tip of the pointer was positioned at the aneurysm in the patient and hence so was the small sphere in the stereoscopic projection. The procedure was carefully controlled also by direct sight by the surgeon. A 3D ultrasound power Doppler volume was acquired in order to compare the stereoscopic projection of the aneurysms visualized by 3D ultrasound and MRI, and the pointing procedure was repeated as shown in figure 6C. One of the aneurysms could easily be identified in the 3D ultrasound volume, but the other was not covered by the 3D ultrasound scan. However, the pointing accuracy as compared to MRI was still acceptable using 3D ultrasound based stereoscopic projections, although the MR angiography of the vessels was better than corresponding ultrasound power Doppler images.

DISCUSSION

In this paper, we have demonstrated technology that integrates navigation systems, interactive 3D stereoscopic display and intraoperative 3D ultrasound imaging for improved image guided neurosurgery.

Stereoscopic display of intraoperative 3D ultrasound images

Most of the conventional navigation systems on the market do not offer intraoperative 3D imaging that can cope with brain shift during surgery. This makes many of these systems to surgery "planning systems" rather than direct surgery guidance systems. The approach to this problem is many, ranging from interventional MRI solutions, to warping procedures or solutions based on intraoperative 2D and 3D ultrasound that recently has been presented (25,32,33,34,35,36). The various approaches to obtain intraoperative 3D imaging as well as the fact that also preoperative images may be useful for planning and to some extent surgery guidance, discloses, however, a demand for 3D display technology that can cope with all the various imaging modalities used both preoperatively and intraoperatively. Most 3D display technology available is demonstrated on CT and MR image data because the images are of high resolution with reasonably good contrast and low noise level. This makes these images easier to differentiate into tissue regions or to classify according to tissue properties as needed for surface rendering, which is most frequently used for 3D display. However, 3D visualizations generated using volume rendering techniques as presented in this paper, does not require segmented objects and is hence more feasible also for ultrasonography images, which normally are relatively inhomogeneous.

Interactive stereoscopy and precision of surgery

Although 3D views have shown to be useful for planning of surgery, less has been published using 3D display for direct surgery guidance. One of the reasons may be the need for high precision when navigating a surgical tool into the brain based on images only. Both MR and ultrasound based neuronavigation systems demonstrate an imaging accuracy in the order of 1-3 mm (37,38,39). However, we experienced that the position of the surgical instrument in the patient was easier interpreted using conventional 2D display with crosshairs rather than a small sphere in the stereoscopic view. The monitoring of the position of the surgical tool in the projection may be optimized for improving the interpretation of the exact location of the instrument in the patient. We experienced, however, that the stereoscopic cut plane visualization made it possible to integrate 2D and 3D display techniques, so that both the precision of 2D display as well as the benefits of easier interpretation of complex anatomy using 3D display technology was achieved.

Technology improvement for 3D vision in the operating room

As the technology is evolving, more 3D display technologies and computer-assisted systems have been demonstrated using smaller computers. The main challenges with the 3D visualization technologies have, however, been the lack of integration with surgical navigation systems used for guiding surgical procedures. The 3D display may then only to a certain extent be used directly for guiding the surgical procedure. However, this is about to change, and navigation technology equipment integrating 3D display is now increasing in number on the market. We believe that by combining different imaging modalities and essential available information, such as functional MRI images and intraoperative 3D ultrasound, with new display technology it will become more efficient to interpret information needed for performance of optimal surgery guidance (22,40,41).

We have demonstrated the concept of stereoscopic vision in the operating theatre simply by using simple red/blue glasses in the operating room, but the possibilities for more advanced display equipment are many, ranging from head mounted shutter glasses, polarizing monitor filters etc. We believe that research in this field is important for obtaining optimal, visual, ergonomic and userfriendly applications of 3D vision for guiding surgical procedures.

Relevance and possible clinical applications of interactive stereoscopic neuronavigational display

We have demonstrated new technology for 3D display that is integrated with navigation technology. The advantages of 3D display technologies have been pointed out by other research groups (8,10,11,12,13). The results from the feasibility case studies presented in this paper are also promising. Especially, the stereoscopic cut plane visualization seems to give many advantages due to improved perception of complex 3D anatomy and easy access to more detailed information inside the 3D volume. The interactive volume rendering 3D display module is also fast and makes stereoscopic projections of intraoperative 3D ultrasound data available immediately after 3D acquisition has been performed, without any need for post processing of the acquired image data. Stereoscopy seems to be useful both for planning and guidance of tumor resections as well as for guidance during cerebrovascular surgery. A potential useful application of the stereoscopy module may also be to interactively locate the feeding artery in artery venous malformations (work in progress) as well as for locating smaller arteries nearby aneurysms that should be avoided when clipsing the aneurysm. Stereoscopic projections of 3D ultrasound power Doppler may also have advantages for evaluating blood flow in normal vessels after an aneurysm has been clipsed. However, these potential benefits of the stereoscopic module remain to be explored and evaluated in larger clinical studies with focus on the benefits for both the surgeon as well as for the patient (work in progress).

CONCLUSION

We have presented technology that integrates intraoperative 3D ultrasound imaging, neuronavigation and interactive 3D display for making it easier to interpret complex 3D geometric anatomy, hence improving planning and image guided neurosurgery. Interactive stereoscopic display techniques have been demonstrated for guidance in three clinical cases with promising results both for tumor resections as well as for cerebral aneurysm surgery. The stereoscopic display technique is interactive and works well on intraoperatively acquired 3D ultrasound images as well as on preoperatively acquired MR images. Especially, by combining 2D and 3D display techniques, both the better precision of image guidance, as well as the interpretation of complex 3D anatomy are maintained simultaneously. The most important feature seems to be, however, that the interactive stereoscopic projections correspond to the orientation of the patient on the operating table, hence making 3D display to an intuitive and userfriendly tool for improved planning and guidance of both tumor resection and in guidance of cerebro-vascular neurosurgery.

ACKNOWLEDGEMENT

This work was supported by the Research Council of Norway (NFR), the Ministry of Health and Social Affairs of Norway, GE Vingmed Ultrasound (Horten, Norway), The Norwegian University of Science and Technology through Strategic University Program for Medical Technology and SINTEF Unimed, through Strategic Institute Program. We also want to thank Aage Gronningsaeter and Atle Kleven, both now at MISON AS, for their contribution to the development of the stereoscopic visualization module when employed at SINTEF Unimed and for helpful discussions during the preparation of this paper.

DISCLOSURE

Torgrim Lie has not been involved in the study after he became a developer in MISON AS in 1999.

REFERENCES

1 Reinhardt H., Trippel B, Westermann B and Gratzl: Computer aided surgery with special focus on neuronavigation, Computerized Medical Imaging and Graphics 23, 237-244, 1999.

2 Gumprecht H, Darius CW, Lumenta CB: BrainLab Vector Vision neuronavigation system: Technology and clinical experiences in 131 cases. **Neurosurgery** 44: 97-105, 1999.

3 Wadley J, Dorward N, Kitchen N, Thomas D: Preoperative planning and intraoperative guidance in modern neurosurgery: a review of 300 cases. **Ann R Coll Surg Engl** 81:217-225, 1999.

4 Wirtz CR, Albert FK, Schwaderer M, Heuer C, Staubert A, Tronnier VM, Knauth M, Kunze S: The benefit of neuronavigation for neurosurgery analyzed by its impact on glioblastoma surgery. **Neurological Research** 22: 354-360, 2000.

5 Psiani LJ, Comeau R, Davey BLK, Peters TM.: Incorporation of stereoscopic video into an image-guided neurosurgery environment. IEEE-EMBC, 365-366, 1995.

6 Peters TM, Comeau RM, Psiani L, Bakar M, Munger P, Davey, BLK: Visualization for image guided neurosurgery, IEEE-EMBC, 399-400, 1995.

7 Glombitza G, Lamade W, Demiris AM, Gøpfert MR, Mayer A, Bahner ML, Meinzer HP, Richter G, Lehnert T, Herfarth C: Virtual planning of liver resection:image processing, visualization and volumetric evaluation. Int. J. of Medical Informatics, 53, 225-237, 1999.

8 Hayashi N, Endo S, Shibata T, Ikeda H, Takaku A: Neurosurgical simulation and navigation with three-dimensional computer graphics. Neurosurgical Research, 21,1999.

9 Gronningsaeter A, Lie T, Kleven A, Mørland T, Langø, T, Unsgård G, Myhre HO, Mårvik R: Initial experience with stereoscopic visualisation of three-dimensional ultrasound data in surgery, **Surgical Endoscopy** 14:1974-1078, 2000.

10 Harbaugh RE, Schlusselberg DS Jeffrey R, Hayden S, Cromwell LD, Pluta D, English RA.:Three-dimensional computer tomograpic angiography in the preoperative evaluation of cerebrovascular lesions. Neurosurgery, 36: 320-326, 1995.

11 Hope JK, Wilson JL, Thomson FJ: Three-dimensional CT angiography in the detection and characterization of intracranial berry aneurysms. Am J. Neuroradiol 17:437-445, 1996.

12 Nakajima S, Atsumi H, Bhalerao AH, Jolesz FA, Kikinis R, Yoshimine T, Moriarty TM, Stieg PE: Computer-assisted surgical planning for cerebrovascular neurosurgery. Neurosurgery, 41:403-409, 1997.

13 Muacevic A, Steiger HJ: Computer-assisted resection of cerebral arteriovenous malformation. Neurosurgery, 45:1164-1171,1999.

14 Pflesser B, Leuwer R, Tiede U, Høhne KH: Planning and rehearsal of surgical interventions in the volume model. Medicine Meets Virtual Reality, 29-264,IOS Press, 2000.

15 Soler L, Delingette H, Malandain G, Ayache N, Koehl C, Clemet JM, Dourthe O, Marescaux J: An automatic virtual patient reconstruction from CT scans for hepatic surgical planning, Medicine meets virtual reality 2000, IOS press, 2000.

16 Hans P, Grant AJ, Laitt RD, Ramsden RT, Kassner A, Jackson A: Comparison of three-dimensional visualization techniques for depicting the scala vestibuli and scala Tympani of the cochlea by using high resolution MR imaging. Am J. Neuroradiol 20:1197-1206, 1999.

17 Kato Y, Sano H, Katada K, Ogura Y, Hayakawa M, Kanaoka N, Kanno T: Application of three-dimensional CT angiography (3D-CTA) to cerebral aneurysms, Surg Neurol, 52:113-22, 1999.

18 Masutani Y, Dohi T, Yamane F, Iseki H, Takakura K: Augmented reality visualization system for intravascular neurosurgery, Computer aided surgery 3:239-247, 1998.

19 Vannier MW: Evaluation of 3D imaging, in Critical reviews in diagnostic imaging 41:315-378, by CRC press LLC, 2000.

20 Anxionnat R, Bracard S, Ducrocq X, Trousset Y, Launay L, Kerrien E, Braun M, Vaillant R, Scomazzoni F, Lebedinsky A, Picard L: Intracranial aneurysms: Clinical value of 3D digital substraction angiography in terapeutic decision and endovascular treatment. Radiology, 218:799-808, 2001.

21 Wilkinson EP, Shahidi R, Wang B, Martin DP, Adler JR, Steinberg GK: Remote-rendered 3D CT angiography (3DCTA) as an intraoperative aid in cerebrovascular neurosurgery. Computer Aided Surgery, 4:256-263, 1999.

22 Walker, DG, Kapur T, kikinis R, Yezzi A, Zollei L, Bramley MD, Ma F,Black P.: Automatic segmentation and its use with an electromagnetic neuronavigation system, Abstract presentet at the 12th World Congress of neurosurgery, Sydney Australia, 16-20 September 2001.

23 Hill DLG, Maurer CR, Maciunas RJ, Barwise JA, Fitzpatrick JM, Wang MY: Measurement of intraoperative brain surface deformation under a craniotomy. **Neurosurgery** 43:514-526, 1998 .

24 Jödicke A, Deinsberger W, Erbe H, Kriete A, Böker DK: Intraoperative Three-Dimensional Ultrasonography: An Approach to Register Brain Shift using Multidimensional Image Processing. **Minim. Invas. Neurosurg** 41:13-19, 1998.

25 Nimsky C, Ganslandt O, Cerny S, Hastreiter P, Greiner G, Fahlbusch R: Quantification of, visualisation of and compensation for brain shift using intraoperative magnetic resonnance imaging. **Neurosurgery** 47:1070-1080, 2000.

26 Unsgaard, G., Ommedal S., Muller T., Gronningsaeter, A, Nagelhus Hernes, TA: Neuronavigation by intraoperative three-dimensional ultrasound: Initial experience during brain tumor surgery. Neurosurgery, 50, no 4, April 2002.

27 Hammoud MA, Ligon BL, ElSouki R, Shi WM, Schomer DF, Sawaya R: Use of intraoperative ultrasound for localizing tumors and determining the extent of resection: a comparative study with magnetic resonance imaging. **J Neurosurg** 84: 737-741,1996.

28 Knauth M, Wirtz CR, Tronnier VM, Aras N, Kunze S, Sartor K: Intraoperative MR imaging increases the extent of tumor resection in patients with high-grade gliomas. **Am J Neuroradiol** 20: 1642-1646, 1999.

29 Paleologos TS, Wadley JP, Kitchen ND, Thomas DGT: Clinical utility and cost-effectiveness of intraoperative image guided craniotomy: clinical comparison between conventional and image-guided meningioma surgery. **Neurosurgery** 47:40-48, 2000.

30 Tronnier VM, Bonsanto MM, Staubert A, Knauth M, Kunze S, Wirtz CR: Comparison of intraoperative MR imaging and 3D-navigated ultrasonography in the detection and resection control of lesions. **Neurosurg Focus** 10:1-5, 2001.

31 Oikarinen J, Hietala R, Jyrkinen L: Volume rendering using seed-filling acceleration:supporting cut planes by fast reseeding. Computer assisted surgery, 4:169-181, 1999.

32 Gronningsaeter A, Kleven A, Ommedal S, Aarseth TE, Lie T, Lindseth F, Langø T, Unsgård G: SonoWand, an ultrasound-based neuronavigation system. **Neurosurgery** 46: 1373-1379, 2000.

33 Bucholz RD, Yeh DD, Trobaugh J, McDurmont LL, Sturm CD, Baumann C, Henderson JM, Levy A, Kessman P: The correction of stereotactic inaccuracy caused by brain shift using an intraoperative ultrasound device. Presented in Lecture Notes in Computer Science Proceedings of the 1997 1st Joint

Conference of Computer Vision: **Virtual Reality and Robotics in Medicine and Medical Robotics and Computer-Assisted Surgery**, Grenoble, France, March, 19-22, 1977.

34 Hata N, Dohi T, Iseki H, Takakura K: Development of a frameless and armless stereotactic neuronavigation system with ultrasonographic registration, **Neurosurgery** 41: 608-614, 2000.

35 Tronnier VM, Wirtz CR, Knauth M, Lenz G, Pastyr O, Bonsanto MM, Albert FK, Kuth R, Staubert A, Sartor K, Kunze S: Intraoperative diagnostic and interventional magnetic resonance imaging in neurosurgery. **Neurosurgery** 40:891-902, 1997.

36 Wirtz CR, Kanuth M, Staubert A, Bonsanto MM, Sartor K, Kunze S, Tronnier VM: Clinical evaluation and follow-up results for intraoperative magnetic resonance imaging in neurosurgey. **Neurosurgery** 46:1112-1122, 2000.

37 Hernes TAN, Langø T, Lindseth F, Bang J, Unsgård G: Intraoperative 3D ultrasound in neuronavigation: Accuracy analysis and clinical considerations. Presented at the 12th World Congress of neurosurgery, Sydney, Australia, September 2001.

38 Wirtz CR, Knaut M, Hassfeld S, Tronnier VM, Albert FK, Bonsanto MM, Kunze S: Neuronavigation – first experiences with three different commercially available systems. Zentralbl Neurochir 59:14-22, 1998.

39 Dorward NL, Alberti O, Palmer JD, Kitchen ND, Thomas DGT: Accuracy of true frameless stereotaxi: in vivo measurement and laboratory phantom studies. J. Neurosurg 90:160-168, 1999.

40 Lindseth F, Ommedal S, Bang J, Unsgård G, Hernes TAN: Image fusion of ultrasound and MRI as an aid for assessing anatomical shifts and for improving overview and interpretation in ultrasound guided neurosurgery. Proc of the 15th International Congress and Exhibition in **Computer Assisted Radiology and Surgery**, (CARS2001) Berlin, June 27-30, 2001.

41 Jannin P, Fleig OJ, Seigneuret E, Grova C, Morandi X, Scarabin JM: A data fusion environment for multimodal and multi-informational neuronavigation. Computer Aided Surgery, %:1-10, 2000.

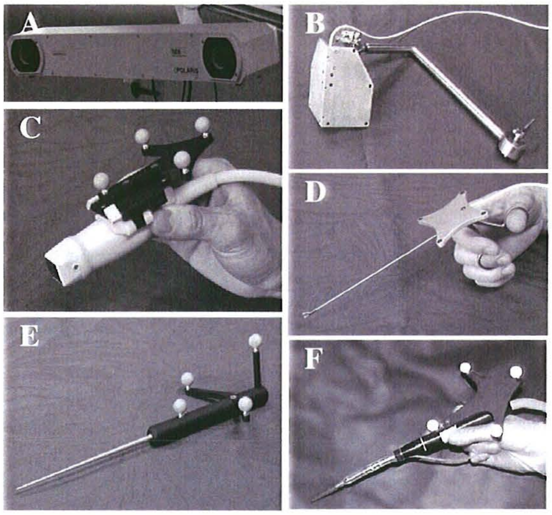

Figure 1: Various equipment used in 3D ultrasound based neuronavigation. A) Infrared cameras (Polaris, NDI, Canada) read the positions of all the sensors attached to the instruments used in the navigation system. B) Patient reference sensor frame. C) 4-8 MHz FPA ultrasound probe with sensor. The ultrasound probe is tilted over the area of interest and a 3D volume is acquired. D) Biopsy forceps with positioning device used for 3D ultrasound guidance of biopsies. E) Pointer. F) CUSA used for tumor resection.

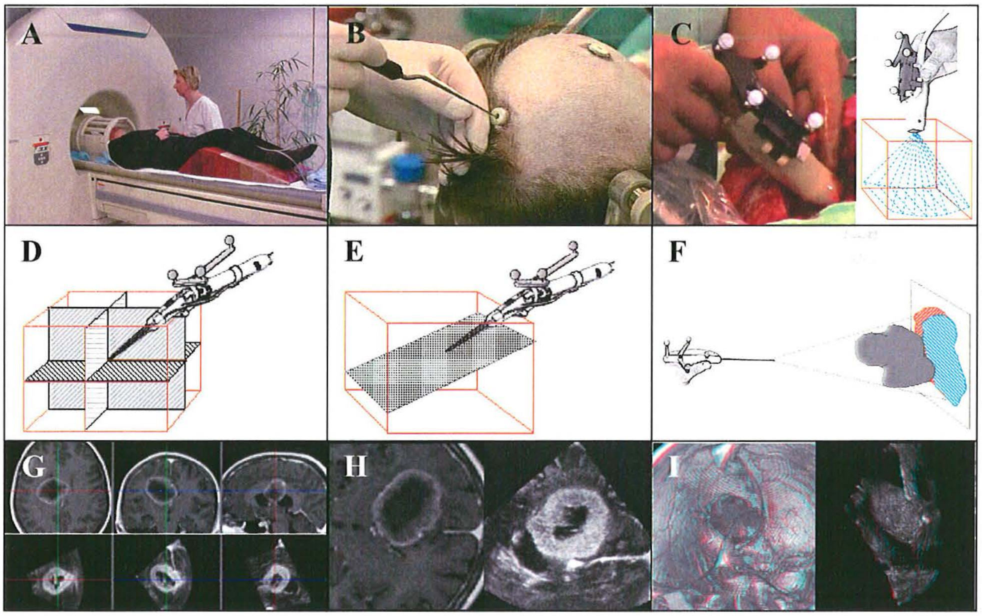

Figure 2: 3D image data acquisition and neuronavigation. A) The patient is scanned by MRI prior to surgery. B) 3D MRI data is registrated to the patient in the navigation system. C) High image quality 3D ultrasound image is acquired when needed. Both MR and ultrasound 3D image data volumes may be displayed using orthogonal slicing (D), anyplane slicing (E) or stereoscopic display (F). In orthogonal slicing (D), three slices are displayed from each 3D volume as shown in G; Six images are shown. Top row: Axial, sagittal and coronal slices from the preoperative MRI volume. Bottom row: Corresponding slices from intraoperative 3D ultrasound volume. In anyplane slicing (E) one slice from each 3D volume is displayed as shown in H; Left: preoperative MRI, Right: intraoperative ultrasound. For stereoscopic display technique (F), one projection from each volume is displayed according to the position of the surgical tool as shown in I; Left: preoperative MRI, Right: intraoperative ultrasound.

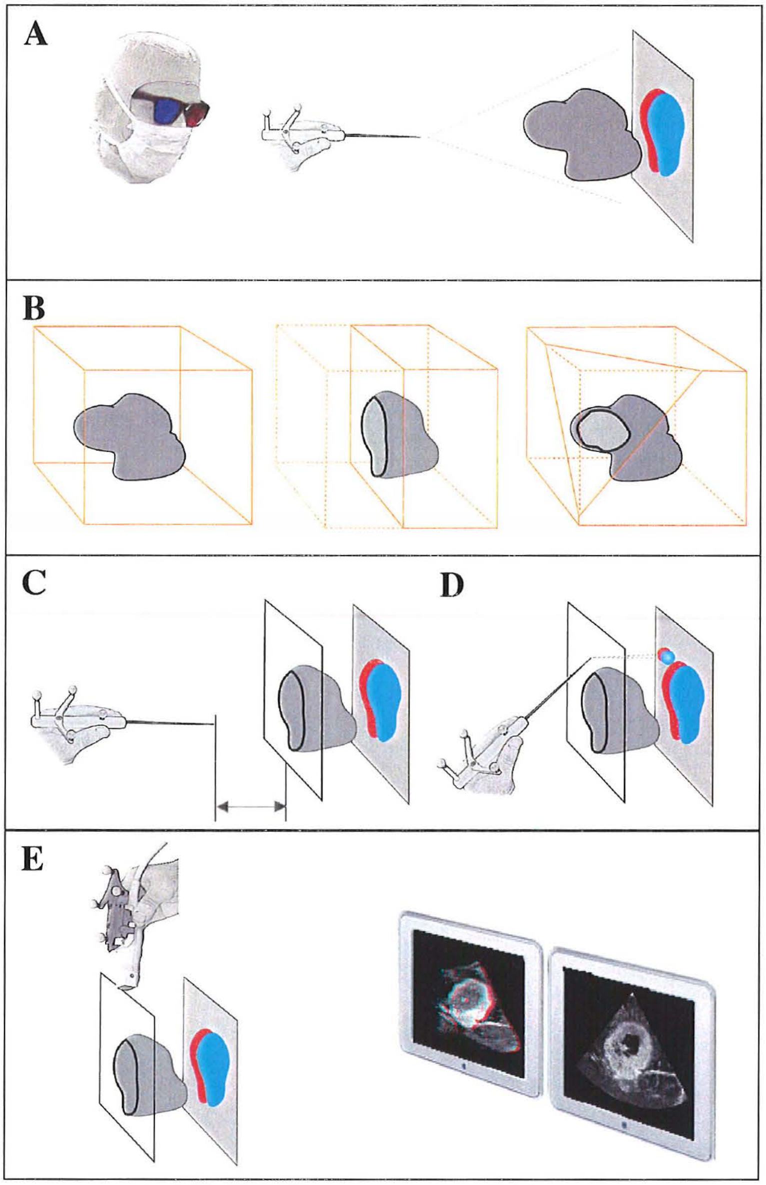

Figure 3: Interactive stereoscopic display techniques. The stereoscopic projection is interactively controlled by a pointer (A) or another surgical instrument. The 3D volume used for generating the stereoscopic projection may be decreased by virtually cutting away part of the volume from any angle (B) using a pointer (C), a surgical tool or the ultrasound probe (E). The 2D plane defining part of the volume to be excluded from the stereoscopic projection is called the "cut plane" of the stereoscopic projection. This plane may be parallel to or perpendicular to any instrument, and the distance from the instrument tip and the 2D plane may be varied interactively. The instruments may not only be used for controlling the projection view, but the position of the instrument may also be displayed in the projection (stereoscopic tool guidance) as shown in D. A sphere in the projection marks the position of the tip of the surgical tool in the patient and the position of the sphere in the projection will be interactively changed due to movement of the tip of the instrument. When the ultrasound probe is used for defining the cut plane (E), both the stereo cut plane projection and the corresponding real-time 2D image may be displayed simultaneously (E, right).

Figure 4: The stereoscopic images may be displayed in various ways; on a CRT screen by alternating the left and right eye views 120 times per second or by simple red/blue projections on conventional monitors as shown in the image. 3D vision is realized in a novel and a low cost way in the operation room and 3D perception of the structures in the brain is obtained. The monitors are easily moved in order to get the 3D view in an optimal distance to the surgeon during guidance.

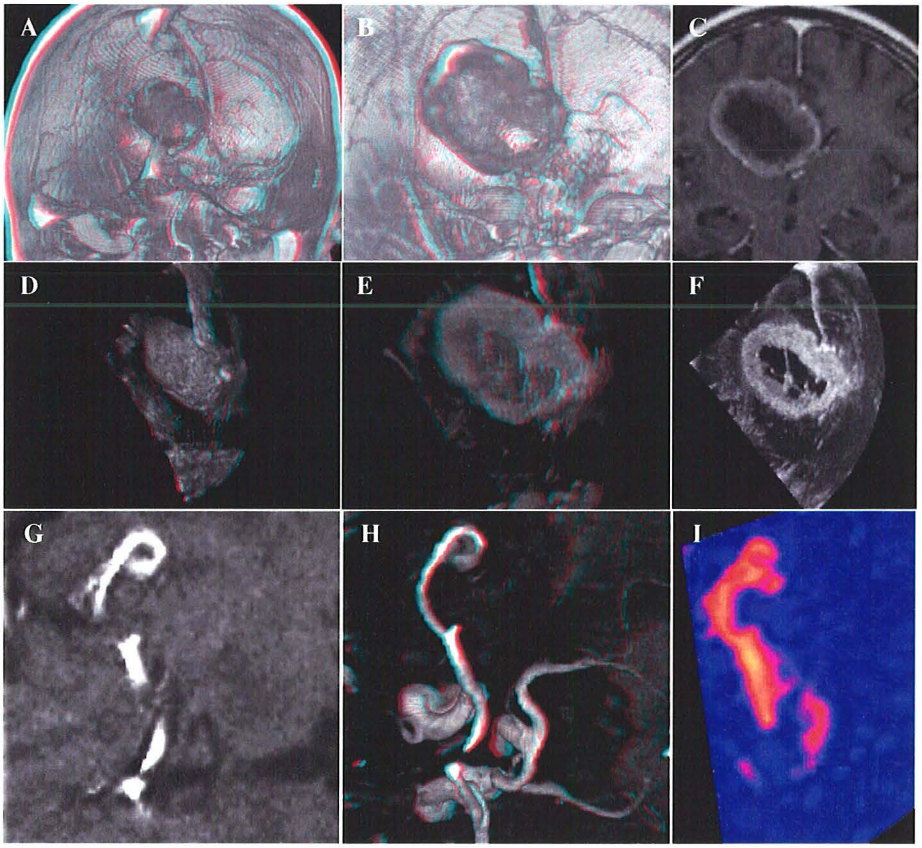

Figure 5: Stereoscopic cut plane visualization demonstrated from the feasibility stuides. Interactive stereoscopic visualization of a metastasis shown by preoperative MRI (A) and corresponding projection from intraoperative 3D ultrasound (D). The cut plane is set far from the tumor, so that the whole tumor may be seen in the projections. Figure B (MR) and E (ultrasound) show stereoscopic projections of the same tumor, but the cut planes are defined in the middle of the tumor. Projection based on MRI data of the tumor (B) gives a nice overview and corresponding projection based on intraoperative 3D ultrasound (E) gives important information of tumor border and characteristics inside the tumor. The anyplane tissue slices from the 3D volumes corresponding to the cut planes in the projections are shown in C (MRI) and F (ultrasound) and give even more detailed information. Figure G-I demonstrate visualizations from an aneurysm operation. Anyplane angiographies (G: MR, I: ultrasound power Doppler) corresponding to the stereoscopic cut plane visualization in H (MR) show that part of the 3D vessel strucures are not visible in the anyplane slices, but the stereoscopic cut plane of MRA (H) gives nice perception of the 3D orientation of the vessels behind the cut plane. Red blue glasses must be used to experience real 3D vision. Glasses may be received by contacting first author at e-mail: Toril.N.Hernes@sintef.no.

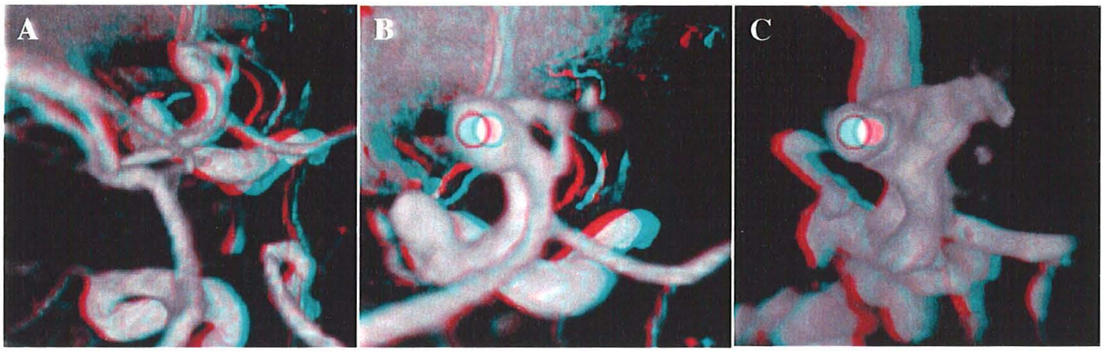

Figure 6: Stereoscopic tool guidance tested during a cerebrovascular aneurysm operation in the brain in a patient with two aneurysms. Figure A shows the two aneurysms from preoperative MR angiographies. Figure B shows a projection closer to the same two aneurysms as in A based on MRA. C: The same projection based on intraoperative 3D ultrasound power Doppler image, but only one of the aneurysms can be seen in the 3D ultrasound Doppler volume. In both B and C the projections were frozed and the pointer was used interactively to point at the aneurysms in the patient. Hence, the position of the tip of the pointer was marked with a sphere in the projections. Red blue glasses must be used to experience real 3D vision. Glasses may be received by contacting first author at e-mail: Toril.N.Hernes@sintef.no.

Paper VII

Paper IX

SonoWand, an Ultrasound-based Neuronavigation System

Aage Gronningsaeter, Ph.D., Atle Kleven, M.S., Steinar Ommedal, B.S., Tore Erling Aarseth, M.S., Torgrim Lie, M.S., Frank Lindseth, M.S., Thomas Langø, M.S., Geirmund Unsgård, M.D.

SINTEF Unimed, Trondheim, Norway (AG, AK, SO, TEA, TLi, FL, TLa), and Department of Neurosurgery (GU), University Hospital and Medical Faculty, Norwegian University of Science and Technology, Trondheim, Norway

OBJECTIVE: We have integrated a neuronavigation system into an ultrasound scanner and developed a single-rack system that enables the surgeon to perform frameless and armless stereotactic neuronavigation using intraoperative three-dimensional ultrasound data as well as preoperative magnetic resonance or computed tomographic images. The purpose of this article is to describe our two-rack prototype and present the results of our work on image quality enhancement.

DESCRIPTION OF INSTRUMENTATION: The system consists of a high-end ultrasound scanner, a modest-cost computer, and an optical positioning/digitizer system. Special technical and clinical efforts have been made to achieve high image quality. A special interface between the ultrasound instrument and the navigation computer ensures rapid transfer of digital three-dimensional data with no loss of image quality.

OPERATIVE TECHNIQUE: The positioning system tracks the position and orientation of the patient, the ultrasound probe, the pointer, and various surgical instruments. This makes it possible to update the three-dimensional map during surgery and navigate by ultrasound data in a similar manner as with magnetic resonance data.

METHODS: The two-rack prototype has been used for clinical testing since November 1997 at the University Hospital in Trondheim.

EXPERIENCE AND RESULTS: The image quality improvements have enabled us, in most cases, to extract information from ultrasound with clinical value similar to that of preoperative magnetic resonance imaging. The overall clinical accuracy of the ultrasound-based navigation system is expected to be comparable to or better than that of a magnetic resonance imaging-based system.

CONCLUSION: The SonoWand system enables neuronavigation through direct use of intraoperative three-dimensional ultrasound. Further research will be necessary to explore the potential clinical value and the limitations of this technology. (Neurosurgery 47:1373–1380, 2000)

Key words: Computer-assisted surgery, Frameless stereotaxy, Three-dimensional imaging, Ultrasonography

Several years of experience with computer-based navigation systems have clearly demonstrated the need for an intraoperative imaging modality that can cope with normal anatomic changes during cranial surgery. Three concepts seem to represent the options for the foreseeable future: 1) open magnetic resonance imaging (MRI), in which the patient must be transported in and out of a sterile draped magnet to update a three-dimensional (3-D) data set, which is typically a 30- to 70-minute process (22); 2) interventional MRI, in which the surgeon operates inside a sterile draped magnet, performing two-dimensional (2-D) imaging at close to real time and using slower 3-D scans (the typical 3-D acquisition time is 5 min); and 3) ultrasound, which requires only a small sterile draped scanhead in the field, rendering real-time 2-D scanning available as needed, as well as rapid 3-D acquisition several times during the procedure. The typical time required to update the 3-D ultrasound data set is 2 to 3 minutes, but in the future, technology will enable 3-D imaging in real time.

Expectations regarding intraoperative MRI systems are significant, but these systems require a large investment as well as a special operating room and surgical equipment, and they are expensive to run. Ultrasound has not been accorded much attention until recently, probably owing to limited image quality, lack of dedicated equipment, and limited skills to interpret such images. Some groups and companies have connected an ultrasound scanner to a conventional navigation system, digitized the analog video signal from the scanner, and displayed a real-time 2-D image on the navigation computer side by side with the corresponding MRI slice. This modality has proven beneficial for simplifying the interpretation of ultrasound and for the bulky identification and quantification of brain shift (4, 10, 11, 14, 20). However, these solutions require two space-consuming racks in the operating room, and they normally involve compromises on image quality and data transfer capability.

We have developed a different system that integrates a neuronavigation system into a high-end ultrasound scanner. The navigation computer and the optical digitizer or camera system are built into the ultrasound instrument, so that only one rack is required in the operating room. A digital interface between the ultrasound scanner and the navigation computer enables rapid communication of digital data with no loss of image quality. A phased array probe is normally selected, which is a convenient probe with a relatively small footprint. The image quality is optimized for the brain through selection of suitable scanning parameters. Furthermore, special actions are taken to optimize image quality during patient preparation and surgical planning as well as during the clinical procedure.

The result is a single-rack neuronavigation system called SonoWand, which can work as a stand-alone ultrasound scanner, a conventional MRI- or computed tomography (CT)- based neuronavigation system, and a neuronavigation system with rapid access to intraoperative 3-D ultrasound data. The system enables the surgeon to plan the operation using conventional MRI navigation, to obtain a 3-D ultrasound scan and compare the two modalities before opening the dura mater, and then to guide the operation through the repeated acquisition of 3-D ultrasound data.

A two-rack prototype has been used for clinical testing since November 1997 at the University Hospital in Trondheim. A single-rack prototype was built recently (*Fig. 1*), and this version will be subjected to clinical trials and further research and development at the University of Heidelberg as well as in Trondheim. Commercialization of the system is managed by MISON AS (Trondheim, Norway), which owns the rights to the SonoWand brand name. This article describes the two-rack prototype and presents the results of our work on image quality enhancement. The resolution and accuracy of the system are described in a companion article (A Gronningsaeter, F Lindseth, T Langø, G Unsgård, submitted for publication), and the clinical experience from more than 45 cases will be described in another article (G Unsgård, manuscript in preparation).

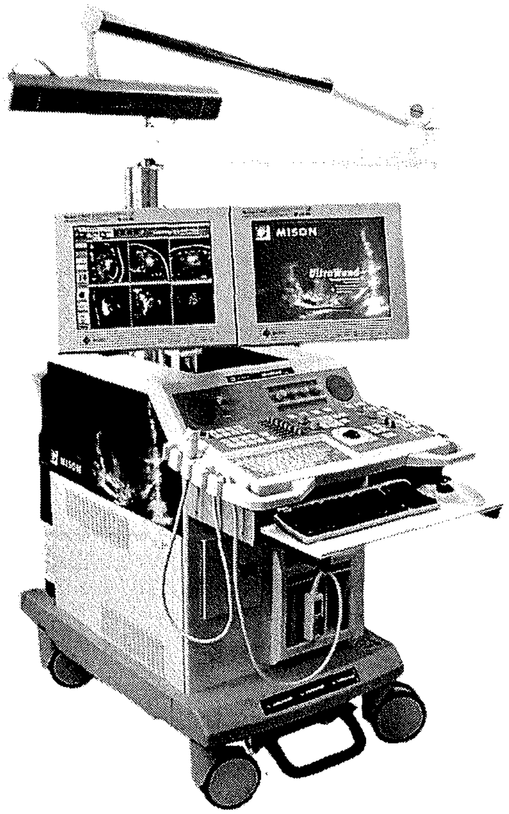

FIGURE 1. The SonoWand prototype is a single-rack system that can operate as a stand-alone ultrasound scanner or a conventional MRI- or CT-based neuronavigation system with rapid access to intraoperative 3-D ultrasound.

TECHNICAL DEVELOPMENTS

The navigation equipment

The prototype system consists of a high-end System FiVe ultrasound scanner (GE Vingmed Ultrasound, Horten, Norway), a medium-cost Genesis MP900 computer (DayStar Digital, Flowery Branch, GA) for image processing and navigation, and an optical positioning system (3-D digitizer or tracking system). We have used the camera unit of the VectorVision system (BrainLAB, Heimstetten, Germany) as the positioning system in the two-rack prototype. However, an interface has lately been made available for the FlashPoint 5000 (Image Guided Technologies, Inc., Boulder, CO) and Polaris (Northern Digital, Waterloo, Ontario, Canada) systems, which is a prerequisite for integration into a commercial single-rack solution. Two adjustable arms have been attached to the top of the scanner, one for the camera system and one for two flat-screen monitors. One monitor is used for the ultrasound scanner, and the other is used for the navigation computer. A direct ethernet link has been established between the ultrasound scanner and the navigation computer to provide rapid transfer of high-quality digital 3-D ultrasound data. MRI or CT data can be imported into the navigation computer through an ethernet connection using the digital imaging and communications in medicine standard.

The position and orientation of the Mayfield frame, pointer devices, ultrasound probes, and surgical instruments can be measured by the camera system when a positioning frame has been attached to the device. All positioning frames are equipped with three reflecting spheres. *Figure 2* shows the three ultrasound probes that have been used in clinical trials. A special adapter is glued to each probe to enable repetitive and precise placement of the positioning frame, even through the sterile drape.

Two different surgical instruments also have been equipped with positioning frames, as illustrated in *Figure 3*. One frame is permanently fixed to biopsy forceps, and another frame can be attached to a Cavitron System 200 ultrasonic surgical aspirator (Valleylab, Boulder, CO) with a simple hand grip. These instruments can be used as pointer devices, and their distal tips can be navigated into the brain using the image information on the monitor. A pointer device with three reflecting spheres (two is normal) also has been designed, which enables the surgeon to measure the position and direction of the pointer as well as the degree of rotation.

Registration and calibration algorithms

The system implements a standard patient registration algorithm (based on skin fiducials or anatomic landmarks) to allow conventional navigation using preoperative magnetic resonance images. Furthermore, we have developed a method to calibrate the ultrasound probe so that the computer can calculate the exact position and orientation of the ultrasound scan plane on the basis of the measured position and orientation of the attached positioning frame. Accurate probe calibration for each individual probe in the laboratory is accomplished with the use of a specially designed water tank. Finally, a specific calibration algorithm has been developed for the ultrasound aspirator because the positioning frame must be mounted to the aspirator under sterile conditions. To acquire 3-D ultrasound data, the probe is tilted approximately 90 degrees by hand for approximately 15 seconds.

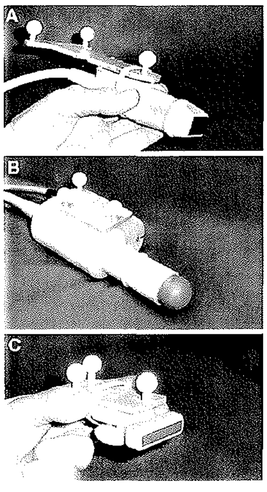

FIGURE 2. Ultrasound probes with passive optical positioning adapters attached: *A*, 4- to 8-MHz phased array for overview imaging and freehand 3-D scans. *B*, motorized 3-D probe with a 5-MHz annular array transducer. *C*, a 5- to 9-MHz linear array for superficial imaging.

The navigation software

The navigation software can import MRI or CT data, perform patient registration, and display navigation images on the monitor. In addition, the system can acquire 3-D ultrasound data by tracking the position and orientation of the ultrasound probe during a freehand probe movement. To acquire a pyramid-shaped volume of the brain, the probe typically is tilted 90 degrees for 15 seconds. The digital images are reconstructed as a regular volume, and the navigation software handles this ultrasound volume in a similar fashion as for the MRI and CT volumes. The system supports three different navigation features as described below.

Ultrasound probe-driven any-plane slicing

The first navigation feature is based on the ultrasound probe used for real-time 2-D scanning, in which the ultrasound image is displayed on the ultrasound monitor. The position and orientation of the probe are tracked by the positioning system, and the corresponding cross sectional slice through the preoperative MRI or CT data set is displayed on the navigation monitor. This technique is similar to that reported previously by other groups, except that we display the two images on two different monitors.

Instrument-driven orthogonal slicing

The second navigation feature is similar to the conventional orthogonal display technique available on most neuronavigation systems. The surgeon can use a pointer to obtain axial, coronal, and sagittal views from a preoperative MRI or CT data set. However, an additional set of axial, coronal, and sagittal views taken from an intraoperative 3-D ultrasound data set also can be provided (*Fig. 4*). Visualization is controlled by the active tool, which can be a pointer, biopsy forceps, or an ultrasound aspirator. The instrument axis is indicated on the images with a dashed line, and the tip is indicated by crosshairs. This display mode facilitates easy identification and localization of residual tumor fractions using the instrument tip.

Instrument-driven any-plane slicing

The third navigation feature represents a combination and simplification of the two methods that have been mentioned. To reduce the amount of information, only two images are displayed: one MRI slice and the corresponding ultrasound slice as described in the first navigation features. However, the navigation device is no longer the ultrasound probe; it is a pointer or surgical instrument. Furthermore, both slices are obtained from 3-D volumes as in the second method, but the slices are not restricted to coronal, axial, or sagittal views. This technique is illustrated in *Figure 5*, and it provides the surgeon more flexibility to display arbitrary cross sections. The re-

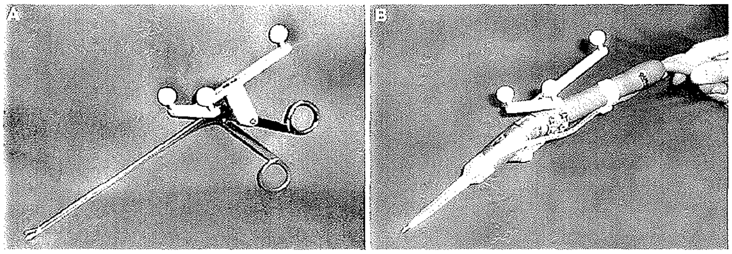

FIGURE 3. Surgical instruments such as biopsy forceps (*A*) and Cavitron ultrasonic surgical ultrasound aspirator (*B*) can be equipped with positioning adapters. The instruments can be navigated deep into the brain using image guidance.

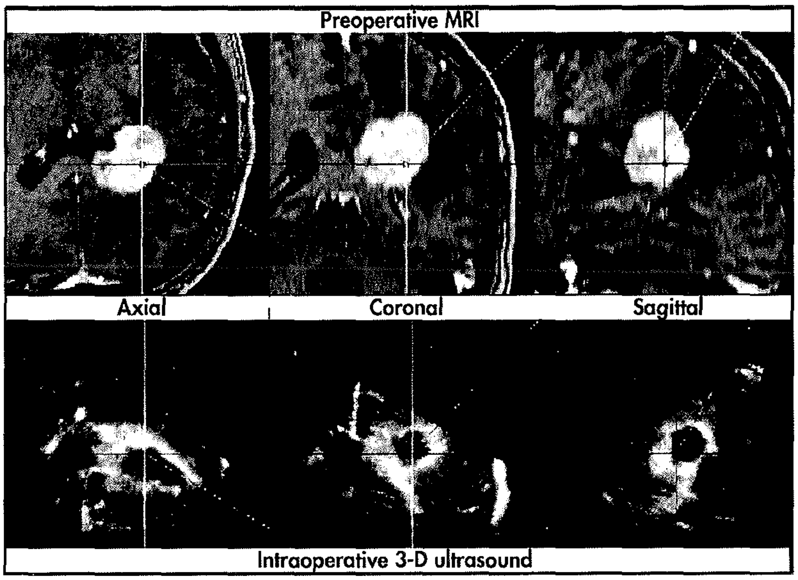

FIGURE 4. The instrument-driven orthogonal slicing technique facilitates comparison between preoperative MRI and intraoperative 3-D ultrasound using pairs of corresponding axial, coronal, and sagittal images. The ultrasound aspirator tip has been navigated into the resection cavity to identify and localize residual tumor tissue in a glioblastoma.

duced information content on the monitor also simplifies the interpretation for the surgeon.

Image quality improvement efforts

Phased array probes (*Fig.* 2*A*) have been developed primarily for cardiac imaging. The probe footprint is relatively small for the beam to pass between the ribs, and the scanning parameters are optimized for imaging deep-seated moving structures such as the valves and the myocardium. The small footprint meets the need for brain imaging from a small craniotomy, but the high frame rate setup does not. We have optimized the scanning setup for stationary structures, building one image by using up to nine beam shots per beam direction and optimize both the transmitter focusing and receiver focusing in each depth zone. The result is very high resolution in both the radial direction (along the beam) as well as in the lateral direction (perpendicular to the beam). Unfortunately, the resolution in the elevation direction (the "thickness" of the scan plane) cannot be adjusted electronically with this type of probe. The resolution along the direction of 3-D acquisition will therefore be limited, especially outside the focal region (very close to and very far from the transducer). Furthermore, the scanning sector is narrow in the near field and broad in the deeper regions. Therefore, this probe is best suited for lesions that are located several centimeters from the surface.

An annular array is an alternative to a phased array transducer. These transducers have a circular symmetric beam, so the resolutions in the lateral and elevation directions are equal and can be adjusted electronically. 2-D sector scanning is achieved through a rapid motorized tilting movement. We expected this probe to yield better spatial resolution, especially in the direction of 3-D acquisition and far from the transducer. Therefore, a motorized 3-D prototype probe (*Fig.* 2*B*) was built to compare the two different arrays and acquisition techniques. 3-D acquisition is achieved by rotating the internal 2-D probe assembly using a second motor.

Linear array probes (*Fig.* 2*C*) have been designed primarily for transcutaneous vascular imaging. The transducer frequency is higher than the phased array probe, yielding better spatial resolution at the expense of lower penetration. The footprint is larger (approximately 10 × 40 mm), and the field of view is rectangular. Because of these properties, this probe

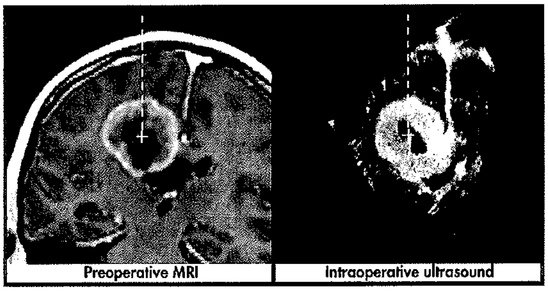

FIGURE 5. The instrument-driven any-plane slicing technique displays only one set of corresponding images. The two images are obtained from their corresponding 3-D volumes in a cross section, which is located in front of the instrument. This technique simplifies the perception and provides more flexibility for the operator to display any desired cross section in the region of interest.

is best suited for imaging superficial lesions from a larger craniotomy. The scanning parameters for this probe have been optimized to improve the quality of brain imaging.

RESULTS

The technical developments and clinical work undertaken to improve image quality have been very successful. The quality of the ultrasound images enables the surgeon to use 3-D ultrasound in a similar manner to other groups acquiring 3-D MRI data for navigation and surgical guidance. An example of the image quality from the 4- to 8-MHz phased array probe is shown in *Figure 6A*. Fine details can be observed with high spatial resolution even at depths of 7 to 8 cm. Because the system is capable of updating the 3-D map several times during surgery, brain shift is no longer a severe problem. Furthermore, we have found that the accuracy of the system is comparable to or even better than conventional navigation systems that are based on preoperative MRI.

The motorized 3-D probe with an annular array transducer did not improve 3-D resolution compared with the phased array transducer as expected. One explanation is that mechanically scanning probes have limited optimization ability for 2-D image quality compared with electronically scanned probes. Furthermore, the transducer array was also slightly smaller, yielding a lower resolution in general. Consequently, the probe was rarely used in the clinic.

The 5- to 9-MHz linear array probe has been used occasionally for superficial lesions. An example from a glioblastoma with multiple cysts is shown in *Figure 6B*, in which spatial resolution seems smaller than 1 mm. Although this is not yet documented, we think that this probe yields better-resolution images than the corresponding preoperative whole-brain magnetic resonance images using the Gyroscan S15 HQ scanner (Philips Medical Systems, Eindhoven, The Netherlands). Regardless of probe type, ultrasound often provides details and structures that cannot be observed in the corresponding MRI data set.

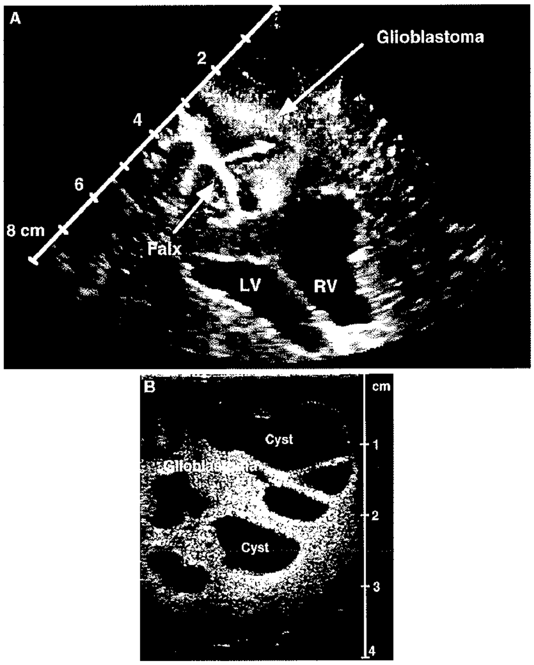

FIGURE 6. High-quality ultrasound is possible to achieve if a high-performance ultrasound scanner is optimized with a convenient probe for brain imaging. *A*, coronal overview image using the 4- to 8-MHz phased array. *LV*, left ventricle; *RV*, right ventricle. *B*, superficial image of a glioblastoma with multiple cysts using the 5- to 9-MHz linear array.

DISCUSSION

The importance of high image quality

On the basis of our experience with ultrasound in neurosurgery (9, 13, 21), we are surprised that ultrasound has not gained more acceptance among neurosurgeons. The first experiments with ultrasound pulse echo in the human brain were performed in the early 1950s (16). However, real-time 2-D imaging was not introduced until the late 1960s to early 1970s. As commercial instruments became available in the 1980s, researchers and surgeons thought the technique would become an important tool for brain surgery. However, the first period of enthusiasm was followed by disappointment. Currently, neurosonography has gained a certain amount of acceptance for localizing various tumors, hematomas, cysts, blood vessels, aneurysms, and necrotic areas (2, 5, 7). Some groups also have used ultrasound to localize residual tumor tissue and improve gross total resection (17, 23). Ultrasound-guided biopsy is quite common, and some research groups are studying more sophisticated projects such as ultrasound-guided endoscopy (1) and 3-D ultrasound (4, 6, 15). However, the use of ultrasound is sparse compared with the use of CT and MRI.

Some possible explanations are addressed by Roberts (19), Kelly (12), Maciunas (18), and Barnett (3) in their comments on an article by Hata et al. (10): 1) ultrasound has demonstrated limited quality owing to poor spatial and contrast resolution and artifacts or dropouts from blood, air, and instruments; and 2) commercial ultrasonography provides only 2-D cross sectional images that are normally obliquely oriented, making it difficult to relate structures observed on the monitor to the anatomy of the patient. All these limitations have been addressed during the design and clinical application of the SonoWand, and we think that these problems have now been minimized.

Direct or indirect use of 3-D ultrasound

Along with other research groups, we find the comparison between real-time 2-D ultrasound and the corresponding MRI slice useful for the interpretation of ultrasound as well as for identification of brain shift (4, 10, 11, 14, 20). However, a conventional MRI-based neuronavigation system benefits only slightly from a 2-D ultrasound system that simply identifies brain shift. The ideal system should be able to modify the images so that the 3-D map corresponds to the anatomy at any time. Some groups have tried to solve this problem using intraoperative 3-D ultrasound in an indirect way by measuring brain shift and transferring this information to the navigation system (6). The movement of some anatomic landmarks can be registered in the ultrasound volumes and transferred to an elastic model that manipulates the preoperative MRI volume correspondingly (4). The surgeon must then trust this manipulated preoperative MRI volume and navigate according to it.

We have solved this problem in a more direct way by navigating with 3-D ultrasound. A direct comparison between preoperative MRI and intraoperative 3-D ultrasound is useful before beginning the resection, because MRI and ultrasound represent the tissue characteristics differently. If brain shift occurs, however, we navigate solely by 3-D ultrasound. This is possible because of the high image quality of SonoWand, its high navigation accuracy, and an acceptable ability to differentiate tumor tissue from normal brain structures, even in low-grade astrocytomas. The latter factor is not yet fully understood and will be subjected to further research.

Real-time 3-D ultrasound

A modern high-end ultrasound scanner is capable of scanning approximately 20 high-quality, wide-sector images per second. By reducing the sector width and spatial resolution, several hundred images per second can be scanned. This means that a limited 3-D sector, for example 30 degrees in both directions, can be scanned several times per second. This technique will require either an advanced scanner with electronic beam steering in both directions or a probe with motorized movement of the 2-D scan plane. Commercial availability of both techniques is expected within a few years. Real-time 3-D imaging will make it possible to observe the moving surgical instrument directly in the image relative to the surrounding structures. Currently, only a computer model of the instruments, such as a colored line with crosshairs, overlays the images. We expect future technological improvements to increase surgeons' confidence in the navigation system, as well as to make possible the development of a simpler and more intuitive user interface for computer-aided neurosurgery. We have prepared the SonoWand system for this future upgrade using a rapid, custom-designed communication protocol between the ultrasound scanner and the navigation computer. This protocol will enable real-time transfer of raw digital data without loss of image quality.

Video signal or digital data transfer

Vendors of conventional neuronavigation systems are working to integrate ultrasound into their products. They hope to provide an interface to any ultrasound scanner that will allow customers the ability to chose their ultrasound system. Because composite video is the only image standard currently provided by all ultrasound vendors, most companies design a video cable between the two systems, using a video-grabbing board in their navigation system. This strategy has a number of limitations, however, including quality loss attributable to digital-to-analog-to-digital conversions, limited control over the exact geometry of the ultrasound image, and a constant and limited frame rate (typically 25–30 interlaced, resulting in 12.5–15.0 full frame images/s). Many ultrasound vendors provide a digital imaging and communications in medicine standard, meaning that the images can be transferred in digital form. However, this standard does not provide real-time data transfer capability, which is a prerequisite for real-time 2-D and future 3-D ultrasound.

SonoWand is based on a custom-designed direct ethernet link between the ultrasound scanner and the navigation computer; therefore, there is no quality loss associated with data transfer because of digital representation. The system also has full control of the geometry of the ultrasound images, because such information is transferred with the 3-D data set. Finally, this interface is well suited for a further upgrade to real-time digital transfer.

CONCLUSION

We have developed an ultrasound-based neuronavigation system that enables the surgeon to perform freehand and armless stereotactic neuronavigation using intraoperative 3-D ultrasound images as well as preoperative magnetic resonance or computed tomographic images. The navigation system is physically integrated into an ultrasound scanner, and this single-rack solution occupies less space in the operating room than more common two-rack systems. A high-performance ultrasound scanner has been selected, and technical and clinical enhancements have been made to improve image quality. The quality of the images and the accuracy of the system make possible direct navigation using 3-D ultrasound in a similar manner to conventional MRI- or CT-based systems. Tight electronic integration between the ultrasound scanner and the navigation computer maintains the rapid transfer of high-quality digital ultrasound data. Therefore, the system is well prepared for a future upgrade to real-time 3-D operation.

ACKNOWLEDGMENTS

This work was supported by the Research Council of Norway, the Ministry of Health and Social Affairs, GE Vingmed Ultrasound (Horten, Norway), the Norwegian Industrial and Regional Development Fund, and the Norwegian Cancer Society.

DISCLOSURE

At the time this study was initiated, all of the authors were research scientists and had no financial involvement or interest in the SonoWand concept. Since the establishment of MISON AS, Trondheim, Norway, and the start of the commercialization phase of the prototype, AG has become Chief Executive Officer of the company, AK is Director of Development, TEA and TL are system developers, and GU is on the board of directors. The authors may therefore benefit in the future from a potential commercial success of the system and company.

Received, May 8, 2000.
Accepted, August 7, 2000.
Reprint requests: Aage Gronningsaeter, Ph.D., MISON AS, Center of Medicine and Technology, 7489 Trondheim, Norway. Email: aage.gronningsaeter@mison.no

REFERENCES

1. Auer LM: Ultrasound stereotaxic endoscopy in neurosurgery. **Acta Neurochir Suppl (Wien)** 54:34–41, 1992.
2. Auer LM, van Velthoven V: Intraoperative ultrasound (US) imaging: Comparison of pathomorphological findings in US and CT. **Acta Neurochir (Wien)** 104:84–95, 1990.
3. Barnett GH: Development of a frameless and armless stereotactic neuronavigation system with ultrasonographic registration. **Neurosurgery** 41:614, 1997 (comment).
4. Bucholz RD, Yeh DD, Trobaugh J, McDurmont LL, Sturm CD, Baumann C, Henderson JM, Levy A, Kessman P: The correction of stereotactic inaccuracy caused by brain shift using an intraoperative ultrasound device. Presented in Lecture Notes in Computer Science Proceedings of the 1997 1st Joint Conference of Computer Vision: Virtual Reality and Robotics in Medicine and Medical Robotics and Computer-Assisted Surgery, Grenoble, France, March 19–22, 1997.
5. Chandler WF, Knake JE, McGillicuddy JE, Lillehei KO, Silver TM: Intraoperative use of real-time ultrasonography in neurosurgery. **J Neurosurg** 57:157–163, 1982.
6. Erbe H, Kriete A, Jödicke A, Deinsburger W, Böker DK: 3D-ultrasonography and image matching for detection of brain shift during intracranial surgery. Presented at the meeting of Computer Assisted Radiology, Paris, France, 1996.
7. Gaab MR: Intraoperative ultrasound imaging in neurosurgery [in German]. **Ultraschall Med** 11:62–71, 1990.
8. *Deleted in proof.*
9. Gronningsaeter A, Unsgård G, Ommedal S, Angelsen BAJ: Ultrasound-guided neurosurgery: A feasibility study in the 3–30 MHz frequency range. **Br J Neurosurg** 10:161–168, 1996.
10. Hata N, Dohi T, Iseki H, Takakura K: Development of a frameless and armless stereotactic neuronavigation system with ultrasonographic registration. **Neurosurgery** 41:608–614, 1997.
11. Hirschberg H, Unsgaard G: Incorporation of ultrasonic imaging in an optically coupled frameless stereotactic system. **Acta Neurochir Suppl (Wien)** 68:75–80, 1997.
12. Kelly PJ: Development of a frameless and armless stereotactic neuronavigation system with ultrasonographic registration. **Neurosurgery** 41:613–614, 1997 (comment).
13. Kleven A, Lie T, Kaspersen JH, Aarseth TE, Lindseth F, Gronningsaeter A, Unsgård G, Myhre HO, Mårvik R: An ultrasound based navigation system for minimally invasive surgery. Presented at the 6th World Congress of Endoscopic Surgery, Rome, Italy, May 31–June 6, 1998.
14. Koivukangas J, Louhisalmi Y, Alakuijala J, Oikarinen J: Ultrasound-controlled neuronavigator-guided brain surgery. **J Neurosurg** 79:36–42, 1993.
15. Koivukangas J, Ylitalo E, Alasaarela E, Tauriainen A: Three-dimensional ultrasound imaging of brain for neurosurgery. **Ann Clin Res** 18[Suppl 47]:65–72, 1986.
16. Leksell L: Echo-encephalography: Part I—Detection of intracranial complications following head injury. **Acta Chir Scand** 110: 301–308, 1955.
17. LeRoux PD, Winter TC, Berger MS, Mack LA, Wang K, Elliott JP: A comparison between preoperative magnetic resonance and intraoperative ultrasound tumor volumes and margins. **J Clin Ultrasound** 22:29–36, 1994.
18. Maciunas RJ: Development of a frameless and armless stereotactic neuronavigation system with ultrasonographic registration. **Neurosurgery** 41:614, 1997 (comment).
19. Roberts DW: Development of a frameless and armless stereotactic neuronavigation system with ultrasonographic registration. **Neurosurgery** 41:613, 1997 (comment).
20. Trobaugh JW, Richard WD, Smith KR, Bucholz RD: Frameless stereotactic ultrasonography: Method and applications. **Comput Med Imaging Graph** 18:235–246, 1994.
21. Unsgård G, Kleven A, Ommedal S, Gronningsaeter A: Intraoperative ultrasound and neuronavigation. Presented at the European Congress of Neurosurgery, Copenhagen, Denmark, September 19–24, 1999.
22. Wirtz CR, Bonsanto MM, Knauth M, Tronnier VM, Albert FK, Staubert A, Kunze S: Intraoperative magnetic resonance imaging to update interactive navigation in neurosurgery: Method and preliminary experience. **Comput Aided Surg** 2:172–179, 1997.
23. Woydt M, Krone A, Becker G, Schmidt K, Roggendorf W, Roosen K: Correlation of intra-operative ultrasound with histopathological findings after tumour resection in supratentorial gliomas: A method to improve gross total tumour resection. **Acta Neurochir (Wien)** 138:1391–1398, 1996.

COMMENTS

This article describes an interesting adaptation of ultrasonography for neurosurgical intraoperative navigation. With ultrasonography comes the promise of both inexpensive and readily available real-time intraoperative neuronavigation. Two major problems associated with ultrasound neuronavigation are poor spatial resolution because of two-dimensional cross-sectional imaging and poor contrast resolution because of signal-to-noise problems. The authors' methods help to minimize these concerns. Considerable differences remain, however, between the spatial resolution obtainable by computed tomography (CT) and the image resolution obtainable by magnetic resonance imaging (MRI). Combining preoperative MRI or CT studies with real-time ultrasonography does not solve that problem. It is far more difficult to identify and accurately navigate to small, benign lesions than to large, malignant ones. In addition, more important questions remain to be answered when deciding whether it is necessary to get that last little bit of tumor. Will it improve the patient's quality of life? Will it improve the patient's survival time? Although the utility of preoperative brain imaging is uncertain, any enhancements are welcome and should ultimately result in improved neurosurgical procedures. This excellent work will serve as a useful tool in advancing the frontiers of neurosurgery.

Roy A.E. Bakay
Chicago, Illinois

This technical article, written by seven engineers and a neurosurgeon, describes the two-rack prototype derived from a single-rack neuronavigational system called SonoWand (MISON, Trondheim, Norway). The focus of the article is the peroperative use during neuronavigation of ultrasonography with instruments equipped with positioning adapters that ultrasonography can recognize, with the aim of correcting brain shift in real time. The idea is not new, but until now the quality of the images obtained by ultrasonography was far below that obtainable by MRI. The figures presented in this article are quite provocative, especially *Figure 5*, which is competitive with peroperative MRI. The authors solved the problem by developing an intraoperative three-dimensional ultrasound that can be coupled with preoperative CT or MRI scans. Of course, this is a preliminary article preceding another submitted report on the accuracy of that system, with clinical experience to be described later. Stereotactic accuracy has to be demonstrated and validated to be compared with the most sophisticated navigation systems already on the market, but this is perhaps an economical alternative to costly operative MRI studies. The authors have made an excellent and original contribution that opens a new window to neuronavigation of the future.

Benoit Pirotte
Jacques Brotchi
Brussels, Belgium

This straightforward technical report describes a logical extension of frameless stereotaxy by the addition of ultrasonic imaging-guided surgery. The concept is simple: have tracking fiducials on the ultrasonic transducer that allow the computer to place the ultrasonic images (obtained intraoperatively) into the three-dimensional surgical workspace defined by the frameless stereotactic system (VectorVision; BrainLAB, Heimstetten, Germany). The system is housed in a convenient and unobtrusive vehicle for the operating room. It allows real-time imaging of the surgical field but also correlation of these real-time ultrasonic images to retrospective databases (CT and MRI). This method is being proposed as a less expensive alternative to MRI and CT scanners in the operating room.

Patrick J. Kelly
New York, New York

Much attention has been paid recently to the possible use of intraoperative MRI during neurosurgical procedures. Although this technique is promising, the possibility of real-time imaging is very limited, the equipment is expensive, and the position of the neurosurgeon and the patient is restricted during the procedure. This article discusses an attractive alternative for intraoperative imaging. Ultrasonography has been used in neurosurgery since the 1950s. Recent developments in the technique allow high-resolution real-time scanning in two dimensions and in the near future will probably allow real-time three-dimensional imaging. The concept of frameless and armless stereotactic neuronavigation by means of intraoperative three-dimensional ultrasonography is clearly very interesting. The present article mainly gives a technical description of the system.

Iver Langmoen
Stockholm, Sweden